

Analysis note [#656](#) for ‘Measurements of e+e- production in Au+Au collisions at  $\sqrt{s_{NN}} = 27, 39$ , and 62.4 GeV from the STAR experiment’

Authors: Joseph Butterworth, Xin Dong, Frank Geurts, Yi Guo, Bingchu Huang, Patrick Huck, Lijuan Ruan, Zebo Tang, Chi Yang, Yifei Zhang, and Jie Zhao

Section on Au+Au @  $\sqrt{s_{NN}} = 39 + 62$  GeV ..... pg. 2

Section on Au+Au @  $\sqrt{s_{NN}} = 27$  GeV ..... pg. 29

# Di-electron spectra for Au+Au 39GeV and 62.4 GeV

Yi Guo

October 14, 2015

## Contents

<b>1</b>	<b>Data Set</b>	<b>5</b>
<b>2</b>	<b>Electron Selection and Purity</b>	<b>6</b>
2.1	Pure sample selection	7
2.2	Purity and hadron contamination	8
<b>3</b>	<b>Background and Signal</b>	<b>9</b>
3.1	Like-sign Background	10
3.2	Photon Conversion Background	11
<b>4</b>	<b>Efficiency</b>	<b>12</b>
4.1	Single electron efficiency	12
4.1.1	TPC tracking efficiency	12
4.1.2	TOF efficiency	13
4.1.3	PID efficiency	14
4.2	Pair efficiency	15
<b>5</b>	<b>Systematic Uncertainty</b>	<b>16</b>
<b>6</b>	<b>Simulation</b>	<b>17</b>
6.1	$p_T$ input	18
6.2	Decay kinematics	18
6.3	Charm contribution	19
6.4	Momentum resolution and $J/\psi$ yield	21
<b>7</b>	<b>Final Result</b>	<b>24</b>
7.1	Di-electron spectra	24
7.2	Acceptance corrected excess spectra	25

## List of Figures

1	Vertex distribution for Au+Au $\sqrt{s_{NN}} = 39$ GeV. Red lines depicts the event selection cuts.	5
2	Vertex distribution for Au+Au $\sqrt{s_{NN}} = 62.4$ GeV. Red lines depicts the event selection cuts.	5
3	Left: the distribution of inverses beta vs momentum for 39 GeV. Right: the $n\sigma_e$ distributions after TOF PID selection. The red lines depict the PID selection cuts.	6
4	Left: the distribution of inverse beta vs momentum for 62.4 GeV. Right: the $n\sigma_e$ distributions after TOF PID selection. The red lines depict the PID selection cuts.	6
5	Pure sample selection criteria. Left panel: $m^2$ distributions, pure hadron samples are selected by cut on the black region. Right panel: the correlation between decay length and primary mass. Pure electron samples are selected by cutting on the two red boxes.	7
6	$n\sigma_e$ distributions from pure samples for Au+Au 39 GeV.	7
7	$n\sigma_e$ distributions from pure samples for Au+Au 62.4 GeV.	8
8	Left: the extrapolation of the fit const of gaussian function within the cross region (grey area). Right: the yield after the PID cuts for different particle species.	9
9	Purity (left) and hadron contamination (right) for Au+Au 39 GeV. The hadron contamination are parameterized by as Landau (low mass) and exponential function (high mass) fit.	9
10	Purity (left) and hadron contamination (right) for Au+Au 62.4 GeV. The hadron contamination are parameterized by as Landau (low mass) and exponential function (high mass) fit.	9
11	Acceptance correction factor in difference $p_T$ region for Au+Au 39 GeV.	10
12	Acceptance correction factor in difference $p_T$ region for Au+Au 62.4 GeV.	10
13	Foreground, background, raw yield and also signal over background ratio for Au+Au 39 GeV (left) and 62.4 GeV (right).	11
14	$\phi_V$ distribution as a function of $M_{ee}$ from photon conversion sample for Au+Au 39 GeV (left) and Au+Au 62.4 GeV (right). The red lines depict the cut used in this analysis.	12
15	QA for Au+Au 39 GeV $e^-$ embedding in $p_T$ range $0.4 \sim 0.6$ GeV/c. nHitsFit, dca and nDedxFit distributions from data selected by pure $\pi$ and electron sample are used to compare with those from embedding sample. And the difference between embedding sample and electron sample is included into systematic uncertainty.	13
16	Left: The comparison of TOF matching from difference samples for Au+Au 39 GeV negative charged particles. Right: the ratio of TOF matching efficiency from phe sample with $\eta \phi$ weight over $\pi$ sample. The black solid line depicts a fit with function defined by Eq. 9. The grey lines shows 66.6% confidential region of that fit.	14
17	$1/\beta$ cut efficiency. Slice gaussian fit and counting methods are used to obtain the efficiency.	15
18	$n\sigma_e$ cut efficiency. The grey bar shows the uncertainty due to the fit error for the parameterization of the mean and sigma momentum dependence.	15
19	$\phi_V$ efficiency calculated by $\pi^0$ Dalitz decay embedding.	16
20	Pair efficiency calculated by virtual method as function of $M_{ee}$ and $p_T$ for Au+Au @ 39 GeV (left) and 62.4 GeV (right).	16
21	The ratio of positive charged pairs over negative charged pairs as a function of $M_{ee}$ . The black circles represent the ratio of same event, while the open red squares depict the ratio from the mix events.	17
22	Systematic uncertainty from data analysis.	17
23	Tsallis fits of $\pi$ , K, p data.	18
24	FONLL upper limit fit to previous measurement of charm cross section.	20
25	Charm simulation with difference assumption for the correlation between daughter $e^+e^-$ pairs.	21
26	momentum resolution from embedding for Au+Au 39 GeV.	21
27	momentum resolution from embedding for Au+Au 39 GeV.	22
28	Gassion+pol(2) fit to the $J/\psi$ signal with different background method: like-sign with geometry mean (left), like-sign with arithmetic mean (middle) and mixed-event (right).	22
29	Tune the mean parameter for the DBC function for 62.4 GeV.	23
30	Cocktail fit for 39 GeV.	23

31	Cocktail fit for 62.4 GeV.	24
32	Efficiency corrected dielectron spectra in the STAR acceptance compared to the cocktail.	25
33	Dielectron mass spectrum in the low mass region measured in the STAR acceptance compared to the model calculations.	25
34	Acceptance calculated by virtual photon method (red grid) and cocktail method (green grid).	26
35	Left: Excess spectra with difference charm cocktail component. Right: Final spectra for 39 GeV.	26
36	Left: Excess spectra with difference charm cocktail component. Right: Final spectra for 62.4 GeV.	26
37	Acceptance corrected excess spectra for STAR Beam Energy Scan.	27

## List of Tables

1	Event selection and track selection	5
2	Parameters for TOF eID function.	6
3	Parameters for TPC $n\sigma_e$ selection	6
4	Selections of pure electron sample. Where $dca_{ep}$ is the dca between two daughter tracks, and decayL is the signed distance from the primary vertex to the conversion vertex. $M_G$ and $M_P$ represent the pair mass calculated with primary momentum and global momentum.	8
5	Parameters for the scale factor of the TOF matching efficiency.	14
6	Systematic uncertainty from efficiency.	17
7	Input value for cocktail simulation.	19
8	Double crystal ball parameterization.	23
9	Uncertainty source for $J/\psi$ $dN/dy$ .	24

# 1 Data Set

The date set involved in this analysis is the Minibias triggered data for Au+Au collisions at  $\sqrt{s_{NN}} = 39, 62.4$  GeV taken by STAR detector system in year 2010. The data analysis is based on the lbnl's PicoDst files. Table 1 shows the event selection and track selection cut. Figure 1 and 2 show the vertex distributions for 39 and 62.4 GeV data as while as the cut (depicted by the red lines). For the centrality definition, the standard class StRefMultCorr is used. A weight is applied event by event to account the difference in reference multiplicity distribution between data and Glauber model. This weight is also provided by the StRefMultCorr class.

Table 1: Event selection and track selection

$\sqrt{s_{NN}}$ (GeV)	39	62.4
Minbias Trigger	280001	2700 01/11/21
Vertex selection	$V_r < 2$ cm $\&\&$ $ V_z  < 40$ cm	
Minimum RefMult	7	
Primary track selection	$p_T > 0.2$ && $p < 10$ GeV/c $n\text{HitsFit} > 15$ && $n\text{HitsFit}/n\text{HitPoss} > 0.52$ && $n\text{DedxFits} \geq 15$ $ \eta  < 1$ && $0 < g\text{Dca} < 1$ cm	
Tof Matching	TofMatchFlag > 0 && $ \text{LocalY}  < 1.8$ cm	
Nevents after cut	131.8M	62.1M
Final(After gWeight)	135.8M	64.9M

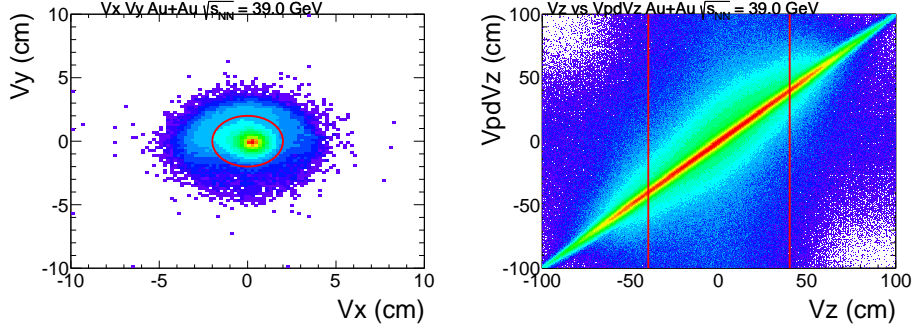


Figure 1: Vertex distribution for Au+Au  $\sqrt{s_{NN}} = 39$  GeV. Red lines depicts the event selection cuts.

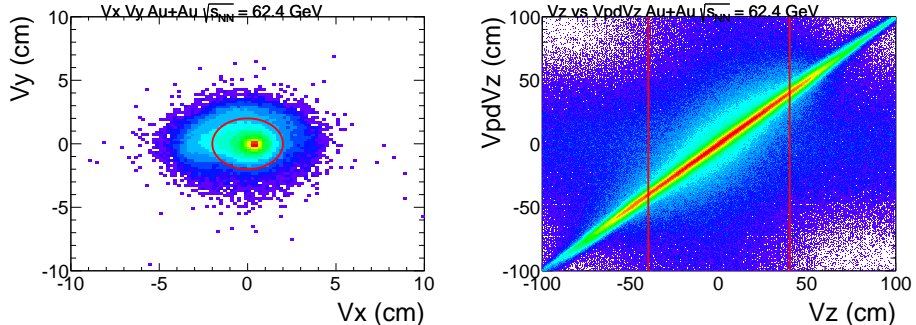


Figure 2: Vertex distribution for Au+Au  $\sqrt{s_{NN}} = 62.4$  GeV. Red lines depicts the event selection cuts.

## 2 Electron Selection and Purity

Electron(means electron and position if not specified) samples are selected by combining the  $dE/dx$  information from TPC and  $1/\beta$  information from TOF. The TOF selection cut and TPC  $dE/dx$  selection cut are defined as Eq. 1 and Eq. 2. Table 2 and 3 show the parameters for these selection functions for difference energy.

$$1/\beta - 1 = A \cdot \left( \frac{\pi}{2} - \arctan(B \cdot (p - C)) \right) + \begin{cases} D, & \text{upper limit} \\ d, & \text{lower limit} \end{cases} \quad (1)$$

$$n\sigma_e = \pm \frac{A}{\pi} \arctan(5p - 3) + \begin{cases} D, & \text{lower limit} \\ d + A/2, & \text{upper limit} \end{cases} \quad (2)$$

Table 2: Parameters for TOF eID function.

$\sqrt{s_{NN}}$	A	B	C	D	d
39	2.0785e-3	18.3	0.2478	2.429e-2	-3.361e-2
62.4	2.158e-3	12.56	0.2265	1.739e-2	-4.174e-2

Table 3: Parameters for TPC  $n\sigma_e$  selection

$\sqrt{s_{NN}}$	A	D	d
39	0.9	-1.65	1.5
62.4	0.9	-1.3	1.7

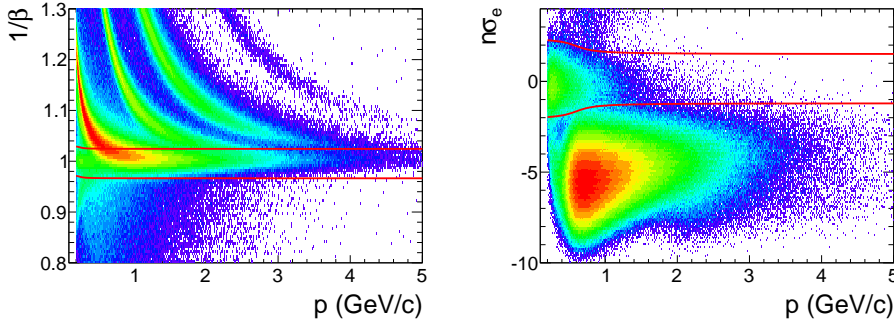


Figure 3: Left: the distribution of inverses beta vs momentum for 39 GeV. Right: the  $n\sigma_e$  distributions after TOF PID selection. The red lines depict the PID selection cuts.

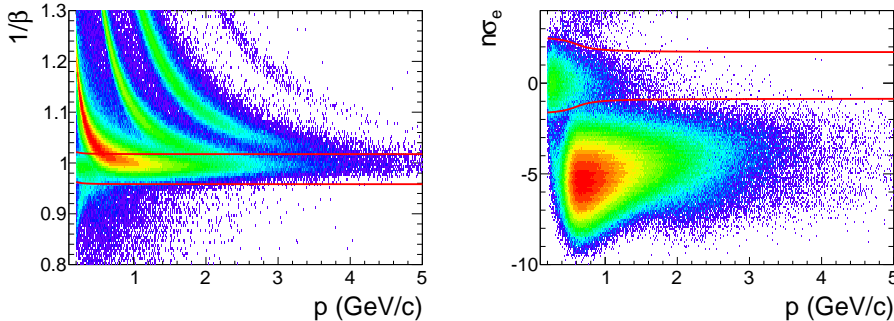


Figure 4: Left: the distribution of inverse beta vs momentum for 62.4 GeV. Right: the  $n\sigma_e$  distributions after TOF PID selection. The red lines depict the PID selection cuts.

## 2.1 Pure sample selection

Pure hadron ( $\pi$ ,  $k$  and  $p$ ) sample (Fig 5 left panel) are selected by very tight  $m^2$  cut provided by TOF and  $|n\sigma_h| < 4$  ( $h = \pi, k, p$ ). The pure electron selection criteria are shown in Table 4. By cutting on the decay length and primary mass, we can select pure electrons from  $\gamma$  conversion and  $\pi_0$  Dalitz decay (Fig. 5 right panel). Then the mean and sigma for the  $n\sigma_e$  distributions are obtained from gaussian fit in differential momentum bins. Figure 6 and 7 show the distributions of  $n\sigma_e$  as a function of momentum for the pure samples and the mean and 1 sigma from the slice fit in differential momentum bins.

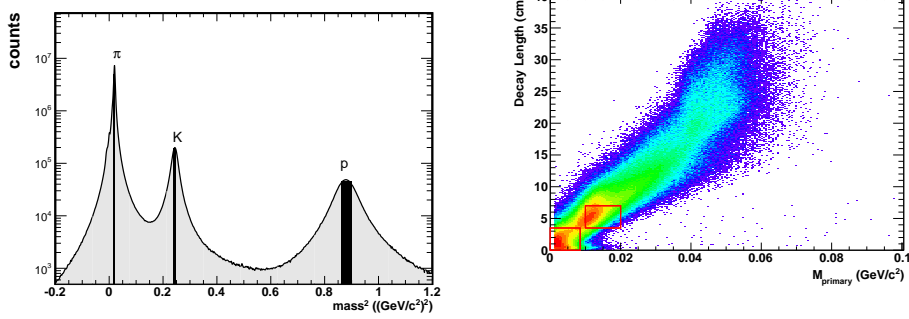


Figure 5: Pure sample selection criteria. Left panel:  $m^2$  distributions, pure hadron samples are selected by cut on the black region. Right panel: the correlation between decay length and primary mass. Pure electron samples are selected by cutting on the two red boxes.

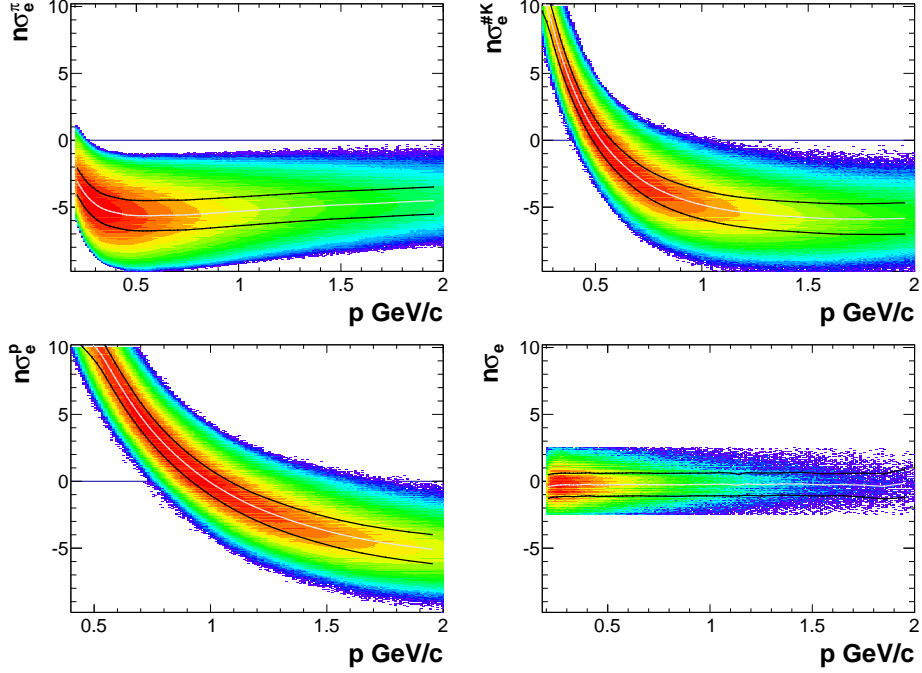


Figure 6:  $n\sigma_e$  distributions from pure samples for Au+Au 39 GeV.

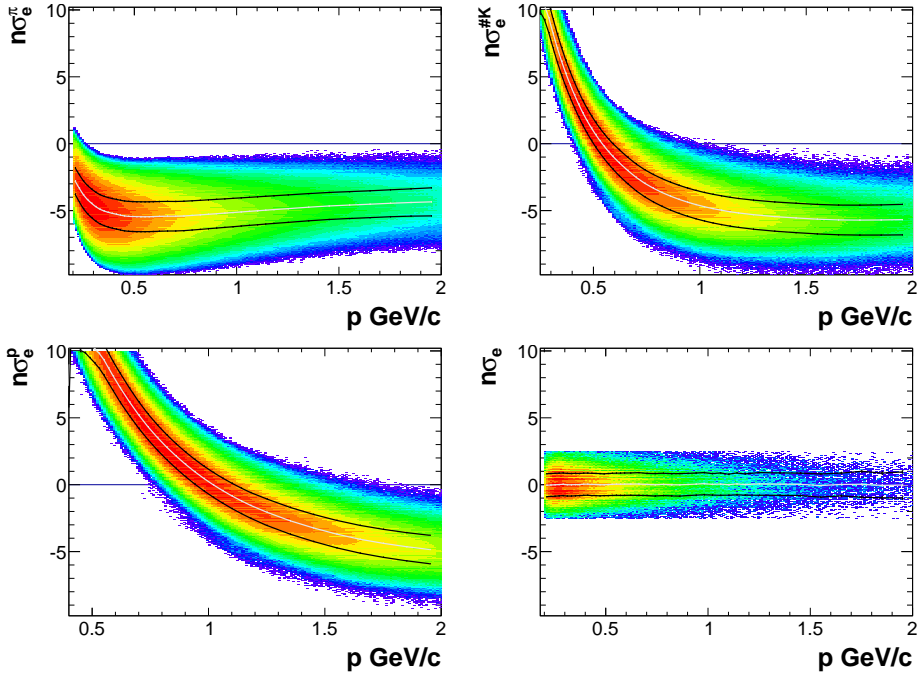


Figure 7:  $n\sigma_e$  distributions from pure samples for Au+Au 62.4 GeV.

Table 4: Selections of pure electron sample. Where  $dca_{ep}$  is the dca between two daughter tracks, and  $\text{decayL}$  is the signed distance from the primary vertex to the conversion vertex.  $M_G$  and  $M_P$  represent the pair mass calculated with primary momentum and global momentum.

General cut	$dca_{ep} < 1 \text{ cm} \& \& 0 < \text{decayL} < 7 \text{ cm} \& \& M_G < 5 \text{ MeV}/c^2$
phe	$10 < M_P < 20 \text{ MeV}/c^2 \& \& 3.5 < \text{decayL} < 7 \text{ cm}$
$\pi_0$ Dalitz	$M_P < 8.5 \text{ MeV}/c^2 \& \& \text{decayL} < 3.5 \text{ cm}$
Tag electron	$ n\sigma_e  < 2.5$
Partner electron	same PID criteria as data analysis.

## 2.2 Purity and hadron contamination

Multi-gaussian fit with mean and sigma fixed from the pure sample are applied to the  $n\sigma_e$  distribution after TOF PID selection to obtain the yields for difference particle species. The fit also included the merged  $\pi$  component which is from the merging of two closed  $\pi$  tracks, and thus has a doubled  $dE/dx$  value compared to a normal  $\pi$  track. In some momentum regions, the electron band crosses with the hadron bands (around 0.5 GeV/c cross with kaon and 1 GeV/c cross with proton), where the multi-gaussian fit may not be reliable. In this analysis, exponential functions are used to extrapolate the particle yields into the cross region. The difference between multi-gaussian fit and the exponential extrapolation are included into the systematic uncertainty. Finally, we can achieve an average purity about 94.0% for 39 GeV and 95% for 62.4 GeV.

Hadron contamination is studied by mixing pure hadron samples into electron sample, we called it mixed sample. The hadron sample is weighted by the ratio of hadron yield over electron yield and the ratio of  $n_e$  over  $n_h$  in corresponding event. The particles in the mixed sample are randomly paired with each other and the signal from each combination is obtained by subtracting the like-sign background from the unlike-sign pairs.

Figure 9 and 10 show the purity as a function of momentum (left) and hadron contamination (right) for Au+Au 39 GeV and 62.4 GeV analysis, respectively. The hadron contamination contribution is parameterized by Landau (low mass) and exponential function (high mass) fit.

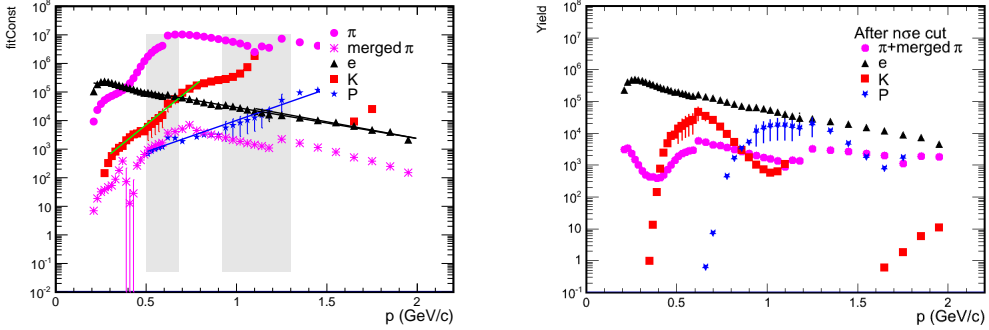


Figure 8: Left: the extrapolation of the fit const of gaussian function within the cross region (grey area). Right: the yield after the PID cuts for different particle species.

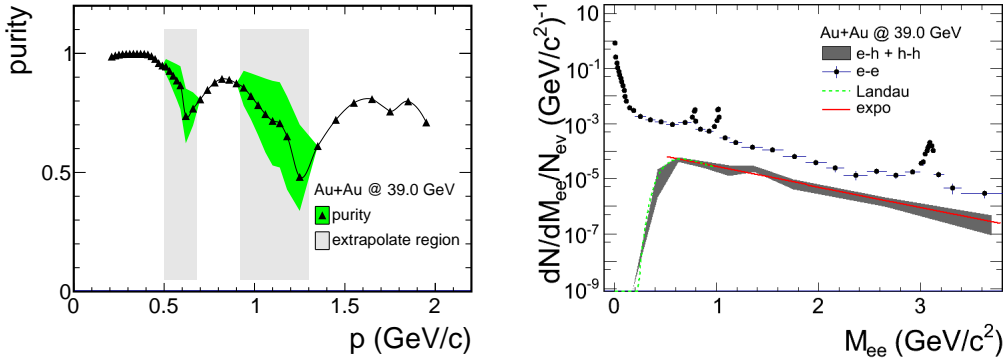


Figure 9: Purity (left) and hadron contamination (right) for Au+Au 39 GeV. The hadron contamination are parameterized by as Landau (low mass) and exponential function (high mass) fit.

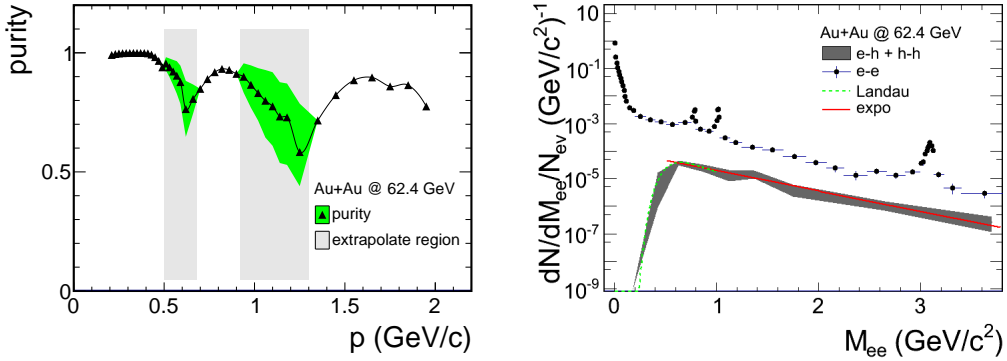


Figure 10: Purity (left) and hadron contamination (right) for Au+Au 62.4 GeV. The hadron contamination are parameterized by as Landau (low mass) and exponential function (high mass) fit.

### 3 Background and Signal

The dielectron pairs (foreground, also marked as unlike-sign pairs) are reconstructed by randomly combining electron and position from the high purity electron (position) sample from the same event. In this analysis like-sign method is used to reproduction the background and mix-event method is used to calculate the acceptance correction factor for the like-sign background.

### 3.1 Like-sign Background

In this analysis, we constructed like-sign background by randomly combining same charge pairs  $N_{++}$ ,  $N_{--}$  from the same event. Geometric mean ( $2\sqrt{N_{++} \times N_{--}}$ ) is used to get the average of positive and negative charged pairs, because as demonstrated in this paper [cite] that when the  $e^+$  and  $e^-$  are produced in statistically independent pairs, the geometric mean fully describes the background in the unlike-sign pair foreground distribution. An acceptance correction factor is used to correct the difference between unlike-sign and like-sign pairs in acceptance due to the acceptance gap of the detectors and difference bend direction of difference charged particles in the magnetic field.

Mixed event method is used to calculate the acceptance correction factor. Mixed event background is reproduced by mixing electron candidate tracks from different events. To ensure events mixed together have similar structure, event sample are classified according centrality, Vz and event plane, and split into  $Centrality \times V_z \times \Psi = 9 \times 10 \times 6$  event pools. Each event pools hold 100 electron candidates at maximum. When the event pool is full, one event is randomly dropped to make space for the new coming event. The acceptance correction factor are applied in 2 dimensions. Figure 11 and 12 show the acceptance correction factor in differential  $p_T$  regions as well as a 2D suffice distribution as a function of  $M_{ee}$  and  $p_T$  for Au+Au 39 and 62.4 GeV. The like-sign background is calculated by following equations:

$$B_{LS}(M_{ee}, p_T) = 2\sqrt{N_{++}(M_{ee}, p_T) \times N_{--}(M_{ee}, p_T)} \cdot F_{acc}(M_{ee}, p_T) \quad (3)$$

$$F_{acc}(M_{ee}, p_T) = \frac{N_{+-}^{Mix}(M_{ee}, p_T)}{2\sqrt{N_{++}^{Mix}(M_{ee}, p_T) \times N_{--}^{Mix}(M_{ee}, p_T)}} \quad (4)$$

The final raw yield is obtained by subtract like-sign background from the unlike-sign foreground in 2 dimension. The final raw yield and signal background ratio are shown in Fig. 13.

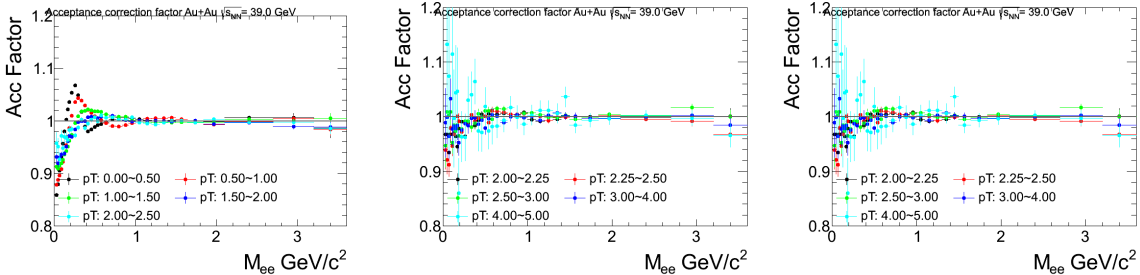


Figure 11: Acceptance correction factor in difference  $p_T$  region for Au+Au 39 GeV.

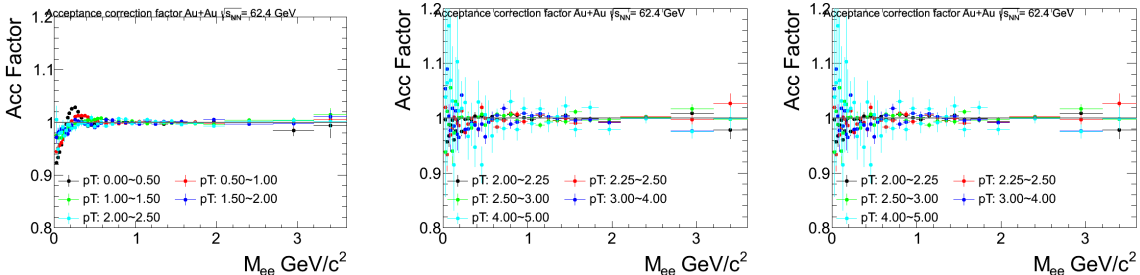


Figure 12: Acceptance correction factor in difference  $p_T$  region for Au+Au 62.4 GeV.

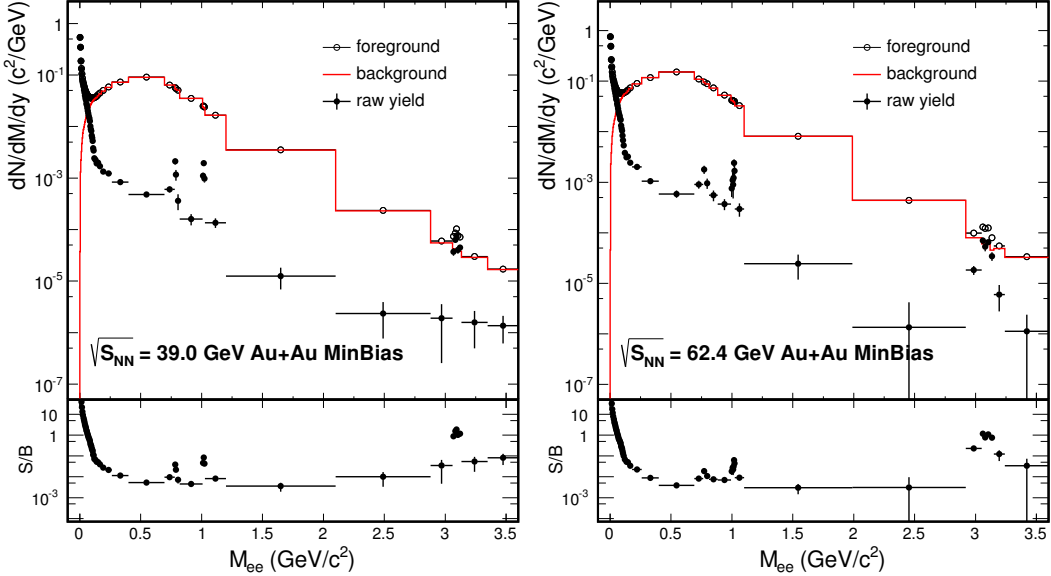


Figure 13: Foreground, background, raw yield and also signal over background ratio for Au+Au 39 GeV (left) and 62.4 GeV (right).

### 3.2 Photon Conversion Background

Photon conversion is that photon hit material of detectors and convert  $e^+e^-$  pairs. When reconstructed unlike-sign foreground, it has contribution to the very low mass region ( $M_{ee} < 0.2 \text{ GeV}/c^2$ ). Mass of photon conversion pairs should be very close to 0. However, momentum of electron tracks from conversion vertex away from primary vertex is biased which lead to a finite pair invariant mass, because the procedure of reconstruction primary tracks also included the primary vertex as a fit point.

In this analysis, we used  $\phi_V$  cut method which is similar to the method used by PHENIX. Considering the zero opening angle of dielectron pairs from photon conversion, electron is bended inside the plate perpendicular to magnet direction. Therefore,  $\phi_V$  is defined as Eq. 5, where  $\vec{p}_+$ ,  $\vec{p}_-$  are the momentum of  $e^+$  and  $e^-$ , respectively,  $\hat{z}$  is the direction of magnet.

$$\begin{aligned}\hat{\mu} &= \frac{\vec{p}_+ + \vec{p}_-}{|\vec{p}_+ + \vec{p}_-|}, \hat{\nu} = \vec{p}_+ \times \vec{p}_- \\ \hat{\omega} &= \hat{\mu} \times \hat{\nu}, \hat{\omega}_c = \hat{\mu} \times \hat{z} \\ \cos \phi_V &= \hat{\omega} \cdot \hat{\omega}_c\end{aligned}\quad (5)$$

$\phi_V$  should be zero (by consistently ordering positive and negative tracks within the pair we avoid  $\phi_V = \pi$  as a solution for photon conversions), if the dielectron pair is originated from photon conversions. While, there is no preferred orientation for combinatorial pairs, and very weak dependence for dielectron pairs from hadron decays. For the like-sign pairs there is no clear definition on the order when do the crossing (in another word: the orientation of vector  $\hat{\nu}$ ), so in this analysis random order is used for like-sign pair  $\phi_V$  calculation. Figure 14 show  $\phi_V$  distribution as a function of  $M_{ee}$  from photon conversion sample and the cut used in this analysis. The  $\phi_V$  cut is only applied in mass region  $M_{ee} < 0.2 \text{ GeV}/c^2$ .

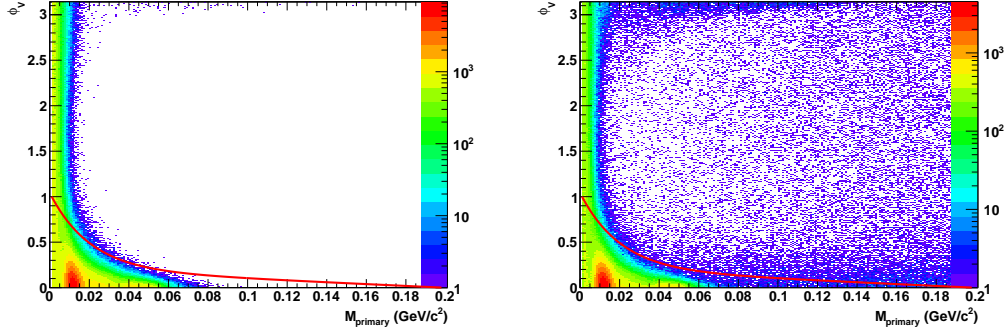


Figure 14:  $\phi_V$  distribution as a function of  $M_{ee}$  from photon conversion sample for Au+Au 39 GeV (left) and Au+Au 62.4 GeV (right). The red lines depict the cut used in this analysis.

## 4 Efficiency

To obtain the real di-electron production within the STAR acceptance, the raw yield need to be corrected for the efficiencies due to the detectors inefficiency and PID cut loss. The pair efficiency is propagated from single electron efficiencies. The single electron efficiency can be separated into two parts: detector efficiency and PID efficiency. Then Monte Carlo method is used to evolved the single efficiency into pair efficiency.

### 4.1 Single electron efficiency

The single electron efficiency in this analysis included the TPC tracking efficiency ( $\varepsilon_{TPC}$ ), TOF matching efficiency ( $\varepsilon_{TOF}$ ) and electron identification efficiency ( $\varepsilon_{PID}$ ) as Eq. 6.

$$\varepsilon_{single} = \varepsilon_{TPC} \times \varepsilon_{TOF} \times \varepsilon_{PID} \quad (6)$$

#### 4.1.1 TPC tracking efficiency

The TPC tracking efficiency includes the track reconstruction efficiency and the TPC acceptance. Also the track quality cut (nHitFits, nDedxFits, dca) efficiency are also combined into TPC tracking efficiency. The TPC tracking efficiency was obtained via the standard STAR embedding process. The tracking efficiency is defined by number of reconstructed MC tracks which satisfy the track quality cut divided by number of input MC tracks, also see Eq. 7.

$$\varepsilon_{TPC} = \frac{N_{rc}(nHitFits > 15 \&& nDedxFits \geq 15 \&& dca < 1cm)}{N_{Mc}} \quad (7)$$

The tracking efficiency is applied in 3 dimension ( $p_T$ ,  $\eta$  and  $\phi$ ), efficiency distributions in each  $\eta$   $\phi$  bins can be found at following links: [39 GeV eminus](#), [39 GeV eplus](#), [62.4 GeV eminus](#) and [62.4 GeV eplus](#).

To qualify whether the embedding sample can reproduce the real data, we compared several track parameters ( $nHitFits$ ,  $nDedxFit$ ,  $dca$ ) from embedding sample with those from the pure electron sample selected by photon conversion and  $\pi^0$  Dalitz decay. Figure 15 shows an example of the comparison in  $p_T$  range 0.4~0.6 GeV/c for 39 GeV. Detailed comparison can be found at link: [39 GeV eminus](#), [39 GeV eplus](#), [62.4 GeV eminus](#) and [62.4 GeV eplus](#). The difference was included in the systematic uncertainty.

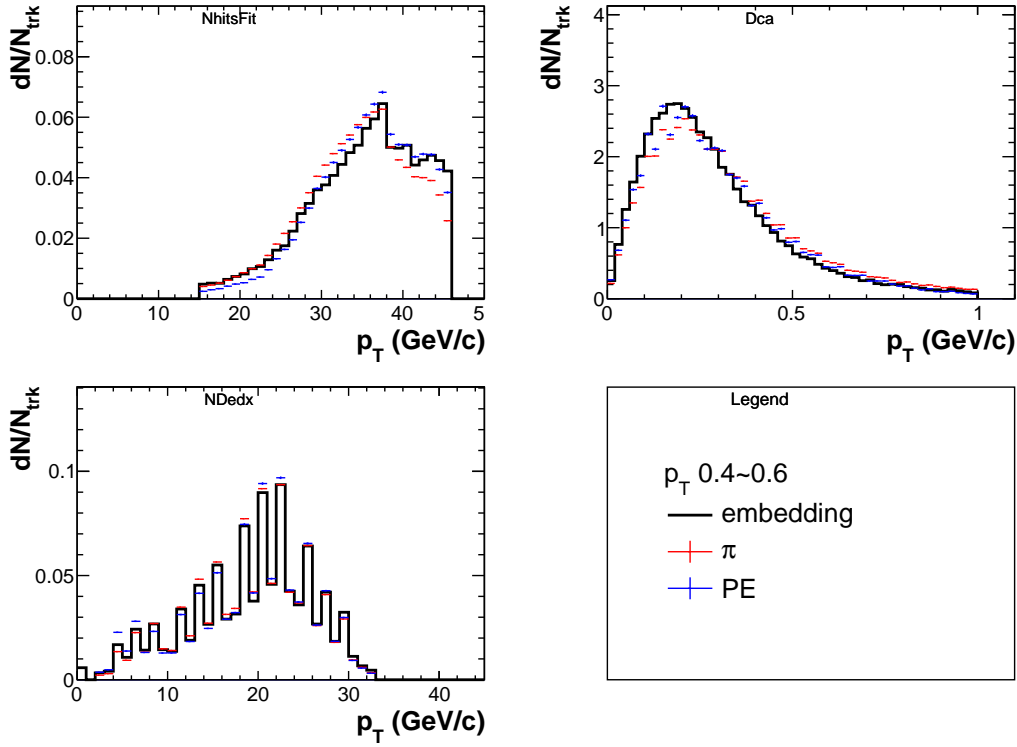


Figure 15: QA for Au+Au 39 GeV  $e^-$  embedding in  $p_T$  range 0.4~0.6 GeV/c.  $n_{\text{HitsFit}}$ ,  $dca$  and  $NDedx$  distributions from data selected by pure  $\pi$  and electron sample are used to compare with those from embedding sample. And the difference between embedding sample and electron sample is included into systematic uncertainty.

#### 4.1.2 TOF efficiency

The TOF efficiency ( $\varepsilon_{TOF}$ ) is studied via comparing the number of track which matches TOF and the total number of TPC primary tracks from real data. A track match to TOF is defined as following:

- The track is projected to the radius of TOF, and there is a valid hit in the corresponding TOF cell ( $\text{tofMatchFlag} > 0$  in data structure).
- The distance between the projection position to the TOF cell center in local y coordinate (Locally) is smaller than 1.8 cm.

The definition of TOF matching efficiency is shown as Eq. 8.

$$\varepsilon_{TOF} = \frac{N_{\text{matched}}(\text{TofMatchFlag} > 0 \&\& \beta > 0 \&\& |\text{LocalY}| < 1.8\text{cm})}{N_{TPC}} \quad (8)$$

To achieve enough statistics to study the efficiency in 3 dimensions ( $p_T$ ,  $\eta$ ,  $\phi$ ), we use pure pion sample selected by a very tight  $dE/dx$  cut ( $|n\sigma_\pi| < 0.5$ ) to study the  $\eta$  and  $\phi$  dependence of the TOF matching efficiency. The TOF matching efficiency of pure electron sample from photon conversion and  $\pi^0$  Dalitz decay is served as a standard of the absolute value of the efficiency. A weight on  $\eta$  and  $\phi$  dimensions is applied to the electron sample to address the difference in acceptance between electron sample and  $\pi$  sample. The efficiency from  $\pi$  sample is scaled to match with the one from electron sample by a  $p_T$  dependent function. In this analysis, we use following function to parameterize the scale factor as a function of  $p_T$  :

$$f(x) = \frac{1}{a + \exp\{(x - b)/c\}} + d \quad (9)$$

The fit result is shown in Fig. 16 for 39 GeV negative charged as an example and the uncertainty of the fit is included into the systematic uncertainty. Table 5 lists the parameters for the function fit for each energy and charged type.

The TPC efficiency and TOF matching efficiency are both studied and applied in 3 dimensions. TPC efficiency was calculated in  $8 \times 24 \eta, \phi$  bins and 50 MeV  $p_T$  bin, while TOF matching efficiency was studied in  $8 \times 24 \eta, \phi$  bins and 50 MeV  $p_T$  bin.

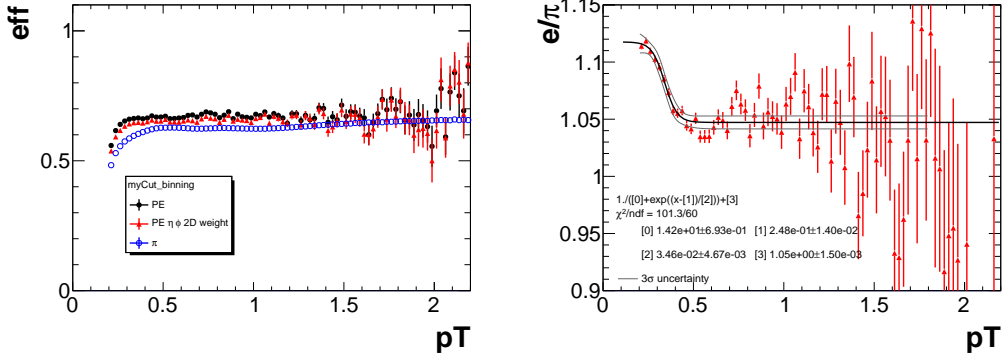


Figure 16: Left: The comparison of TOF matching from difference samples for Au+Au 39 GeV negative charged particles. Right: the ratio of TOF matching efficiency from phe sample with  $\eta \phi$  weight over  $\pi$  sample. The black solid line depicts a fit with function defined by Eq. 9. The grey lines shows 66.6% confidential region of that fit.

Table 5: Parameters for the scale factor of the TOF matching efficiency.

	a	b	c	d
39 GeV -	14.2	0.248	3.46e-2	1.05
39 GeV +	19.2	0.266	2.92e-2	1.05
62.4 GeV -	15.1	0.273	4.05e-2	1.02
62.4 GeV +	23.6	0.342	1.44e-2	1.03

#### 4.1.3 PID efficiency

The PID efficiency included efficiencies of  $1/\beta$  and  $n\sigma_e$  cut.  $1/\beta$  cut efficiency is studied by pure electron sample from real data shown as Fig. 17. Two methods are used to calculate the efficiency: gaussian fit method and direct histogram counting method, and their difference are included into the systematic uncertainty. The pure electron sample is also used to study the  $n\sigma_e$  distribution for electrons as mention in section 2.1 which provides the mean and sigma of the gaussian distribution in each momentum slice. The polynomial functions are used to describe momentum dependence of the mean and sigma, to minimize the statistics fluctuation. The efficiency is calculation with the parameterized mean and sigma, and due to the statistics limit of the pure electron sample, in this analysis only data within momentum range 0.2~1.5 GeV/c are used in the fit and we assume the value and mean and sigma at higher momentum region are the same as  $p = 1.5$  GeV/c. Figure 18 shows the  $n\sigma_e$  cut efficiency for each energy.

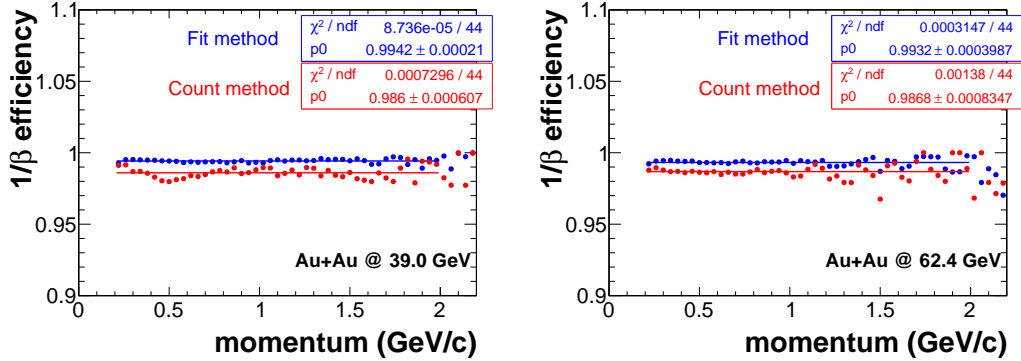


Figure 17:  $1/\beta$  cut efficiency. Slice gaussian fit and counting methods are used to obtain the efficiency.

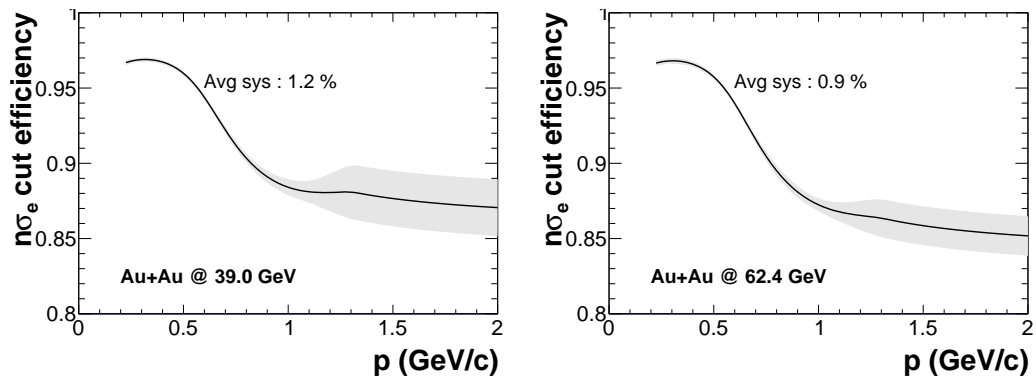


Figure 18:  $n\sigma_e$  cut efficiency. The grey bar shows the uncertainty due to the fit error for the parameterization of the mean and sigma momentum dependence.

## 4.2 Pair efficiency

The single electron efficiency is folded in for each daughter track in full 3D ( $p_T$ ,  $\eta$ ,  $\phi$ ) momentum space. The virtual photon method is used to evaluate the pair efficiency: virtual photons with flat mass, rapidity and  $p_T$  distributions are generated and decay randomly into  $e^+e^-$  pairs. The pair efficiency is applied in 2 dimension ( $M_{ee}$  vs  $p_T$ ), within STAR acceptance ( $|y_{ee}| < 1$ ,  $p_T^e > 0.2 \text{ GeV}/c$ ,  $|\eta_e| < 1$ ) (Fig. 20). The photon conversion rejection cut efficiency is calculated by  $\pi^0$  Dalitz decay embedding sample and included in the pair efficiency, shown in Figure 19.

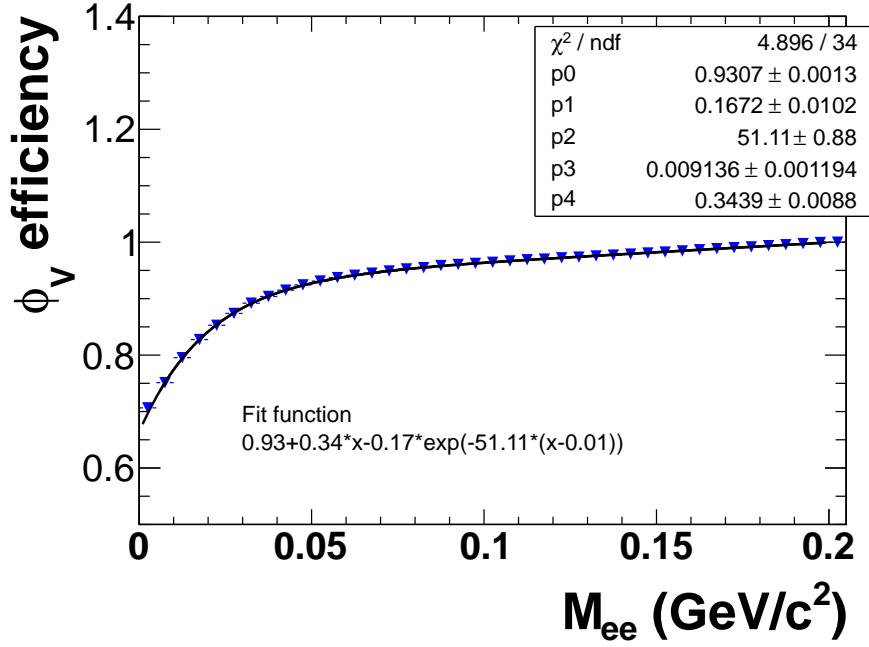


Figure 19:  $\phi_V$  efficiency calculated by  $\pi^0$  Dalitz decay embedding.

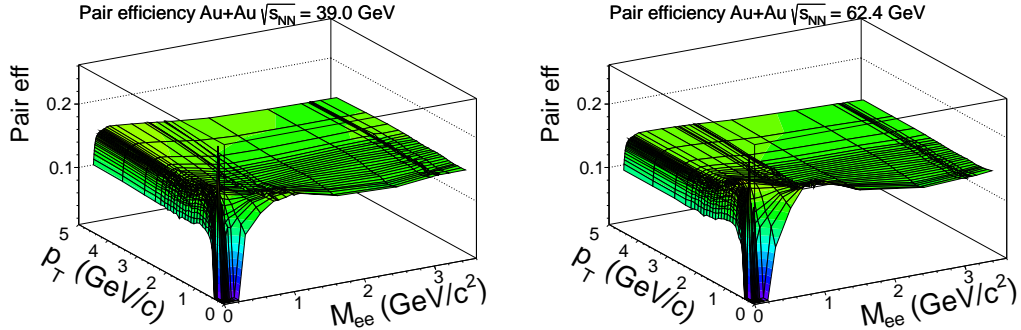


Figure 20: Pair efficiency calculated by virtual method as function of  $M_{ee}$  and  $p_T$  for Au+Au @ 39 GeV (left) and 62.4 GeV (right).

## 5 Systematic Uncertainty

In this analysis, the systematic uncertainty was split into two main parts: from data analysis which is highly correlated with  $M_{ee}$  (summed by direct sum), and from efficiency which is uncorrelated with  $M_{ee}$  (summed by error propagation formula).

The systematic uncertainties source from data analysis are listed below:

1. Uncertainties of the acceptance factor for like-sign background.
2. Different average methods (direct average and geometry mean) when calculating the like-sign background.
3. Hadron contamination (mentioned in section 2.2).

The uncertainty from acceptance factor is come from difference between 1D ( $p_T$ ) and 2D ( $M_{ee}$  vs  $p_T$ ) acceptance factor correction as mentioned in section 3.1. The systematic uncertainty from difference

average methods are estimated by mix event to minimize the statistic fluctuation. Figure 21 show the ratio between positive charged pairs over negative charged pairs as a function of  $M_{ee}$  from same event and mixed event. The mixed event can reproduce the same event well up to  $1.5 \text{ GeV}/c^2$ . Figure 22 shows a summary of the systematic uncertainty from data analysis.

The systematic uncertainties from efficiency are list in Table 6. Detail can be find in Section 4.1.

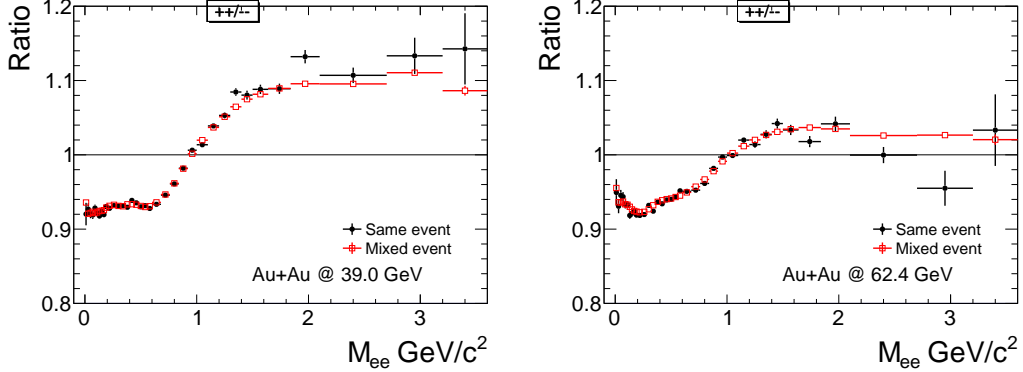


Figure 21: The ratio of positive charged pairs over negative charged pairs as a function of  $M_{ee}$ . The black circles represent the ratio of same event, while the open red squares depict the ratio from the mix events.

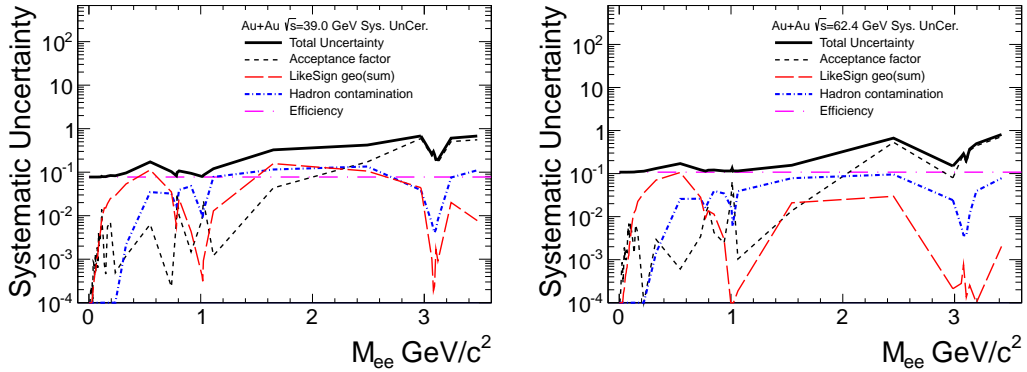


Figure 22: Systematic uncertainty from data analysis.

Table 6: Systematic uncertainty from efficiency.

	39 GeV	62.4 GeV
nHitsFit	2.1%	2.2%
Dca	0.6%	1.1%
nDedxFit	2.8%	4.6%
TOF matching	0.54%	0.84%
$n\sigma_e$ cut	1.2%	0.9%
$1/\beta$ cut	0.8%	0.6%
Total single track	3.87%	5.39%
Total pair	7.74%	10.8%

## 6 Simulation

The cocktail is the contribute from the decays of long life hadrons after chemical freeze out. These components can be well understood by measuring the corresponding decay channels. In this analysis,

cocktails contains contributions from decays and Dalitz decays of  $\pi^0$ ,  $\eta$ ,  $\eta'$ ,  $\omega$ ,  $\phi$ ,  $J/\psi$  and  $c\bar{c}$ , which include:

- Dalitz decays:  $\pi^0 \rightarrow \gamma e^+ e^-$ ,  $\eta \rightarrow \gamma e^+ e^-$ ,  $\omega \rightarrow \pi^0 e^+ e^-$ ,  $\phi \rightarrow \eta e^+ e^-$  and  $\eta' \rightarrow \gamma e^+ e^-$ .
- Dielectron decay:  $\omega \rightarrow e^+ e^-$ ,  $\omega \rightarrow e^+ e^-$ ,  $\phi \rightarrow e^+ e^-$  and  $J/\psi \rightarrow e^+ e^-$ .
- Heavy flavor hadron semi-leptonic decays :  $c\bar{c} \rightarrow e^+ e^-$ .

$\rho^0$  contributions is considered highly modified by the medium which is left open for in-medium theory calculation.

## 6.1 $p_T$ input

The input  $p_T$  spectra is obtained from STAR measurement. A Tsallis blast-wave fit is used to fit the  $\pi$ ,  $K$  and  $p$  spectra and predict for other mesons without measurement. For 62.4 GeV, the data is taken from [STAR PRC 79, 034909 (2009)]. For 39 GeV, data is from Lokesh's preliminary analysis. The  $J/\psi$   $p_T$  spectra is estimated by fit to Wangmei's analysis result with function  $\frac{dN}{2\pi m_T dm_T dy} = \frac{dN}{dy} \times \frac{1}{2\pi T(T+m_0)} \exp\left\{-\frac{m_T-m_0}{T}\right\}$ .

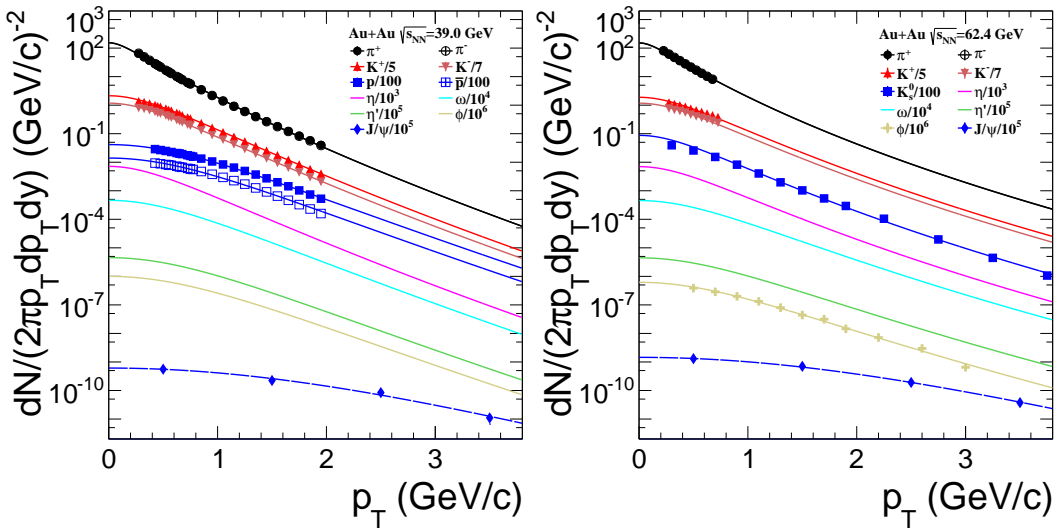


Figure 23: Tsallis fits of  $\pi$ ,  $K$ ,  $p$  data.

## 6.2 Decay kinematics

Dalitz decay ( $h \rightarrow xe^+e^-$ ) is described by the Kroll-Wada equation:

$$\frac{dN}{dM_{ee}} = PhaseSpace \times |F(M_{ee}^2)|^2 \times QED \quad (10)$$

Which can be separated into 3 parts :

1. phase space term, which is defined as eq 11.
2. form factor, for  $\pi^0$  equation 14 is used, while for other particle's Dalitz decay, we use equation 13. The value of  $\Lambda^{-2}$  and  $\Gamma_0^2$  used are listed in Table 7.
3. QED component, which is described by eq 12, where  $N$  is the degeneracy factor which is 4 for  $\omega$  and  $\phi$ , and 2 for the others.

$$PhaseSpace = \left( \left( 1 + \frac{m_{ee}^2}{m_h^2 - m_x^2} \right)^2 - \frac{4m_h^2 m_{ee}^2}{m_h^2 - m_x^2} \right)^{\frac{3}{2}} \quad (11)$$

$$QED = \frac{N}{3\pi} \sqrt{1 - \frac{4m_e^2}{m_{ee}^2}} \left(1 + \frac{2m_e^2}{m_{ee}^2}\right) \frac{1}{m_{ee}} \quad (12)$$

$$|F(m_{ee}^2)|^2 = \frac{1}{(1 - m_{ee}^2 \Lambda^{-2})^2 + \Gamma_0^2 \Lambda^{-2}} \quad (13)$$

$$|F(m_{ee}^2)|^2 = (1 + m_{ee}^2 \Lambda^{-2})^2 \quad (14)$$

Table 7: Input value for cocktail simulation.

	$\pi$	$\eta$	$\eta'$	$\omega$	$\phi$	$J/\psi$
$BR_{ee}$	-	-	-	7.28e-5	2.96e-4	5.94e-2
$BR_{da}$	1.174e-2	6.9e-3	4.7e-4	7.7e-4	1.15e-4	-
Width $\Gamma$	-	-	-	8.49e-3	4.266e-3	9.29e-5
$\Lambda^{-2}$	1.756	1.95	1.8396	2.24	3.8	-
$\Gamma_0^2$	0	0	0.01989	0	0	0
$M/\pi$	1	0.085	0.0078	0.018	0.069	5.76e-6
sys $M/\pi$	8%	14%	16%	13%	17%	-
	TBW parameters			$dN/dy_{\pi_0}$	Charm Xsec	
	T	q	$\beta$		$\sigma_{mb}^{NN}$	$\sigma_{cc}^{NN}$
39 GeV	0.1229	1.023	0.3841	$61.1 \pm 2.7$	34mb	$57.8 \pm 16.5 \mu b$
62.4 GeV	0.1168	1.049	0.3457	$77.2 \pm 2.1$	36mb	$129.0 \pm 36.8 \mu b$
BR(open charm $\rightarrow e$ )		$D^\pm$	$D^0$	$D_s$	$\Lambda_c$	
		0.1607	0.0649	0.065	0.045	

For 2 body decays, Breit-Wigner function is used to describe the mass distribution. Rapidity distributions are parameterized by the CERES group as following equations:

$$\frac{dN}{dy} = \cosh^{-2} \left( \frac{3y}{4\sigma_{Landau}(1 - \frac{y^2}{2\sqrt{s}/m})} \right) \quad (15)$$

$$\sigma_{Landau} = \sqrt{\log(\sqrt{s}/(2m_N))} \quad (16)$$

where  $\sqrt{s}$  is center of mass energy per nucleon,  $m$  is the particle mass and  $m_N$  is nucleon mass.

### 6.3 Charm contribution

Charm component is simulated by PYTHIA 6.4 with the STAR heavy flavor tune (MSEL=1, PARP(91) = 1.0 GeV/c, PARP(67) = 1.0). We use FONLL upper limit curve to the data from world wide measurement in p+p collisions. Finally, the charm cross section is determined by the average of scaled FONLL upper limit curve and FONLL upper limit curve, their difference is taken as systematic uncertainty.

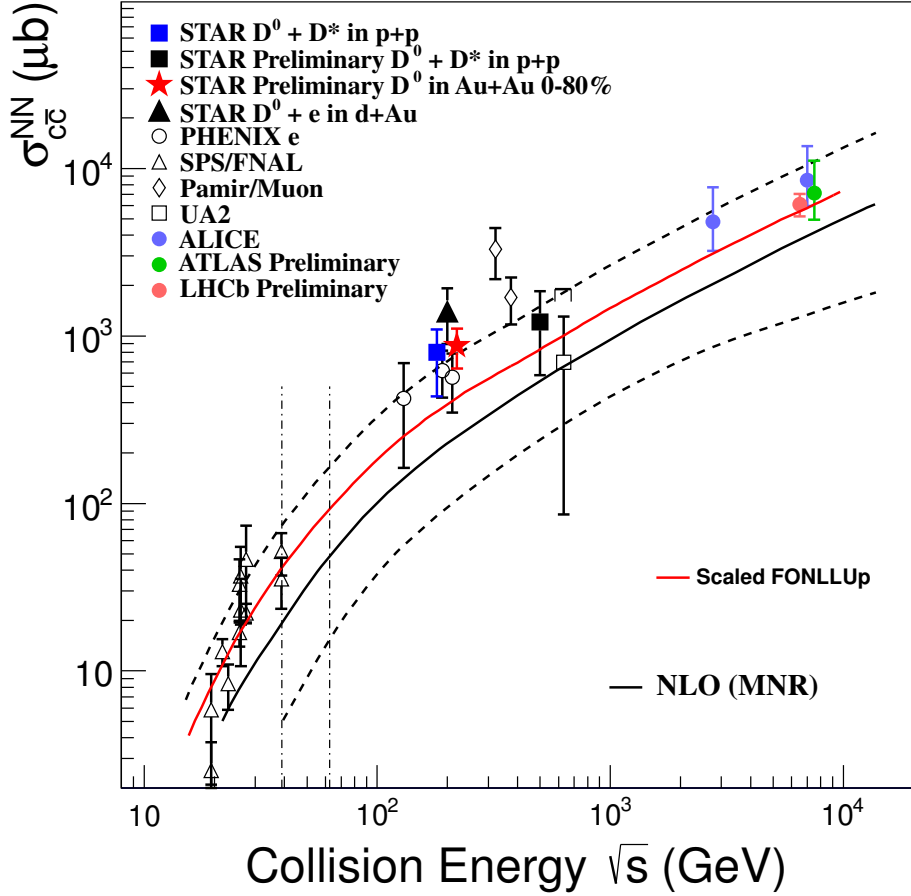


Figure 24: FONLL upper limit fit to previous measurement of charm cross section.

The correlation between  $c\bar{c}$  pair is excepted to be modified in Au+Au collisions w.r.t p+p collisions. In this analysis, we chose the following difference configuration to study their impact on the spectrum:

1. Default PYTHIA simulation. Black solid line in fig 25.
2. Keep the momentum magnitude of daughter electrons in PYTHIA, but randomly select the open angle between daughter electrons pairs. Red dot-dash line in fig 25.
3. Keep the transverse momentum magnitude of daughter electrons in PYTHIA, but randomly select the  $\eta$  and  $\phi$  of the daughter electrons base on the distribution from PYTHIA. Green dash line in fig 25.
4. Randomly sample daughter electrons with single electron  $p_T$ ,  $\eta$  and  $\phi$  distributions from PYTHIA. The correlation between daughter electrons are completely washed out. Blue dash line in fig 25.

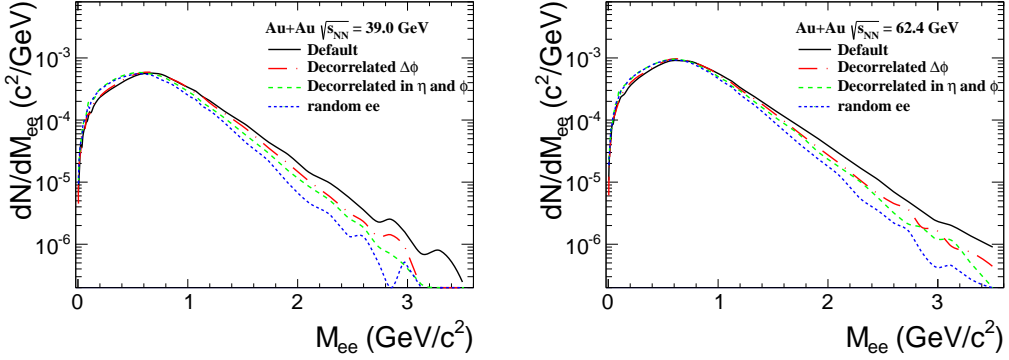


Figure 25: Charm simulation with difference assumption for the correlation between daughter  $e^+e^-$  pairs.

#### 6.4 Momentum resolution and $J/\psi$ yield

The momentum resolution and energy loss for TPC tracks is studied by embedding sample with the full detector simulation.  $\sigma_{p_T}/p_T$  is used as a measure of the  $p_T$  resolution. It is assumed to follow:

$$\left(\frac{\sigma_{p_T}}{p_T}\right)^2 = a^2 p_T^2 + \left(\frac{b}{\beta}\right)^2 \quad \beta = \frac{p}{E} \sim 1 \quad (17)$$

Figure 26 and 27 shows the reconstructed electron  $p_T^{rec}$  probability distribution at a given input  $p_T^{MC}$  from embedding sample. The distribution is parametrized with a double Crystal-Ball function, defined in Eq. 18:

$$P(p_T^{rec}, p_T^{MC}) \propto \begin{cases} A \times (B - R)^{-n_1}, & R < -\alpha_1 \\ e^{-R^2/2}, & -\alpha_1 < R < \alpha_2 \\ C \times (D + R)^{-n_2}, & R > \alpha_2 \end{cases} \quad (18)$$

$$\begin{aligned} A &= \left(\frac{n_1}{|\alpha_1|}\right)^{n_1} \times e^{-\alpha_1^2/2} \\ B &= \frac{n_1}{|\alpha_1|} - |\alpha_1| \\ C &= \left(\frac{n_2}{|\alpha_2|}\right)^{n_2} \times e^{-\alpha_2^2/2} \\ D &= \frac{n_2}{|\alpha_2|} - |\alpha_2| \\ R &= \left(\frac{p_T^{rec} - p_T^{MC}}{p_T^{MC}} - \mu\right) / \frac{\sigma_{p_T}}{p_T} \end{aligned} \quad (19)$$

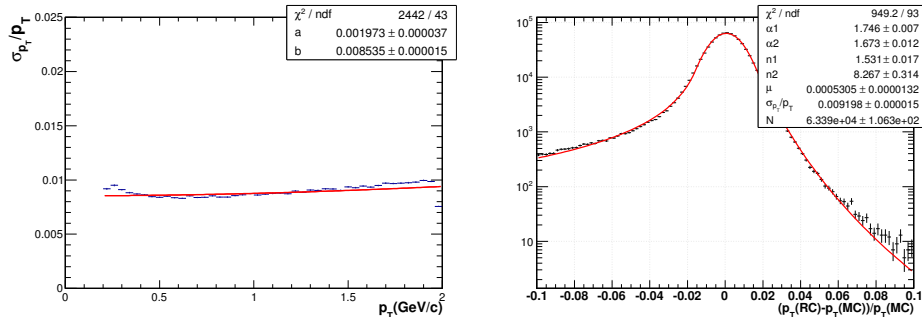


Figure 26: momentum resolution from embedding for Au+Au 39 GeV.

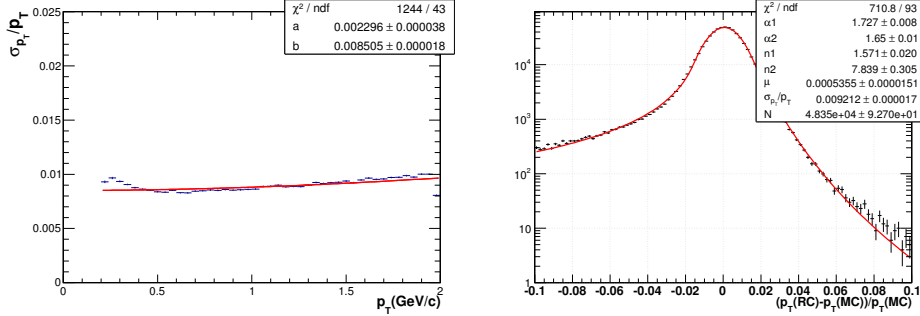


Figure 27: momentum resolution from embedding for Au+Au 39 GeV.

With the default momentum smearing from the embedding sample, the  $J/\psi$  cocktail peak does not match with the data, due to the STAR tracking only accounted for the energy loss assuming pion tracks. So these parameter need to be further tuned. A data-driven method is used in the analysis : the momentum resolution is tuned by matching cocktail to data in  $J/\psi$  mass region. To suppress the large statistic fluctuation of the like-sign background, arithmetic average is used. Also mixed-event method is also used for comparison. The mixed-event background is normalized to the like-sign background in mass region  $2.8 \sim 3.2$   $\text{GeV}/c^2$ .

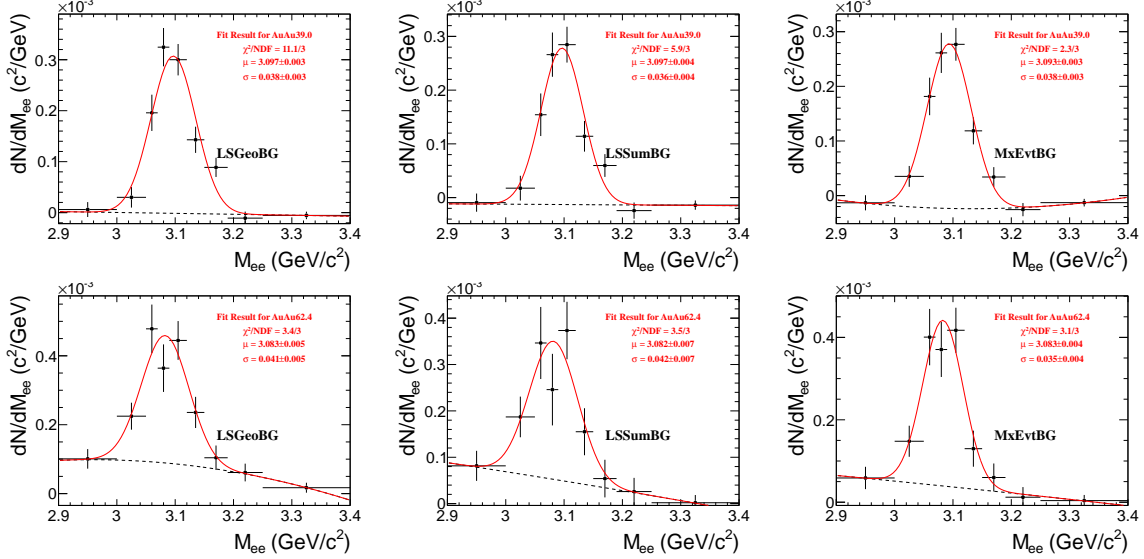


Figure 28: Gassion+pol(2) fit to the  $J/\psi$  signal with different background method: like-sign with geometry mean (left), like-sign with arithmetic mean (middle) and mixed-event (right).

For 62 GeV, the peak position of the cocktail  $J/\psi$  with the default parameter of the DBC function from embedding is found to be unable to match the peak position of data. So the mean parameter  $\mu$  in eq 19 need to be tuned first. Sets of cocktail are generated with different mean parameter for the DBC function and the mean position of the  $J/\psi$  peak is determined by Gaussian fit method and maximum bin method. The tuned parameters of DBC function are listed in table 8.

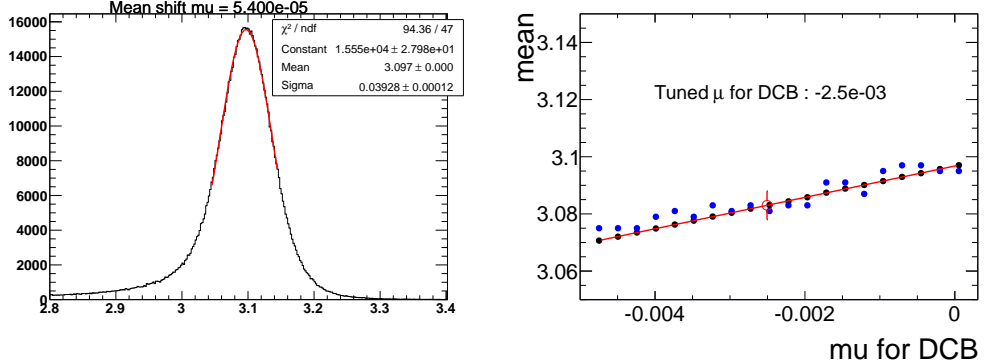


Figure 29: Tune the mean parameter for the DBC function for 62.4 GeV.

Table 8: Double crystal ball parameterization.

	$\alpha_1$	$\alpha_2$	$n_1$	$n_2$	$\mu$	$\sigma$
39 GeV	1.746	1.673	1.531	8.267	5.3e-4	9.2e-3
62.4 GeV	1.727	1.65	1.571	7.839	-2.5e-3	9.2e-3

Then A set of cocktails are generate with different momentum resolution (parameter  $a$  in eq 17). Chi2 test is used to determine the best parameter set, shown in figure 30 and 31. Finally the chi2 test result from the  $J/\psi$  signal with mixed-event method are taken as default in the cocktail simulation. The  $dN/dy$  and uncertainty sources are list in table 9.

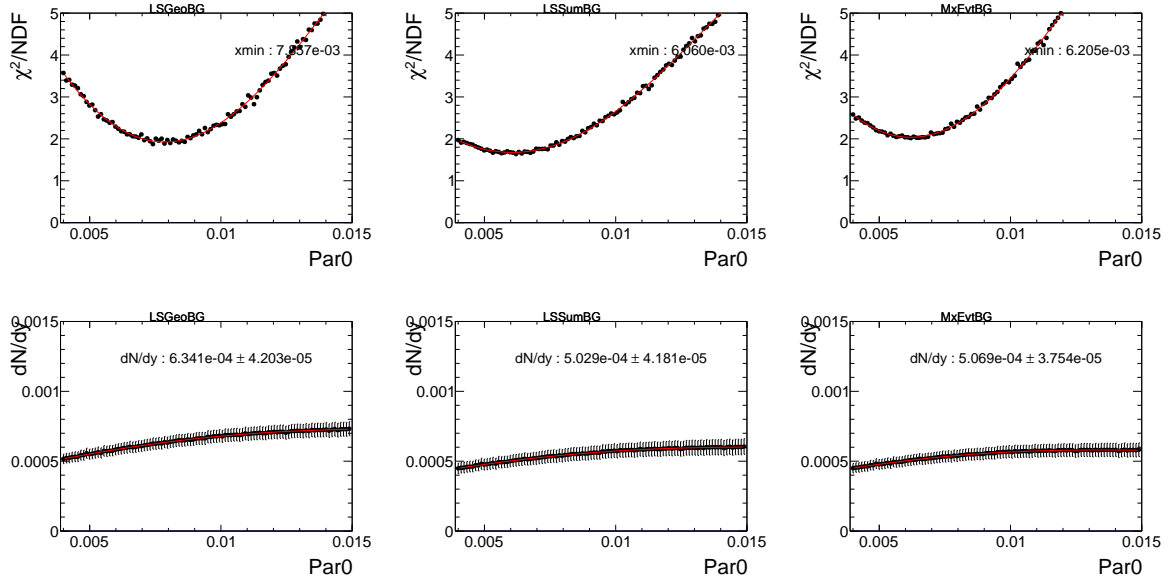


Figure 30: Cocktail fit for 39 GeV.

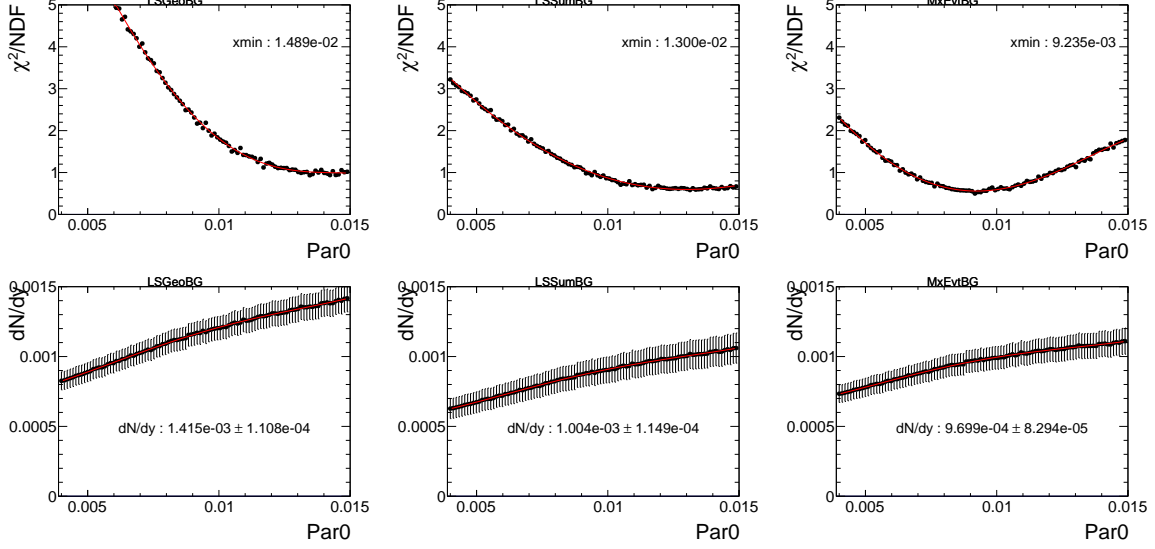


Figure 31: Cocktail fit for 62.4 GeV.

Table 9: Uncertainty source for  $J/\psi$   $dN/dy$ .

	39 GeV	62.4 GeV
Different charm	0.5%	0.1%
Different pT input	1.1%	2.02%
Eff	7.8%	10.8%
Stat.Err.	7.4%	8.5%
Different BG	0.7%	3%
Total	10.8%	14%
$dN/dy$	5.07e-4	9.70e-4

## 7 Final Result

### 7.1 Di-electron spectra

Finally the data are corrected for detectors efficiency and compared with cocktail and theory calculation. Figure 32 show the di-electron spectra for Au+Au 39 GeV (left) and 62.4 GeV (right) within the STAR acceptance and comparison with cocktail simulations. The low mass di-electron spectra are also compared with R.Rapp's model calculation which is an effective many body model based on in medium modification of  $\rho$  spectral function. The comparison are shown in fig 33.

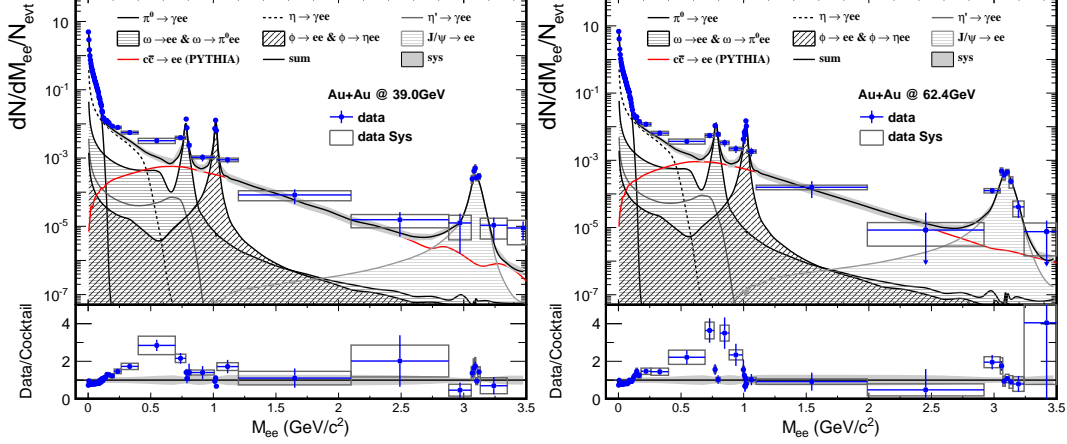


Figure 32: Efficiency corrected dielectron spectra in the STAR acceptance compared to the cocktail.

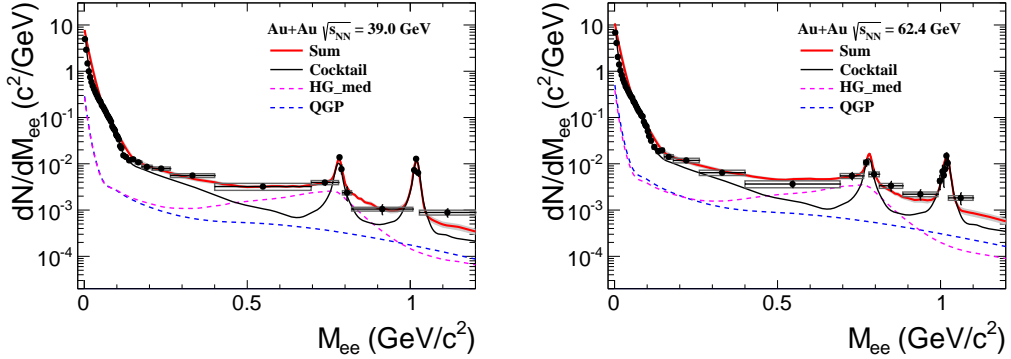


Figure 33: Dielectron mass spectrum in the low mass region measured in the STAR acceptance compared to the model calculations.

## 7.2 Acceptance corrected excess spectra

The excess spectra (data-cocktail without  $\rho$ ) are corrected for the STAR acceptance. Figure 34 show acceptance correction evaluated by two different method:

- virtual method, flat mass,  $p_T$ ,  $\eta$  and  $\phi$  input for parent particles. And parent particles decay into di-electron pairs randomly.
- cocktail decay method, cocktail as input and parent particles decay into di-electron pairs through their decay kinematics. The charm component is simulated by PYTHIA, so the daughter di-electron pairs carry strongly correlation inherited from parent charm pairs .

The difference between these two method is mainly from the difference assumption for correlation between daughter di-electron pair, and it increases with the collision energy due to a more significant charm contribution at higher collision energy. The virtual photon method is taken as default and the difference between these two method is taken as systematic uncertainty.

The acceptance corrected excess spectra are shown in fig 35 and 36 and in figure 37 the acceptance corrected excess spectra from Au+Au 19.6, 39, 62.4 and 200 GeV are scaled by  $dN_{ch}/dy$  and summarized together. The  $dN_{ch}/dy$  is  $151 \pm 4$  for 39 GeV and  $191 \pm 3$  for 62.4 GeV.

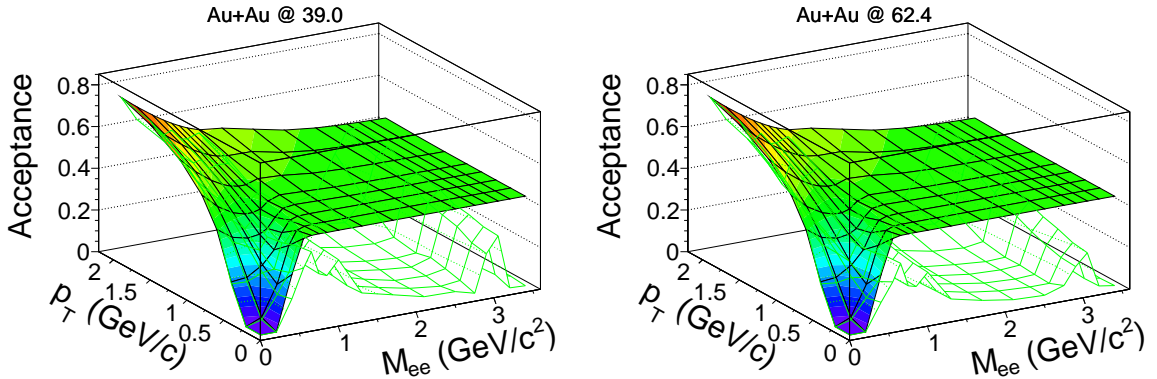


Figure 34: Acceptance calculated by virtual photon method (red grid) and cocktail method (green grid).

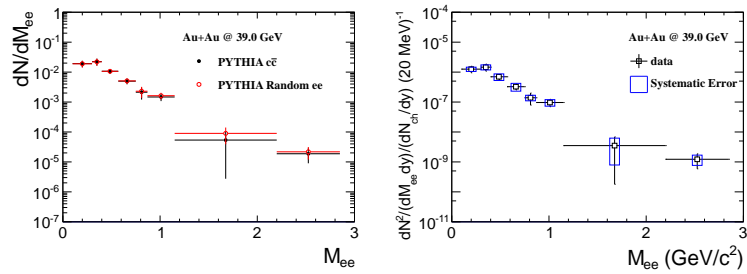


Figure 35: Left: Excess spectra with difference charm cocktail component. Right: Final spectra for 39 GeV.

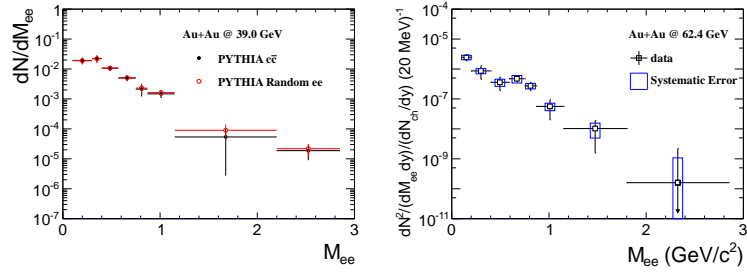


Figure 36: Left: Excess spectra with difference charm cocktail component. Right: Final spectra for 62.4 GeV.

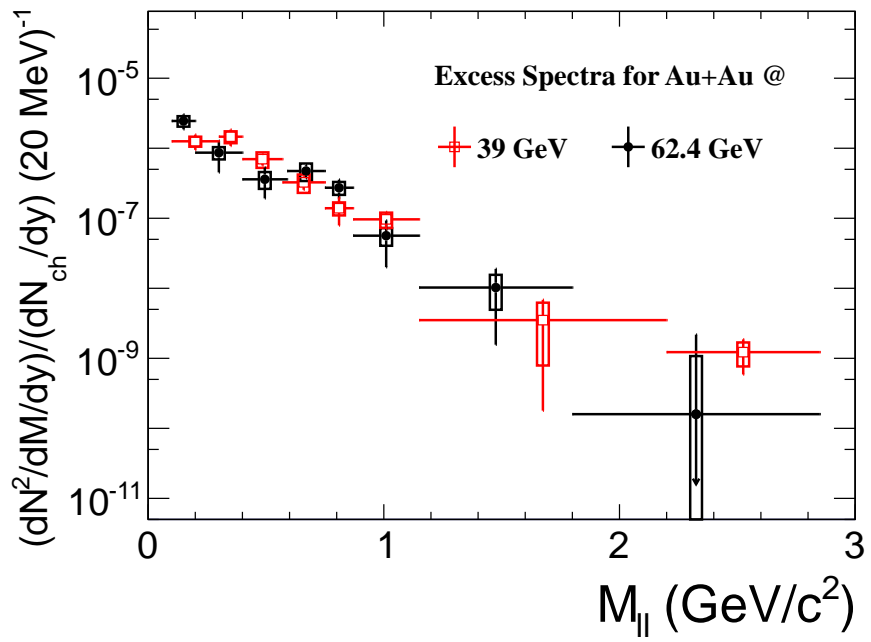


Figure 37: Acceptance corrected excess spectra for STAR Beam Energy Scan.



## Analysis Note

Authors: Joseph Butterworth, Xin Dong, Frank Geurts, Yi Guo, Bingchu Huang, Patrick Huck, Lijuan Ruan, Zebo Tang, Chi Yang, Yifei Zhang, and Jie Zhao

*Experiment Location: Upton, NY*

---

### 1 Contents

2	<b>1 Data Sample</b>	<b>3</b>
3	<b>2 Event Selection</b>	<b>3</b>
4	<b>3 Track Selection</b>	<b>4</b>
5	3.1 Purity . . . . .	5
6	<b>4 Pair Formation</b>	<b>10</b>
7	<b>5 Efficiency Corrections</b>	<b>16</b>
8	5.1 Tracking Efficiency . . . . .	16
9	5.2 Matching Efficiency . . . . .	18
10	5.3 PID Efficiency . . . . .	22
11	5.4 Pair Efficiency . . . . .	23
12	<b>6 Cocktail</b>	<b>26</b>
13	6.1 Mass Distribution . . . . .	26
14	6.2 $p_T$ Distribution . . . . .	27
15	6.2.1 Tsallis Blast Wave Fits . . . . .	28
16	6.2.2 Boltzmann Distribution . . . . .	28
17	6.3 Rapidity Distribution . . . . .	29
18	6.4 Parent Decay . . . . .	29
19	6.4.1 $p_T$ Smearing . . . . .	30
20	6.5 Scaling Yields . . . . .	32
21	6.6 $c\bar{c}$ Contribution . . . . .	33
22	6.7 Drell-Yan Contribution . . . . .	37
23	6.8 Total Cocktail . . . . .	39
24	6.9 Cocktail Uncertainties . . . . .	39

25	<b>7 Systematics</b>	<b>39</b>
26	7.1 Tracking . . . . .	40
27	7.2 Matching . . . . .	40
28	7.3 Electron Identification . . . . .	41
29	7.4 Efficiency Systematics . . . . .	41
30	7.5 Charge Acceptance Factor . . . . .	41
31	7.6 Like Sign Means . . . . .	43
32	7.7 Hadron Contamination . . . . .	44
33	7.8 JPsi Uncertainties . . . . .	51
34	7.9 Charm Correlation . . . . .	53
35	7.10 STAR to Full Phase Space Acceptance Factor . . . . .	53
36	<b>8 Final Product</b>	<b>54</b>
37	8.1 Systematic uncertainty propagation . . . . .	56
38	8.2 Agreement with Rapp . . . . .	57
39	8.3 Lifetime Dependence on $dN_{ch}/dy$ . . . . .	57
40	<b>9 HBT</b>	<b>59</b>
41	<b>Appendix A Run-by-run QA Averages</b>	<b>61</b>
42	<b>Appendix B Pure Sample Figures</b>	<b>78</b>
43	<b>Appendix C Electron Tracking Efficiency Figures</b>	<b>88</b>
44	<b>Appendix D Positron Tracking Efficiency Figures</b>	<b>90</b>
45	<b>Appendix E Electron Matching Efficiency Figures</b>	<b>92</b>
46	<b>Appendix F Positron Matching Efficiency Figures</b>	<b>94</b>
47	<b>Appendix G Comparison of Matching Efficiency Figures - Acceptance Correcting All Tracks for AuAu200 Method</b>	<b>96</b>
49	<b>Appendix H Comparison of Matching Efficiency Figures - Acceptance Correcting All Tracks and TOF Match Only Separately for AuAu200 Method</b>	<b>99</b>
51	<b>Appendix I Comparison of Matching Efficiency Figures - Acceptance Correcting All Tracks for AuAu200 Method and Variance Method</b>	<b>102</b>
53	<b>Appendix J Comparison of Matching Efficiency Figures - Acceptance Correcting All Tracks and TOF Match Only Separately for AuAu200 Method and Variance Method</b>	<b>105</b>
55	<b>Appendix K PID Efficiency Figures</b>	<b>108</b>
56	<b>Appendix L Pair Efficiency Figures</b>	<b>110</b>
57	<b>Appendix M Analysis Cuts</b>	<b>112</b>
58	<b>Appendix N Tsallis Blast Wave Fits</b>	<b>113</b>
59	<b>Appendix O Hadron Cocktail Yields</b>	<b>115</b>
60	<b>Appendix P Tracking Systematic Uncertainties Quality Assurance I</b>	<b>117</b>

## 61 Appendix Q Tracking Systematic Uncertainties Quality Assurance II

120

### 62 1. Data Sample

63 The targeted data sample is Run 11's Au+Au minimum bias collisions at  $\sqrt{s_{NN}} = 27$  GeV. These collisions were  
64 recorded by STAR with the trigger, mb1-fast(360001), starting on day 172 and continued through day 179. The STAR  
65 scheduler was used to retrieve 27GeV's MuDsts and the following catalog query parameters were used: trgsetup-  
66 name = AuAu27\_production\_2011, tpx = 1, sanity = 1, production = P11id, filetype = daq\_reco\_mudst, runnumber =  
67 &runnumber;, and filename ~ st\_physics. Runnumber is provided by the user/script.

68 The MuDst files were then transferred into "picoDsts". The picos were produced under the STAR computing  
69 environment conditions of SL12d and sl53\_gcc432. For information to be propagated to these trees, events must  
70 satisfy these conditions:  $|V_z| < 70$  cm and  $V_r < 2$  cm, while tracks must satisfy these conditions: nHitsFit > 14,  
71 nHitsPoss > 0, nHitsFit/nHitsPoss > 0.52, nHitsdEdx > 14, and  $\beta > 0$ .

### 72 2. Event Selection

73 Here we go with event selection. For selecting events, this is done based on run-by-run and event-by-event scopes.  
74 For run-by-run event selection, the aim is to look for global properties that deviate from their typical values and then  
75 reject the runs that are outliers. Typically, outliers represent poor data taking conditions, which vary from incorrect  
76 detector settings to beam background. For event-by-event event selection, these are typically cuts that reflect a physical  
77 reasoning.

78 Run-by-run QA may be seen in Appendix A. When compiling the averages, the following cuts were used to  
79 ensure data sanity:  $|V_z| < 70$  cm,  $V_r < 2$  cm, nHitsFit > 14 pts, nHitsPoss > 0 pts, nHitsFit/nHitsPoss > 0.52,  
80 nHitsdEdx > 14 pts,  $\beta > 0$ , and  $|y_{Local}| < 1.8$  cm. The variables plotted are Reference Multiplicity, dE/dx,  $p_T$ ,  $\eta$ ,  
81  $\phi$ , and  $n\sigma_{\pi,P,K,e}$ . By averaging these variables on a per run basis, changes in data taking conditions are easy to spot  
82 and facilitates bad run rejection. When looking at Day 172 run averages, you can see where the minimum bias trigger,  
83 mb1-fast(360001), is turned on at run number 12172043; hence, any run beforehand is deemed bad since it was  
84 not taken with the minimum bias trigger. On Day 173, there is a drop in Reference Multiplicity and an increase in  
85 dE/dx and  $n\sigma$ . This variation corresponds to an incorrect setting of the Time Projection Chamber(TPC)'s inner  
86 sector for run numbers 12173053 to 12173057. On Day 174, run number 12174096 is zero. This is due to Time of  
87 Flight(TOF) not being included in the run, which we rely on, so it is rejected. On Day 177, there is a 20% drop in  
88 Reference Multiplicity, since there is no BEMC included and has been rejected to maintain a uniform Reference Multi-  
89 plicity. Other run-by-run QA may be found at [www.bonner.rice.edu/jb31/protected/27GeVDielectron/PicoQA926](http://www.bonner.rice.edu/jb31/protected/27GeVDielectron/PicoQA926).

90 Separate from the run-by-run QA, the StRefMult bad run list has been used to reject runs. These are those  
91 runs: 12172050, 12172051, 12172055, 12173030, 12173031, 12173032, 12173033, 12173034, 12174067, 12174085,  
92 12175062, 12175087, 12175113, 12175114, 12175115, 12176001, 12176044, 12176054, 12176071, 12177015,  
93 12177061, 12177092, 12177099, 12177101, 12177106, 12177107, 12177108, 12178003, 12178004, 12178005,  
94 12178006, 12178013, 12178099, and 12178120.

95 Runs taken during the Vernier Scan have also been removed: 12174077, 12174085, and 12174086.

96 The following runs were used in this analysis: 12172043, 12172044, 12172045, 12172046, 12172048, 12172049,  
97 12172056, 12172057, 12172058, 12173001, 12173006, 12173007, 12173008, 12173009, 12173014, 12173015,  
98 12173016, 12173017, 12173018, 12173023, 12173024, 12173025, 12173026, 12173035, 12173044, 12173045,  
99 12173046, 12173047, 12173058, 12173064, 12173065, 12173071, 12173072, 12173073, 12173078, 12173079,  
100 12173080, 12173085, 12173086, 12173087, 12174005, 12174006, 12174007, 12174013, 12174014, 12174015,  
101 12174021, 12174022, 12174023, 12174024, 12174030, 12174031, 12174032, 12174037, 12174038, 12174039,  
102 12174044, 12174045, 12174047, 12174048, 12174054, 12174056, 12174057, 12174064, 12174065, 12174066,  
103 12174074, 12174075, 12174076, 12174082, 12174083, 12174084, 12174097, 12174100, 12174106, 12174107,  
104 12174108, 12174109, 12174115, 12174116, 12174117, 12175004, 12175005, 12175007, 12175008, 12175013,  
105 12175014, 12175015, 12175017, 12175021, 12175022, 12175023, 12175024, 12175028, 12175029, 12175030,  
106 12175031, 12175032, 12175037, 12175038, 12175039, 12175040, 12175044, 12175045, 12175046, 12175047,  
107 12175051, 12175052, 12175053, 12175054, 12175059, 12175061, 12175088, 12175089, 12175094, 12175095,

108 12175096, 12175097, 12175105, 12175106, 12175107, 12175116, 12175121, 12175122, 12175123, 12176002,  
 109 12176007, 12176008, 12176009, 12176010, 12176011, 12176017, 12176018, 12176019, 12176020, 12176025,  
 110 12176026, 12176027, 12176028, 12176029, 12176030, 12176034, 12176035, 12176036, 12176037, 12176041,  
 111 12176042, 12176043, 12176045, 12176046, 12176047, 12176052, 12176053, 12176055, 12176056, 12176057,  
 112 12176058, 12176066, 12176067, 12176069, 12176076, 12176077, 12176078, 12176083, 12176084, 12176085,  
 113 12176092, 12176093, 12176094, 12176095, 12176100, 12176101, 12176102, 12176103, 12176104, 12176109,  
 114 12176110, 12176111, 12176112, 12176117, 12176118, 12176119, 12176120, 12176121, 12176127, 12176128,  
 115 12176129, 12176130, 12176135, 12176136, 12176137, 12176138, 12177003, 12177004, 12177005, 12177006,  
 116 12177011, 12177012, 12177013, 12177014, 12177019, 12177020, 12177021, 12177022, 12177027, 12177028,  
 117 12177029, 12177030, 12177035, 12177036, 12177037, 12177038, 12177042, 12177044, 12177045, 12177046,  
 118 12177050, 12177051, 12177052, 12177053, 12177058, 12177059, 12177060, 12177062, 12177066, 12177067,  
 119 12177068, 12177069, 12177076, 12177077, 12177078, 12177079, 12177083, 12177084, 12177085, 12177086,  
 120 12177091, 12177098, 12177105, 12177113, 12177114, 12177115, 12177116, 12177122, 12177123, 12177124,  
 121 12177125, 12177126, 12178002, 12178010, 12178011, 12178012, 12178018, 12178019, 12178020, 12178021,  
 122 12178026, 12178027, 12178028, 12178029, 12178034, 12178035, 12178036, 12178038, 12178047, 12178048,  
 123 12178049, 12178050, 12178051, 12178059, 12178060, 12178061, 12178062, 12178063, 12178070, 12178071,  
 124 12178072, 12178073, 12178074, 12178075, 12178077, 12178082, 12178083, 12178084, 12178085, 12178090,  
 125 12178091, 12178093, 12178094, 12178100, 12178101, 12178102, 12178103, 12178108, 12178109, 12178110,  
 126 12178119, 12178121, 12178122, 12178123, 12179002, 12179004, 12179005, 12179009, 12179010, 12179011,  
 127 12179012, 12179020, 12179021, 12179022, 12179023, 12179028, 12179029, 12179030, 12179031, 12179036,  
 128 12179037, 12179038, 12179039, 12179043, 12179044, 12179045, 12179052, 12179053, 12179054, 12179059,  
 129 12179060, 12179061, 12179062, 12179063, 12179068, 12179083, 12179084, 12179085, 12179086, 12179093,  
 130 12179094, 12179095, 12179096, 12179097

131 For event-by-event selection, the following cuts were used:  $|V_z| < 70$  cm,  $V_r < 2$  cm, StRefMult returns OK ( $\geq 6$ ),  
 132 trigger ID = 360001, and must contain one primary track that satisfies:  $n\text{HitsFit} > 14$  points,  $n\text{HitsPoss} > 0$  points,  $0.52$   
 133  $< n\text{HitsFit}/n\text{HitsPoss} < 1.05$ ,  $0.2 \leq p_T \leq 2 \text{ GeVc}^{-1}$ , and  $|\eta| < 1$ .

134 The  $V_z$  cut is motivated by the collider group delivering collisions over this range and to gain maximum statistics;  
 135 however, there is a large material budget associated to such a large range and it contributes to the conversion  
 136 background. The  $V_r$  cut is intended to cut out collisions with the beam pipe. StRefMult is a package used to cor-  
 137 rect and provide the proper reference multiplicity. Ensuring a multiplicity of at least six will give collisions with  
 138 a centrality of at least 80%. The trigger ID is designed to give a minimum bias data sample and a centrality of  
 139 0-80%. Lastly, the track requirement has a minimal effect, but is used to ensure that event class information is avail-  
 140 able such as  $\hat{Q}$  and  $\Psi$ -capable of determining the event plane for mixing events within the appropriate event class.

141

### 142 3. Track Selection

143 The following track cuts have been made to ensure quality tracks:  $p_T > 0.2 \text{ GeVc}^{-1}$ ,  $n\text{HitsPoss} > 0$  points,  
 144  $n\text{HitsFit} \geq 15$  points,  $n\text{HitsFit}/n\text{HitsPoss} > 0.52$ ,  $\text{gDCA} < 1$  cm,  $|\eta| < 1$ ,  $\beta > 0$ , and TOF's  $|\text{y}_{\text{Local}}| < 1.8$  cm.  
 145 The transverse momentum cut is motivated by a particle requiring slightly less than  $0.2 \text{ GeVc}^{-1}$  to escape the  
 146 magnetic field and reach the TOF. The  $n\text{HitsFit}$  and  $n\text{HitsPoss}$  are used to make sure that the tracking by the  
 147 TPC is reasonable. The gDCA cut is selected to cut down on conversion pairs. This is important because of the  
 148 beam/data-taking conditions provided for the Beam Energy Scan program and it is seen as a background source  
 149 in  $\eta$ . Selecting  $\beta > 0$  ensures a primary track being matched to the TOF and the  $\text{y}_{\text{Local}}$  constrains it to the phys-  
 150 ical size of a module and reduces the amount of tracks that have been mismatched to conversion electrons.

151 With these quality cuts in place, electrons and positrons are selected from the remaining sample through the  
 152 use of the TPC and TOF. The TPC measures the particle's ionization energy loss,  $dE/dx$ , and can be transformed into  
 153 a Gaussian quantification of a particle's id. This is done by normalizing the  $dE/dx$  to the Bichsel function's expected

155  $dE/dx$  for a given particle and is shown in Equation 1.

$$n\sigma_{type} = (R_{dE/dx})^{-1} \log \left( \frac{dE/dx_{Measured}}{dE/dx_{Bichsel}} \right) \quad (1)$$

156 To improve  $n\sigma$ , the TOF can be used to remove hadronic contamination in the signal by rejecting slower particles. In  
 157 this analysis, a cut of  $|\beta^{-1} - 1| < 0.03$  is used to reject the slower hadrons. Figure 1 contains the  $\beta^{-1}$  distribution as  
 158 a function of momentum and illustrates the separation of particles based on their speed. Shown in Figure 2 is the  $n\sigma$   
 159 distribution as a function of momentum before the cut and shown in Figure 3 is the distribution after the cut. At this  
 160 point, an  $n\sigma_{el}$  cut is used to select a pure sample from which the electron-positron pairs are generated. The cuts are  
 161 listed in Eq. 2.

$$\begin{aligned} n\sigma_e &< -0.687342 * p + 2.1 \\ n\sigma_e &> -0.663252 \text{ when } p \geq 0.637 \\ n\sigma_e &> 1.604 * p - 1.685 \text{ when } p < 0.637 \end{aligned} \quad (2)$$

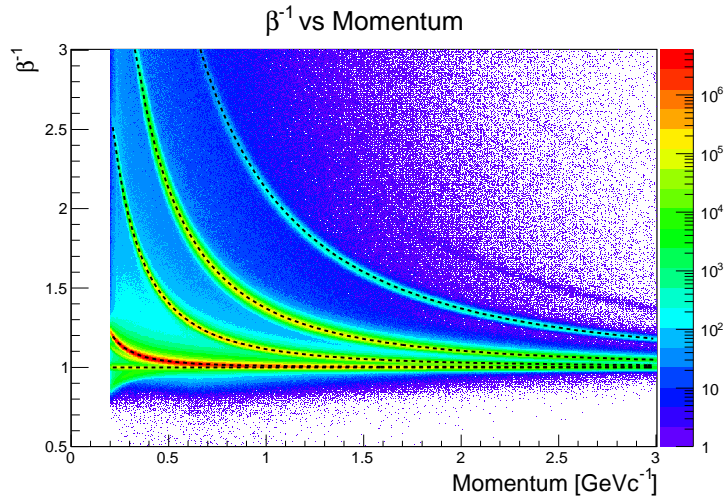


Figure 1. The  $\beta^{-1}$  distribution as a function of momentum. Dash lines represent the expected velocity for a given particle type. The following particles are used to draw the lines: e,  $\pi$ , K, p, and d.

### 162 3.1. Purity

163 To estimate the purity of the data sample, a multi-Gaussian fit where each Gaussian component represents a dif-  
 164 ferent particle species,  $e/\pi/K/p/\pi\pi$ . The area under each curve is used to estimate the quantity of each species, and  
 165 ultimately, the purity. To help constrain each component, Gaussian fits to pure samples are used to constrain the mean  
 166 and width of each component. And in the regions where the particle contributions overlap, exponential extrapolati-  
 167 ons of the yields are used to constrain the amplitude. Both the data and pure samples are stored in 2D histograms  
 168 of momentum vs  $n\sigma_{El}$  with  $dP = 5 \text{ MeVc}^{-1}$  and  $dn\sigma = 0.8$ . Each are studied in  $n\sigma$  slices, -6 to 6, as a function  
 169 of momentum, where  $dP = 20 \text{ MeVc}^{-1}$  when  $p < 1.48 \text{ GeVc}^{-1}$  and  $dP = 40 \text{ MeVc}^{-1}$  when  $p < 1.48 \text{ GeVc}^{-1}$ .

170 Pure samples of  $\pi$ , K, and p are generated from a sample with the event and quality track selection criteria listed in  
 171 Sections 2 and 3 in addition to the following criteria:  $|n\sigma_x| < 1$  (or 0.5 in 27GeV), where x is the particle of interest [ $\pi$ ,  
 172 K, or p], and  $|\beta^{-1} - \beta_{expected}^{-1}| < 0.03$ .

173 The merged  $\pi$  sample is generated from a sample with the event and quality track selection criteria listed in  
 174 Sections 2 and 3 in addition to the following criteria:  $n\sigma_\pi > 3$  (aka 6) and then fitting the peak around  $n\sigma_{El} = 2$  as  
 175 shown in Figure 4.

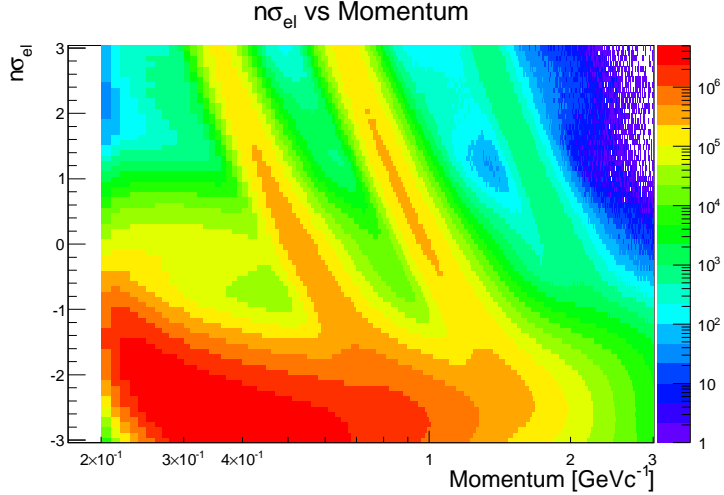


Figure 2. The  $n\sigma_{electron}$  distribution as a function of momentum before a cut to remove slower hadrons.

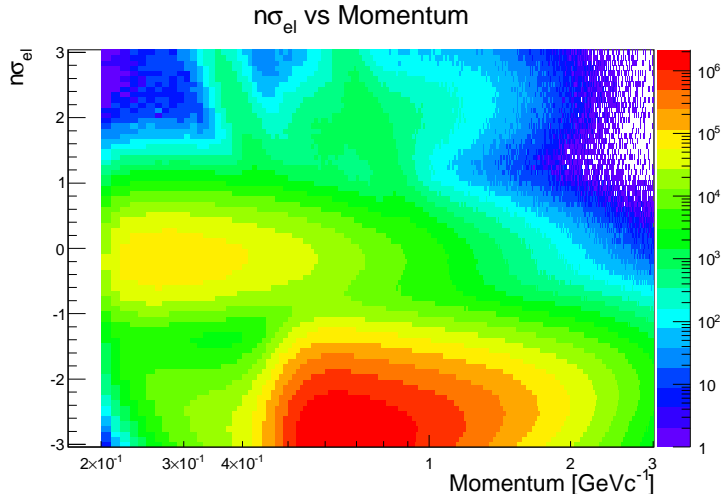


Figure 3. The  $n\sigma_{electron}$  distribution as a function of momentum after a cut to remove slower hadrons.

176     The pure sample of electrons is generated with the same method used in the Matching Efficiency Section, Section  
 177     5.2, with the exception that all electrons are required to have a match with the Time of Flight detector and  $|\beta^{-1} -$   
 178      $\beta_{expected}^{-1}| < 0.03$ .

179     To aid ROOT in fitting the pure samples'  $n\sigma_{El}$ , multiple attempts at the fit are made, and for each iteration,  
 180     constraints are varied based on the previous fit. In the cases pertaining to e,  $\pi$ , K, and p, there are four iterations of fits with  
 181     the ROOT defined Gaussian function. The first Gaussian function requires the option "M", improved Minuit fit. Each  
 182     successive iteration uses the previous fits mean and sigma to constrain the fit with the options "BMR", where "B" ena-  
 183     bles the use of set parameters. The previous mean is also used to set the fitting range with the option "R". The second  
 184     fit, constrains the range to the previous mean  $\pm 0.5$ . The third fit uses the range based on the previous mean  $\pm 1$ . And  
 185     finally, The fourth fit uses the previous mean  $\pm 4$ . In the case of electrons, the mean is constrained to  $\pm 0.5$ , while  $\pi$ , K,  
 186     and p have no such limits.

187     In the instance of merged  $\pi$ , two fits with the default Gaussian function are made. The first fit uses the opti-  
 188     ons "BMR" where the fit range is confined to 1.1 to 2.8. The final fit uses the same options and a fit range defined as  
 189     the previous mean - 0.4 and + 0.7. In addition to the fit range constraints, the mean and sigma parameters are limited to

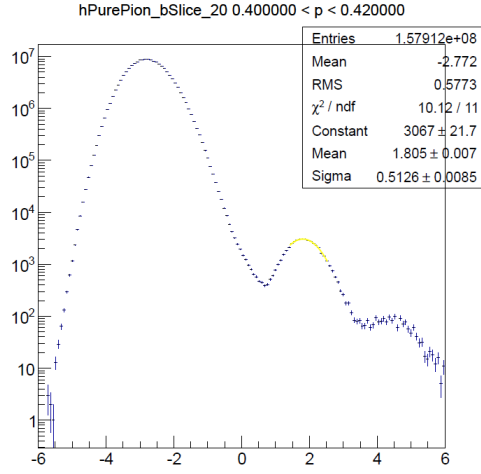


Figure 4. The  $n\sigma_{electron}$  distribution for tracks with  $n\sigma_\pi > 3$ . The yellow Gaussian fit at about  $n\sigma_{electron} = 2$  is used to constrain the mean and width for the  $\pi\pi$  sample.

[1.7,3.4] and [0.4,0.65], respectively. The parameter limits are to help with the fitting when the  $\pi\pi$  peak is crossed-over by the proton and kaon peaks.

Plots demonstrating the pure sample selection and fits may be found in Appendix B, where the Gaussian fits for each species are as follows:  $\pi$  = black, electron = orange, kaon = cyan, proton = green, and  $\pi\pi$  = yellow. It is from these curves that the mean and width values are obtained to constrain the Gaussian components in the multi-Gaussian curve that fits the data sample. To ensure ROOT does not undergo too many undesirable actions, the Gaussian curve for  $\pi\pi$  are zeroed out until  $p > 0.44 \text{ GeVc}^{-1}$  and the curve for kaons are zeroed until  $p > 0.24 \text{ GeVc}^{-1}$ .

In the momentum regions where the kaon and proton dE/dx bands overlap with the electrons band, their corresponding Gaussian curves are fixed. The width and mean are still fixed from fitting pure samples, while the constant is fixed by extrapolating from an exponential fit of the particle raw yields, where yield is defined as the integral of the curve from -6 to  $6n\sigma_e$ . The exponential fits are done with the exponential function listed in Eq. 3. A few different exponential fits were preformed and some will act as a systematic difference.

$$y = e^{A \cdot x + B} \quad (3)$$

Two sets of fits are considered for electron extrapolation, two sets for kaon extrapolation, and two sets for proton extrapolation. One electron set fits the yield over the momentum range  $0.29$  to  $1.5 \text{ GeVc}^{-1}$ , while excluding the ranges between  $0.46$  to  $0.7 \text{ GeVc}^{-1}$  and  $0.86$  to  $1.2 \text{ GeVc}^{-1}$  and constraining the raw yield to between  $1\text{E}4$  and  $1\text{E}6$ . The other electron set, takes two fits into account. One fit covers the range from  $0.29$  to  $1.2 \text{ GeVc}^{-1}$  while excluding the ranges between  $0.46$  to  $0.7 \text{ GeVc}^{-1}$  and  $0.86$  to  $1.2 \text{ GeVc}^{-1}$  and constraining the yield between  $1\text{E}4$  and  $1\text{E}6$ . The other fit of the set covers from  $0.6$  to  $1.5 \text{ GeVc}^{-1}$  while excluding the ranges between  $0.46$  to  $0.7 \text{ GeVc}^{-1}$  and  $0.86$  to  $1.2 \text{ GeVc}^{-1}$  and constrains the yield between  $1\text{E}4$  and  $6\text{E}4$ . The projection of these fits can be seen from left to right in Fig. 5 respectively. Constraints on the yields were there to aid the fits.

For the kaon extrapolations, three sets of fits were performed, and all three fits are considered. The first set fit the yield over the momentum range from  $0.32$  to  $0.8 \text{ GeVc}^{-1}$  while excluding from  $0.46$  to  $0.7 \text{ GeVc}^{-1}$  and no constraint on the yield. The second set fit the yield over the momentum range from  $0.32$  to  $0.6 \text{ GeVc}^{-1}$  while excluding the range from  $0.46$  to  $0.7 \text{ GeVc}^{-1}$  and no constraint on the yield. The third set fit the yield over the momentum range from  $0.6$  to  $0.8 \text{ GeVc}^{-1}$  while excluding from  $0.46$  to  $0.7 \text{ GeVc}^{-1}$ . The extrapolations of these fits are shown in Fig. 6 from left to right respectively. The third set should probably be excluded from consideration, but it gives an uncertainty band that helps the connecting regions(conservative estimation). The higher momentum ranges, the third fit, are a bit off because the kaon yield is difficult to extrapolate here as the kaon band crossed into the dominate pion band.

For the proton extrapolations, three sets of fits were performed, but only two sets are considered. The first set fit

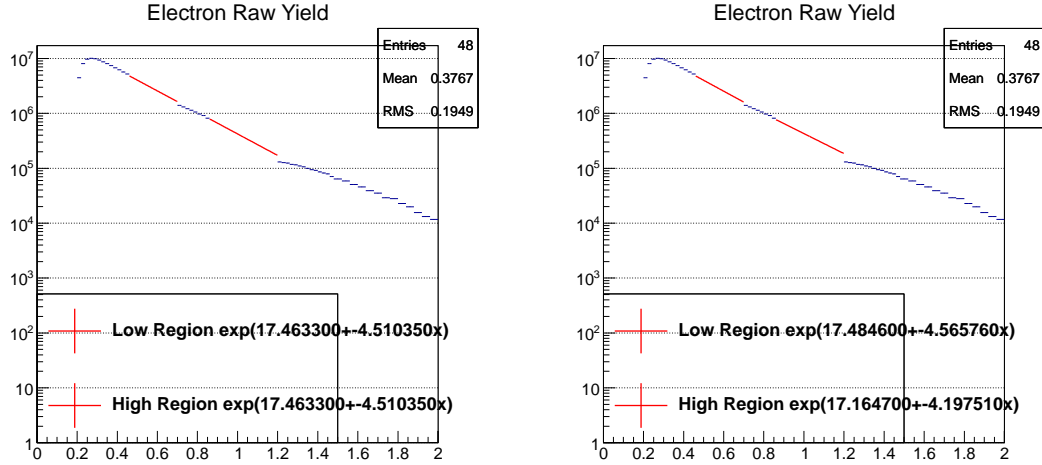


Figure 5. Using configuration of ...

220 the yield over the momentum range from 0.49 to  $1.4 \text{ GeVc}^{-1}$  while excluding the ranges 0.64 to  $1.2 \text{ GeVc}^{-1}$  and 1.36  
 221 to  $4 \text{ GeVc}^{-1}$  with no constraint on the yield. The second set fit the yield over the momentum range from 0.49 to 0.7  
 222  $\text{GeVc}^{-1}$  while excluding the range from 0.64 to  $1.2 \text{ GeVc}^{-1}$  and 1.36 to  $4 \text{ GeVc}^{-1}$  with no constraint on the yield.  
 223 The third set fit the yield over the momentum range from 0.7 to  $1.4 \text{ GeVc}^{-1}$  while excluding the ranges from 0.64 to  
 224 1.2  $\text{GeVc}^{-1}$  and 1.36 to  $4 \text{ GeVc}^{-1}$  with no constraint on the yield. The extrapolations of the fits are shown in Fig. 7  
 225 from left to right respectively. The third set was not considered.

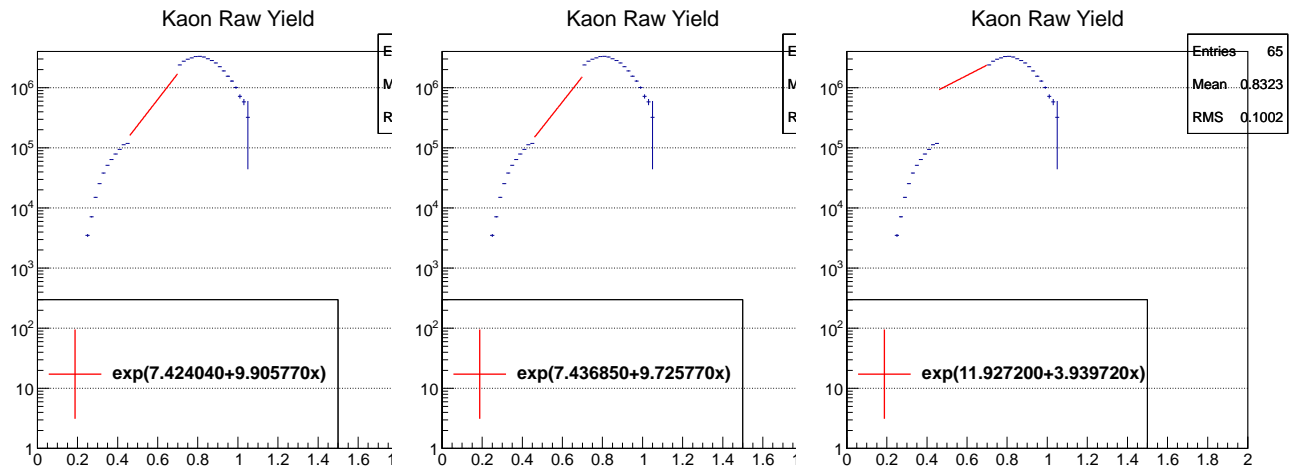


Figure 6. Using configuration of ...

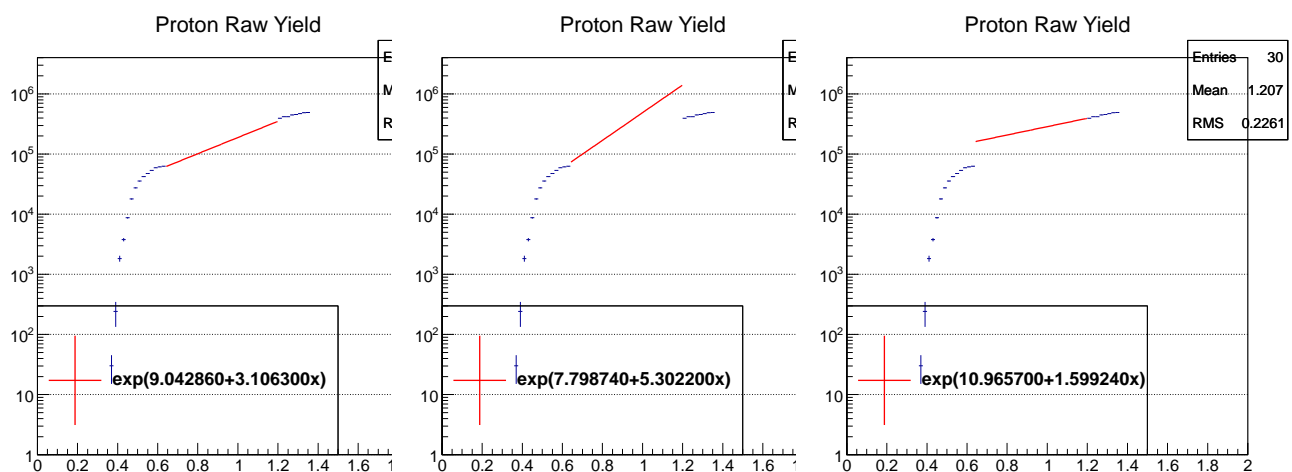


Figure 7. Using configuration of ...

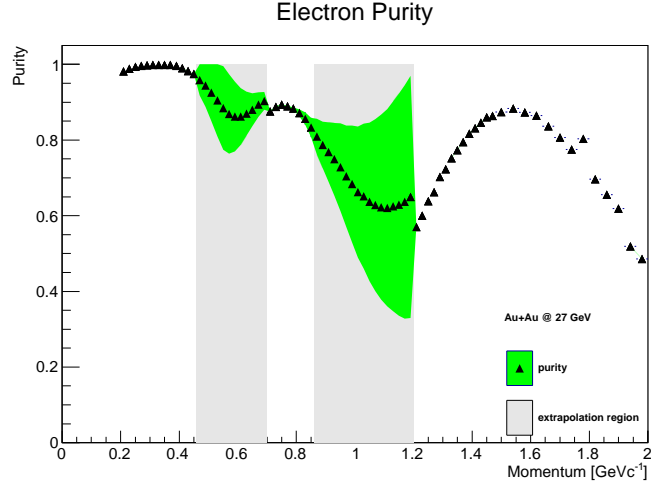


Figure 8. The electron purity while using electron fit set 2, kaon fit set 1, and proton fit set 1. The grey shaded regions are where the electron yields have been extrapolated. The green band represents the systematic uncertainty that are derived from using other raw yield extrapolations for electrons, protons, and kaons.

226 The purity of electrons is calculated when using the fits from the electron set 2, the kaon set 1, and proton set 1.  
 227 The purity is shown in Fig. 8. The systematic uncertainty is calculated by taking the maximum difference between  
 228 the extrapolated yields from the considered fit sets and propagating them as the systematic uncertainty for that particle  
 229 species. If the propagated uncertainty exceeds a purity of 1, the maximum is capped at 1. Bayesian uncertainty  
 230 determination should probably be used; however, adding in quadrature was used. The average electron purity from  
 231 0.2 to 2.0 GeVc<sup>-1</sup> is 94.5±0.74%, where the error is systematic. The statistical error is negligible for the total sample.  
 232 To see how the hadron contamination affects the signal, see Sec. 7.7.

#### 233 4. Pair Formation

234 Ultimately, we want to study the electron-positron production from Au+Au collisions and, in particular, the in-  
 235 variant mass distribution. To extract the pairs from the data, a combinatorial method is used to reconstruct the pairs  
 236 by taking each electron and pairing them with each positron from the same event. The resulting distributions, the fo-  
 237 reground, contains background that arises from combinatorial pairs, correlated pairs, and photonic conversions. The  
 238 combinatorial pair background is from matching unrelated electrons and positrons. The correlated pair background is  
 239 from pairing correlated electrons and positrons; for example, pairs from double Dalitz decays or jets. The photonic  
 240 conversion background are from where the photons interact with the detector and decay into an electron-positron pair.

241 To estimate the combinatorial and correlated backgrounds, a geometric mean of the like-sign signed pairs with an  
 242 acceptance correction based on mixed event pairs is used. This is expressed in Equation 4, where N<sub>++</sub> are positron  
 243 pairs from the same event, N<sub>--</sub> are electron pairs from the same event, ME<sub>+-</sub> are electron-positron pairs from different  
 244 events, ME<sub>++</sub> are positron pairs from different events, and ME<sub>--</sub> are electron pairs from different events.

$$BG = 2 \sqrt{N_{++} N_{--}} \frac{ME_{+-}}{2 \sqrt{ME_{++} ME_{--}}} \quad (4)$$

245 The mixed event pairs are comprised of electrons and positrons that originate from events with similar characteris-  
 246 tics. This is to ensure similar data recording conditions. The differential characteristics considered in this study are the  
 247 z vertex position, reference multiplicity, and event plane angle. The z vertex position is divided into 25 equi-distant  
 248 pools with a dz that ranges from -70 cm to +70 cm. The reference multiplicity is divided into 16 pools ranging from  
 249 0-80% centrality as provided by the StRefMult package. The event plane angle,  $\Psi_2$ , is divided into 12 pools. These  
 250 event pools were decided by varying the number of the pools, comparing the invariant mass distributions for each

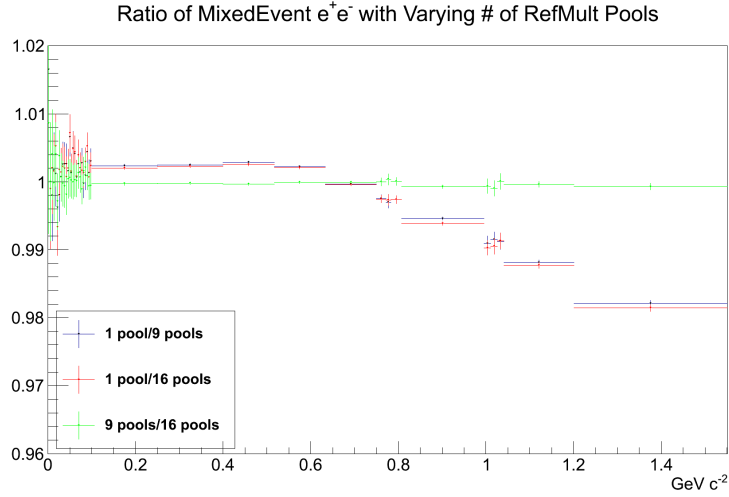


Figure 9. The ratio of the invariant mass spectrum of  $e^-e^+$  mixed from different events. The pairs are formed as function of their reference multiplicity class.

251 variation, and selecting the number as the distribution levels off for each variation. The reference multiplicity,  $\Psi_2$ , and  
 252  $z$  vertex position invariant mass ratios are shown in Figs. 9, 10, and 11, respectively.

253  $\Psi_2$  is defined in Equation 5, where  $Q_x$  and  $Q_y$  are the event's total momentum in the x and y directions and are  
 254 defined by Equations 6 and 7, respectively.

$$\Psi_2 = ATan2(Q_y, Q_x)/2. \quad (5)$$

$$Q_x = \sum_{\text{tracks}} \hat{Q}_x = \sum_{\text{tracks}} p_T \cos(2\phi) \quad (6)$$

$$Q_y = \sum_{\text{tracks}} \hat{Q}_y = \sum_{\text{tracks}} p_T \sin(2\phi) \quad (7)$$

257  $Q_{x,y}$  have been recentered to flatten the event plane in order to remove acceptance correlations, and to further  
 258 the removal of acceptance correlations while making the event plane even flatter, a shifting method has been used in  
 259 succession to the recentering correction. This methods are presented in the following reference [1]. To recenter  $Q_{x,y}$ ,  
 260 each  $\hat{Q}$  is corrected with the mean  $\hat{Q}$  value, or in other words, the total  $Q_{x,y}$  is corrected by the mean  $\hat{Q}_{x,y}$  scaled by  
 261 the number of tracks in the event. This is demonstrated in Equation 8.

$$\text{Corrected } Q_x = Q_x - N_{\text{tracks}} \cdot \langle \hat{Q} \rangle \quad (8)$$

262 The corrected  $Q_{x,y}$  values are then used to determine  $\Psi_2$  via Equation 5.  
 263  $Q$  is calculated with primary tracks that meet the following requirements:  $n\text{HitsFit} > 14$ ,  $n\text{HitsPoss} > 0$ ,  $0.52 < n\text{HitsFitRatio} < 1.05$ ,  $0.2 \leq p_T \leq 2.0 \text{ GeVc}^{-1}$ , and  $|\eta| < 1$ . The upper limit on  $p_T$  is to exclude jets from the calculation. Figures 12 and 13 show the uncorrected  $Q_{x,y}$  and event plane angle, and Figure 14 shows the uncorrected  $\hat{Q}_{x,y}$  distribution. This is the distribution used to determine the recentering offsets, where  $\langle \hat{Q}_x \rangle = 0.00116153$  and  $\langle \hat{Q}_y \rangle = 0.0060679$ . Figure 15 shows the result of applying the recentering method with the values given above. Since the event plane is not completely isotropic, the shifting method is used to make it flatter. This entails fitting a Fourier expansion, Equation 9, to the recentered event plane angles for all events and then shifting the recentered event plane angle on an event-by-event basis with Equation 10, where  $\langle \cos(2\Psi_2) \rangle = -2.74700\text{e-}03$ ,  $\langle \sin(2\Psi_2) \rangle = -4.23629\text{e-}03$ ,  $\langle \cos(4\Psi_2) \rangle = 6.59813\text{e-}04$ , and  $\langle \sin(4\Psi_2) \rangle = 4.15457\text{e-}03$ . The fit is shown in Figure 16 and the results after correcting each event plane angle with the shift is shown in Figure 17.

$$P(\Psi_2) \sim 1 + 2\langle \cos(2\Psi_2) \rangle \cos(2\Psi_2) + 2\langle \sin(2\Psi_2) \rangle \sin(2\Psi_2) + 2\langle \cos(4\Psi_2) \rangle \cos(4\Psi_2) + 2\langle \sin(4\Psi_2) \rangle \sin(4\Psi_2) \quad (9)$$

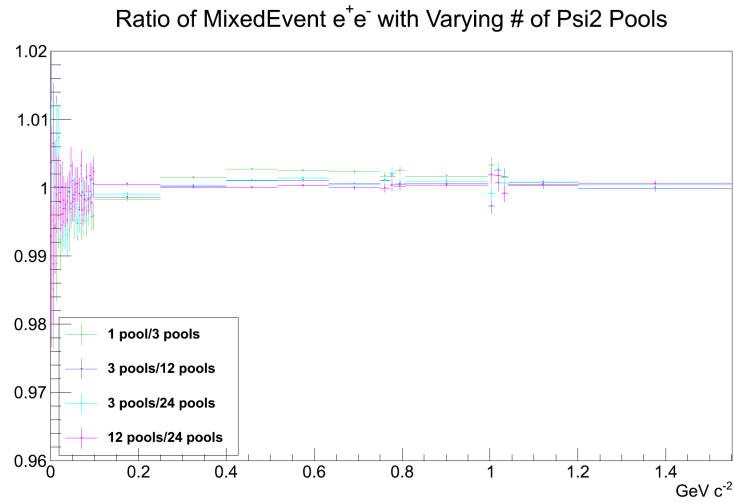


Figure 10. The ratio of the invariant mass spectrum of  $e^-e^+$  mixed from different events. The pairs are formed as function of their event plane angle.

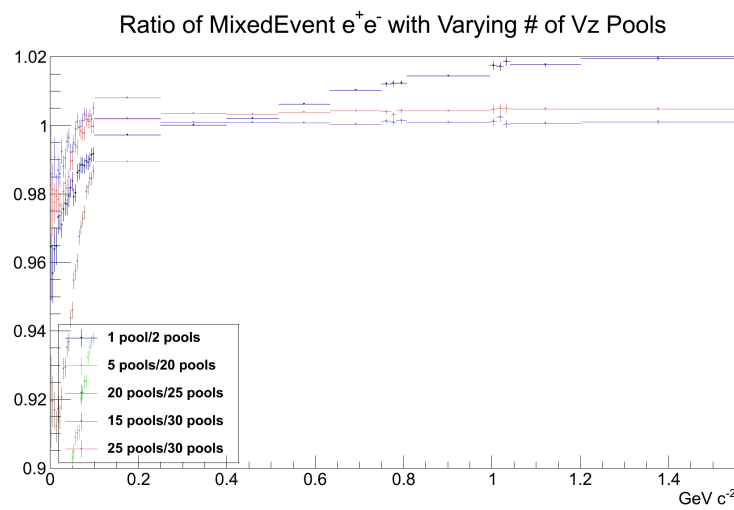


Figure 11. The ratio of the invariant mass spectrum of  $e^-e^+$  mixed from different events. The pairs are formed as function of their z vertex position.

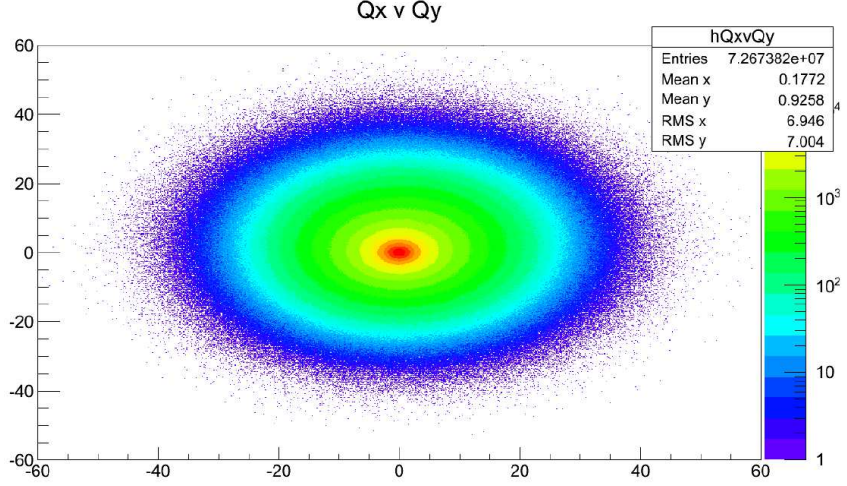


Figure 12. The uncorrected  $Q_x$  vs  $Q_y$  for all events. Notice that the distribution is not centered around zero.

$$\Delta\Psi_2 = \frac{1}{2}(2\langle\cos(2\Psi_2)\rangle\sin(2\Psi_2) - 2\langle\sin(2\Psi_2)\rangle\cos(2\Psi_2) + \sin(4\Psi_2)\langle\cos(4\Psi_2)\rangle - \langle\sin(4\Psi_2)\rangle\cos(4\Psi_2)) \quad (10)$$

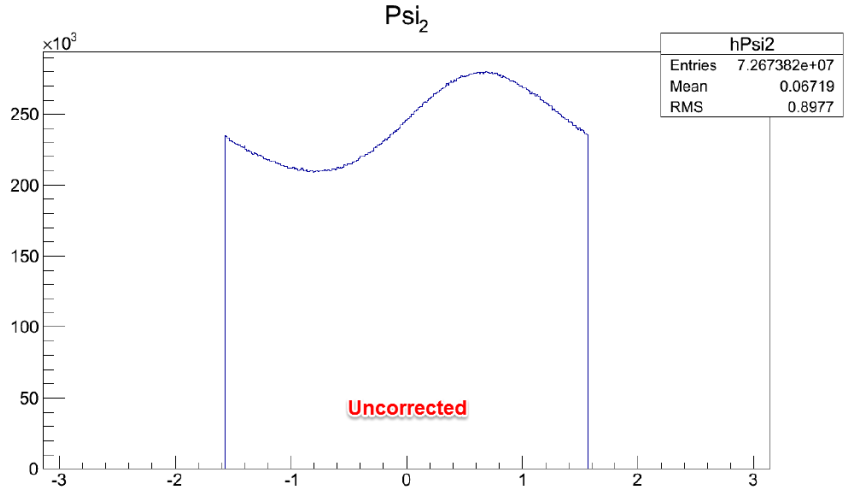


Figure 13. The uncorrected event plane angle,  $\Psi_2$ .

The conversion background is rejected by applying a  $\Phi_V$  selection criteria to every generated pair, which includes both same-event pairs and mixed-event pairs.  $\Phi_V$  is defined in Equation 11 and represents the angle between the pair's orientation of the opening angle and the orientation of the opening angle if the pair was from conversion. This is done by defining the pair's momentum direction as  $\hat{u}$  and the plane perpendicular to the pair as  $\hat{v}$ . Then orientation of the opening angle would be  $\hat{w}$  and the orientation of the opening angle if the pair originated from a conversion would be  $\hat{w}_c$ .

$$\hat{u} = \frac{\vec{p}_+ + \vec{p}_-}{|\vec{p}_+ + \vec{p}_-|}$$

$$\hat{v} = \vec{p}_+ \times \vec{p}_-$$

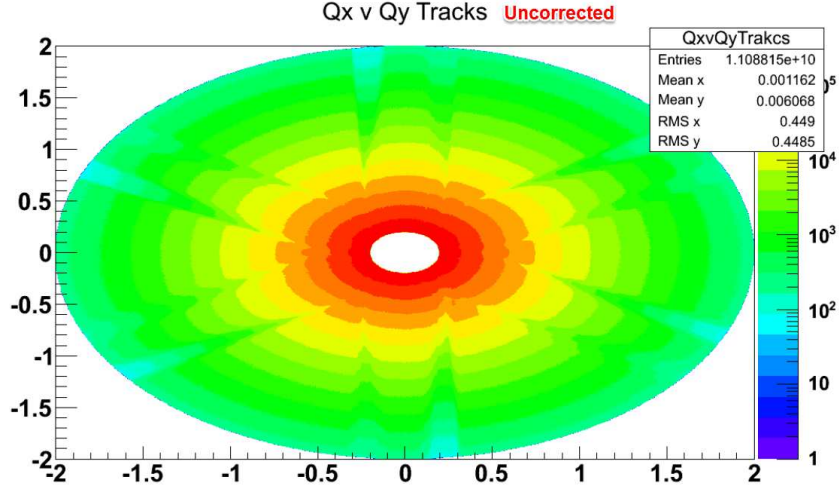


Figure 14. The  $\hat{Q}_x$  vs  $\hat{Q}_y$  distribution for all events. The mean values for  $\hat{Q}_x$  and  $\hat{Q}_y$  are used to recenter and correct the event plane.

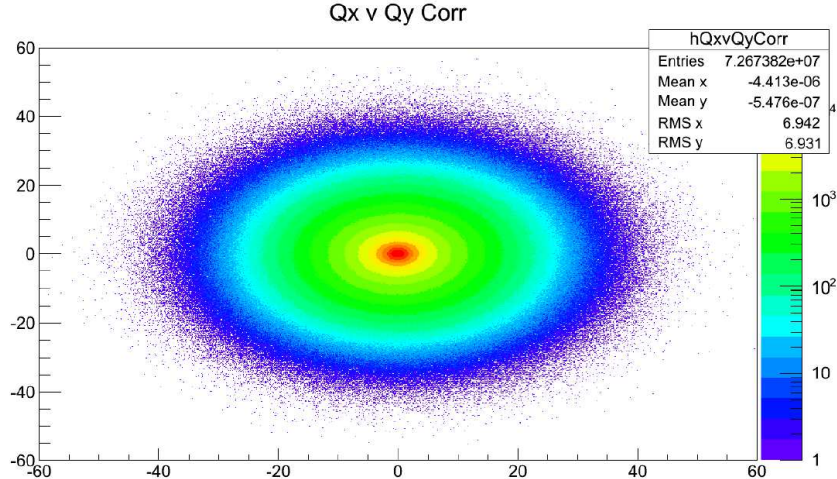


Figure 15. The  $Q_x$  vs  $Q_y$  for all events after being recentered. Notice that the distribution has been centered.

$$\begin{aligned}\hat{w} &= \hat{u} \times \hat{v} \\ \hat{w}_c &= \hat{u} \times \hat{z} \\ \cos\Phi_V &= \hat{w} \cdot \hat{w}_c \\ \Phi_V &= \arccos(\hat{w} \cdot \hat{w}_c)\end{aligned}\tag{11}$$

279 To illustrate the effect of the cut, Eq. 12 and Eq. 13, on the invariant mass as function of  $\Phi_V$ , Figures 18 and 19  
280 are shown to illustrate the before and after  $\Phi_V$  vs  $M_{ee}$  distributions.

$$M_{ee} > -0.219936137 \cdot \phi_V + 0.113235\tag{12}$$

$$M_{ee} > -0.0323866619 \cdot \phi_V + 0.0356548\tag{13}$$

281 For same-event like-sign pairs, the  $\phi_V$  calculation has no preferred order; however, the filling of tracks does appear  
282 to have an azimuthal dependence. So to remove the filling effect on the  $\phi_V$  calculation, the like-sign same-event

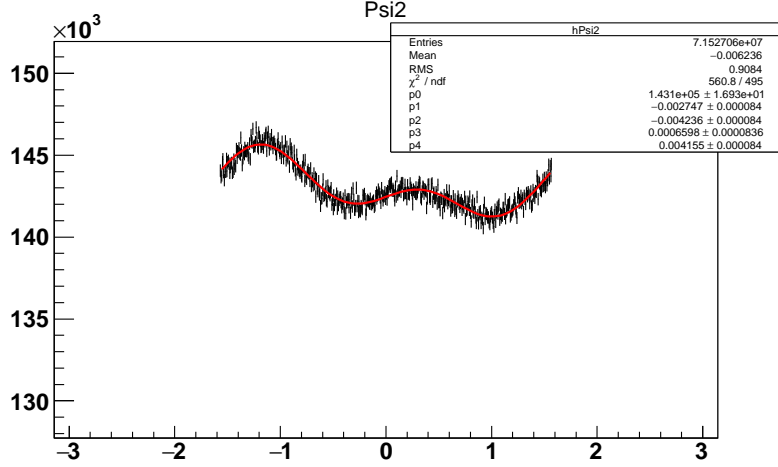


Figure 16. The event plane angle,  $\Psi_2$ , after  $Q_{x,y}$  being recentered, is fitted by Equation 9. The fit is used to determine parameters involved in the shifting of the event plane angle after recentering.

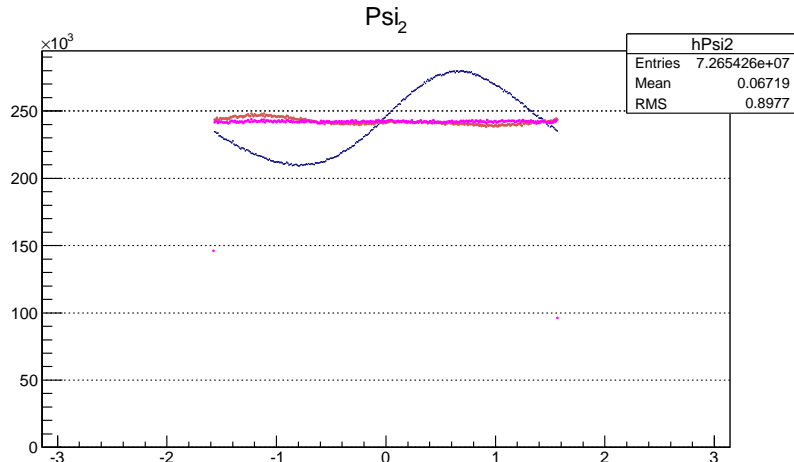


Figure 17. The event plane angle,  $\Psi_2$ , through the progression of corrections. The blue points represent the uncorrected event plane angles. The red points represent the event plane angle after the recentering correction. The pink histogram represents the event plane angle after applying the shifting correction to the recentered plane.

283 electron and positron lists are std::shuffled to ensure randomization when calculating  $\phi_V$ .

284 The foreground and background are treated in a two-dimensional manner based on the pair's  $p_T$  and  $M_{ee}$ . This  
 285 enables a more accurate description of the background, and in turn, a better description of the signal or the signal  
 286 provides a better description of the underlying physics. Here are images of the foreground, background, and acceptance  
 287 as function of  $dM_{ee}$  and  $p_T$ : Figs. 20, 21, and 22. Subtracting the background from the foreground leaves hadronic  
 288 and medium contributions that is called the signal. All three distributions are shown overlaid in Fig. 23 as the top  
 289 panel. None of these distributions have been efficiency corrected. The ratio of signal to background is shown in Fig.  
 290 23 as the bottom panel. This ratio indicates that pairs with a low invariant mass have a 1/300 and demonstrates the  
 291 need for statistics and an understanding of the background.

292 Note: The dielectron sample is processed as one computing job. This ensures that the mixed event sample buffer  
 293 is large enough not to bias it.

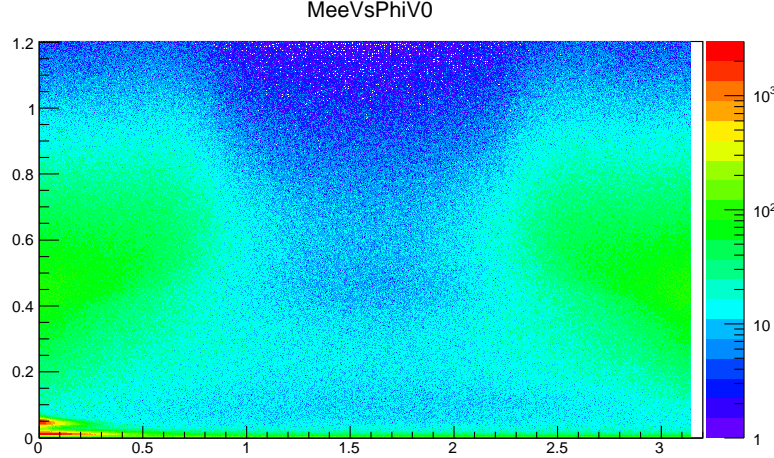


Figure 18.  $\phi_V$  vs  $M_{ee}$  before implementing the cuts in Eq. 12 and Eq. 13. Notice the two conversion peaks in the lower left hand corner. These peaks correspond to the beam pipe and supporting structure/inner TPC field cage.

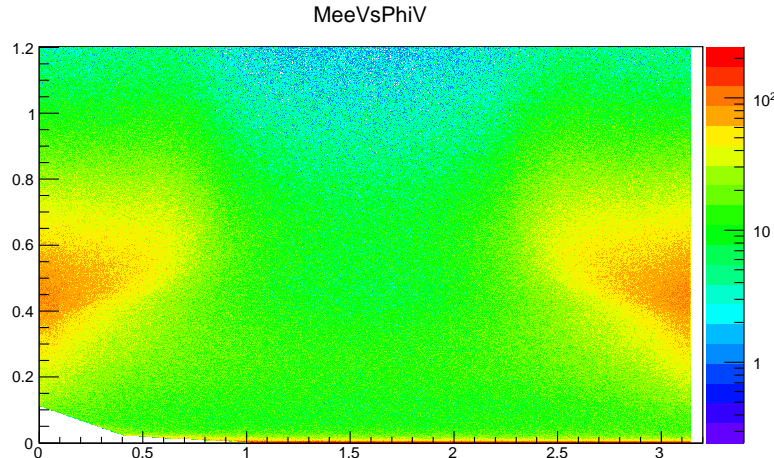


Figure 19.  $\phi_V$  vs  $M_{ee}$  after implementing the cuts in Eq. 12 and Eq. 13.

## 294 5. Efficiency Corrections

295 The following section discusses the efficiencies derived to correct the raw signal found in 4. This is done to  
 296 approximate the amount of signal loss due to our analysis methods and is broken into four subsections: Tracking  
 297 Efficiency, Matching Efficiency, Particle Identification Efficiency, and Pair Efficiency.

### 298 5.1. Tracking Efficiency

299 The tracking efficiency is used to capture the efficiency of the tracking capabilities of STAR (TPC). For this study,  
 300 these efficiencies are determined through the use of embedding. Embedding is where simulated data is inserted into  
 301 real physics data events and reconstructed. Then the efficiency and acceptance effects may be studied as the same se-  
 302 lection criteria that is applied in the analysis is applied to the embedding sample.

303 For this study, an embedding request submitted by Patrick Huck was used. It requested the Z Vertex position  
 304 to vary between -50 and +50 cm, a flat  $p_T$  distribution from 0.2 to 4.0  $\text{GeV c}^{-1}$ , flat  $\eta$  between -1.2 to 1.2, and the  
 305 production library P11id. The resulting minimc.root files were used as the data sample. The tracking efficiency is

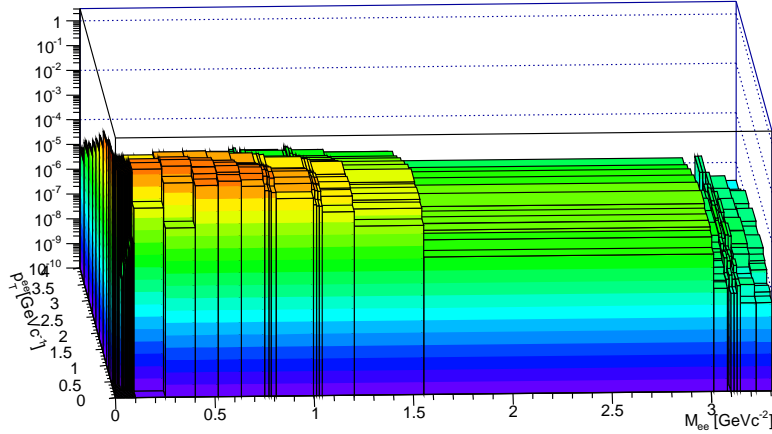


Figure 20. The foreground distribution as a function of  $M_{ee}$  and  $p_T^{ee}$ .

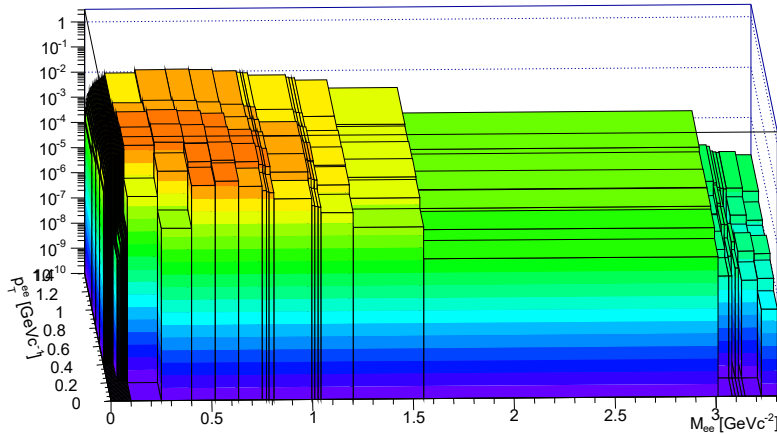


Figure 21. The background distribution as a function of  $M_{ee}$  and  $p_T^{ee}$ .

estimated by comparing the number of tracks created through simulation to the number of those tracks that survive reconstruction and track property cuts. This comparison is done under the same event selection criteria and acceptance. The events were required to have  $|V_z| < 70$  cm,  $V_r < 2$  cm, and weighting from StRefMultCorr. The acceptance requirements were as follows:  $p_T \geq 0.2 \text{ GeVc}^{-1}$  and  $|\eta| \leq 1$ . Additional requirements, which are unique to embedding, are the Geant ID must match the particle of interest, either 2 ( $e^+$ ) or 3( $e^-$ ), and the Parent ID must be 0, the particle is the parent. These additional requirements are applied to both the simulated tracks and reconstructed tracks.

The following data analysis cuts are applied to the reconstructed tracks:  $\text{gDCA} < 1$  cm,  $\text{nHitsFit} > 14$  points,  $\text{nHitsFitRatio} > 0.52$ , and  $\text{nHitsdEdx} > 14$  points. The tracks that satisfy the cuts are compared to the original simulated tracks as a function of  $p_T$ ,  $\eta$ , and  $\phi$ , where efficiency is defined in Equation 14 and the uncertainty calculation follows [2]. The  $\eta$  slices are in units of 0.25,  $\phi$  slices are in units of  $15^\circ$ , and  $p_T$  slices of  $0.2 \text{ GeVc}^{-1}$ .

$$\text{Efficiency} = \frac{N_{\text{Reco}}}{N_{\text{MC}}} \quad (14)$$

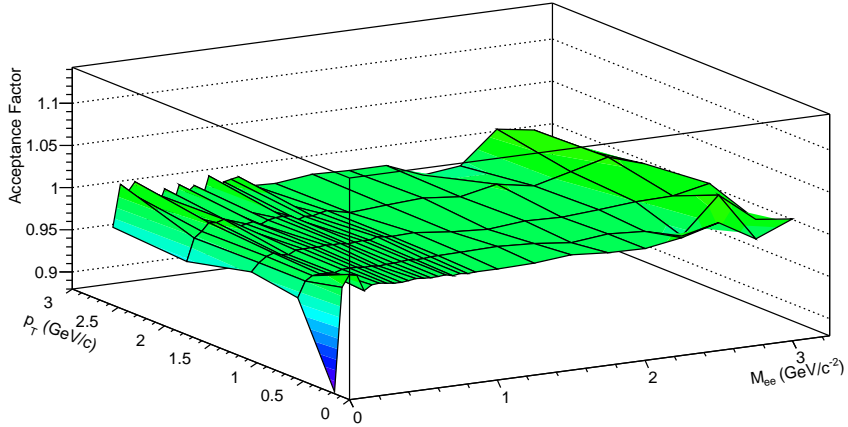


Figure 22. The acceptance correction factor distribution as a function of  $M_{ee}$  and  $p_T^{ee}$ .

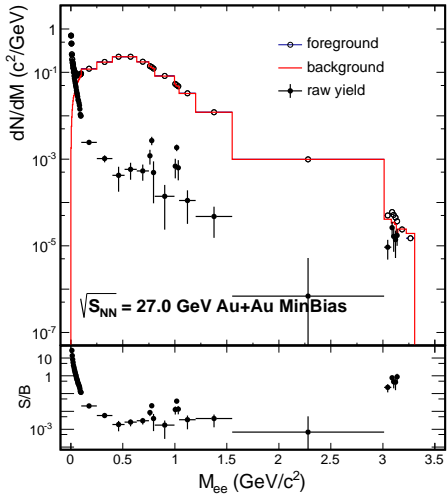


Figure 23. The top panel is the invariant mass distribution of the raw  $e^-e^+$  yield. The red line represents the background, the open points represent the foreground, and the closed points represent the signal (foreground - background). The bottom panel is the signal to background ratio as a function of invariant mass. The error bars in both panels represent the statistical errors.

316     The electron tracking efficiency figures may be found at Appendix C and the positron tracking efficiency figures  
317     may be found at Appendix D.

### 318     5.2. Matching Efficiency

319     The matching efficiency is intended to account for the tracks lost when requiring them to match to TOF. Initially,  
320     this is done by counting the tracks before and after TOF requirements with a pure electron sample as indicated in  
321     Equation 15. This is performed on a slightly different data sample(different picos) as used in the data analysis as a  
322     function of  $p_T$ ,  $\eta$ , and  $\phi$ . The picos are generated the same way as the analysis picos except that all tracks have a  
323      $|\ln\sigma_{\pi,K,p,e}| < 1$  and  $gDCA < 3$  cm with no  $\beta > 0$  requirement.

324     Event properties imposed are the same as the analysis, which are  $|V_z| < 70$  cm,  $V_r < 2$  cm, trigger id = 360001,  
325     StRefMult is valid, and the  $\hat{Q}$  requirement is satisfied. The track quality cuts are the same as the analysis and should  
326     match the cuts used in the tracking efficiency, which are primary tracks with  $p_T \geq 0.2$   $\text{GeV}\text{c}^{-1}$ ,  $|\eta| < 1$ ,  $gDCA \leq 1$   
327     cm,  $n\text{HitsFitRatio} \geq 0.52$ ,  $n\text{HitsFit} \geq 15$ , and  $n\text{HitsdEdx} \geq 15$ . The matching criteria are as follows: a TOF Match (

328 Match Flag > 0 ), a hit positioned within the module (  $|y_{Local}| < 1.8$  cm ), and  $\beta > 0$ . The pure sample is comprised  
 329 of electrons(positrons) from photon conversion and  $\pi^0$  decay and rely on pair reconstruction for identification. The  
 330 sample is selected with the following cuts:  $|n\sigma_e| < 1$  (actually 0.5 in 27 GeV, but there is a feature in the reconstruction  
 331 that nearly doubles it), the distance of closest approach between the reconstructed helices  $< 2$  cm, the opening angle  
 332 within  $0.1 \pi$ , the invariant mass based on the global track properties  $\leq 5$  MeVc $^{-2}$ , and  $\phi_V < 0.5$ .

$$Efficiency = \frac{track\ quality\ cuts + |n\sigma_e| < 1. + PE\ cuts + TOF\ Match\ Flag > 0 + \beta > 0 + |y_{Local}| < 1.8\ cm}{track\ quality\ cuts + |n\sigma_E| < 1. + PE\ cuts} \quad (15)$$

333 The photonic electron efficiencies are calculated in slices of  $d\phi = 15^\circ$ ,  $d\eta = 0.125$ , and varying  $dp_T$ . The low  
 334 edges used for the 31  $p_T$  bins are 0.2, 0.225, 0.25, 0.275, 0.3, 0.325, 0.35, 0.375, 0.4, 0.45, 0.5, 0.55, 0.6, 0.65, 0.7,  
 335 0.75, 0.8, 0.85, 0.9, 0.95, 1., 1.3, 1.6, 1.9, 2.2, 2.5, 2.8, 3.1, 3.4, 3.7, 4.0, and 10 GeVc $^{-1}$ . While the photonic electron  
 336 sample is pure, it is limited in statistics and does not extend to higher values of  $p_T$ . To remedy this limitation, pion  
 337 matching efficiencies are scaled to match the electron efficiencies and used as a substitute for the electron efficiencies.  
 338 The pion matching efficiency criteria is the same as the photonic electron efficiency indicated in Eq. 15 except for the  
 339 PID criteria, where the pions are only determined by  $|n\sigma_\pi| < 1$ . The scaling is done by determining the weighted  $p_T$   
 340 efficiency mean for each  $\phi$  and  $\eta$  slice for both the electrons (positrons) and pions by following Equation 16. Once  
 341 both weighted means are determined, the electron mean is divided by the pion mean is used to scale the pion matching  
 342 efficiencies. The uncertainty method used in the matching efficiency calculations is defined in [2].

$$\bar{x} = \frac{\sum \frac{x_i}{\sigma_i^2}}{\sum \frac{1}{\sigma_i^2}} \quad (16)$$

343 Electron matching efficiency figures may be found at Appendix E and positron matching efficiency figures may  
 344 be found at Appendix F.

345 Note: Adding StRefMultCorr event weighting would be advisable.

346 The matching efficiency method has been updated to correspond to the methods used in the AuAu200 analysis. It  
 347 uses a similar concept, where a scaled pion matched track efficiency is used. The difference lies in how the scaling is  
 348 done. Previously, the weighted mean was used for scaling, this method uses a bin to bin comparison as function of  
 349 transverse momentum for integrated  $\phi$  and  $\eta$ .

350 Since the pure electron sample consists primarily of photonic electrons, the  $d^2N/d\phi d\eta$  distribution might be dis-  
 351 proportionate between matched and not-matched tracks at the edges of  $\eta$  [ $\pm 1$ ]. This is because there is a large material  
 352 budget in the forward direction. To correct  $d^2N/d\phi d\eta$ , a pure pion sample is used for reference and the pure electron  
 353 sample is corrected to match the pion sample. This correction is done by determining the weights for each  $d\eta d\phi$   
 354 slice(Eqn. 17), applying the weights to the 3D distribution( $p_T$ ,  $d\eta$ ,  $d\phi$ )(Eqn. 18), and then normalizing the corrected  
 355 distributions(Eqn. 19). This correction needs to be completed for both TOF matched tracks and all tracks.

$$W_{Match}(d\eta, d\phi) = \frac{N_{\pi_{TOF}^+}}{N_{e_{TOF}^+}} \quad (17)$$

$$h'_{Match}(p_T, d\eta, d\phi) = W_{Match}(d\eta, d\phi) * h_{Match}(p_T, d\eta, d\phi) \quad (18)$$

$$h''_{Match}(p_T, d\eta, d\phi) = \frac{N_{Match}^{BeforeWeight}}{N_{Match}^{AfterWeight}} * h'_{Match}(p_T, d\eta, d\phi) \quad (19)$$

356 The  $dN/d\eta$  distributions are shown before and after the acceptance correction of electrons with all tracks in Figures  
 357 24 and 25 and TOF match tracks in Figures 26 and 27. Notice that the electrons (solid symbols) before the correction  
 358 (left figures) do not align with the pions (open symbols), but after the correction (right figures), the electron symbols  
 359 overlay the pions. Hence, the correction worked.

360 After correcting the pure electron sample's acceptance, the matching efficiency as a function of transverse mo-  
 361 mentum is found by following Equation 15. The efficiency is shown in Figures 28 and 29.

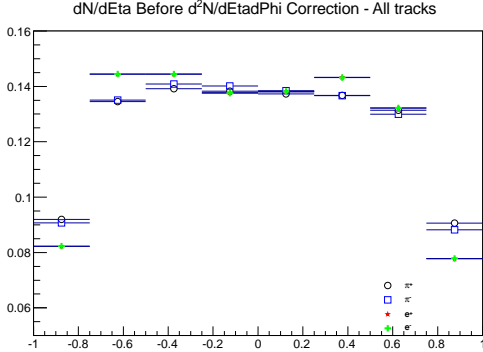


Figure 24. The  $dN/d\eta$  distribution for tracks with and without matches to TOF before correcting the electrons acceptance. The open black dots are  $\pi^+$ , the open blue squares are  $\pi^-$ , the red stars are  $e^+$ , and the green crosses are  $e^-$ . Notice how the electrons and pions disagree the most at the  $\eta$  edges.

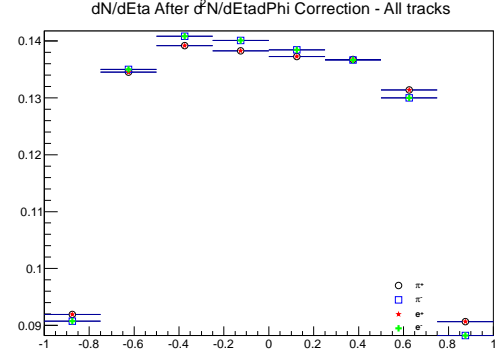


Figure 25. The  $dN/d\eta$  distribution for tracks with and without matches to TOF after correcting the electron acceptance to match that of the pions. The open black dots are  $\pi^+$ , the open blue squares are  $\pi^-$ , the red stars are  $e^+$ , and the green crosses are  $e^-$ . Notice how the electrons and pions agree for all  $\eta$ , as expected.

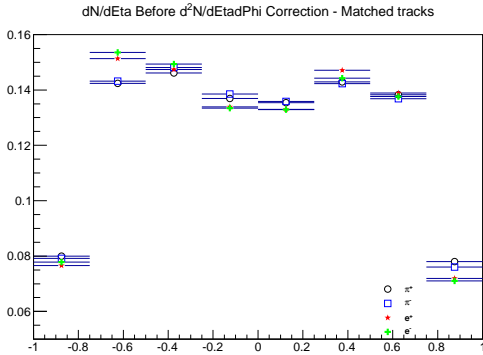


Figure 26. The  $dN/d\eta$  distribution for tracks with matches to TOF before correcting the electrons acceptance. The open black dots are  $\pi^+$ , the open blue squares are  $\pi^-$ , the red stars are  $e^+$ , and the green crosses are  $e^-$ . Notice how the electrons and pions are in the biggest disagreement at the edges of  $\eta$ .

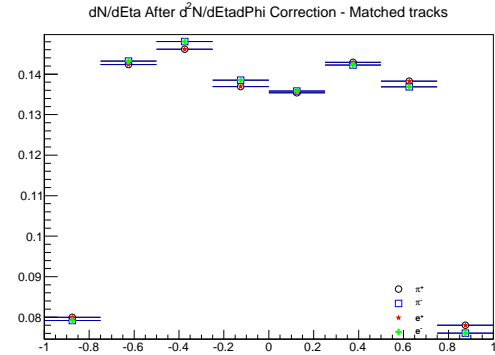


Figure 27. The  $dN/d\eta$  distribution for tracks with matches to TOF after correcting the electron acceptance to match that of the pions. The open black dots are  $\pi^+$ , the open blue squares are  $\pi^-$ , the red stars are  $e^+$ , and the green crosses are  $e^-$ . Notice how the electrons and pions agree for all  $\eta$ , as expected.

362 Next, a functional description is determined such that the pions may be scaled to match the pure electron sample.  
 363 To determine the function, the electron efficiencies are divided by the pion efficiencies and then fitted with Equation  
 364 20.

$$f(x) = \frac{1}{a + e^{\frac{x-b}{c}}} + d \quad (20)$$

365 The ratio of electrons to pions are shown in Figures 30 and 31. The fit parameters are assigned as follows:  $a$  is  
 366  $p0$ ,  $b$  is  $p1$ ,  $c$  is  $p2$ , and  $d$  is  $p3$ . The 66.6% confidence band is performed by using ROOT's TVirtualFitter::GetFitter's  
 367 GetConfidenceInterval. Both the fit and confidence interval are performed over the transverse momentum range of  
 368 0.2 to  $3.0 \text{ GeV}^{-1}$ .

369 Equation 20 is then applied to the pion matching efficiency and the result is used as the single track matching  
 370 efficiency propagated in the pair efficiency calculation.

371 For comparison's sake, the variance scaling method and AuAu200 method matching efficiencies are compared  
 372 with different conditions on the pure electron sample acceptance correction. This is done as a function of transverse  
 373 momentum in slices of  $\eta$  and  $\phi$ . Results may be found in the Appendix for the cases where the acceptance correction

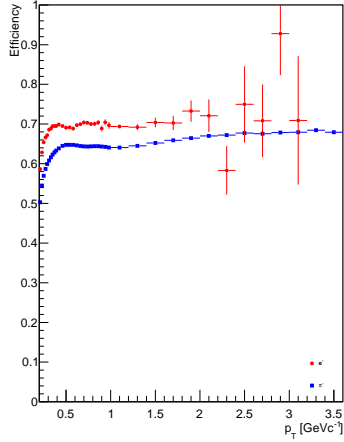


Figure 28. The matching efficiency as a function of transverse momentum for  $\pi^-$  (blue squares) and  $e^-$  (red circles).

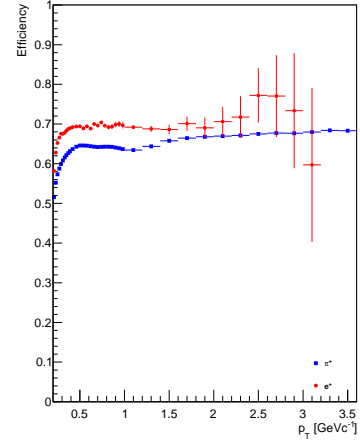


Figure 29. The matching efficiency as a function of transverse momentum for  $\pi^+$  (blue squares) and  $e^+$  (red circles).

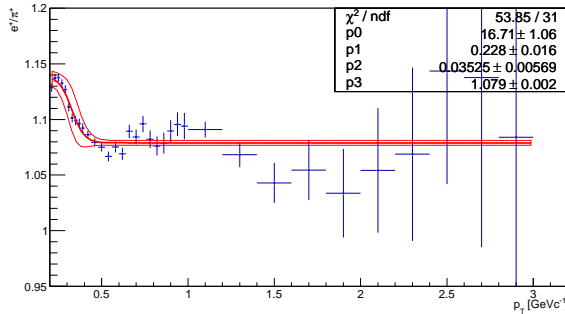


Figure 30. The ratio of positrons over positive pions as a function of transverse momentum with a fit by Equation 20 and a 66.6% confidence band where p0 represents a, p1 represents b, p2 represents c, and p3 represents d.

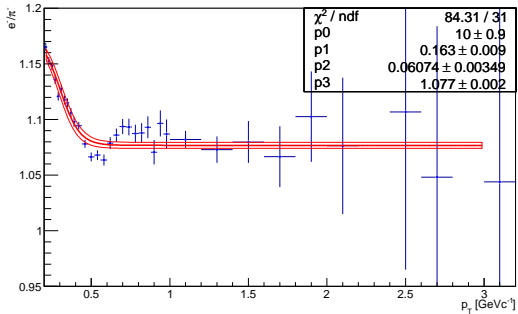


Figure 31. The ratio of electrons over negative pions as a function of transverse momentum with a fit by Equation 20 and a 66.6% confidence band where p0 represents a, p1 represents b, p2 represents c, and p3 represents d.

is created by studying all tracks and using it with the AuAu200 method, Appendix G; the acceptance correction is created by studying the case of all tracks and tracks with TOF matches separately and using them with the AuAu200 method, Appendix H; the acceptance correction is used by studying all tracks and used by both the AuAu200 method and variance scaling method, Appendix I; and the acceptance correction is used by studying all tracks and tracks with TOF matches separately and used by both methods, Appendix J. In the four studies, listed first are the efficiencies from negative particles and then the efficiencies from positive particles. In each histogram, the uncorrected pure electron sample is represented by the pink triangles( $e^-$ )/cyan triangles( $e^+$ ), the corrected pure electron sample is represented by the yellow crosses, the variance scaled pions are represented by the blue circles, and the AuAu200 method scaled pions are represented by the green stars.

Tidbit: When making matching efficiency comparisons with Patrick (and then Yi). Patrick noted that we had larger differences at the  $\eta$  edges. The cause for the disagreement has to do with the formation of the photonic electron track. In this analysis, the global track momentum and helix parameters are saved from the MuDST and the parameters are used to reconstruct the track and the dca to the helix given the origin. The LBNL picos do not store the global track's momentum from the MuDST, but rather it is calculated slightly differently. It has no energy loss correction from the primary vertex, while mine does. So as the idea for the difference goes, at larger  $\eta$ , there is more beam pipe material, a larger correction, and a larger difference.

### 390 5.3. PID Efficiency

391 The particle identification efficiency is intended to capture the performance of the PID (remaining) cuts used in  
 392 the data analysis. The efficiency is derived from a pure electron sample generated out of the data analysis picos.

393 Event properties imposed are the same as the analysis, which are  $|V_z| < 70$  cm,  $V_r < 2$  cm, trigger id = 360001,  
 394 StRefMult is valid, and the  $\hat{Q}$  requirement is satisfied. The track quality cuts are the same as the analysis and should  
 395 match the cuts used in the tracking efficiency, which are primary tracks with  $p_T \geq 0.2$  GeVc $^{-1}$ ,  $|\eta| < 1$ , gDCA  $\leq 1$   
 396 cm, nHitsFitRatio  $\geq 0.52$ , nHitsFit  $\geq 15$ , and nHitsdEdx  $\geq 15$ . The matching criteria, which should also match the  
 397 efficiency study, are as follows: Match Flag  $> 0$ ,  $|y_{Local}| < 1.8$  cm, and  $\beta > 0$ . *Check that this does in fact match the*  
 398 *criteria listed for the purity study sample.* The pure electron sample is created with the additional cuts:  $\beta < 1.1$ ,  $1.4$   
 399  $< n\sigma_e < 2$ , the distance of closest approach between the reconstructed helices  $< 2$  cm, the opening angle within  $0.1$   
 400  $\pi$ , the invariant mass based on the global track properties  $\leq 5$  MeVc $^{-2}$ , and  $\phi_V < 0.5$ . The efficiencies are calculated  
 401 by dividing the quantities before and after the PID cuts. The PID cuts are  $\beta - 1 < .03$  and  $2$ . The efficiencies were  
 402 determined in slices of  $d\eta = 0.2$  and  $d\phi = 30^\circ$  as a function of  $p_T$  in  $0.2$  GeVc $^{-1}$  bins. The efficiency figures may be  
 403 found at Appendix K. These figures are dated and were done as a function of  $p_T$ ,  $\phi$ ,  $\eta$ , and charge. This was done as  
 404 a counting method. However, this have now been updated as to determine the efficiency as a function of momentum  
 405 for one charge. It is based on the pure sample used in the Purity estimation (Sec. 3.1). The PID efficiency has now  
 406 been separated into two parts: the efficiency of the  $\beta^{-1}$  cut and the efficiency of the  $n\sigma$  cuts.

407 Note: Adding StRefMultCorr event weighting would be advisable.

408 A count method was used to determine the  $\beta^{-1}$  efficiency. This was done by looping over the momentum bins  
 409 of the 2D histograms, momentum vs  $\beta^{-1}$ , counting the number of electrons before and after the  $\beta - 1 < .03$  cut and  
 410 dividing to determine the efficiency. The results are shown in Fig. 32 as the blue points and fit.

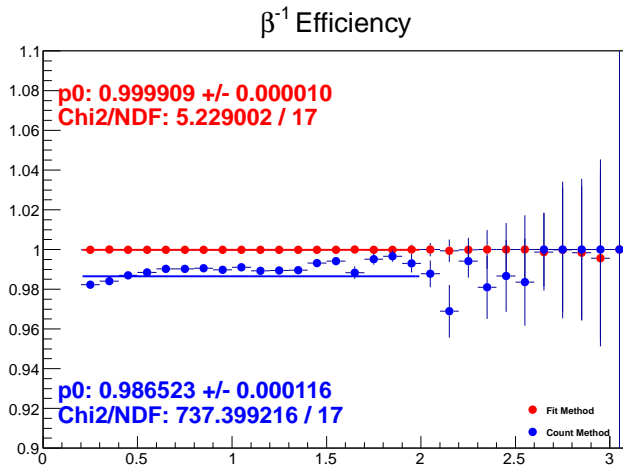


Figure 32. The  $\beta^{-1}$  efficiency where the count method is shown in blue and the fit method is shown in red.

411 A fit method was used to provide an alternative method and provide a reference for a systematic uncertainty. The  
 412 fit method starts out with momentum versus  $\beta^{-1}$  with both following the range of 0 to 5 across 50 bins and 1000 bins  
 413 respectively. Then the default FitSlices was performed on  $\beta^{-1}$ , where  $\beta^{-1}$  ranges from 0.9 to 1.1, for each momentum  
 414 bin. These values are used as a guidance for the next round of fits used to determine the before and after contributions.  
 415 The next round of fits were Gaussian and initialized with the sigma and means from the previous FitSlices and a range  
 416 from mean-3\*sigma to mean+3\*sigma. The Gaussian curve resulting from the fits are evaluated with Eq. 21 for the  
 417 before contribution and with Eq. 22 for the after contribution. Then the efficiency is Eq. 22 / Eq. 21. The results are  
 418 shown in Fig. 32 as the red points. The difference between the two methods is shown in Fig. 33.

$$Before = \frac{1}{d\beta^{-1}} \int_{0.8}^{1.1} Ae^{-0.5((\beta^{-1}-B)/C)^2} d\beta^{-1} \quad (21)$$

$$After = \frac{1}{d\beta^{-1}} \int_{0.97}^{1.03} A e^{-0.5((\beta^{-1}-B)/C)^2} d\beta^{-1} \quad (22)$$

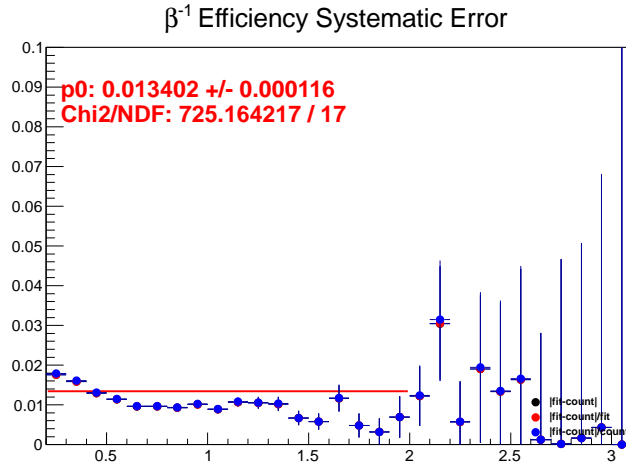


Figure 33. The difference between the  $\beta^{-1}$  efficiency calculation methods and is taken as the systematic uncertainty for the  $\beta^{-1}$  cut.

To estimate the  $n\sigma$  cut efficiency and systematics, count and fit methods were used after the  $\beta^{-1}$  cut. The count method uses histograms to keep track of the number of electrons before and after the  $n\sigma$  cuts and their ratio as a function of momentum is used to determine the efficiency. Bayesian statistical, Ullrich+Xu, errors were used. The efficiency is shown in Fig. 34 as the red-brown crosses. This method has been used as an alternative to the fit method and to determine the systematic uncertainty.

The fit method has been used as the quoted efficiency. This method used the Gaussian fits of the pure sample to evaluate the quantities before and after the  $n\sigma$  cuts. The limits of the  $n\sigma$  cuts were taken to be at the center of the momentum bin for that purity slice. The before quantity estimation spanned from -6 to  $6^{**} n\sigma_e$  and the after quantity used the  $n\sigma_e$  limits. The efficiency is shown in Fig. 34 as the open circles. Also shown in the figure are past ePID efficiency calculation, the squares, and the combination of the  $n\sigma$  and  $\beta^{-1}$  efficiencies, the triangles.

The systematic uncertainty has been estimated by taken the difference between the fit and count methods. This is shown in Fig. 35. The uncertainty was assigned 2%. This number was determined primarily by eye and during a dielectron group meeting.

For reference and comparison's sake, shown in Figs. 36 and 37 are the old 3D based eID efficiencies, red squares, compared to Patrick Huck's eID efficiencies at 27 GeV, black squares, from way back when. We used different eID cuts, so not too surprising.

#### 5.4. Pair Efficiency

The pair efficiencies are generated by simulating virtual photon to electron-positron decay with a toy Monte Carlo, and the pairs are reconstructed based on the single track efficiencies. The event generation follows the diagram illustrated in Figure 38.

The virtual photons are created with a center of mass energy,  $W$ , from 0 to 5 GeV, a rapidity,  $Y$ , from -2 to 2, and a  $p_T$  from 0 to  $5 \text{ GeVc}^{-1}$ .  $W$ ,  $Y$ , and  $p_T$  all are randomly drawn from a flat distribution using ROOT's TRandom3. Once drawn, the energy and  $p_z$  of the system are determined via Equations 23 and 24.

$$E = \sqrt{W^2 + p_T^2} \cosh(Y) \quad (23)$$

$$p_z = \sqrt{W^2 + p_T^2} \sinh(Y) \quad (24)$$

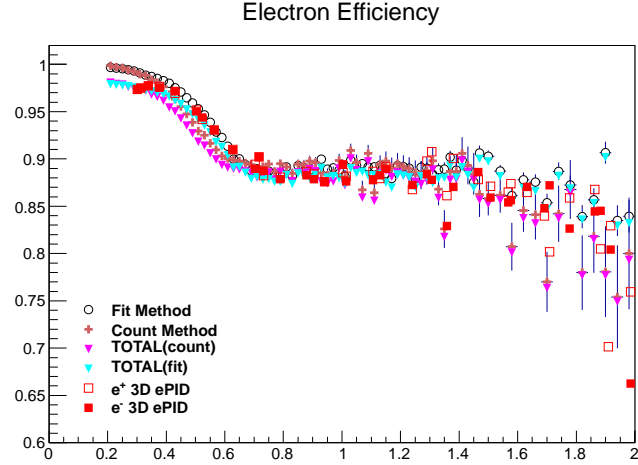


Figure 34. The electron identification efficiencies. The red-brown cross represent the count method evaluation of the  $n\sigma$  efficiencies. The open circle represent the fit method evaluation of the  $n\sigma$  efficiencies. The combination of  $\beta^{-1}$  and  $n\sigma$  efficiencies are represented by the solid triangles where cyan is the fit method and pink is the count method. The squares represent the old method for calculating the ePID efficiencies as a function of charge,  $p$ ,  $\eta$ , and  $\phi$ .

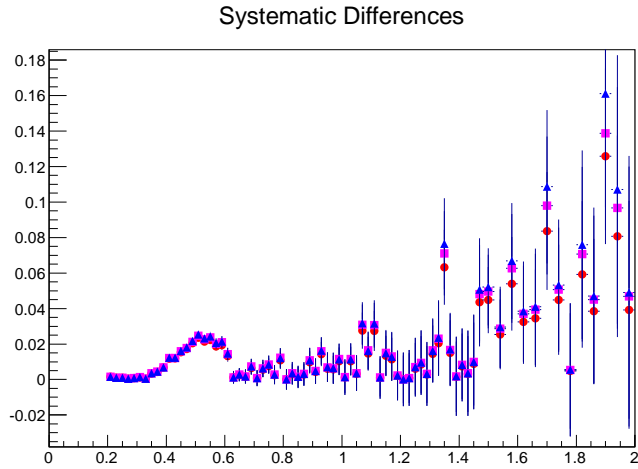


Figure 35. The electron identification efficiency systematic uncertainties. 2% was used to estimate the uncertainty as the majority of the electrons are in the low momentum region, but there is some uncertainty as one shifts to higher momentum.

With  $E$  and  $p_z$ ,  $p_x$  and  $p_y$  are determined with a randomly drawn  $\phi[0-2\pi]$  as shown in Equations 25 and 26.

$$p_x = \cos(\phi)p_T \quad (25)$$

$$p_y = \sin(\phi)p_T \quad (26)$$

With the momentum and energy determined, the photon is decayed into the electron positron pair in the center of mass frame. Since the electron and positron are decay back-to-back, only one daughter's kinematics are listed while the other daughter follows the same determination with the opposite momentum. Angles  $\phi[0-\pi]$  and  $\cos(\theta)[-1$  to  $1]$  are randomly drawn from a flat distribution, which are used to determine the momentum. The rest of the kinematics may be found in the Equations 27-31.

$$p = \sqrt{\frac{W^2}{4} - m_e^2} \quad (27)$$

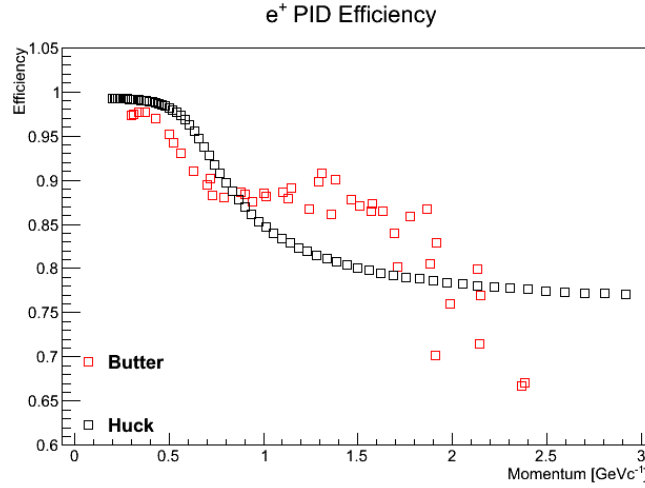


Figure 36. The positron identification efficiency determined based on  $p_T$ ,  $\eta$ , and  $\phi$  then converted to momentum (red square) and compared to Patrick's efficiencies (black square).

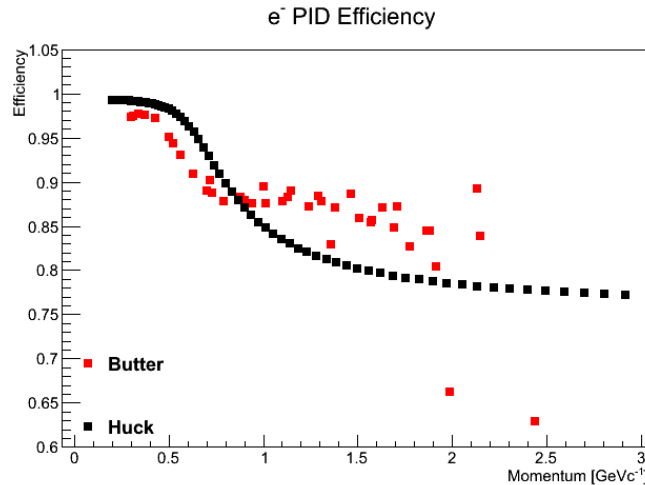


Figure 37. The electron identification efficiency determined based on  $p_T$ ,  $\eta$ , and  $\phi$  then converted to momentum (red square) and compared to Patrick's efficiencies (black square).

$$p_{x1} = \sin(\theta) \cos(\phi)p \quad (28)$$

$$p_{y1} = \sin(\theta) \sin(\phi)p \quad (29)$$

$$p_{z1} = \cos(\theta)p \quad (30)$$

$$E_1 = \sqrt{m^2 + p_{x1}^2 + p_{y1}^2 + p_{z1}^2} \quad (31)$$

Once the daughters have been created, they are boosted into the lab frame. And at this point, the daughters are ready to be *detected*. The acceptance cuts,  $p_{T,e} \geq 0.2 \text{ GeVc}^{-1}$  and  $|\eta| < 1$ , are applied to match the STAR acceptance. Then the daughters are reconstructed into a pair based on the single track efficiencies.

The total single track efficiency is compared to a flat-randomly drawn number[0,1]. If the total efficiency is larger than the random number, then it is *detected*. If both daughters' efficiencies are larger than their corresponding random number, then the pair is reconstructed and *detected*. To determine the total single track efficiency for a daughter, the

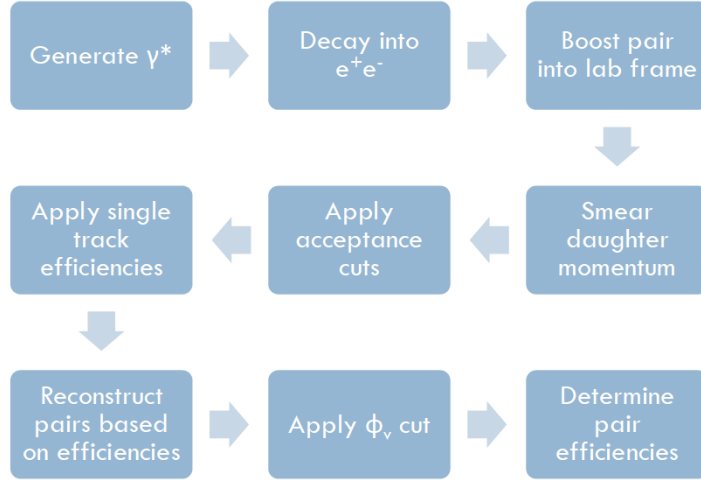


Figure 38. The generation of pair efficiencies work flow.

single track efficiencies for tracking (5.1), matching (5.2), and pid (5.3) are picked up from their respective tables using the daughter's  $p_T$ ,  $\phi$ , and  $\eta$ , which are then used to form the total efficiency as calculated in Equation 32. Note that the efficiencies given by each table are not interpolated, but are the efficiencies for the corresponding slices of  $p_T$ ,  $\eta$ , and  $\phi$ .

$$\epsilon_{total} = \epsilon_{track} * \epsilon_{match} * \epsilon_{pid} \quad (32)$$

After applying the acceptance cuts and single track efficiencies, the  $\Phi_V$  cut, Equation ??, is applied to the pair. This is the final selection criteria applied before determining the pair efficiencies. The pair efficiencies are determined by dividing the number of pairs generated within the acceptance by the number of pairs after the single track efficiency and  $\Phi_V$  cuts. The pair efficiencies are determined as a function of the  $p_{Tee}$  and  $M_{ee}$  with the same binning as used in the analysis. Figures of the pair efficiencies may be found at Appendix L. It is these efficiencies that are used to correct the data analysis' raw signal.

## 6. Cocktail

The cocktail comprises of contributions to the  $e^+e^-$  continuum that are produced through hadronic decays. The contributions are  $\pi^0 \rightarrow \gamma e^+e^-$ ,  $\eta \rightarrow \gamma e^+e^-$ ,  $\eta' \rightarrow \gamma e^+e^-$ ,  $\omega \rightarrow \pi e^+e^-$ ,  $\omega \rightarrow e^+e^-$ ,  $\phi \rightarrow \eta e^+e^-$ ,  $\phi \rightarrow e^+e^-$ ,  $J/\psi \rightarrow e^+e^-$ , and  $c\bar{c} \rightarrow e^+e^-$ . Each cocktail contribution is produced by decaying the hadron for many events and scaling the contribution to the appropriate yield. The  $c\bar{c}$  contribution is handled by PYTHIA and ultimately scaled by the number of binary collisions. This will be discussed in more detail later in 6.6. The remaining hadronic contributions are handled by a toy Monte Carlo. To generate each parent, an invariant mass,  $p_T$ , and rapidity parameters are required and selected from given distributions. Once generated, it is decayed. This will be discussed in sections 6.1, 6.2, 6.3, and 6.4.

### 6.1. Mass Distribution

The parent hadron masses depend upon if the channel is decaying directly into a dielectron pair or undergoes a Dalitz decay process. The direct decay process follows a narrow Breit-Wigner distribution as given in Equation 33, where  $\Gamma_0$  represents the PDG width and set with the range: [2  $M_e$ , 4  $GeV/c^2$ ]. The following processes use the Breit-Wigner distribution:  $\omega \rightarrow e^+e^-$ ,  $\phi \rightarrow e^+e^-$ , and  $J/\psi \rightarrow e^+e^-$ .

$$\frac{dN}{dM_{ee}} = \frac{2 \Gamma_0}{(M_{ee} - M_h)^2 + \Gamma_0^2/4} \quad (33)$$

Particle	$\Lambda^{-2}$	$\Gamma^2$
$\pi^0$ [7]	1.756	N/A
$\eta$ [5]	1.95	0
$\eta'$	1.8396	0.01989
$\omega$ [5]	2.24	0
$\phi$ [4]	3.8	0

Table 1. Hadron values used in the Form Factor calculation.

483 Dalitz decays follow the Kroll-Wada equation given by Equation 34, where PS is the Phase Space, QED is the  
 484 Quantum ElectroDynamic kinematics, and  $|F(x)|$  is the Form Factor. The following process use Equation 34:  $\pi^0 \rightarrow \gamma$   
 485  $e^+e^-$ ,  $\eta \rightarrow \gamma e^+e^-$ ,  $\eta' \rightarrow \gamma e^+e^-$ ,  $\omega \rightarrow \pi e^+e^-$ , and  $\phi \rightarrow \eta e^+e^-$ . Notice that each process is a three-body decay.

$$\frac{dN}{dM_{ee}} = PS * |F(m_{ee}^2)|^2 * QED \quad (34)$$

486 The Phase Space factor for a three-body decay is given in Equation 35, and if the third body is massless, the factor  
 487 simplifies to Equation 36.

$$PS = \left( \left( 1 + \frac{m_{ee}^2}{m_\omega^2 - m_{\pi^0}^2} \right)^2 - \frac{4m_\omega^2 m_{ee}^2}{(m_\omega^2 - m_{\pi^0}^2)^2} \right)^{\frac{3}{2}} \quad (35)$$

$$PS = \left( 1 - \frac{m_{ee}^2}{M_h^2} \right)^3 \quad (36)$$

488 The QED component is described by Equation 37 where N is a degeneracy factor that depends on how many  
 489 photons can convert. N is 4 for  $\omega$  and  $\phi$  while it is 2 for the rest of the processes.

$$QED = \frac{N}{3\pi} \sqrt{1 - \frac{4m_e^2}{m_{ee}^2}} \left( 1 + \frac{2m_e^2}{m_{ee}^2} \right) \frac{1}{m_{ee}} \quad (37)$$

490 The Form Factor component for  $\eta$ ,  $\eta'$ ,  $\omega$ , and  $\phi$  is given by Equation 38, where  $\Lambda^{-2}$  and  $\Gamma^2$  are defined in Table 1.  
 491 The  $\Gamma^2$  was determined by fits to the data presented in [6] by Bingchu Huang.

$$|F(m_{ee}^2)|^2 = \frac{1}{(1 - m_{ee}^2 \Lambda^{-2})^2 + \Gamma_0^2 \Lambda^{-2}} \quad (38)$$

492 In the case of  $\pi^0$ , the Form Factor component is given by Equation 39.

$$|F(m_{ee}^2)|^2 = (1 + m_{ee}^2 \Lambda^{-2})^2 \quad (39)$$

## 493 6.2. $p_T$ Distribution

494 The  $p_T$  distributions are described by a Tsallis Blast Wave model in [8] and given by Equation 40, where r is the  
 495 radial direction, y is the rapidity,  $\phi$  is the azimuthal angle, q represents the non-equilibrium of the system, T is the  
 496 temperature, and  $E_T$  is given by Equation 41. The limits for y is [-6,6] and r is [0,R]. However, the  $p_T$  distribution for  
 497  $J/\Psi$  is given by a Boltzmann distribution and is discussed in Sec. 6.2.2.

$$\frac{dN}{dp_T} \propto p_T m_T \int_{-\pi}^{\pi} d\phi \int_{-Y}^Y \cosh y dy \int_0^R r dr \left( 1 + \frac{q-1}{T} E_T \right)^{\frac{-1}{q-1}} \quad (40)$$

498 In Equation 41,  $\rho$  represents the flow profile and is expressed in Equation 42. It is zero at the center of the collision  
 499 and expands radially to  $\beta_s$  at the hard-spherical edge, R.

Parameter	Initial Value	Step Size	Limits	Final Value
$\beta$	0.4	0.001	0,0.7	$0.3927 \pm 0.00374$
T	0.08825	0.001	0.040,0.2	$0.1222 \pm 0.0008302$
q	1.0535	0.001	0.8,1.2	$1.014 \pm 0.0019$
$C_\pi$	300	5	0,1E4	$323.4 \pm 6.104$
$M_\pi$	0.13957	Fixed	Fixed	0.13957
$C_{K^+}$	300	5	0,1E4	$292.12 \pm 6.891$
$M_{K^+}$	0.493677	Fixed	Fixed	0.493677
$C_{K^-}$	300	5	0,1E4	$208.948 \pm 4.915$
$M_{K^-}$	0.493677	Fixed	Fixed	0.493677
$C_{p^+}$	300	5	0,1E4	$3664.37 \pm 164.676$
$M_{p^+}$	0.938272	Fixed	Fixed	0.938272
$C_{p^-}$	300	5	0,1E4	$795.264 \pm 35.8599$
$M_{p^-}$	0.938272	Fixed	Fixed	0.938272

Table 2. Variables used in the Tsallis Blast Wave model fits to the  $\pi/K/p$  spectra

$$E_T = m_T \cosh y \cosh \rho - p_T \sinh \rho \cos \phi \quad (41)$$

500 In Equation 42,  $\beta_s$  represents the maximum flow velocity.

$$\rho = \arctan\left(\beta_s \left(\frac{r}{R}\right)^n\right) \quad (42)$$

501  $\beta_s$  can be rewritten in terms of the average flow velocity,  $\beta$ , and is expressed in Equation 43, where  $n = 1$  is used.

$$\beta_s = \beta \left(1 + \frac{1}{n+1}\right) \quad (43)$$

### 502 6.2.1. Tsallis Blast Wave Fits

503 To generate the  $p_T$  distribution from the Tsallis Blast Wave fit, we need three parameters to complete the three-dimensional integral. For this study,  $q = 1.014$ ,  $T = 0.1222$  GeV, and  $\beta = 0.3927c$  are used. These were determined by fitting preliminary  $\pi^{+-}$ ,  $K^{+-}$ , and  $p^{+-} \frac{1}{2\pi} \frac{d^2N}{p_T dp_T dy} [(GeV/c)^{-2}]$  as a function of  $p_T$  from Sabita Das and Lokesh Kumar. The spectra given were for the centralities 0-5%, 5-10%, 10-20%, 20-30%, 30-40%, 40-50%, 50-60%, 60-70%, and 70-80%. The centralities were combined to estimate the minimum bias contribution by weighting each distribution by 5%, 5%, 10%, 10%, 10%, 10%, and 10% respectively and then divided by 0.8 to account for the 80% centrality coverage. The fits were performed by inserting the Tsallis Blast Wave model into ROOT's Combined Fit tutorial. The simultaneous fit is done over thirteen variables and the parameters may be found in Table 2. The fits are shown in Appendix N.

### 512 6.2.2. Boltzmann Distribution

513 The  $p_T$  distribution for  $J/\Psi$  is given by a Boltzmann distribution. The Boltzmann distribution follows

$$p_T * \frac{dN}{dy} \frac{1}{2\pi T(T + m_{J/\Psi})} e^{-\frac{(\sqrt{p_T^2 + m_{J/\Psi}^2} - m_{J/\Psi})}{T}}, \quad (44)$$

514 where  $T = 0.4049$ ,  $m_{J/\Psi}$  is  $J/\Psi$ 's PDG mass, and  $\frac{dN}{dy} = 3.237E-5$ . These parameters are from the AuAu39 dielectron simulation, where Yi Guo had fitted the  $J/\Psi$   $p_T$  spectra from Wangmei Zha *et al.*'s  $J/\Psi$  study.

### 516 6.3. Rapidity Distribution

517 The rapidity distribution is given by Equation 45 and is from CERES' Monte Carlo event generator GENSIS,  
 518 which has been parameterized to CERES data. In Equation 45,  $\sqrt{s}$  is the center-of-mass energy per nucleon pair, 27  
 519 GeV, m is the mass of the parent hadron, and  $\sigma_L$  is defined in Equation 46.

$$\frac{dN}{dy} = \cosh^{-2} \left( \frac{3y}{4\sigma_L(1 - \frac{y^2}{2\sqrt{s}/m})} \right) \quad (45)$$

520 In Equation 46,  $m_N$  is the nucleon mass, which is approximated to 0.939 GeV, and  $\sqrt{s}$  is the center-of-mass energy  
 521 per nucleon.

$$\sigma_L = \sqrt{\log \left( \frac{\sqrt{s}}{2m_N} \right)} \quad (46)$$

### 522 6.4. Parent Decay

523 The parent hadrons are generated by selecting from the appropriate mass, rapidity, and  $p_T$  distributions, mentioned  
 524 previously, while the azimuthal distribution is flat [0,2π]. With this information, the parent hadron is created and  
 525 decayed. The decay is either a three-body (hadron/γ+e<sup>+</sup>+e<sup>-</sup>) or two-body (e<sup>+</sup>+e<sup>-</sup>) decay.

526 For two-body decays, the dielectrons are decayed in the parent hadron's rest frame and then boosted into the lab  
 527 frame. The corresponding kinematic equations are Equations 47, 48, 49, 50, and 51, where  $\cos(\theta)$  is selected from a  
 528 flat distribution [-1,1],  $\phi$  is selected from a flat distribution, and  $M_{ee}$  is selected from 33.

$$p = \sqrt{\frac{M_{ee}^2}{4} - m_e^2} \quad (47)$$

$$p_{x1} = \sin(\theta) \cos(\phi)p; p_{x2} = -p_{x1} \quad (48)$$

$$p_{y1} = \sin(\theta) \sin(\phi)p; p_{y2} = -p_{y1} \quad (49)$$

$$p_{z1} = \cos(\theta)p; p_{z2} = -p_{z1} \quad (50)$$

$$E_{1,2} = \sqrt{m_e^2 + p_{x1,2}^2 + p_{y1,2}^2 + p_{z1,2}^2} \quad (51)$$

533 Three-body decays start by decaying the hadron/γ daughter and dielectron as a two-body decay in the parent's rest  
 534 frame. The dielectron pair then undergoes a decay in their center-of-mass frame. The pair is then boosted into the  
 535 parent's rest frame with the other daughter, and then all three bodies are boosted into the lab frame. The kinematics  
 536 in the first decay frame are given in Equations 52, 53, 54, 55, 56, and 57, where  $\phi$  is from a flat distribution [0,2π],  
 537  $\cos \theta$  is from a flat distribution [-1,1], and  $M_{ee}$  is selected from Equation 34.

$$E_{h/\gamma} = \frac{\sqrt{M_{parentHadron}^2 + M_{h/\gamma}^2 - M_{ee}^2}}{2M_{parentHadron}} \quad (52)$$

$$P_{h/\gamma} = \frac{\sqrt{(M_{parentHadron}^2 - (M_{ee} + M_{h/\gamma})^2) * (M_{parentHadron}^2 - (M_{ee} - M_{h/\gamma})^2)}}{2M_{parentHadron}} \quad (53)$$

$$p_{h/\gamma,x} = \sin(\theta) \cos(\phi)P_{h/\gamma}; p_{e,x} = -p_{h/\gamma,x} \quad (54)$$

$$p_{h/\gamma,y} = \sin(\theta) \sin(\phi)P_{h/\gamma}; p_{e,y} = -p_{h/\gamma,y} \quad (55)$$

$$p_{h/\gamma,z} = \cos(\theta)P_{h/\gamma}; p_{e,z} = -p_{h/\gamma,z} \quad (56)$$

$$E_{ee} = \sqrt{M_{ee}^2 + p_{ee,x}^2 + p_{ee,y}^2 + p_{ee,z}^2} \quad (57)$$

N	n	$\alpha$	m	$\beta$	$\bar{x}$	$\sigma$	a	b
1	1.22442	1.81215	4.32508	2.1451	-3.27782E-4	9.3194E-3	9.45E-3	7.934E-3

Table 3. The values are used in Equations 58, 59, 60, 61, 62, and 64 to smear the Monte Carlo transverse momenta.

The electron pair is then decayed in its center-of-mass frame as it is mentioned earlier for two-body decays, except that the daughters are then boosted into the parent hadron's rest frame with the third body, either a hadron or photon. Finally, all three bodies are boosted in the lab frame.

Now, the electron daughters' transverse momenta are smeared to simulate the detector's reconstruction resolution and then the daughters are paired together and stored with the other reconstructed daughters to be scaled and analyzed.

#### 6.4.1. $p_T$ Smearing

This is done according to a double crystal ball function that has been parameterized to embedding data for the tail/line shape while  $J/\psi \rightarrow e^-e^+$  data has been used to tune the smearing/ $p_T$  resolution(a la Eq. 64). The double crystal ball is given by Equation 58, where A is given by Equation 59, B is given by Equation 60, C is given by Equation 61, D is given by Equation 62, x is the relative shift between the simulated and reconstructed momenta ( $\frac{p_T^{reco} - p_T^{sim}}{p_T^{reco}}$ ) and the variables are defined in Table 3. The shift is applied by taking the simulated track's  $p_T$  and adding aforementioned parameterization and is expressed in Equation 63, where  $\delta p_T$  is given by Equation 64.

$$\frac{dN}{dx} = \begin{cases} A(B - \frac{x-\bar{x}}{\sigma})^{-n} & \text{if } \frac{x-\bar{x}}{\sigma} < -\alpha \\ e^{\frac{-(x-\bar{x})^2}{2\sigma^2}} & \text{if } -\alpha \leq \frac{x-\bar{x}}{\sigma} < \beta \\ C(D + \frac{x-\bar{x}}{\sigma})^{-m} & \text{if } \frac{x-\bar{x}}{\sigma} \geq \beta \end{cases} \quad (58)$$

$$A = \left( \frac{n}{|\alpha|} \right)^n e^{\frac{-|\alpha|^2}{2}} \quad (59)$$

$$B = \frac{n}{|\alpha|} - |\alpha| \quad (60)$$

$$C = \left( \frac{m}{|\beta|} \right)^m e^{\frac{-|\beta|^2}{2}} \quad (61)$$

$$D = \frac{m}{|\beta|} - |\beta| \quad (62)$$

$$p_T = p_T + \frac{dN}{dx} \frac{\delta p_T}{0.01} \quad (63)$$

$$\delta p_T = \frac{\sigma}{p_T} = \sqrt{a^2 p_T^2 + b^2} \quad (64)$$

The parameters for the double crystal ball were obtained after scaling the embedding resolution to 1%. The resolution in this case is determined in a similar manner as the resolution defined in the TPC's NIM paper's Fig. 10. In other words, the Gaussian sigma was found as a function of  $p_T$  for  $\frac{p_T^{reco} - p_T^{sim}}{p_T^{reco}}$  and fitted with Eq. 64. This shown in Fig. 39 and the parameters (a & b) are given in 3.

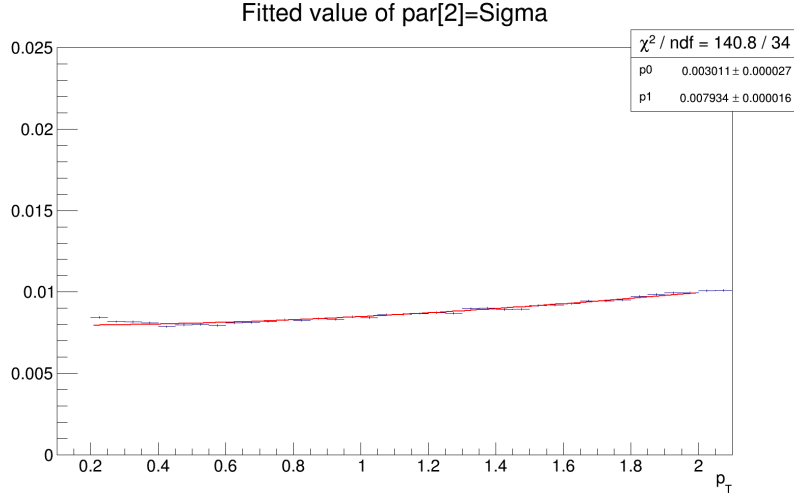


Figure 39. The  $p_T$  resolution as a function of  $p_T$ . It has been fit with the function Eq. 64.

558 After scaling 1% based on the resolution fit from Eq. 64, the double crystal ball is fit to the embedding data to  
 559 get the energy loss/tail shape of the  $p_T$  smearing. This is shown in Fig. 40 and the parameters are listed in Table 3.  
 560 Note: the resolution is scaled to 1% because embedding underestimates the smearing and the smearing increases as a  
 561 function of  $p_T$  while the double crystal ball is fitted over the  $p_T$  range from 0.2 to 2.0  $\text{GeV}\text{c}^{-1}$  for statistics purposes.

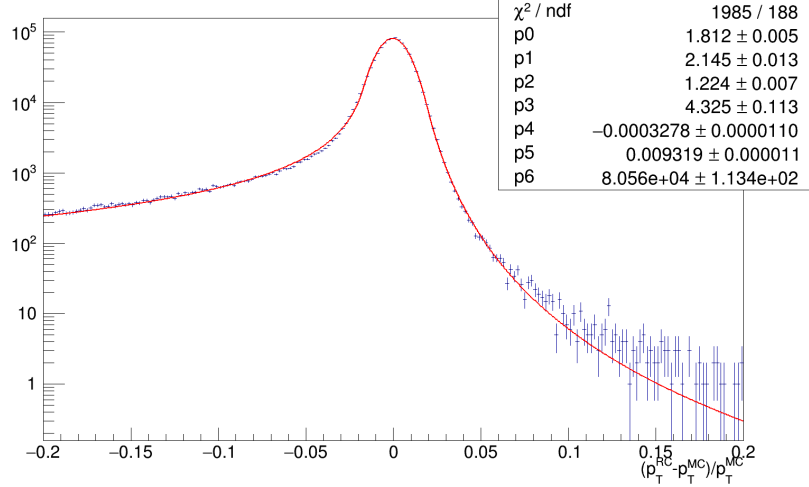


Figure 40. This is the double crystal ball fit to the  $\frac{p_T^{reco} - p_T^{sim}}{p_T^{sim}}$  for  $p_T$  from 0.2 to 2.  $\text{GeV}\text{c}^{-1}$ . It has been fit with the function Eq. 58.

With the double crystal ball and initial  $p_T$  resolution parameters, a minimization of  $\chi^2$  is used to determine the appropriate resolution parameters. In this case, b is fixed and a is varied. Note: a represents the calibration driven effect on the resolution and b represents the single hit effect on the resolution, which should be OK in embedding. The  $\chi^2$  is from the fit of the cocktail histogram to the data. The cocktail histogram consisted of  $J/\psi$  and  $c\bar{c}$  contributions and shown in Fig. 41 is an example to give an idea of the relative contributions [note: only the  $J/\psi$  is affected by the  $p_T$  smearing since charm is handled by PYTHIA]. Cocktails were generated with a ranging from 3.0E-3 to 1.8E-2 in increments of 1.5E-4 and then fitted to the data in invariant mass from 2.8 to 3.2  $\text{GeV}^{-2}$ . UPDATE[July 22nd, 2016]: The cocktail histogram consisted of  $J/\psi$ ,  $c\bar{c}$ , and Drell-Yan contributions, where each contribution has been smeared to the incremental a value. The updated values from the updated minimization are: a = 9.6E-3 and b = 7.9E-3.

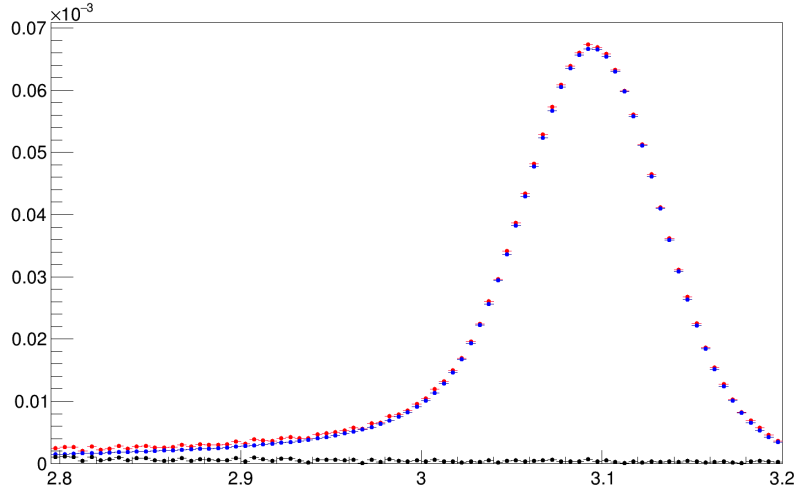


Figure 41. This is an example of the invariant mass contributions of  $J/\psi$  and  $c\bar{c}$  to the cocktail histogram used to fit the data. The black points represent  $c\bar{c}$ , the blue points represent  $J/\psi$ , and the red points represent the total contribution.

The  $\chi^2$  for each variation of a is shown in Fig. 42. It is minimized at a = 9.45E-3. This value of a will be used in the cocktail. The minimized fit to data is shown in Fig. 43. Since there is an estimation of  $dN/dM_{ee}$  from the cocktail, this can be used to estimate the  $dN/dy$  of  $J/\psi$  and tune the  $\frac{\sigma_{J/\psi}}{\sigma_{\pi^0}}$  used in the cocktail. The following equation was used to calculate  $dN/dy$ :

$$\frac{dN}{dy} = \frac{dN}{dM} \times dM \times \frac{1}{dy} \times \frac{J/\psi_r}{J/\psi_r + c\bar{c}_r} \times \frac{J/\psi_t}{J/\psi_r} \times \frac{J/\psi_t^N}{J/\psi_t} \times \frac{1}{BR_{J/\psi \rightarrow ee}} \quad (65)$$

where  $\frac{1}{dy}$  is estimated by the CERES rapidity parameterization from -1 to 1, the subscript r denotes that these values are from the  $M_{ee}$  range 2.8 to 3.2  $\text{GeV}^{-2}$ , the subscript t denotes the total range of  $M_{ee}$ , the superscript N denotes contribution outside the STAR acceptance, and BR is the branching ratio. So all of the contributions are within the STAR acceptance unless noted otherwise, superscript N; however, the parent hadron,  $J/\psi$  is always produced within -1 to 1 rapidity. The  $dN/dy$  for  $J/\psi$  is 4.84E-4. An example of  $dN/dy$  for the various a values are shown in Fig. 44 where the error bars are from the uncertainty in the fit of the cocktail histogram to the data. Update [July 22nd, 2016]: Changed the rapidity range from -1:1 to -3:3 to match the updated cocktail.  $dN/dy$  is 1.6E-4 and the cross-section ratio comes out to be 5.47859E-6. Note, scaling factor of the cocktail matching the  $\pi^0$  region changed from 0.863511 to 0.847134.

To determine the  $\frac{\sigma_{J/\psi}}{\sigma_{\pi^0}}$  used in the cocktail, the contribution needed to account for the scale factor used to scale the cocktail to match the data. The matching is done in the very low mass region, 0.0 to 0.1  $\text{GeV}^{-2}$ , and comes to 0.863511\*cocktail. Also, a  $dN/dy_{\pi^0} = 55.8$  was used. This gives  $\frac{\sigma_{J/\psi}}{\sigma_{\pi^0}} = 9.35008E-6$ .

### 6.5. Scaling Yields

With the kinematics of the electron-positron pair produced, the generated histograms need to be scaled to match the expected yields. This is done by taking the STAR  $\pi^{+/-}$  yield as our candle and scaling the rest of the parent hadrons'

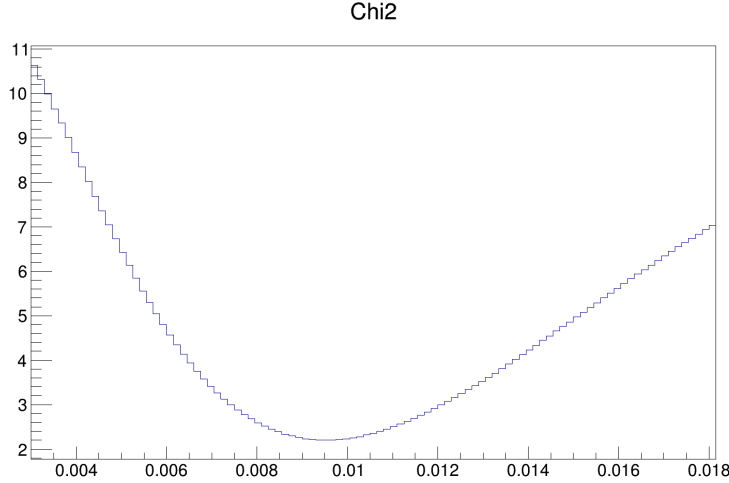


Figure 42. The  $\chi^2$  of each fit of the cocktail histogram to the data (2.8-3.2  $\text{GeV}^{-2}$ ) as a function of the smearing parameter  $a$ . The minimum  $\chi^2$  is 2.19844 for  $a = 9.45\text{E-}3$ .

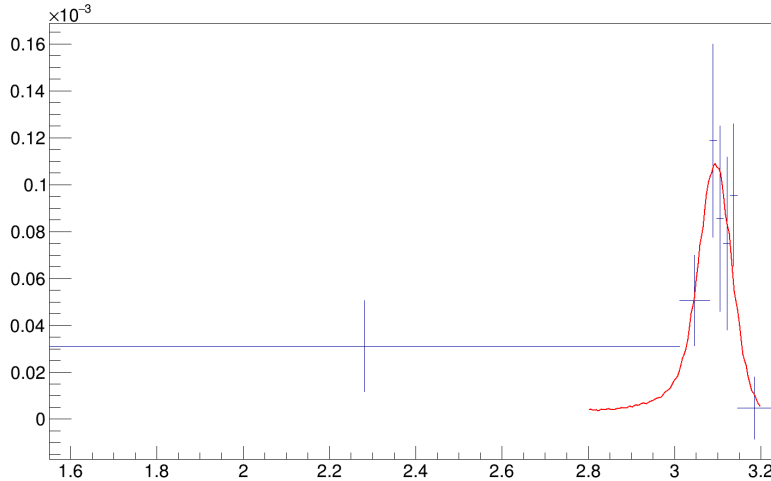


Figure 43. The cocktail histogram fit to the data.

590 yields with their SPS cross-section ratio to the  $\pi^0$ s and corresponding branching ratio. This scaling is dictated in  
 591 Equation 66, where  $(\frac{dN}{dY})_{\pi^0}$  is the mean of  $(\frac{dN}{dY})_{\pi^+}$  and  $(\frac{dN}{dY})_{\pi^-}$ ,  $dY$  is the differential rapidity,  $\frac{\sigma_{had}}{\sigma_{\pi^0}}$  is the cross-section  
 592 ratios given by SPS and found in Table 4,  $BR_{had \rightarrow (X)e^+e^-}$  is the branching ratio given by the Particle Data Group and  
 593 found in Table 5, and  $\frac{dN}{dM}$  is the histogram of dielectron yield within the acceptance region of  $p_T^e > 0.2 \text{ GeV}/c$ ,  $|\eta^e| <$   
 594 1, and  $|Y^{ee}| < 1$ .

$$\frac{1}{N} \frac{dN}{dM} = \frac{1}{nDecays} \left( \frac{dN}{dY} \right)_{\pi^0} dY \frac{\sigma_{had}}{\sigma_{\pi^0}} BR_{had \rightarrow (X)e^+e^-} \frac{dN}{dM} \quad (66)$$

595 The figures of the individual hadron  $dN/dM$  contributions may be found in Appendix O.

#### 596 6.6. $c\bar{c}$ Contribution

597 The  $c\bar{c}$  contribution is formed by using PYTHIA 6.416 to simulate the production of  $c\bar{c}$  pairs from p+p collisions  
 598 at  $\sqrt{s} = 27 \text{ GeV}$  and then it is scaled using  $N_{Binary}$  to approximate the contribution from Au+Au collisions. PYTHIA

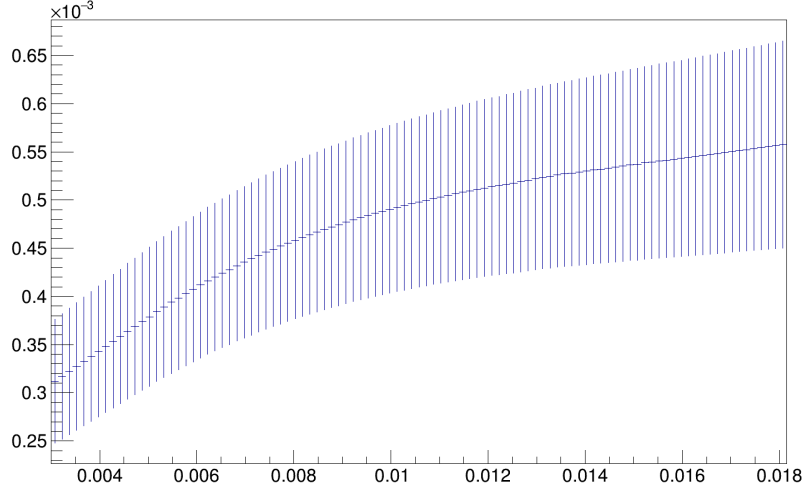


Figure 44. The projected  $dN/dy$  for  $J/\psi$  corrected for the STAR acceptance as a function of parameter  $a$ . The errors shown comes from the uncertainty on the fit parameter.

Channel	$\eta$	$\omega$	$\phi$	$\eta'$	$J/\psi$
Ratio to $\sigma_{\pi^0}$	0.085	0.069	0.018	0.0078	5.76E-6

Table 4. This table lists the ratio of the  $\pi^0$  cross-section to the hadron's cross-section. These values are used for scaling the yields to the  $\pi$  production. The  $\eta$ ,  $\omega$ ,  $\phi$ , and  $\eta'$  ratios are from NA45 data [9] and  $J/\psi$  from NA50.

599 is setup with the following settings [with descriptions from the manual [12]] MSEL = 1, pp minimum bias production;  
600 exactly two strings from either  $c$  or  $\bar{c}$ ; PARM(91,1.), width of the Gaussian primordial  $k_T$  distribution inside hadron;  
601 and PARM(67,1), the  $Q^2$  scale of the hard scattering is multiplied by this value. These PYTHIA settings match the  
602 settings used in the other STAR dielectron continuum studies. The  $c\bar{c}$  pairs decay through  $D^{+/-}$ ,  $D^0$ ,  $\bar{D}^0$ ,  $D_s^{+/-}$ ,  
603 and  $\Lambda_c^{+/-}$  channels and the  $e^+e^-$  are reconstructed within the STAR acceptance ( $p_T^e > 0.2 \text{ GeV}^{-1}$ ,  $|\eta^e| < 1$ , and  
604  $|Y^{ee}| < 1$ ). The yield is determined by scaling the resulting  $dN/dM_{pp}$  distribution with Equation 67, where the p+p  
605  $c\bar{c}$  cross-section,  $\sigma_{c\bar{c}}$ , is  $0.0188707 \text{ mb}$  and determined from fitting the upper limit of the FONLL curve, the p+p  
606 minimum bias cross-section,  $\sigma_{mb}$ , is  $33 \text{ mb}$  and determined by subtracting the elastic cross-section,  $7 \text{ mb}$ , from the  
607 total cross-section,  $40 \text{ mb}$ , listed by the Particle Data Group [7], and  $N_{binary}$ ,  $238.70037$  [10]. To appropriately weight  
608 the contribution from each hadron, their branching ratios to decay into a channel with an electron/positron are used  
609 as the weight. The branching ratios from the 2014 Particle Data Group are as follows  $D^{+/-}$ :  $16.07\%$ ,  $D^0/\bar{D}^0$ :  $6.49\%$ ,  
610  $D_s^{+/-}$ :  $6.5\%$ , and  $\Lambda_c$ :  $4.5\%$ .

611 *Update(01/20/16):* The charm cross-section used is  $26.4 \pm 7.5 \mu\text{b}$ . This is done by taking the midpoint between  
612 the upper FONLL limit(dashed curve) and the fitted FONLL upper limit(red curve) in Fig. 45, and the uncertainty is  
613 taken as the absolute difference.

$$\frac{1}{N} \frac{dN}{dM} = \frac{1}{nDecays} \left( \frac{dN}{dM} \right)_{pp} \frac{\sigma_{c\bar{c}}}{\sigma_{mb}} N_{Binary} BR(c \rightarrow e^+) BR(\bar{c} \rightarrow e^-) \quad (67)$$

614 An alternative method to determine  $N_{binary}$  gives 230, which is in agreement and determined by Equation 68 where  
615 0.375 is given by Figure 7 in [11] and  $N_{Part}$  is 123.2 from averaging 27 GeV spectra tables.  
616

$$N_{Binary} = 0.375 N_{Part}^{\frac{4}{3}} \quad (68)$$

617 *Update(01/20/16):* 19 GeV updated the charm  $\rightarrow e$  branching ratios used—so the distributions match when the  
618 same settings are used. The "Xin tune" was originally configured to use with an older PYTHIA 6 setting, which  
619 explains some of the differences and does not make complete sense to use with 6.416.

Channel	$\pi \rightarrow \gamma e^- e^+$	$\eta \rightarrow \gamma e^- e^+$	$\omega \rightarrow \pi^0 e^- e^+$	$\omega \rightarrow e^- e^+$	$\phi \rightarrow \eta e^- e^+$	$\phi \rightarrow e^- e^+$	$\eta' \rightarrow \gamma e^- e^+$	$J/\psi \rightarrow e^- e^+$
Branching Ratio	1.174E-2	6.9E-3	7.7E-4	7.28E-5	1.15E-4	2.954E-4	9E-4	5.94E-2

Table 5. These are the branching ratios used in scaling he yields and are from the Particle Data Group [7].

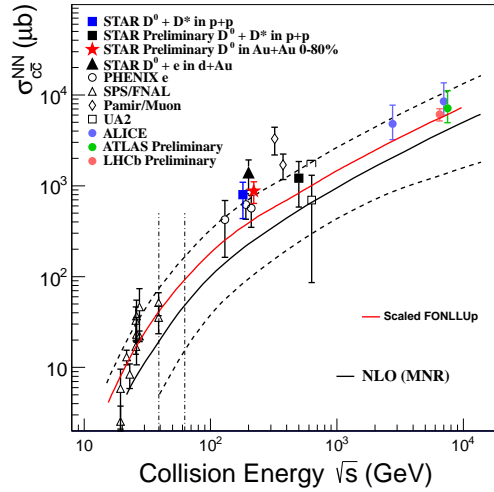


Figure 45. Total  $c\bar{c}$  cross-section measurements. The dashed curves are the upper and lower limits to the FONLL measurements and teh red curve the upper FONLL limit fitted to the data points.

To ensure that the contribution is modeled correctly, comparisons to the charm contribution published in the AuAu 19 GeV dielectron paper have been made. The comparisons are shown in Figures 46 and 47. Figure 46 lists nine different distributions and shows incremental changes to the configuration options to visualize how the different settings affect the mass spectrum. In this study, the scaling of the yield is consistent throughout while using the parameters:  $\sigma_{c\bar{c}}/\sigma_{mb} = 0.25E-3$  and  $N_{binary} = 231.8$ . The meaning for each label is given as follows:

- 620 **pp mb:** The settings mentioned previously for the 27 GeV contribution without the 2-strings requirement.
- 621 **pp charm-trigger:** The same as above except MSEL is 4 instead of 1 to produce only  $c\bar{c}$
- 622 **pp charm-trigger + BR:** The same as above, but the branching ratio values used in the weighting are from
- 623 Particle Data Group 2006 instead of 2014 to match the ones used in the 19 GeV publication. The 2009 branching
- 624 ratios are as follows  $D^{+-}$ : 17.02%,  $D^0/\bar{D}^0$ : 6.71%,  $D_s^{+-}$ : 8%, and  $\Lambda_c$ : 4.5%.
- 625 **pp charm-trigger + BR + Smear:** The same as above, but the daughters are smeared to simulate STAR's re-
- 626 solution and follows a similar method as mentioned earlier in Section 6.4 with  $a = 8E-3$  and  $b = 7.6E-3$ .
- 627 **pp charm-trigger + Xin Tune:** The same as *pp charm-trigger* except there are additional PYTHIA settings:
- 628 MSTP(82,4), PARP(82,2.0), PARP(83,0.5), PARP(84,0.4), PARP(85,0.09), PARP(86,0.95), PARP(89,1800), and
- 629 PARP(90,0.25). item[**pp charm-trigger + Xin Tune + BR + Smear:**] The same as *pp charm-trigger + BR + Smear*, but adding in Xin Tune.
- 630 **pp charm-trigger + 2-Strings:** The same as *pp charm-trigger* except the requirement of having exactly two
- 631 strings from either  $c$  or  $\bar{c}$  is implemented.
- 632 **pp charm-trigger + Xin Tune + BR + Smear + 2-Strings:** The same as *pp charm-trigger + Xin Tune + BR + Smear* except it requires two strings.
- 633 **Bingchu:** The charm contribution used in 19 GeV by Bingchu at the time of this study.

To emphasize the difference of each setting change, Figure 47 shows a series of comparisons between *pp charm-trigger* and the various changes with the former being the denominator. As indicated by the black points, the pp's minimum bias and charm production triggers show a difference in yield within the STAR acceptance; hence, the

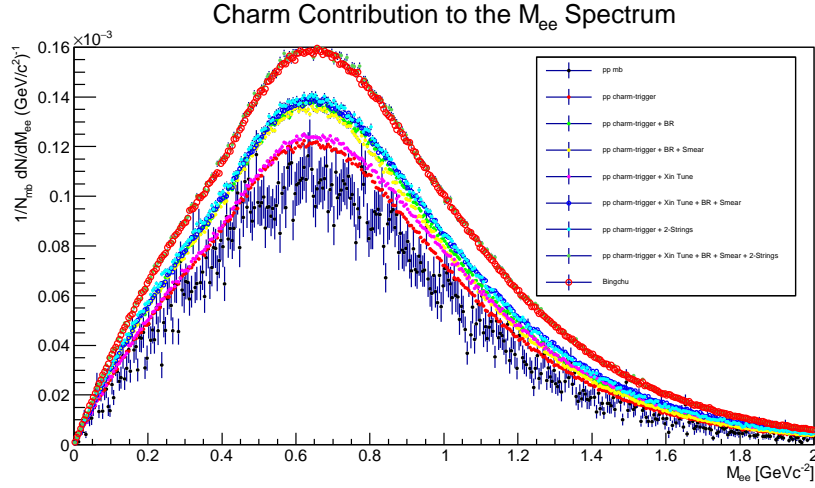


Figure 46. The dielectron yield from charms production simulated by PYTHIA v6.416 within the STAR acceptance. Each histogram represents a different running condition and their descriptions may be found in the main body of the text.

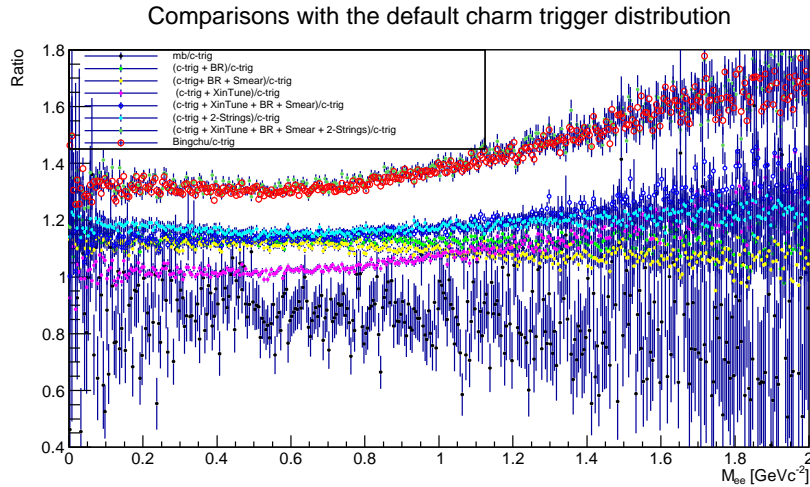


Figure 47. These histograms represent a ratio of the histograms shown in Figure 46 where the *pp charm-trigger* is the denominator. The most important thing to note is the agreement between the dark green and open red circle histograms. This indicates that Bingchu's dielectron yield from charm production is understood and reproducible, which provides a nice sanity check for the simulations.

minimum bias production must have additional contributions produced near the STAR acceptance threshold. The green and yellow points show that changing the branching ratio weights to PDG 2006 values will increase the yield by 15-20%. The pink points indicate the that *Xin's Tune* modifies the behavior at higher masses. The cyan points represent the 2-string requirement, which increase the yield about 20%. Finally, the green points demonstrate that Bingchu's results at the time of this study are reproducible when using the same settings.

Update[July 22nd,2016]: Momentum smearing has now been enabled and follows the method used in Sec. 6.4.1.

Update[January 11, 2018]: This update is to note the change in the ccbar normalization scheme. In Eq. 67, *nDecays* represents the normalization scheme in question. Originally, *nDecays* represented the number of events with exactly 2 charmed strings and exactly  $1e^+1e^-$ . Now, *nDecays* represents the number of ground-state charmed hadrons/2, where ground-state charmed hadrons are D0,  $D_s^+$ ,  $D^+$ ,  $\Lambda_c^+$ , and their anti-particles. The change arised out of discussions with PHSD folks about differences between our AuAu200 and pp200 cocktails.

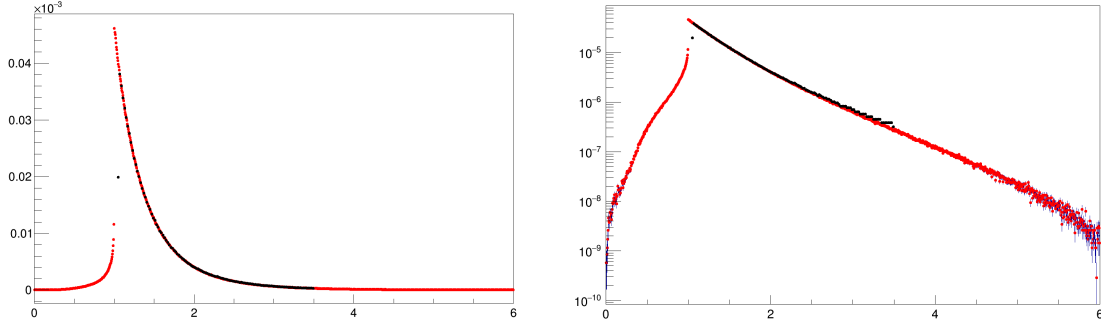


Figure 48. Comparisons between the Drell-Yan cocktail contribution published in the AuAu19  $e^+e^-$  paper [black points] and the Pythia setup used for AuAu27,39, and 62 [red points]. The comparisons of  $dN/dM_{ee}$  is as a function of invariant mass ( $\text{GeVc-2}$ ).

### 655 6.7. Drell-Yan Contribution

656 During the review process for a God Parent Committee, a request was made to add the Drell-Yan to  $e^+e^-$  657 contribution to the cocktail. To simulate the contribution, the same Pythia 6 settings were used as in the AuAu19 and 658 AuAu200  $e^+e^-$  papers. The settings used(v6.416):

- 659 • MSEL = 11
- 660 • MSTP(43) = 1
- 661 • MSTP(33) = 1
- 662 • MSTP(32) = 4
- 663 • PARP(31) = 1.8
- 664 • PARP(91) = 1.5
- 665 • PARP(67) = 4
- 666 • MDME(174-189,1) = 0
- 667 • MDME(182,1) = 1
- 668 • CKIN(1) = 1.0

669 Comparisons were made to AuAu19 and AuAu200 simulations to ensure that the setup was consistent. Examples 670 of the comparisons are shown in Fig. 48 and 49, respectively. Note the slight differences: in AuAu19 the pairs 671 with invariant masses below  $\approx 1.0 \text{ GeV}/c^2$  were not included, and in AuAu200, momentum smearing had also been 672 implemented. For the simulations used in this analysis (and AuAu39+AuAu62), momentum smearing has not been 673 implemented. In order to scale the  $pp$  simulations (PYTHIA) for use in the AuAu cocktail, the distributions have been 674 scaled in a similar method as the  $c\bar{c}$  simulations; however, the  $pp$  Drell-Yan cross-section is approximated differently. 675 It takes the Drell-Yan cross-section used in the AuAu19 paper and scales it with the PYTHIA cross-sections at 19 GeV 676 and the desired energy, e.g.  $\sigma_{DY27\text{Pythia}} * \frac{\sigma_{DY19\text{Paper}}}{\sigma_{DY19\text{Pythia}}}$ .

677 Results comparing the Drell-Yan contributions across  $\sqrt{s_{NN}} = 19.6, 27, 39, 62.4$ , and 200 GeV are shown in Fig. 678 50 and the values used in the scaling are listed in Table 6. The PYTHIA Drell-Yan cross-section for  $pp$   $\sqrt{s_{NN}} =$  679 19.6 GeV is 13.44 nb and the cross-section used in the AuAu19 paper is 9.88 nb. So each Drell-Yan  $pp$  PYTHIA 680 cross-section given for 27, 39, and 62.4 GeV are scaled by 9.88/13.44.

681 Update[July 22nd, 2016]: The Drell-Yan contributions now incorporate momentum smearing that follows Sec. 682 6.4.1.

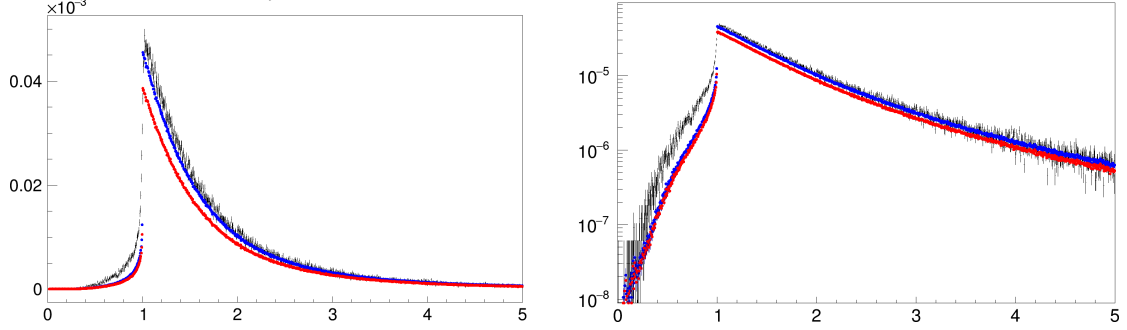


Figure 49. Comparisons between the Drell-Yan cocktail contribution published in the AuAu200  $e^+e^-$  paper (PRL+PRC) and the Pythia setup used for AuAu27,39, and 62. The comparisons of  $dN/dM_{ee}$  is as a function of invariant mass ( $\text{GeVc}^{-2}$ ). The black marks represent the published Drell-Yan, the blue points represent this note's Pythia setup, and the red points represent this Pythia's setup but using Pythia's Drell-Yan cross-section values from 200GeV and 19GeV to scale the Drell-Yan cross-section for  $pp$  19GeV (*i.e.* number quoted in the AuAu19 paper). There is a 30% uncertainty associated with the AuAu200 Drell-Yan results and the red points are within 30% of the black points.

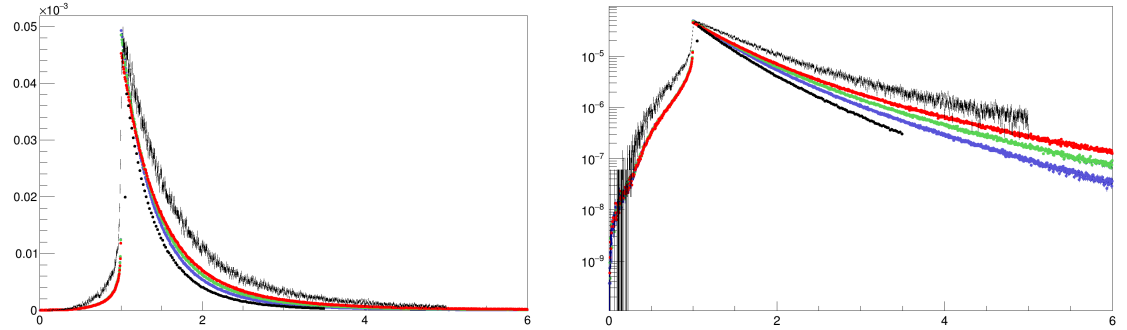


Figure 50. Comparisons between the Drell-Yan cocktail contributions as  $dN/dM_{ee}$  for the published  $e^+e^-$  results at  $\sqrt{s_{NN}} = 19.6$  [black points] and 200 GeV [black crosses] with  $e^+e^-$  results at  $\sqrt{s_{NN}} = 27$  [purple points], 39 [green points], and 62.4 [red points] GeV as a function of invariant mass [ $\text{GeVc}^{-2}$ ].

$\sqrt{s_{NN}}$	$\sigma_{mb}$	$N_{coll}$	$\sigma_{DY\text{Pythia}}$
27 GeV	33 mb	238.7004	17.27 nb
39 GeV	34 mb	243.16085	21.95 nb
62.4 GeV	36 mb	252.90090	28.3 nb

Table 6. This table lists the Drell-Yan input parameters used to scale the PYTHIA simulations to a yield comparable for Au+Au collisions at  $\sqrt{s_{NN}} = 27, 39$ , and 62.4 GeV.

### 683 6.8. Total Cocktail

684 The individual yields are then added together to form the total cocktail yield. Note the  $\rho$  and medium contributions  
 685 to the yield are not added in this cocktail. This is because those contributions are given by the theory community and  
 686 discussed later in the note.

### 687 6.9. Cocktail Uncertainties

688 This subsection describes the cocktail uncertainties for the hadron components scaled to the  $\pi$  yield and  $c\bar{c}$  branching  
 689 ratios. The  $J/\Psi$  uncertainties and  $c\bar{c}$  correlated uncertainties are discussed in Sec. 7.

690 The  $\pi^0$  uncertainty is derived from the uncertainties quoted in Sabita&Lokesh's (STAR) PID paper and the Dalitz  
 691 decay's branching ratio uncertainty. Took the weighted mean of the  $\pi^{+-}$  yield uncertainties and then averaged them  
 692 to determine the  $\pi^0$  yield uncertainty ( $\Delta \frac{dN}{dy_{\pi^0}}$ ). This gave a relative uncertainty ( $\Delta \frac{dN}{dy_{\pi^0}}$ ) of 11.04% and the branching  
 693 ratio used is  $1.174 \pm 0.035\%$ . Giving a total uncertainty of 14.02%.

694 The  $\pi^0$  scaled hadrons ( $\eta$ ,  $\omega$ ,  $\phi$ , and  $\eta'$ ) have the following uncertainties:

695  $\eta$ :  $(0.49/6.9 + 0.005/0.069 + 0.1104)$ , where the first set corresponds to the branching ratio uncertainty, the second  
 696 set corresponds to the  $\sigma_\eta/\sigma_\pi$  uncertainty listed in EPJC4 p242, and the third set is the  $\pi^0$  yield uncertainty.

697  $\omega$  Dalitz decay:  $(0.6/7.7 + 0.01/0.096 + 0.1104)$ , where the first set corresponds to the branching ratio uncertainty,  
 698 the second set corresponds to the  $\sigma_\omega/\sigma_\pi$  uncertainty listed in EPJC4 p242, and the third set is the  $\pi^0$  yield uncertainty.

699  $\omega$  direct decay:  $(0.14/7.28 + 0.01/0.096 + 0.1104)$ , where the first set corresponds to the branching ratio uncer-  
 700 tainty, the second set corresponds to the  $\sigma_\omega/\sigma_\pi$  uncertainty listed in EPJC4 p242, and the third set is the  $\pi^0$  yield  
 701 uncertainty.

702  $\phi$  Dalitz decay:  $(0.1/1.15 + 0.05 + 0.1104)$ , where the first set corresponds to the branching ratio uncertainty, the  
 703 second set corresponds to the value extracted from Bingchu's AuAu19 results( $13\% = \sqrt{0.12 * 0.12 + x * x}$ , where  
 704 12% is the  $\pi^0$  yield uncertainty and  $x = 5\%$ ), and the third set is the  $\pi^0$  yield uncertainty.

705  $\phi$  direct decay:  $(0.03/2.954 + 0.05 + 0.1104)$ , where the first set corresponds to the branching ratio uncertainty,  
 706 the second set corresponds to the value extracted from Bingchu's AuAu19 results( $13\% = \sqrt{0.12 * 0.12 + x * x}$ , where  
 707 12% is the  $\pi^0$  yield uncertainty and  $x = 5\%$ ), and the third set is the  $\pi^0$  yield uncertainty.

708  $\eta'$ :  $(0.1 + 0.12 + 0.1104)$ , where the first set corresponds to the branching ratio uncertainty from Bingchu's  
 709 AuAu19 results, the second set corresponds to the value extracted from Bingchu's AuAu19 results( $17\% = \sqrt{0.12 * 0.12 + x * x}$ ,  
 710 where 12% is the  $\pi^0$  yield uncertainty and  $x = 12\%$ ), and the third set is the  $\pi^0$  yield uncertainty.

711 The branching ratio uncertainty from  $c\bar{c}$  is also considered. A flat relative uncertainty is used for both invariant  
 712 mass and transverse momentum. The relative contributions from  $D^0$ ,  $D^+$ ,  $D_s^+$ ,  $\Lambda_c^+$ , and their corresponding anti-particle  
 713 are 62%, 20%, 12%, and 6%, respectively. The relative contributions have been determined by studying the charmed  
 714 meson production in the PYTHIA simulations for root-s = 27 and 200 GeV. The branching ratio uncertainties are:  
 715  $D^+ \rightarrow e+\text{semileptonic}$  ( $16.07 \pm 0.30\%$ ),  $D^0 \rightarrow e+\text{anything}$  [d] ( $6.49 \pm 0.11\%$ ),  $D_s^+ \rightarrow e+\text{semileptonic}$  [a] ( $6.5 \pm 0.4\%$ ), and  $\Lambda_c \rightarrow e+\text{anything}$  ( $4.5 \pm 1.7\%$ ). Hence, the  $c\bar{c}$  uncertainty based on branching ratios would be:  
 717 yield  $\times (0.62 * 0.11/6.49 + 0.2 * 0.3/16.07 + 0.12 * 0.4/6.5 + 0.06 * 1.7/4.5)$ .

## 718 7. Systematics

719 The systematic uncertainties presented here are used to give a handle on the uncertainty of the methods used.  
 720 First, I'll present the single track efficiency systematics, which are averaged and added together in quadrature to  
 721 determine the pair efficiency systematic uncertainty. Second are the pair systematic uncertainties from the STAR  
 722 acceptance correction factor and the hadron contamination. Third, the determination of the  $J/\Psi$  cocktail component

723 uncertainty. Fourth, the uncertainty in the  $c\bar{c}$  yield from assumption that the electron-positron daughters are fully  
 724 correlated. Finally, the systematic uncertainty in determining the acceptance correction factor from STAR to no  
 725 geometric acceptance constraint.

### 726 7.1. Tracking

727 The single tracking efficiency was determined with embedding and is discussed in Section 5.1. To determine  
 728 the systematic uncertainty, a different method was used for finding the tracking efficiency and then compared to the  
 729 embedding efficiency for nHitsFit, gDCA, and ndEdxFit. This method consisted of using data that is primarily a pure  
 730 electron sample (electrons from  $\pi^0$  decays). The picoDSTs were generated from the microDSTs, much like the ones  
 731 listed in Sec. 1 and have the same event and run selection criteria; however, there were a couple different track quality  
 732 cuts at the level of producing picoDSTs. The track quality cuts were  $p_T \geq 0.2 \text{ GeV}^{-1}$ ,  $|\eta| \leq 1$ ,  $n\sigma_e < 1$ \*, and  $\text{gDCA} < 3 \text{ cm}$ . From the picoDST sample,  $\pi^0$  daughter candidates were selected in a similar fashion as the pure electron  
 734 sample mentioned in Sec. 5.2, but with less of an emphasis on conversion daughters. Selection requirements were as  
 735 follows: A perpendicular decay length, the distance between primary and secondary vertices in the x-y plane,  $\leq 2.0$   
 736 cm, the  $\phi_V$  of the conversion pair  $\leq \pi$ , the invariant mass of the pair using global track properties  $\leq 4 \text{ MeV}^{-2}$ , the  
 737 invariant mass of the pair with primary track properties  $\leq 5 \text{ MeV}^{-2}$ , and the distance of closest approach between  
 738 the pair helices  $\leq 1 \text{ cm}$ .

739 To determine the efficiencies for nHitsFit, gDCA, and ndEdxFit, the pure candidates are counted before and after  
 740 the respective cuts. nHitsFit refers to  $\geq 15$  fit points and the ratio of fit points to available points  $\geq 0.52$ , gDCA refers  
 741 to the global DCA  $\geq 1 \text{ cm}$ , and ndEdxFit refers to the number of fit points used in the dE/dx calculation and  $\geq 15$   
 742 points. Data and embedding distributions overlaid from these parameters for  $\eta$  [-1,1],  $\phi$  [-180,180], and  $p_T$  slices are  
 743 shown in Appendix P. The overall comparisons between the efficiencies as a function of  $p_T$  are shown in Appendix  
 744 Q. The differences between these efficiencies are shown in Figs. 51, 52, 53, 54, 55, and 56, and the fit results shown  
 745 in the figure are taken into account when determining the overall systematic uncertainty by averaging between charge  
 746 species results. So, this leads to systematic uncertainties of nHitsFit, nHitsdEdx, gDCA: 1% (1.013), 1.1% (1.1142),  
 747 2.8% (2.7705) respectively.

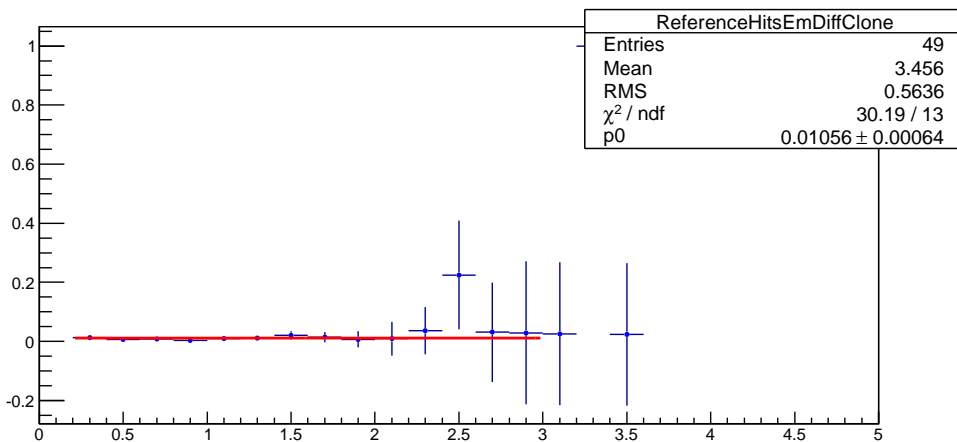


Figure 51. The difference between the data and embedding nHitsFit electron efficiency calculations. The line, p0, fit results are used in the systematic uncertainty approximation.

### 748 7.2. Matching

749 The matching systematic uncertainty is determined by comparing the acceptance corrected pure electron sample  
 750 to the scaled pion sample from Sec. 5.2. The difference is compared as a function of  $p_T$  and fitted with "pol0" from  
 751 0 to 3  $\text{GeV}^{-1}$ . The fit results are shown in Fig. 57 and 58. The average systematic uncertainty from the matching  
 752 efficiency is 0.53%.

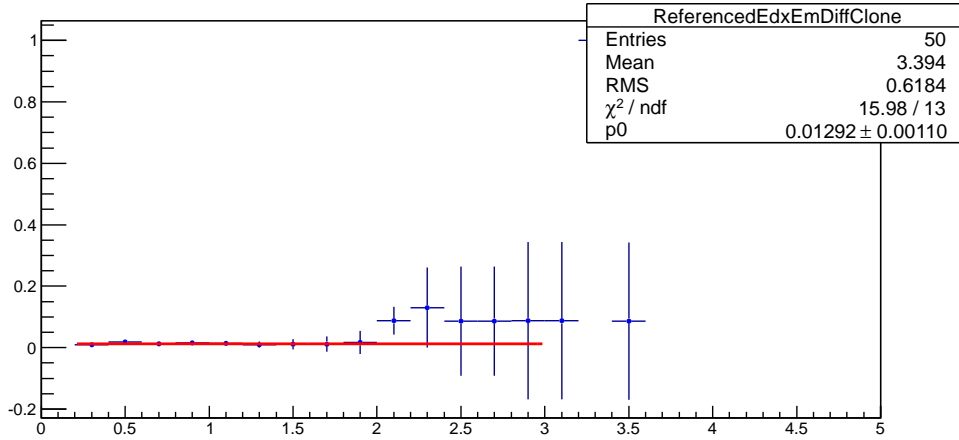


Figure 52. The difference between the data and embedding ndEdxFit electron efficiency calculations. The line, p0, fit results are used in the systematic uncertainty approximation.

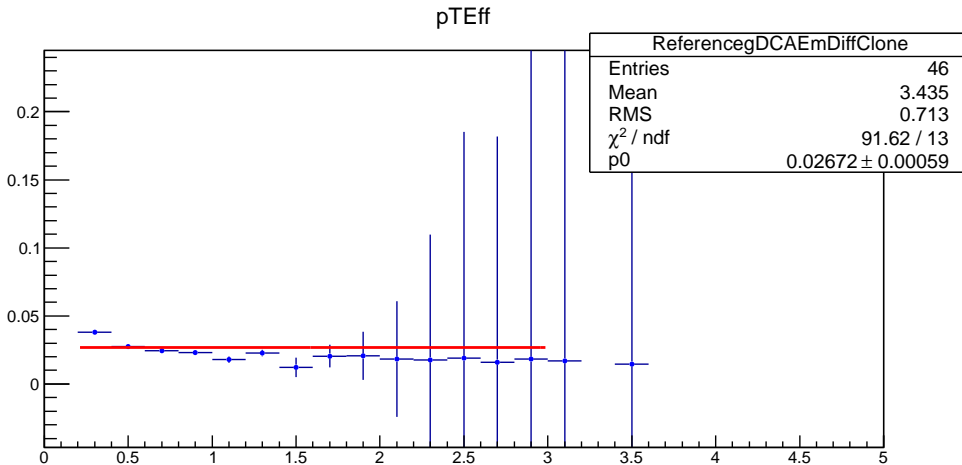


Figure 53. The difference between the data and embedding gDCA positron efficiency calculations. The line, p0, fit results are used in the systematic uncertainty approximation.

### 753 7.3. Electron Identification

754 This has been covered in Sec. 3.1.

### 755 7.4. Efficiency Systematics

756 Table 7 represents a list of all the efficiency systematic uncertainties combined. The efficiency uncertainties are  
 757 added in quadrature to determine the single track systematic uncertainty and then doubled to approximate the pair  
 758 systematic uncertainty from the efficiency measurements.

### 759 7.5. Charge Acceptance Factor

760 The systematic uncertainty of the charge acceptance correction factor,  $\frac{ME_{+-}}{2\sqrt{ME_{-}ME_{++}}}$ , is estimated by evaluating the  
 761 geometric mean with the acceptance factor as function of  $M_{ee}$  and  $M_{ee}$ ,  $p_T^{ee}$ . To do this, the mixed-event sample was  
 762 used to evaluate the differences because of the minimal statistics in the same-event estimation. To demonstrate that

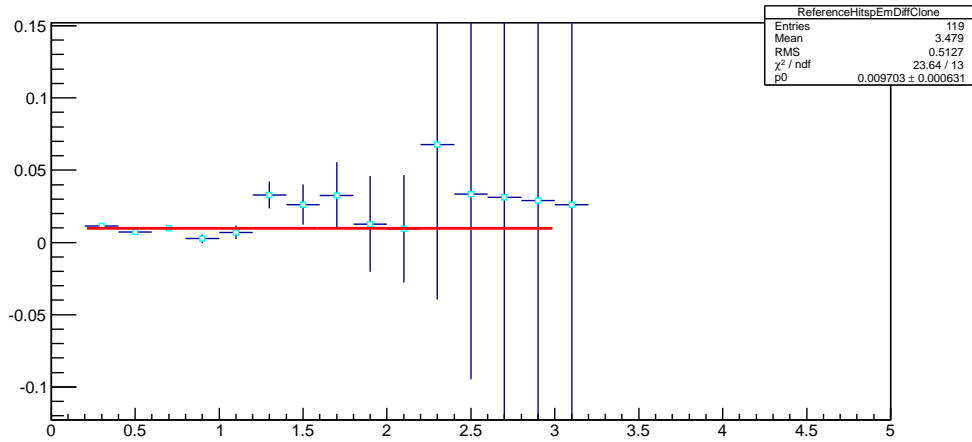


Figure 54. The difference between the data and embedding nHitsFit positron efficiency calculations. The line, p0, fit results are used in the systematic uncertainty approximation.

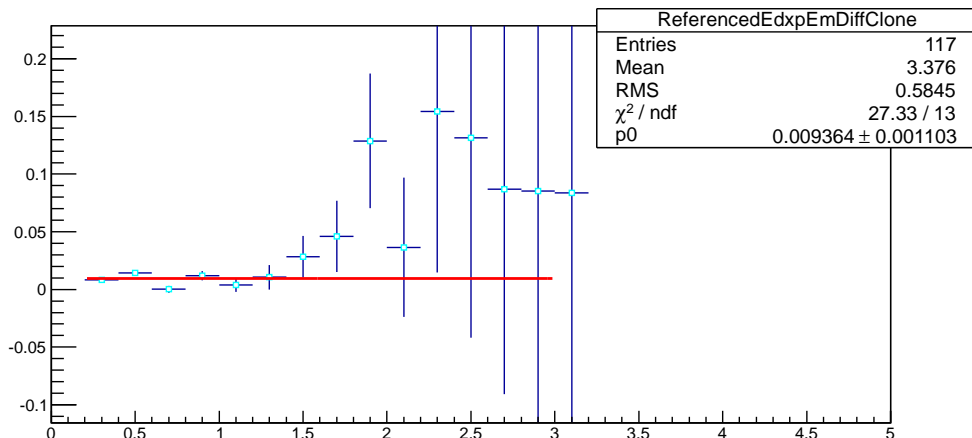


Figure 55. The difference between the data and embedding ndEdxFit positron efficiency calculations. The line, p0, fit results are used in the systematic uncertainty approximation.

Table 7. Systematic uncertainties from efficiency measurements.

	Rel. Uncert.
nHitsFit	1 %
DCA	2.8%
ndEdxFit	1.1%
TOF matching	0.53%
$n\sigma_e$	2%
$1/\beta$	1.3%
Total single track	4%
Total pair	8%

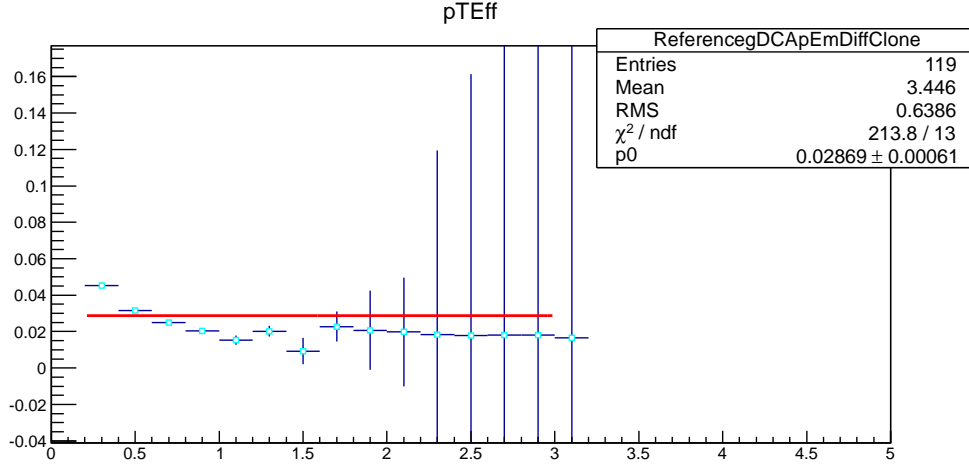


Figure 56. The difference between the data and embedding gDCA positron efficiency calculations. The line, p0, fit results are used in the systematic uncertainty approximation.

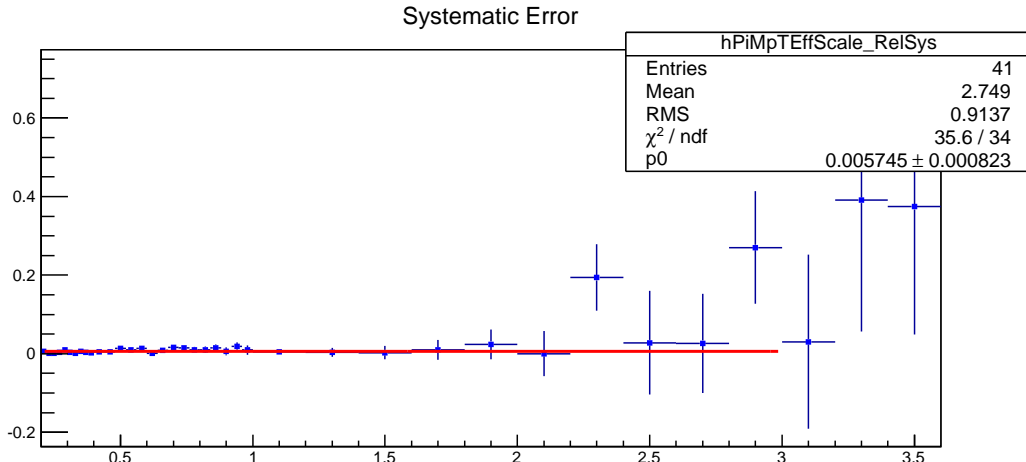


Figure 57. The difference between the scaled  $\pi^-$  efficiency and the pure electron sample efficiency as a function of  $p_T$  with respect to the scaled pion efficiency. The line, p0, fit results are used in the systematic uncertainty approximation.

763 the mixed-event sample is OK, the ratio of ++ to – was studied for same-event and mixed-event pairs, and both ratios  
 764 show similar behavior. This study is shown in Figs. 59 and 60 with slightly different binning-QA and data binning.

765 The differences between 1D and 2D acceptance factors with respect to the 2D acceptance factor are shown in Fig.  
 766 61.

### 767 7.6. Like Sign Means

768 When using like-sign electron/positron pairs as an approximation for the background, the geometric mean,  $2 \times$   
 769  $\sqrt{N_{++}N_{--}}$  was used. To estimate the systematic uncertainty, a direct sum,  $N_{++} + N_{--}$ , was used to compare the  
 770 differences and is shown in Fig. 62. Mixed event data was used to determine estimate the differences, which is  
 771 justified as OK by the similarity of the ratios of ++ to – for same-event and mixed-event pairs as shown in Sec. 7.5.  
 772 The higher systematic differences at higher invariant masses are most likely due to the smaller amount

773 The uncertainty was not accounted for in the pair systematic uncertainties, because it is a relatively small contribu-  
 774 tion and at high invariant masses the difference is skewed by low statistics—geometric mean is artificially lower due

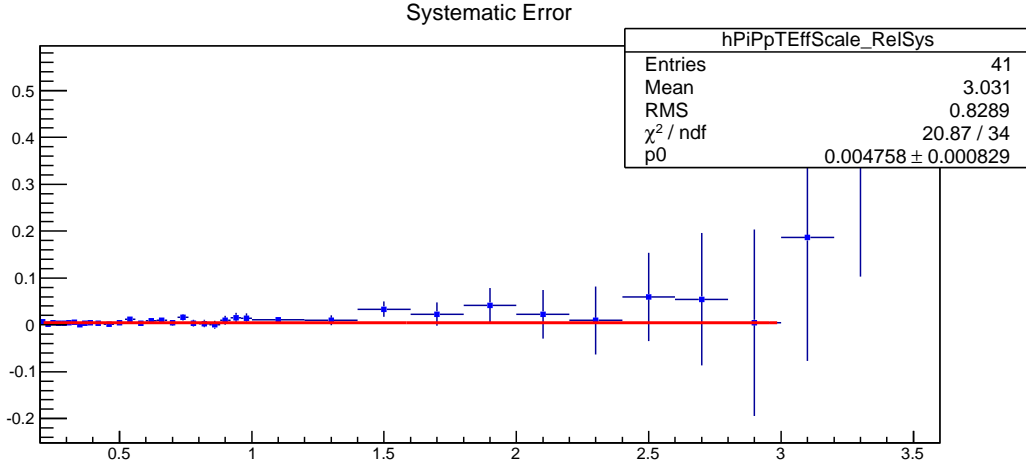


Figure 58. The difference between the scaled  $\pi^+$  efficiency and the pure positron sample efficiency as a function of  $p_T$  with respect to the scaled pion efficiency. The line, p0, fit results are used in the systematic uncertainty approximation.

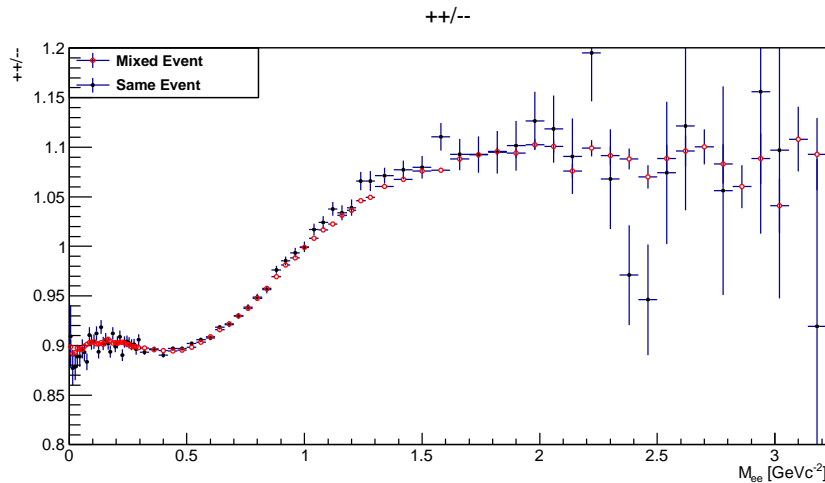


Figure 59. The ratio of ++ to -- for same-event (black solid points) and mixed-event (red open points) pairs. This invariant mass binning was selected for QA purposes.

775 to 0s for one of the two charges. For this reason, a direct sum is used in the  $J/\psi$  mass range. Also, we know that the  
776 geometric mean is a better approximation than the direct sum.

### 777 7.7. Hadron Contamination

778 This is a continuation of the purity study in Sec. 3.1.  
779 To determine the effect the hadron contamination has on our dielectron yield, pure hadron ( $\pi$ , K, p) samples  
780 are mixed in with the electron sample and paired to form h-h, h-e, and e-e samples. Then the signal extraction techniques  
781 were performed to find the magnitude of h-h/e-h signal in the e-e signal, or hadron contamination in the signal.  
782 An approximation of the contamination was performed with the data's picoDST sample using the same event and  
783 track selection criteria as the data analysis. The only difference is in the identification methods. Electrons were selected  
784 in the same fashion as the data analysis. To select pions,  $|\beta^{-1} - \beta_\pi^{-1}| < 0.01$  and  $n\sigma_\pi < 2$  (4) were required  
785 [aside: only 5% of the pions were used]. To select kaons and protons,  $|\beta^{-1} - \beta_{K/P}^{-1}| < 0.01$  and  $n\sigma_{K/P} < 2$  (4) were  
786 required. To prevent double counting, tracks associated to multiple identifications were ignored, except for the case

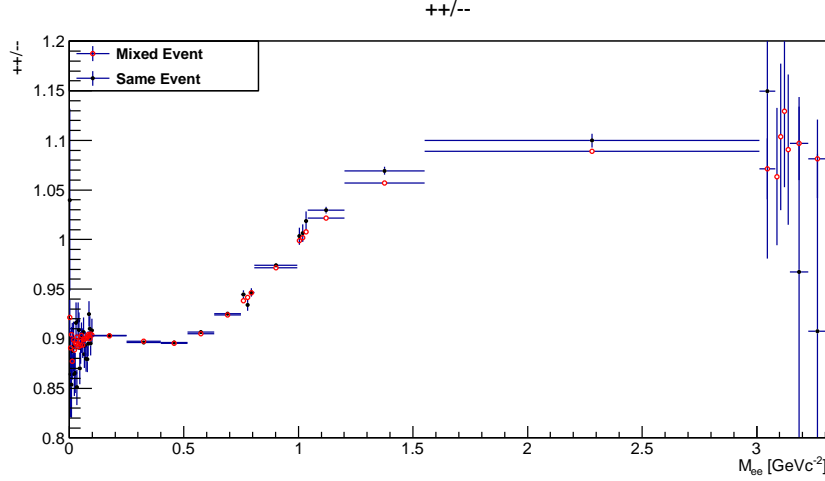


Figure 60. The ratio of ++ to – for same-event (black solid points) and mixed-event (red open points) pairs. This invariant mass binning was selected to match that of the presented data.

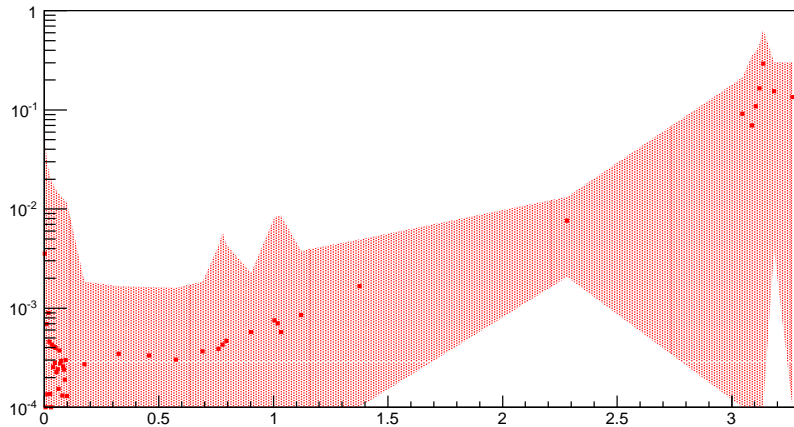


Figure 61. The difference between the geometric mean corrected with a 1D ( $M_{ee}$ ) and 2D( $M_{ee}, p_T^{ee}$ ) acceptance correction with respect to the geometric mean with a 2D correction.

when one of the identifications is electron. In this case, the track is identified as electron, just like the analysis.

In order to adequately weight the hadron contributions, the following weight was used for each track as a function of momentum:

$$W_{had} = \frac{Purity_{had}}{Purity_e} \times \frac{N_e}{N_{had}} \quad (69)$$

where the *Purity* is from Sec. 3.1 and N is the total number of electrons and hadrons used in the analysis. Because the total number of particles used is necessary, two passes were made through the data sample.

For QA and the fun of it, pair and acceptance correction distributions of  $\pi\pi$ , KK, pp, and ee have been made. The invariant mass distributions are made with the pure hadron distributions assuming an electron mass in the reconstruction. The  $\pi\pi$  distributions are found in Fig. 63.

The KK distributions [ $\phi \rightarrow K^+K^-$  is visible at  $250\text{MeVc}^{-2}$ ] are shown in Fig. 64.

The pp distributions are shown in Fig. 65.

The ee distributions are shown in Fig. 66.

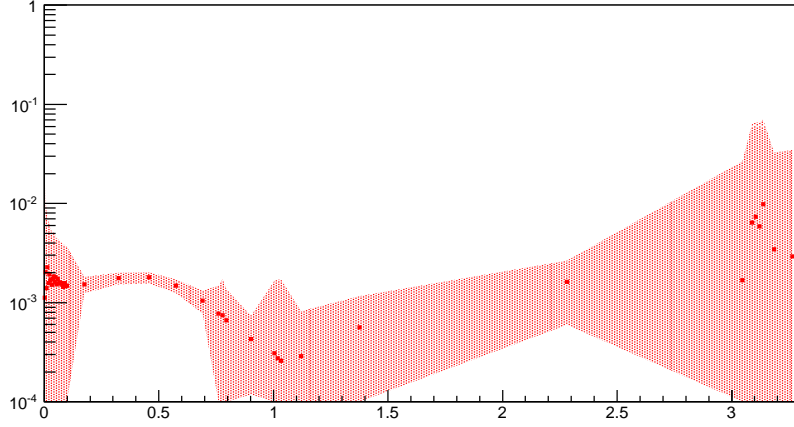


Figure 62. The relative difference between using a geometric mean and direct sum for like-sign background approximation. It is relative to the geometric mean.

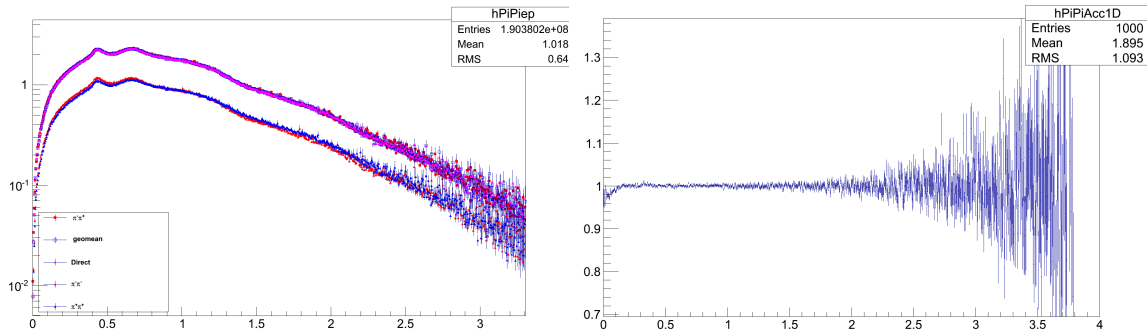


Figure 63. (Left) The invariant mass distributions of  $\pi^+\pi^-$ ,  $\pi^+\pi^+$ ,  $\pi^-\pi^-$ , geometric mean background approximation, and direct sum background approximation. (Right) The acceptance correction,  $\sqrt{2 \frac{ME_{+-}}{ME_{--} + ME_{++}}}$ , for the like sign background distributions.

798 Invariant mass distributions of the electron foreground, electron background, electron signal, hadron foreground,  
 799 hadron background, and hadron signal are shown in Fig. 67. The signals are result of the background distributions  
 800 subtracted from the foreground as a function of invariant mass (ie 1D). The figure is used to give an overall idea of  
 801 the level contamination inside the electron signal. Note that the Y-axis is an arbitrary scale and should not be taken  
 802 too seriously.

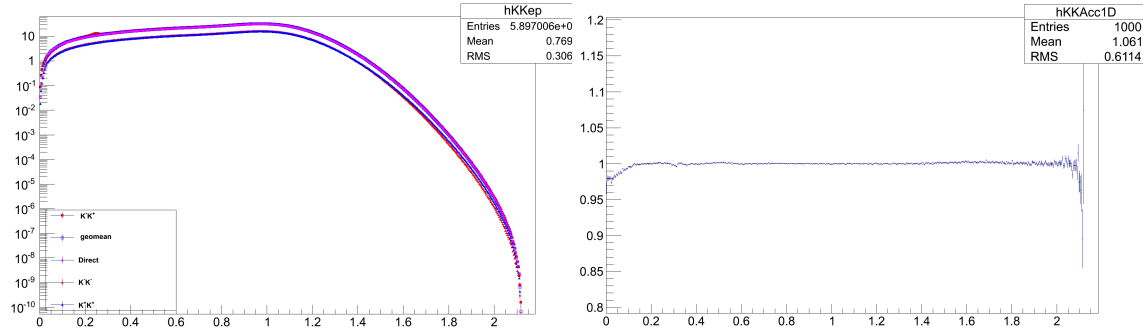


Figure 64. (Left) The invariant mass distributions of  $K^+K^-$ ,  $K^+K^+$ ,  $K^-K^-$ , geometric mean background approximation, and direct sum background approximation. (Right) The acceptance correction,  $\sqrt{2 \frac{ME_{+-}}{ME--ME_{++}}}$ , for the like sign background distributions.

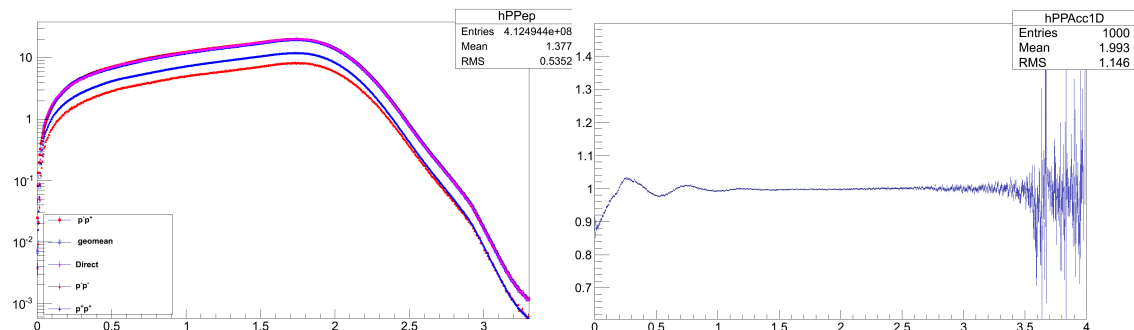


Figure 65. (Left) The invariant mass distributions of  $p\bar{p}$ ,  $pp$ ,  $\bar{p}\bar{p}$ , geometric mean background approximation, and direct sum background approximation. (Right) The acceptance correction,  $\sqrt{2 \frac{ME_{+-}}{ME--ME_{++}}}$ , for the like sign background distributions.

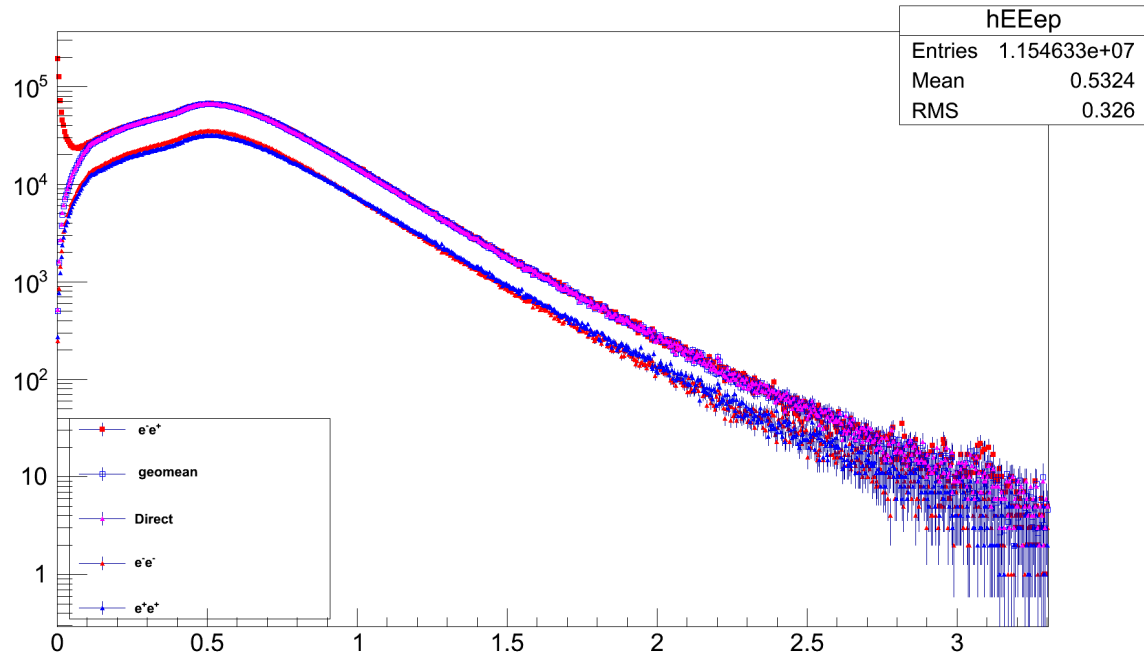


Figure 66. (Left) The invariant mass distributions of  $e^+e^-$ ,  $e^+e^+$ ,  $e^-e^-$ , geometric mean background approximation, and direct sum background approximation. (Right) The acceptance correction,  $\sqrt{2 \frac{ME_{+-}}{ME--ME_{++}}}$ , for the like sign background distributions.

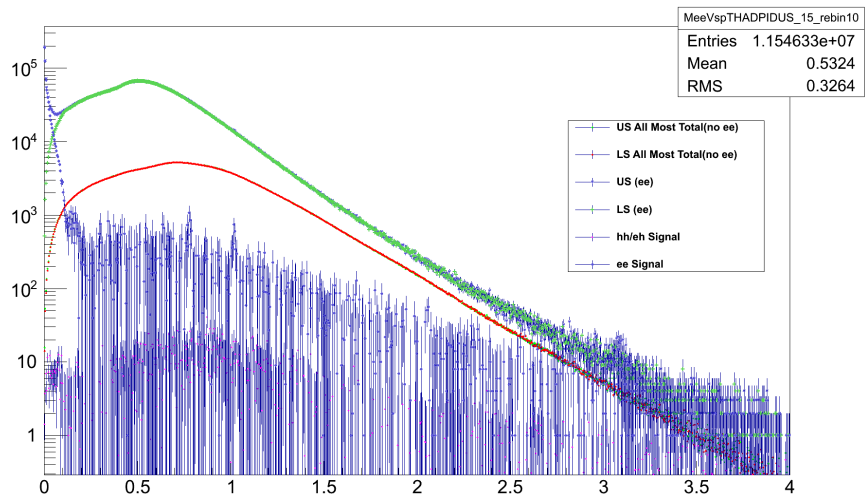


Figure 67. The invariant mass distribution

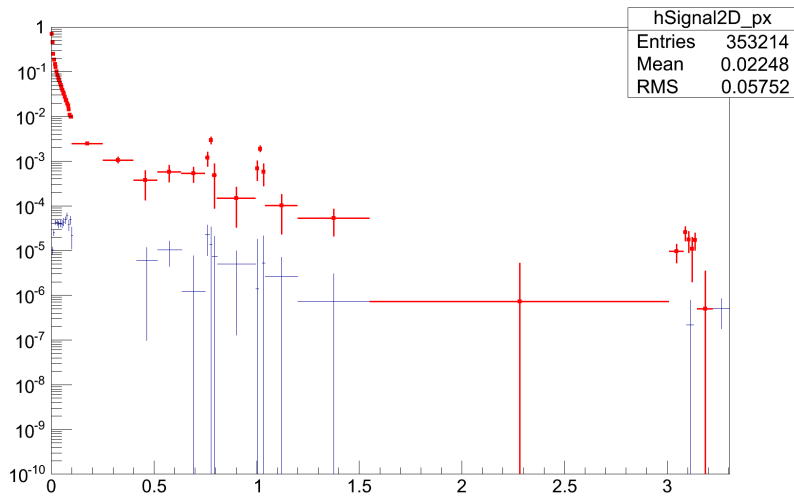


Figure 68. The invariant mass distribution of the e-e (red) and h-h/e-h (blue) signals after subtracting the geometric mean with an acceptance correction background as a function of invariant mass and transverse momentum from the foreground.

803 Now, the electron and hadron signal invariant mass distributions, after subtracting the background as a function of  
804 invariant mass and transverse momentum, are shown in Fig. 68.

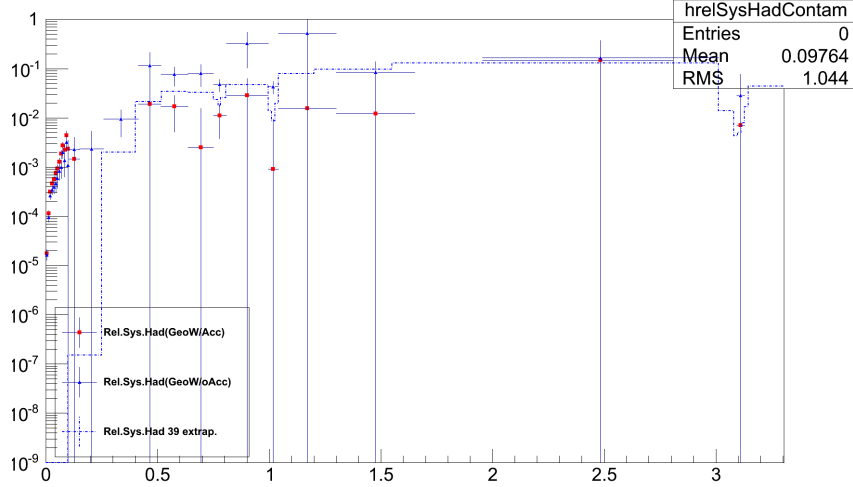


Figure 69. The relative systematic uncertainty caused by hadron contamination in the signal. The uncertainty is shown as a function of invariant mass ( $\text{GeV}\text{c}^{-2}$ ). The blue marks represent the uncertainty if the background is approximated without an acceptance correction. The dashed blue histogram is the 39 GeV systematic uncertainty interpolated to this analysis' binning. The red marks represent the uncertainty if the background is approximated with an acceptance correction.

805     The contribution of the hadron signal with respect to the electron signal leads to the relative uncertainty in hadron  
 806     contamination of the data's electron signal. Shown in Fig. 69 is the relative systematic uncertainty caused by possible  
 807     hadron contamination for three different cases. The blue hash marks represent the uncertainty if the background  
 808     is estimated without an acceptance correction. The blue dashed histogram represents the systematic uncertainty  
 809     interpolated to match the binning used in this analysis. Also, the 39 GeV uncertainty is derived by using a 200 GeV  
 810     sample with purity levels and numbers from the 39 GeV analysis. The red points are systematically lower than the 39 GeV  
 811     uncertainties and given the level of statistics in this approximation. This analysis will use the 39 GeV uncertainties to  
 812     be conservative.  
 813

### 814 7.8. JPsi Uncertainties

815 The total JPsi uncertainty (cocktail) is approximated by taking into account the change in JPsi yield when using  
 816 either a correlated or a 'decorrelated' charm distribution, the effect of using different transverse momentum distri-  
 817 butions, the total pair efficiency uncertainty, the statistical uncertainty, and the effect of using different methods to  
 818 approximate the background. For the charm uncertainty, the JPsi yield is approximated by fitting the data [ $M_{ee}$ : 2.8-  
 819 3.2  $\text{GeVc}^{-2}$ ] with a fixed cocktail (w/out JPsi) for the background and a cocktail JPsi shape with a free amplitude.  
 820 More information about the decorrelation method may be found in Sec. 7.9. The charm contribution has < 1% effect.  
 821 The effect of using different transverse momentum distributions is measured by taking the relative difference between  
 822 the invariant mass yields from JPsi cocktail components with a Boltzmann distribution and a Tsallis Blast Wave  
 823 distribution. The Boltzmann and Tsallis Blast Wave distributions are the same as the ones mentioned in Sec. 6.2. The  
 824 invariant mass yields are shown in Fig. 70.

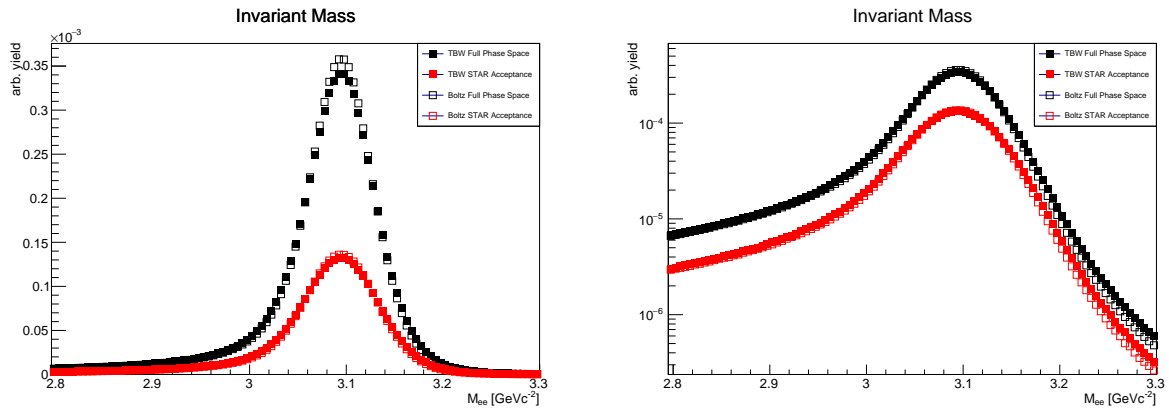


Figure 70. The JPsi invariant mass yields for cocktail components generated with a Boltzmann  $p_T$  distribution (open square) and Tsallis Blave Wave distribution (closed square) as an input distribution. The yields are shown in full phase space (black) and the STAR acceptance (red).

825 The ratio between the different invariant mass yields with the Tsallis Blast Wave input to the Boltzmann input are  
 826 shown in Fig. 71.

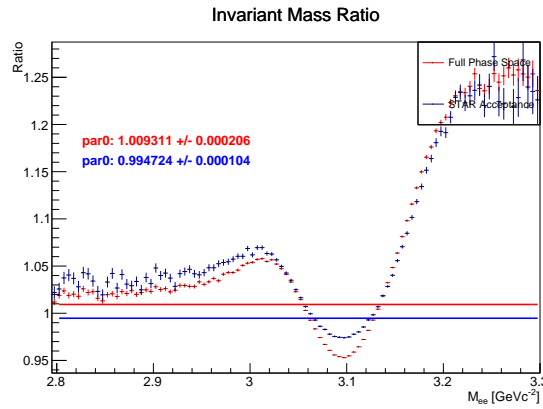


Figure 71. The ratio of JPsi invariant mass yields for cocktail components generated with a Boltzmann  $p_T$  distribution and Tsallis Blave Wave distribution as an input distribution – TBW/Boltzmann. The ratios are shown for the full phase space (red) and the STAR acceptance (blue). The lines are straight line fits to each ratio distribution.

827 The relative difference with respect to the yield with a Boltzmann distribution is shown in Fig. 72.  
 828 Took the uncertainty from  $p_T$  distribution selection to be 3.7%.

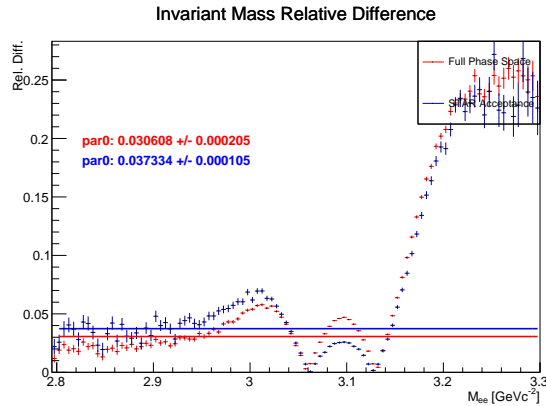


Figure 72. The absolute relative difference of the JPsi invariant mass yields for cocktail components generated with a Boltzmann  $p_T$  distribution and Tsallis Blave Wave distribution as an input distribution with respect to the yield with a Boltzmann distribution. The ratios are shown for the full phase space (red) and the STAR acceptance (blue). The lines are straight line fits to each ratio distribution.

829     The total pair uncertainty is 8% and the statistical uncertainty is 11.7%. The uncertainty from background choice  
 830     is determined by varying between two background estimations. The first estimation uses a polynomial ( $a + b \cdot x + c \cdot x^2$ )  
 831     to estimate the background, and the second estimation uses a cocktail to estimate the background. The uncertainty is  
 832     about 1.3%. The total uncertainty for the JPsi yield used in the cocktail is approximated to be 15%.

### 833 7.9. Charm Correlation

834 In the charm contributions to the cocktail, we assume correlated contributions(take what PYTHIA gives us).  
 835 But, there are uncorrelated contributions from charm too. To estimate this uncertainty, the given  $c\bar{c} \rightarrow e^-e^+$  sample is  
 836 compared to distributions where the correlation between the electron daughters is broken for  $\phi$ ,  $\eta$ , and  $p_T$ . This is done  
 837 by determining the  $e^{+/-}$  distributions for  $\phi$ ,  $\eta$ , and  $p_T$  and then reassigning the daughters' kinematics by randomly  
 838 selecting the new kinematic properties based on the predetermined distributions. This should break the correlations.  
 839 Shown in Fig. 73 are the  $e^-e^+$  invariant mass distributions and how correlation affects the distribution, where the  
 840 black line is completely correlated, the red line is the decorrelated daughter azimuthal angles, the green line is the  
 841 decorrelated daughter azimuthal angles and  $\eta$ , the blue line is the completely decorrelated daughters ( $\phi$ ,  $\eta$ , and  $p_T$ ).

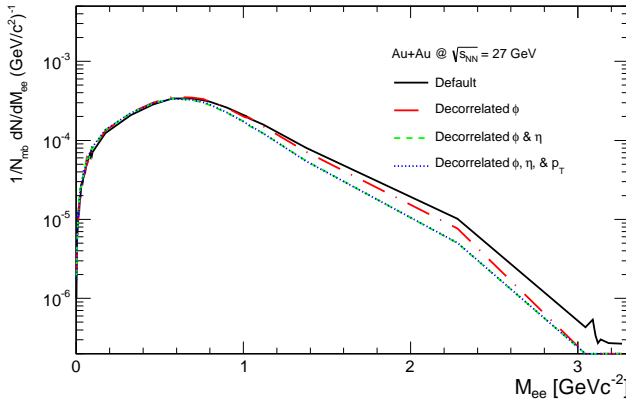


Figure 73. The  $c\bar{c} \rightarrow e^-e^+$  contributions to the cocktail with different configurations to demonstrate how correlation of the daughter electrons affects the invariant mass spectrum. The black line represents the default (and used in Cocktail) configuration. The red dot-dashed line represents the randomization of the daughters'  $\phi$ . The green dashed line represents the randomization of the daughters'  $\phi$  and  $\eta$ . The blue dotted line represents the randomization of the daughters'  $\phi$ ,  $\eta$ , and  $p_T$ .

842 The systematic uncertainty is taken as the relative difference between the default contribution and the completely  
 843 decorrelated contribution with respect to the default contribution. This is shown in Fig. 74. The correlation uncertainty  
 844 is folded into the charm yield uncertainty as a function of invariant mass.

### 845 7.10. STAR to Full Phase Space Acceptance Factor

846 The data excess is converted from the STAR Acceptance ( $p_T^e > 0.2 \text{ GeVc}^{-1}$ ,  $|\eta^e| < 1$ , and  $|Y^{ee}| < 1$ ) to full phase  
 847 space to be able to show our results in a detector independent fashion, and hence, be able to compare our results to  
 848 other theory and detector results. To correct for the STAR acceptance, the same toy  $\gamma^* \rightarrow e^-e^+$  Monte Carlo as used  
 849 in the Pair Efficiency determination in Sec. 5.4 was used. The acceptance correction factor was evaluated by looking  
 850 at the number of pairs as a function of  $M_{ee}$  and  $p_T^{ee}$  and projecting to  $M_{ee}$  before and after implementing the STAR  
 851 acceptance in the toy Monte Carlo and find the ratio between the two distributions. This gave a correction factor  
 852 shown in Fig. 75.

853 While we look at the acceptance factor in 2D, it is actually applied in 1D due to statistics issues at the acceptance  
 854 edges ( $M_{ee}$  &  $p_T^{ee} < 0.5$ ). The systematic uncertainty from applying the 1D correction is determined by comparing  
 855 the toy Monte Carlo correction factor and a correction factor derived from Rapp's many-body calculations ( $\rho$  and  
 856 medium dielectron yields) within the STAR acceptance and full phase space. The 1D correction factors are shown in  
 857 Fig. 76 and the differences used for the systematic uncertainty determination are shown in Fig. 77. A 6% systematic  
 858 uncertainty was used to account for the acceptance correction method.

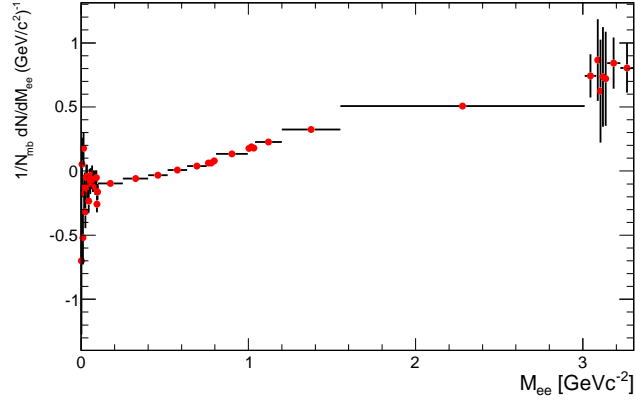


Figure 74. The difference between  $c\bar{c} \rightarrow e^-e^+$  contributions with the default setting and completely decorrelated setting with respect to the default setting. This is the relative systematic uncertainty applied to the  $e^-e^+$  excess.

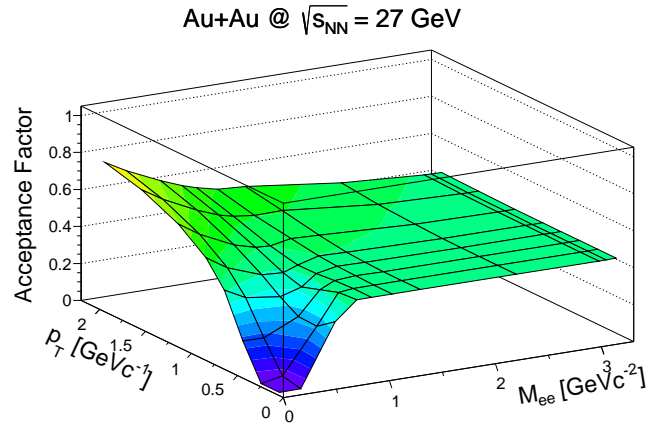


Figure 75. The acceptance correction factor to transform from the STAR acceptance to full phase space as a function of  $M_{ee}$  and  $p_T^{ee}$ . This was derived by using a toy  $\gamma^* \rightarrow e^-e^+$  Monte Carlo.

## 859 8. Final Product

860 The raw spectra is corrected with the pair efficiencies listed in Sec. 5.4. The invariant mass distribution of the  
 861 corrected  $e^-e^+$  yield is shown in Fig. 78 in the top panel along with the total hadronic cocktail and its contributions  
 862 within the STAR acceptance ( $p_T^e > 0.2 \text{ GeVc}^{-1}$ ,  $|\eta_e| < 1$ , and  $|Y_{ee}| < 1$ ). The cocktail has been scaled to match the  
 863 corrected data in the very low mass region,  $0-100 \text{ MeVc}^{-2}$ . This scale factor used was 0.847332. Figure 78 shows the  
 864 data to cocktail ratio.

865 Contributions from  $\rho$  and medium contributions have been provided by Ralf Rapp and his many body effective  
 866 field theory. Contributions are shown with the hadron cocktail and data within the STAR acceptance in Fig. 79. Rapp's  
 867 contributions were scaled by 2 (dy) and 140 ( $dN_{ch}/dy$ ) to convert the contributions to match that of the data as his  
 868 contributions were normalized for rapidity and a  $dN_{ch}/dy = 140$ .

869 The cocktail sans  $\rho$  and medium contributions is subtracted from the data and then the excess is corrected to  
 870 transform from the STAR acceptance to full phase space. The acceptance correction factor is applied as noted in

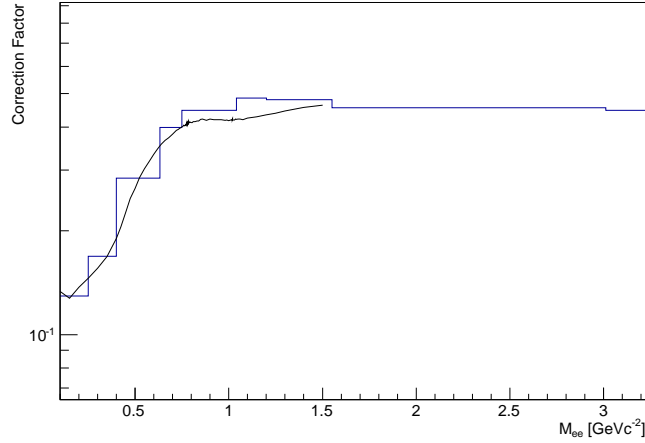


Figure 76. The acceptance correction factor to transform from the STAR acceptance to full phase space as a function of  $M_{ee}$ . The toy Monte Carlo correction factor is represented by the histogram bars while the line represents the correction factor derived from Rapp's calculations.

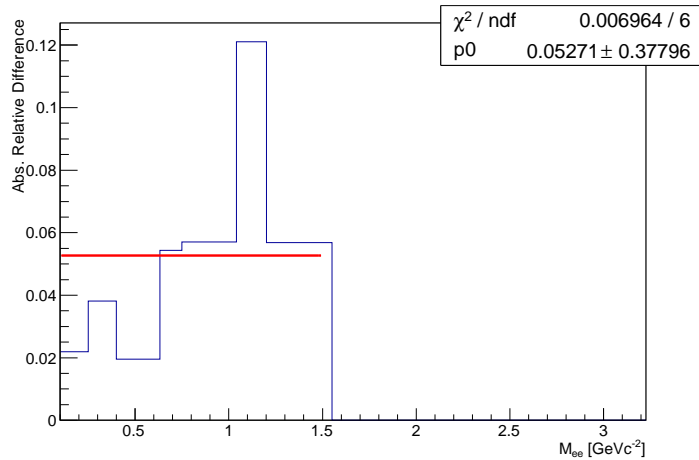


Figure 77. The relative difference between Rapp's and the toy Monte Carlo's correction factor with respect to the toy Monte Carlo's factor. The fit gives a systematic uncertainty  $\sim 5\%$ , but to be conservative, an uncertainty of 6% was assigned.

Sec. 7.10. While the acceptance correction factor is applied to the data, the theory calculations are provided in the full phase space as function of  $M_{ee}$  for comparisons. Comparisons of the acceptance corrected  $e^-e^+$  and theory calculations are shown in Fig. 80.  $dN/dy = 0.5$ ,  $dN_{ch}/dy = 140$ , and a unit conversion was used to scale the excess to match previously published 19GeV(STAR/Bingchu Huang) and NA60 data. The rebinning of the data used the following  $M_{ee}$  ( $\text{GeVc}^{-2}$ ) edges: 0., 0.1, 0.25, 0.4, 0.6332, 0.75, 1.0408, 1.2008, 1.5508, 3.011, and 3.225.

The integrated acceptance corrected excess yield for  $(dN/dy)/(dN_{ch}/dy)$  within the  $M_{ee}$  from 0.4 to 0.75  $\text{GeVc}^{-2}$  is  $5.65083\text{E-}06 \pm 2.07116\text{E-}06 \pm 1.13181\text{e-}06$  (stat,sys). If we separate out the data and cocktail systematic uncertainties (and acceptance 6%), we get  $5.65083\text{E-}06 \pm 2.07116\text{E-}06 \pm 7.17982\text{e-}07 \pm 6.37822\text{e-}07$  (stat, data sys, ck sys) do not forget to add the 6% for acceptance correction. The  $dN_{ch}/dy = 145$  was used for these excess numbers, which is derived from the STAR BES spectra paper draft version 7's AuAu27 yields.

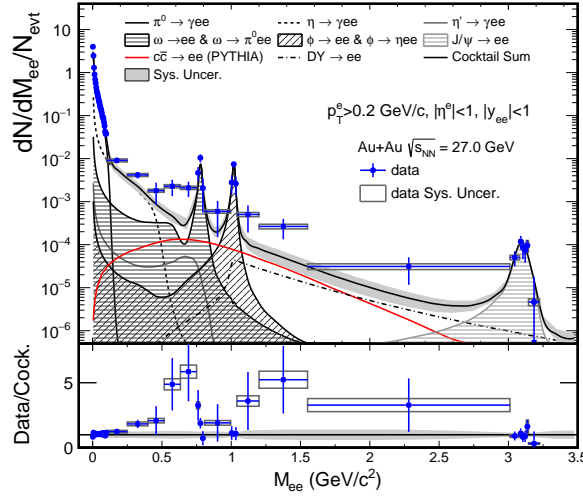


Figure 78. Top panel: The corrected invariant mass yield of  $e^-e^+$ , blue points, compared to the hadronic cocktail without  $\rho$  or medium contributions, lines and shaded fills. The error bars represent the statistical uncertainties and the open boxes represent the systematic uncertainties. Bottom panel: the data over cocktail ratio where the error bars represent the statistical uncertainty and the open boxes represent the systematic uncertainty.

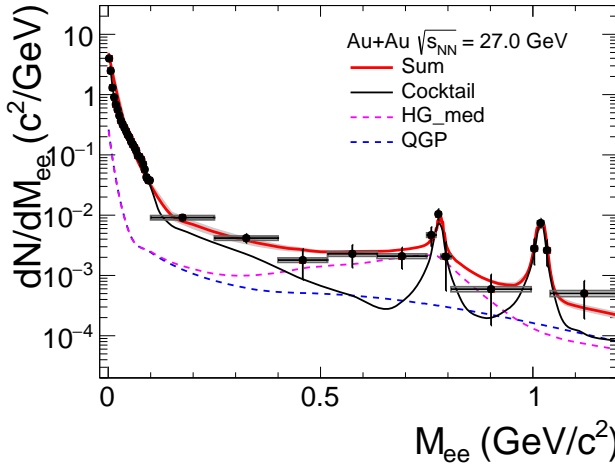


Figure 79. The corrected invariant mass yield of  $e^-e^+$ , black points, compared to the hadronic cocktail without  $\rho$  or medium contributions, solid black line; the  $\rho$  contribution that had a medium broadened spectral function, dashed pink line; the thermal medium contribution, dashed blue line; and the sum of all the contributions, the solid red line. The error bars represent the statistical uncertainties and the open boxes represent the systematic uncertainties. This is all within the STAR acceptance.

### 8.1. Systematic uncertainty propagation

Uncertainties from the cocktail were added directly when combining the different components. E.g.,  $SysRelPi0 * BinContentPi0 + SysRelEta * BinContentEta$

When rebinning the mass,  $M_{ee}$ , axis to do the excess and acceptance corrected excess figures, the relative systematic error was interpolated between the combined bins to find a new relative systematic error. This was done by taking the  $1/N_{\text{events}} * dN/dM$  values listed in Fig. 78 and performing the following operation to rebin the x-axis( $M_{ee}$ ):  $\frac{\sum SysErr_i * dM_i}{\sum data_i * dM_i}$ . The new relative systematic uncertainty was applied to the rebinned  $1/N_{\text{events}} * dN/dM$  data.

When determining the excess(data-cocktail), the error was propagated in quadrature between the data and cocktail uncertainties. Also, assumed 0% statistical uncertainty in the cocktail.

Once the acceptance factor was applied, a flat 6% was added in quadrature to the excess error. This accounts for

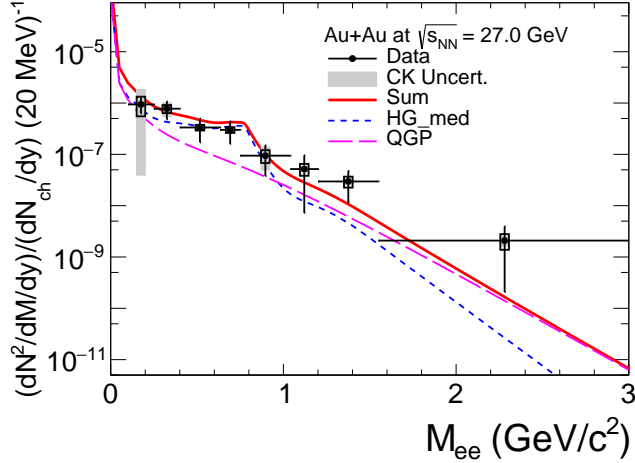


Figure 80. The acceptance corrected excess yield of  $e^-e^+$ , black points, compared to the  $\rho$  contribution that had an in-medium broadened spectral function, dashed blue line; the thermal medium contribution, dashed pink line; and the sum of the contributions, the solid red line. The error bars represent the statistical uncertainties, the open boxes represent the systematic uncertainties, and the gray boxes represent the cocktail uncertainties. Uncertainties from the phase-space acceptance correction has not been included (6%).

891 the systematic uncertainty in the determination of the acceptance correction factor and is discussed in Sec. 7.10.

892 Updated Feb. 2018: The data and cocktail systematic uncertainties have been separated from excess yield calculations to illustrate the different sources of uncertainties and where future measurements may improve the uncertainties.  
 893 Since the data and cocktail uncertainties have been separated, the phase-space acceptance correction uncertainty (6%)  
 894 has not been applied. When integrating across multiple invariant mass bins to determine the integrated yield, the  
 895 systematic uncertainties are added as a direct sum. Total systematic uncertainty as a function of the pair's invariant  
 896 mass has been determined by adding in quadrature the pair efficiency uncertainty, the charge acceptance correction  
 897 uncertainty, and the hadron contamination uncertainty.

### 898 8.2. Agreement with Rapp

900 Note: these studies were done prior to the charm yield updated with a new normalization scheme and updated  
 901 cocktail uncertainties to include branching ratio uncertainties.

902 In the process of requesting a God Parent Committee, a request was made to quantify the *robustness* of Rapp de-  
 903 scribing our excess yields. To quantify the yields, a  $\chi^2$  and p-value was determined between Rapp and the normalized,  
 904 acceptance-corrected excess yields were made. The  $\chi^2$  calculation followed:  $\chi^2 = \sum \frac{(data - Rapp)^2}{data Err^2}$  where the data is sta-  
 905 tistical only. Since Rapp's data did not have points that exactly correspond to bin center value of the excess yields, an  
 906 interpolation between the points were made; *i.e* TGraph::Eval(binCenter). For fitting points between 0.1-1.2  $\text{GeV}/c^2$ ,  
 see Table 8. And then too look at the extended range from the new Rapp calculations, comparisons have been made

Rapp	$\chi^2$	NDF	p-value
old Rapp	7.73635	7	0.3564
Rapp 232 MeV	5.99253	7	0.5406
Rapp 255 MeV	5.52847	7	0.59575

Table 8. Comparing Rapp and Data normalized, acceptance-corrected excess yields between 0.1 - 1.2  $\text{GeV}/c^2$ .

907 between 0.1-1.5  $\text{GeV}/c^2$ , which are shown in Table 9.

### 909 8.3. Lifetime Dependence on $dN_{ch}/dy$

910 Note: these studies were done prior to the charm yield updated with a new normalization scheme.

Rapp	$\chi^2$	NDF	p-value
Rapp 232 MeV	6.528	8	0.5883
Rapp 255 MeV	6.00799	8	0.646337

Table 9. Comparing Rapp and Data normalized, acceptance-corrected excess yields between 0.1 - 1.5 GeV/c<sup>2</sup>.

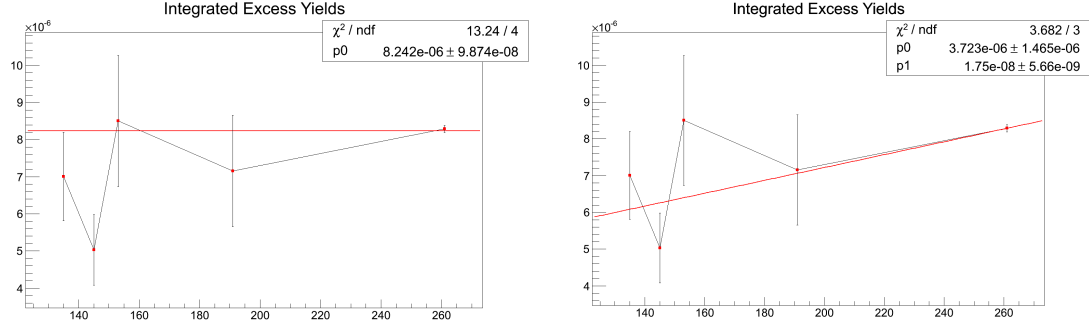


Figure 81. Fits of the normalized, acceptance-corrected excess yields as a function of  $dN_{ch}/dy$  with statistical errors only. (Left) Fit with ROOT's "pol0" so 0<sup>th</sup> order polynomial. (Right) Fit with ROOT's "pol1" so a 1<sup>st</sup> order polynomial.

911 In the process of requesting a God Parent Committee, it was suggested to study/quantify how a line fits the  
 912 lifetime(excess yield) as a function of  $dN_{ch}/dy$ . The fits were performed on excess yields listed in the PRC draft  
 913 table(6/2/2016). Only statistical errors were considered. The fits are shown in Fig. 81 and the results are listed in  
 914 Table 10.

Fit	$\chi^2$	NDF	p-value
0 <sup>th</sup> Order Polynomial	13.2418	4	0.0101529
1 <sup>st</sup> Order Polynomial	3.68162	3	0.297958

Table 10. Line fits of the normalized, acceptance-corrected excess yields as a function of  $dN_{ch}/dy$ .

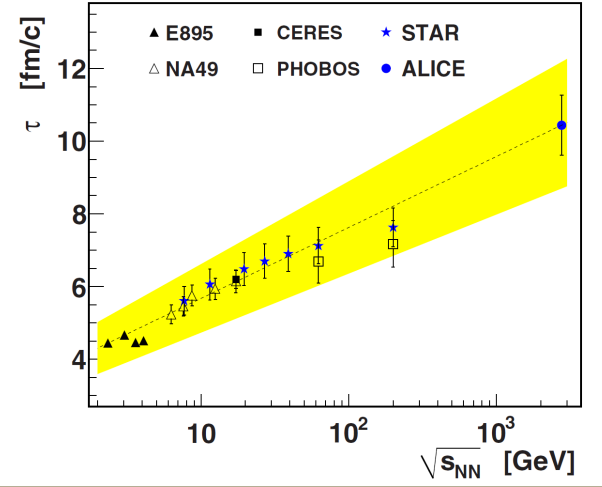


Figure 82. The lifetimes quoted in the STAR BES HBT paper [13].

## 9. HBT

Note: these studies were done prior to the charm yield updated with a new normalization scheme.

During the process of requesting a God Parent Committee, it was suggested to make a comparison of the BES dielectron lifetimes with the HBT lifetimes reported in STAR's BES HBT paper [13]. The HBT lifetimes are shown in Fig. 9.

In order to make comparisons with the HBT measurements, data tables were grabbed from the paper's drupal page, <https://drupal.star.bnl.gov/STAR/files/starpublications/214/data.html>, and plotted it against Rapp's "old" lifetime values in the PRC draft as solid red stars and against scaled normalized by  $dN_{ch}/dy$ , acceptance-corrected excess yields as solid blue stars in Fig. 9. The Rapp lifetimes are  $6.8 \pm 1.0$ ,  $7.7 \pm 1.5$ ,  $8 \pm 1.6$ ,  $8.2 \pm 1.64$ ,  $9.2 \pm 1.84$ ,  $10.5 \pm 2.1$  for 17.3, 19.6, 27, 39, 62.4, and 200 GeV, respectively. Note that 17.3 isn't really STAR, but NA60, and the errors for 27, 39, and 62.4 GeV have been provided by me at 20%(other energies looked like 20%). The excess yields has been scaled by the same scale used to match the right and left axes in our PRC+PRL drafts; the factor:  $y * \frac{20.5 - 3.5}{(1.925E-5) - (1.75E-6)}$ .

Now, some differences between the HBT lifetimes and Rapp's lifetimes. Rapp's lifetimes are indicative of the emission of the dielectrons ( $\rho$  and QGP) being produced over the entire collision lifetime, while HBT is a measurement of kinetic-freeze out and the shape of the fireball. HBT is for 0-5% centrality, different Vz ranges, and different event plane corrections used for 19.6, 27, and 39 GeV. Also, the HBT lifetimes neglect non-zero transverse flow and chemical potential for pions...it could underestimate lifetimes up to 25% [14]. The HBT lifetimes were extracted with the following equation:

$$R_{Long} = \tau \sqrt{\frac{T}{m_T} \frac{K_2(m_T/T)}{K_1(m_T/T)}} \quad (70)$$

where T is the kinetic freeze-out temperature at 0.12 GeV, K is a modified Bessel function,  $m_T$  is the transverse mass of the pions, and  $\tau$  is the lifetime.

To extend this to other centralities and perhaps get a better feel how the lifetime for minimum-bias collisions would change as a function of energy, these fits have been continued to include the other  $R_{Long}$  measurements given in Fig. 8 of [13]. The extracted lifetimes may be found in Fig. 9. To check that the lifetimes from the fit are accurate, comparisons between the 19.6, 27, 39, 62.4, and 200 GeV 0-5% drupal page and fit values were made. Drupal page: 6.485, 6.699, 6.904, 7.125, and 7.628 fm/c vs. 6.48466, 6.69883, 6.90421, 7.12468, and 7.62586 fm/c. Almost all lifetimes are within rounding except for 200 GeV, which is close enough for qualitative comparisons. Also, since the same kinetic freeze-out temperature has been used for each energy and centrality, it may make sense to use STAR's

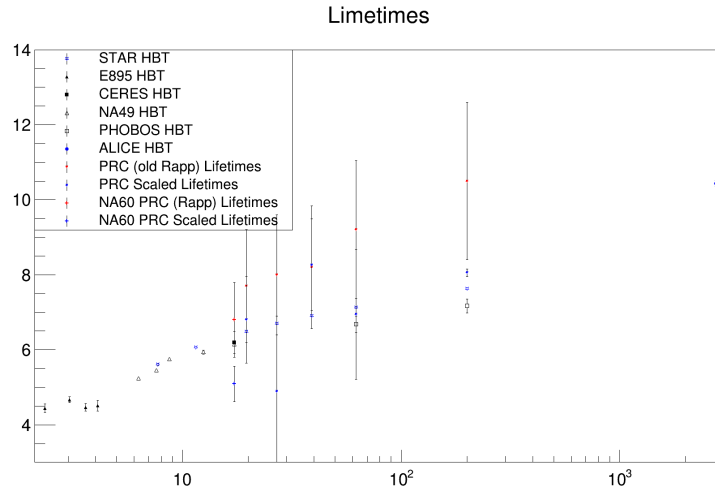


Figure 83. The lifetimes quoted in the STAR BES HBT paper [13] from the drupal page, Rapp's lifetimes, and the scaled normalized, acceptance-corrected excess yields.

943 spectra papers to fix that value. *E.g.* 39 GeV at 60-70% centrality have a freeze-out temperate of 0.142 GeV and gives  
 944 a lifetime of 3.063 fm/c, which is a drop from the value shown in Fig. 9.

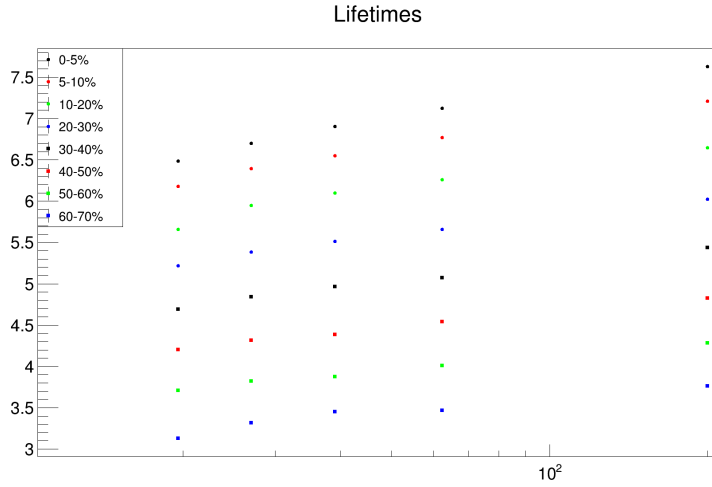


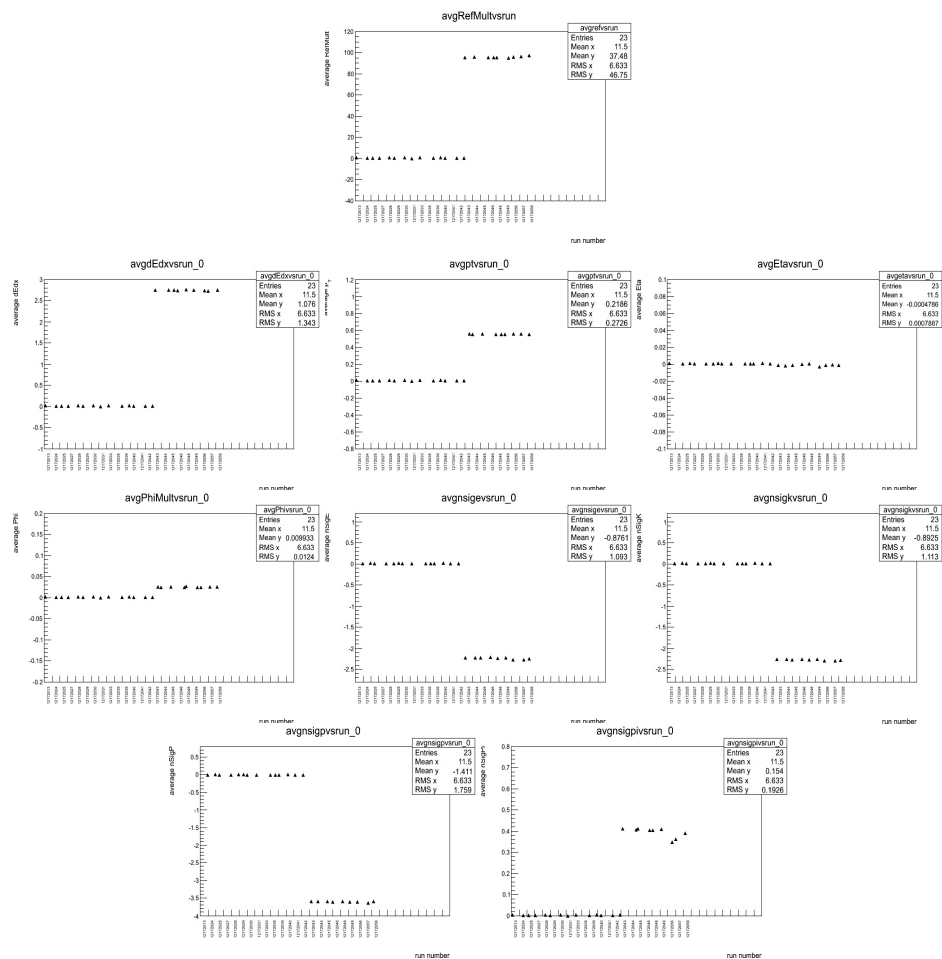
Figure 84. Extracted lifetimes from the  $R_{Long}$  Fig.8 in [13].

945 **Appendix A. Run-by-run QA Averages**

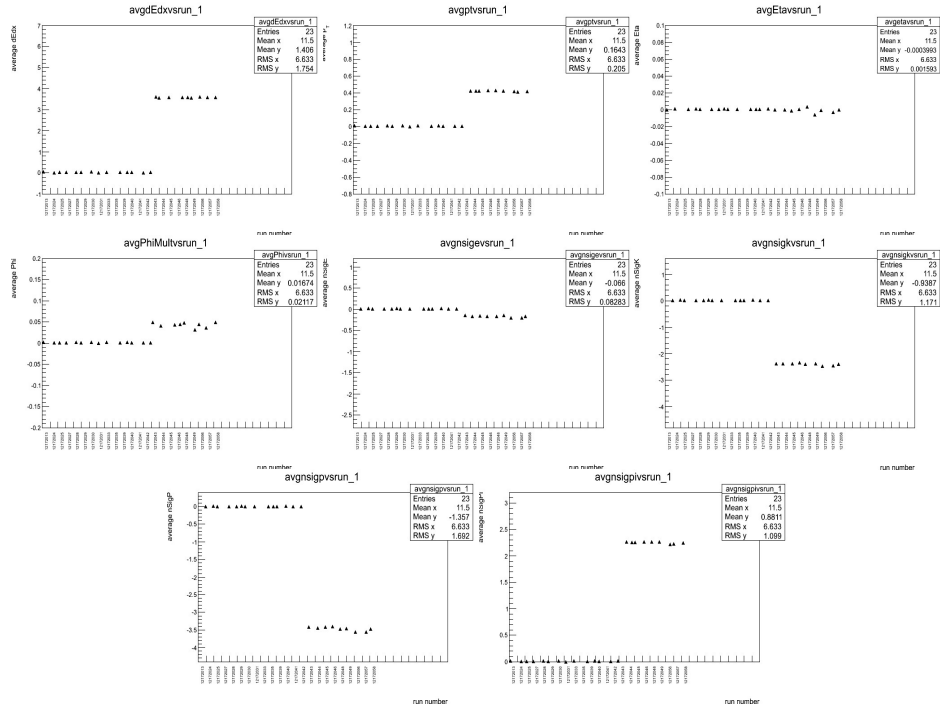
## AuAu 27-Day# : 172

< Previous > Next

After cuts of  $|Vz| < 70\text{cm}$ ,  $r < 2\text{cm}$ ,  $\text{nHitsFit} > 14$ ,  $\text{nHitsPoss} > 0$ ,  $\text{nHitsFit}/\text{nHitsPoss} > .52$ ,  $\text{nHitsdEdx} > 14$ ,  $\beta > 0$ ,  $|\text{yLocal}| < 1.8$  :



After cutting an ellipse with the equation (invBeta - .999767)^2/(1.01741)^2 + (nSigmaEl + .127321)^2/(0.0180772)^2 <=1



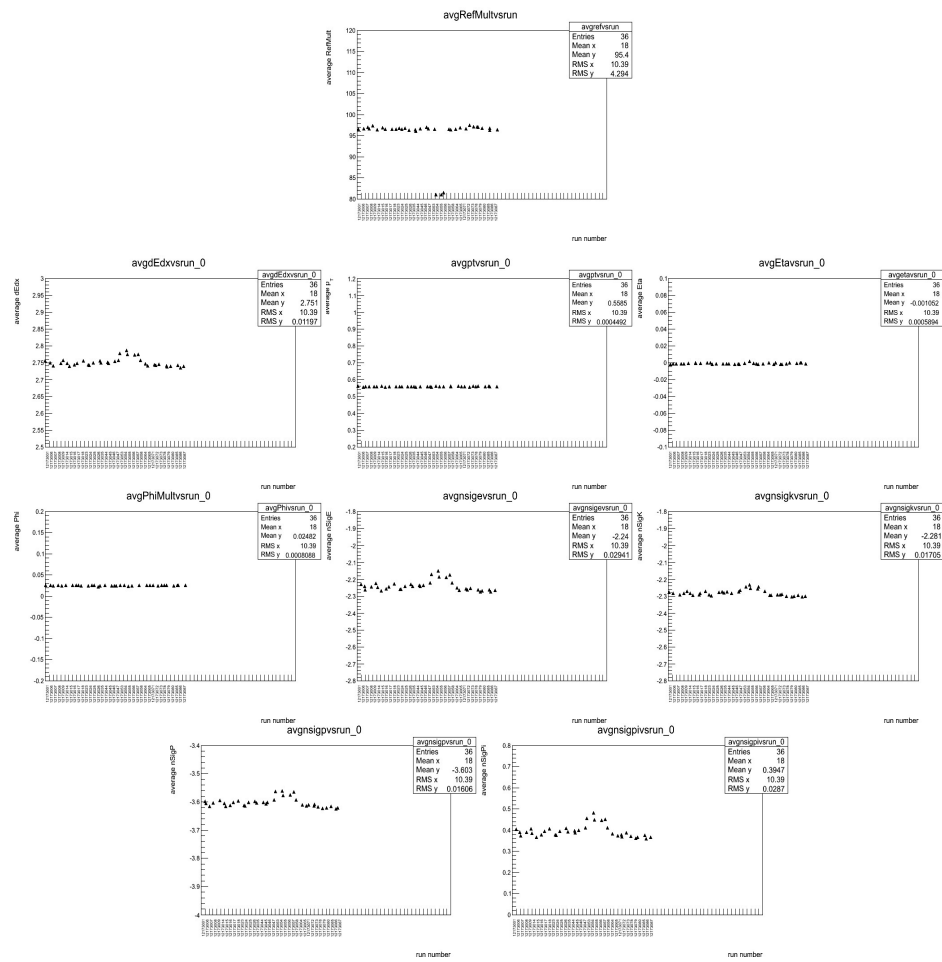
[Follow me back to Day 172.](#)

[< Previous](#) [Next >](#)

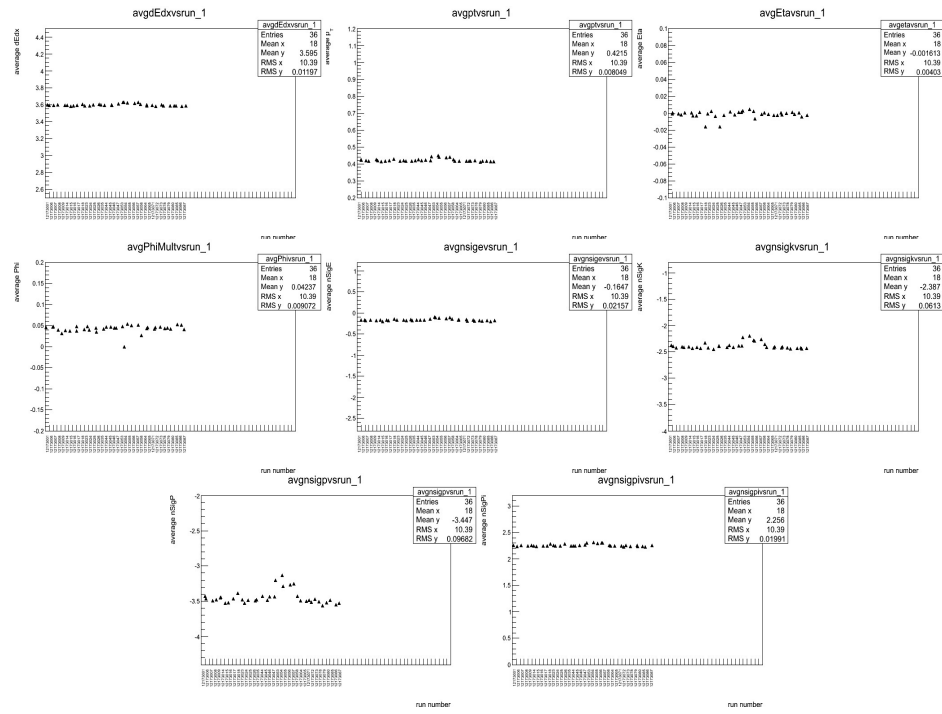
## AuAu 27-Day#: 173

[< Previous](#) [Next](#)

After cuts of  $|Vz| < 70\text{cm}$ ,  $r < 2\text{cm}$ ,  $n\text{HitsFit} > 14$ ,  $n\text{HitsPoss} > 0$ ,  $n\text{HitsFit}/n\text{HitsPoss} > .52$ ,  $n\text{HitsdEdx} > 14$ ,  $\beta > 0$ ,  $|y_{\text{Local}}| < 1.8$ :



After cutting an ellipse with the equation (invBeta - .999767)^2/(1.01741)^2 + (nSigmaEl + .127321)^2/(0.0180772)^2 <=1



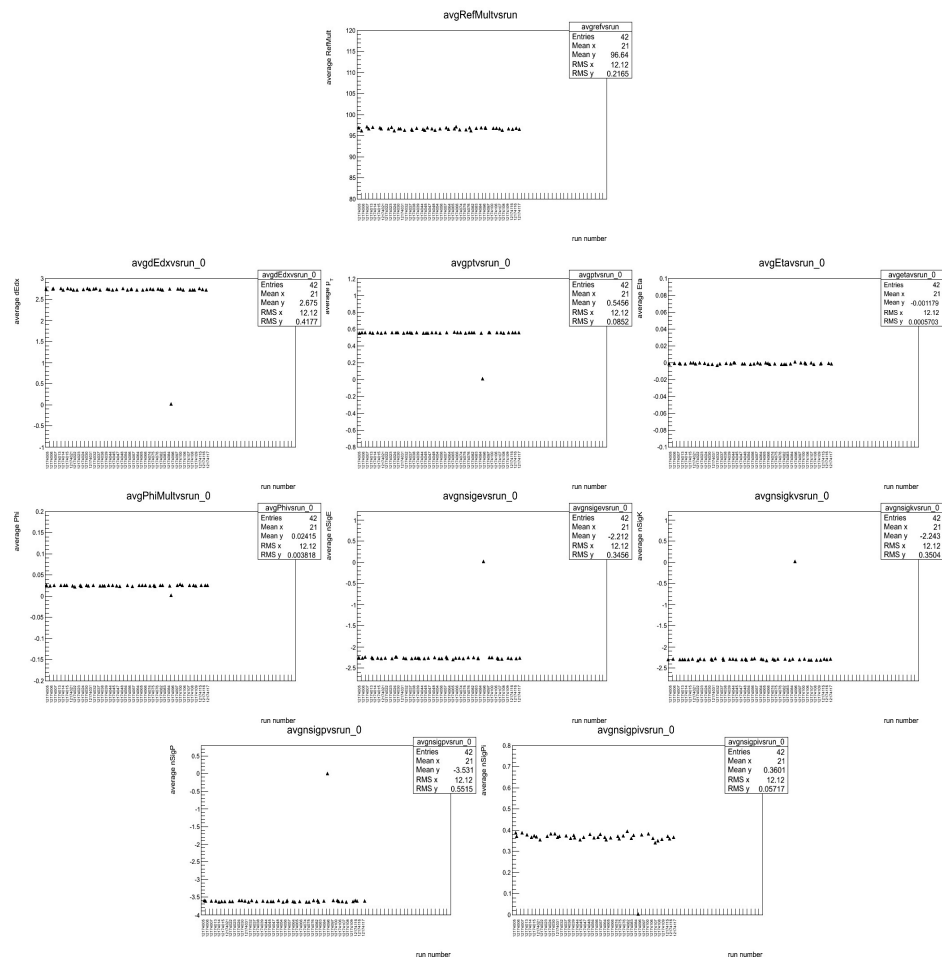
[Follow me back to Day 173.](#)

[< Previous](#) [Next >](#)

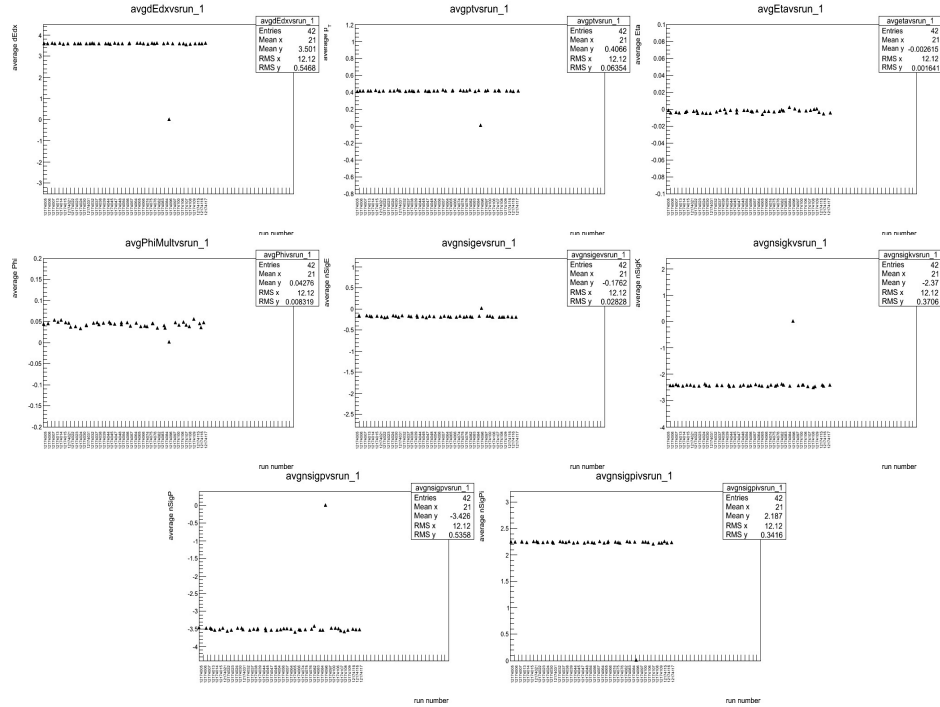
## AuAu 27-Day#: 174

[< Previous](#) [Next](#)

After cuts of  $|Vz| < 70\text{cm}$ ,  $r < 2\text{cm}$ ,  $n\text{HitsFit} > 14$ ,  $n\text{HitsPoss} > 0$ ,  $n\text{HitsFit}/n\text{HitsPoss} > .52$ ,  $n\text{HitsdEdx} > 14$ ,  $\beta > 0$ ,  $|y_{\text{Local}}| < 1.8$ :



After cutting an ellipse with the equation (invBeta - .999767)^2/(1.01741)^2 + (nSigmaEl + .127321)^2/(0.0180772)^2 <=1



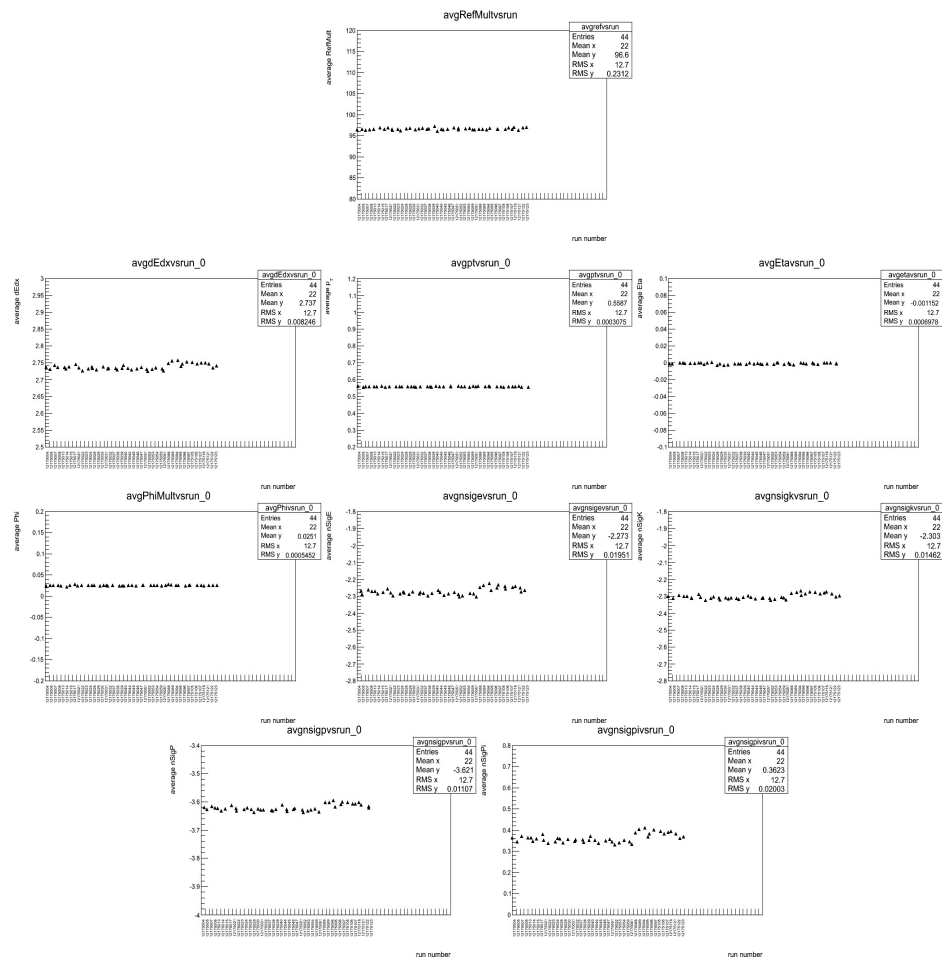
[Follow me back to Day 174.](#)

[< Previous](#) [Next >](#)

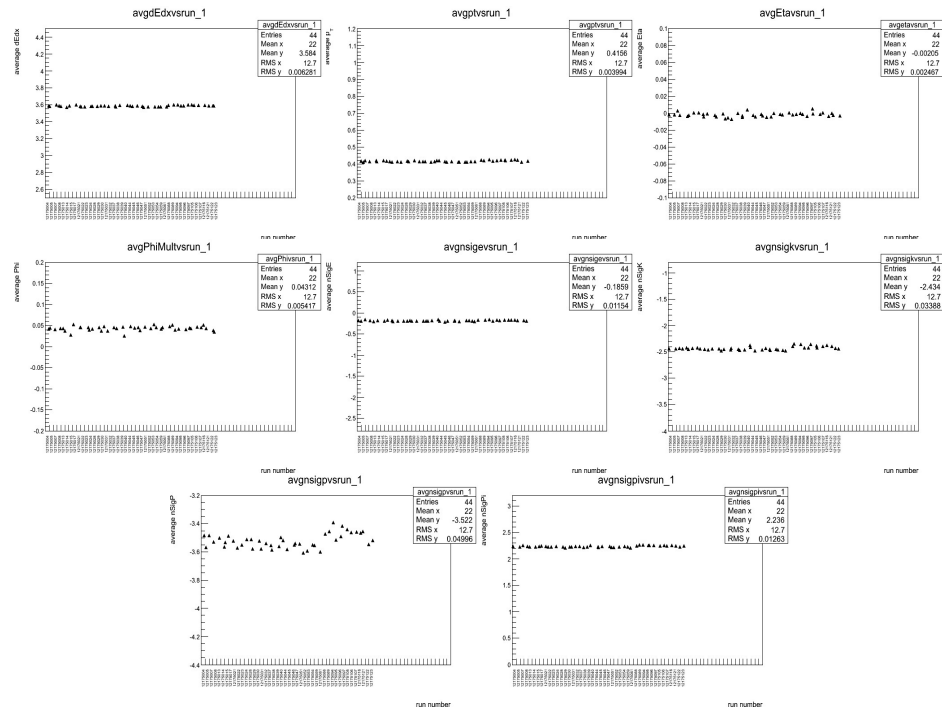
## AuAu 27-Day#: 175

[< Previous](#) [Next](#)

After cuts of  $|Vz| < 70\text{cm}$ ,  $r < 2\text{cm}$ ,  $n\text{HitsFit} > 14$ ,  $n\text{HitsPoss} > 0$ ,  $n\text{HitsFit}/n\text{HitsPoss} > .52$ ,  $n\text{HitsdEdx} > 14$ ,  $\beta > 0$ ,  $|y_{\text{Local}}| < 1.8$ :



After cutting an ellipse with the equation (invBeta - .999767)^2/(1.01741)^2 + (nSigmaEl + .127321)^2/(0.0180772)^2 <=1



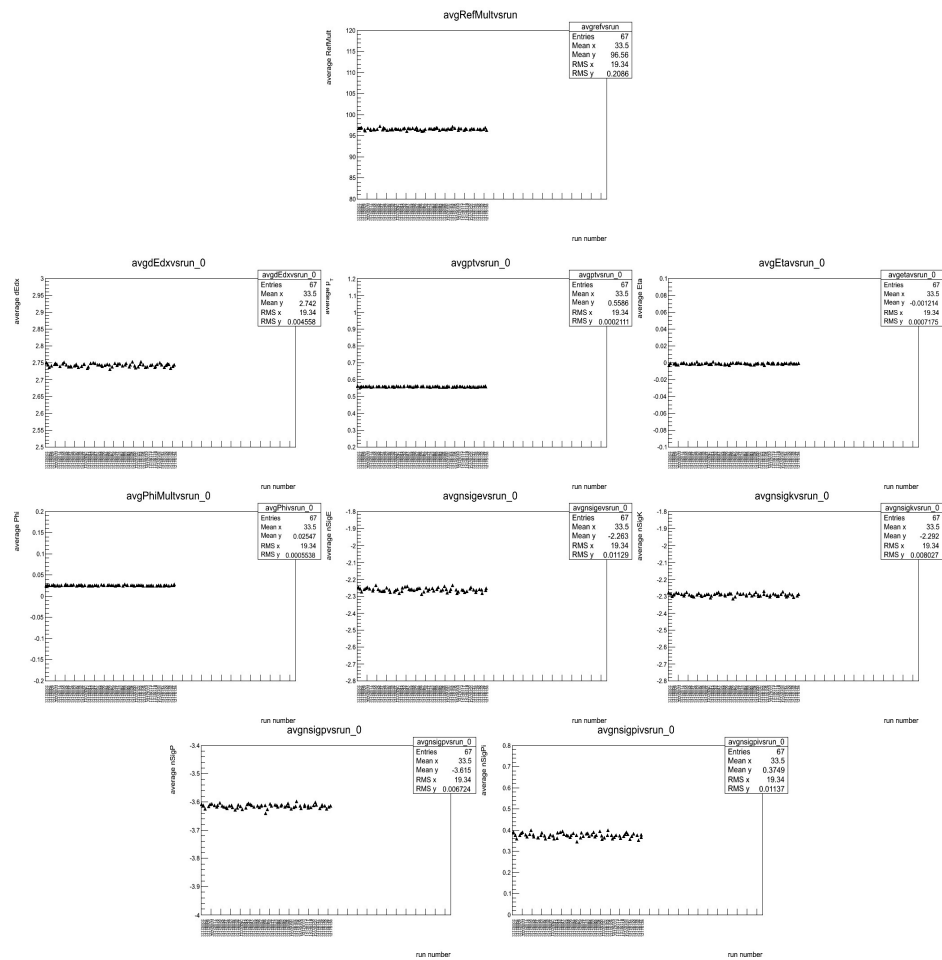
[Follow me back to Day 175.](#)

[< Previous](#) [Next >](#)

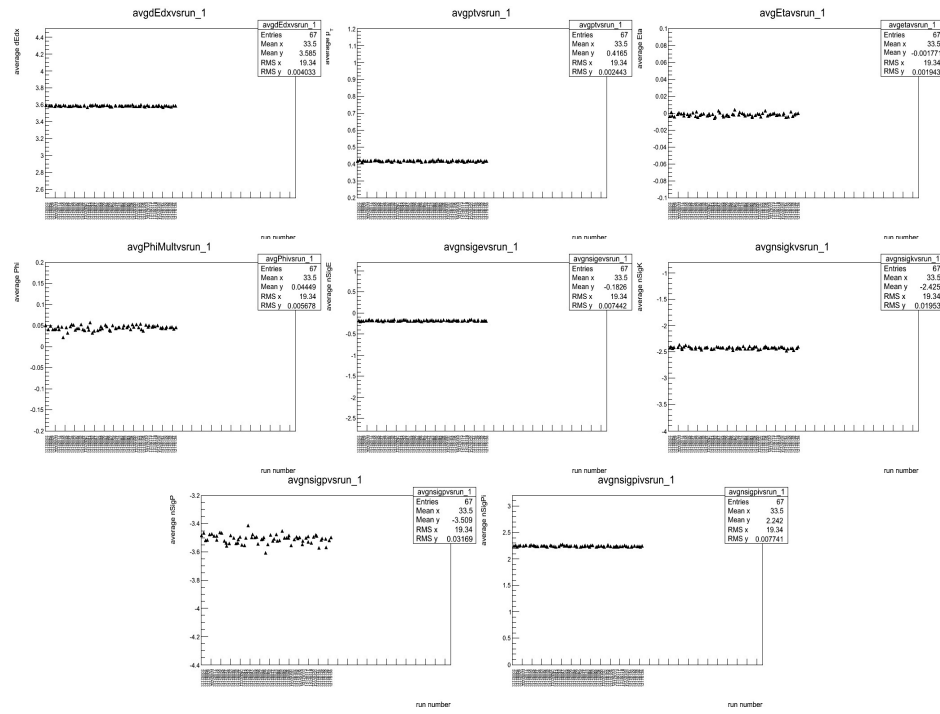
## AuAu 27-Day#: 176

[< Previous](#) [Next](#)

After cuts of  $|Vz| < 70\text{cm}$ ,  $r < 2\text{cm}$ ,  $\text{nHitsFit} > 14$ ,  $\text{nHitsPoss} > 0$ ,  $\text{nHitsFit}/\text{nHitsPoss} > .52$ ,  $\text{nHitsdEdx} > 14$ ,  $\beta > 0$ ,  $|\text{yLocal}| < 1.8$ :



After cutting an ellipse with the equation (invBeta - .999767)^2/(1.01741)^2 + (nSigmaEl + .127321)^2/(0.0180772)^2 <=1



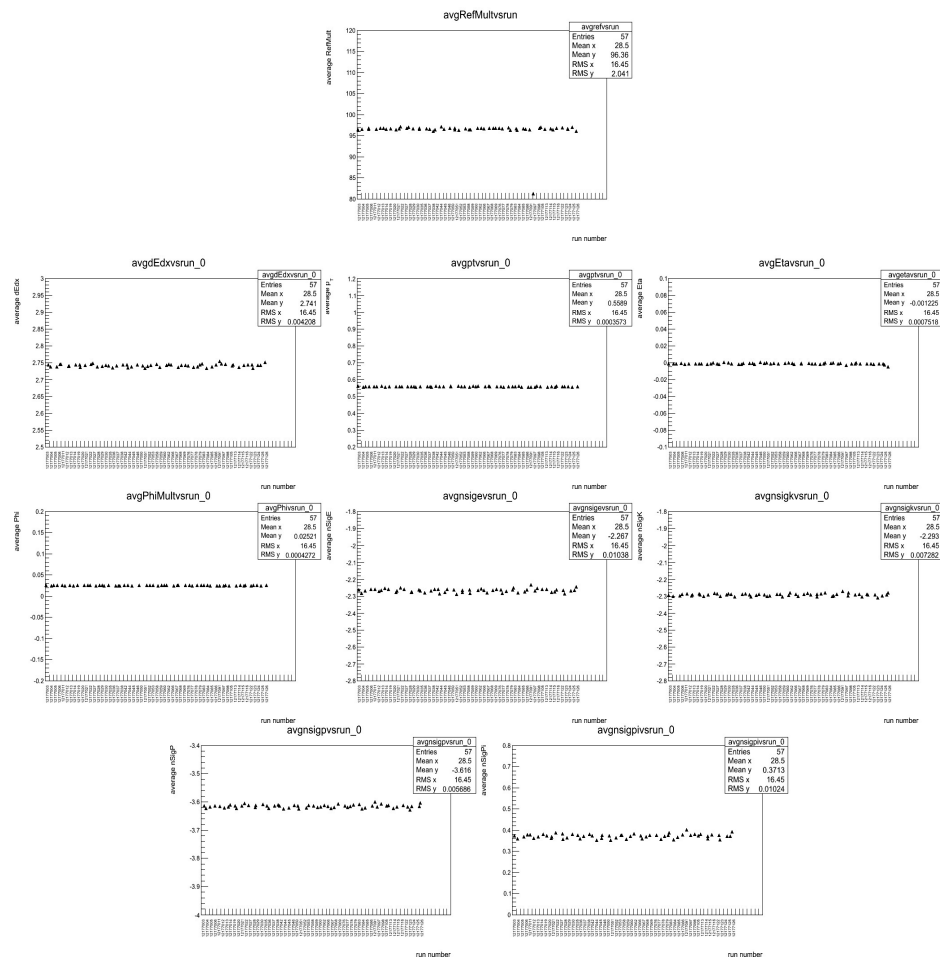
[Follow me back to Day 176.](#)

[< Previous](#) [Next >](#)

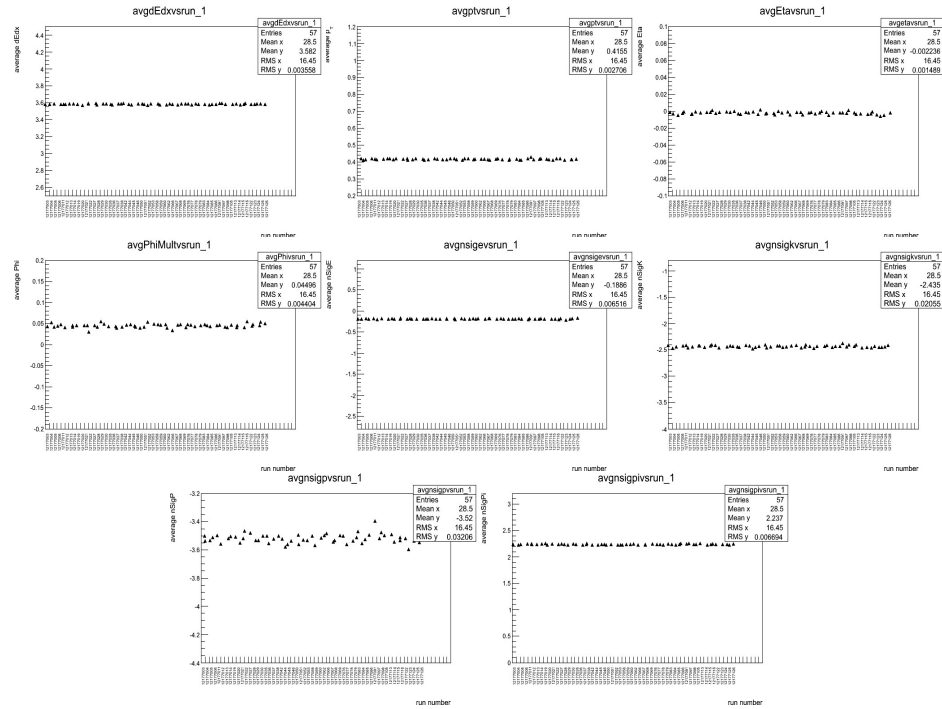
## AuAu 27-Day#: 177

[< Previous](#) [Next](#)

After cuts of  $|Vz| < 70\text{cm}$ ,  $r < 2\text{cm}$ ,  $\text{nHitsFit} > 14$ ,  $\text{nHitsPoss} > 0$ ,  $\text{nHitsFit}/\text{nHitsPoss} > .52$ ,  $\text{nHitsdEdx} > 14$ ,  $\beta > 0$ ,  $|\text{yLocal}| < 1.8$ :



After cutting an ellipse with the equation (invBeta - .999767)^2/(1.01741)^2 + (nSigmaEl + .127321)^2/(0.0180772)^2 <=1



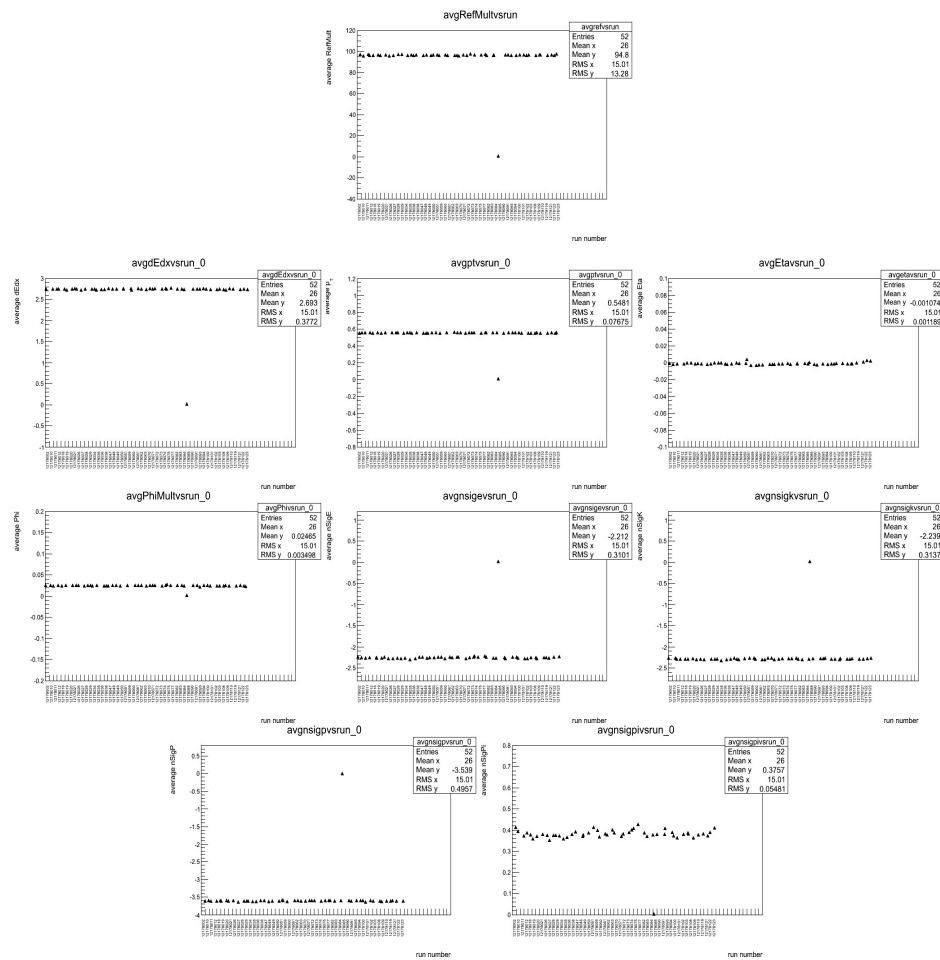
[Follow me back to Day 177.](#)

[< Previous](#) [Next >](#)

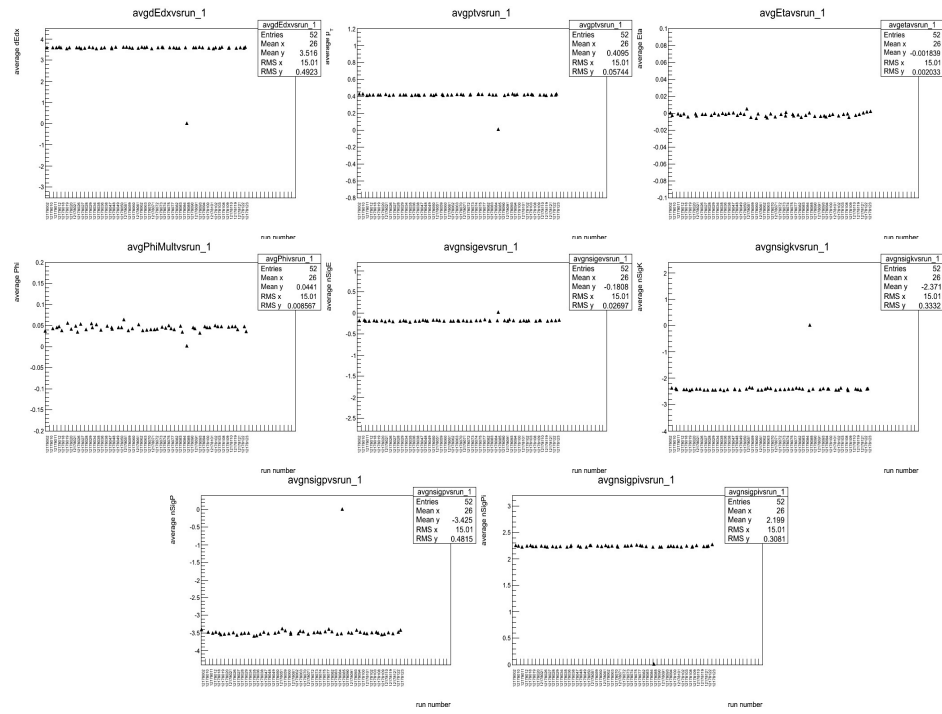
## AuAu 27-Day#: 178

[< Previous](#) [Next](#)

After cuts of  $|Vz| < 70\text{cm}$ ,  $r < 2\text{cm}$ ,  $n\text{HitsFit} > 14$ ,  $n\text{HitsPoss} > 0$ ,  $n\text{HitsFit}/n\text{HitsPoss} > .52$ ,  $n\text{HitsdEdx} > 14$ ,  $\beta > 0$ ,  $|y_{\text{Local}}| < 1.8$ :



After cutting an ellipse with the equation (invBeta - .999767)^2/(1.01741)^2 + (nSigmaEl + .127321)^2/(0.0180772)^2 <=1



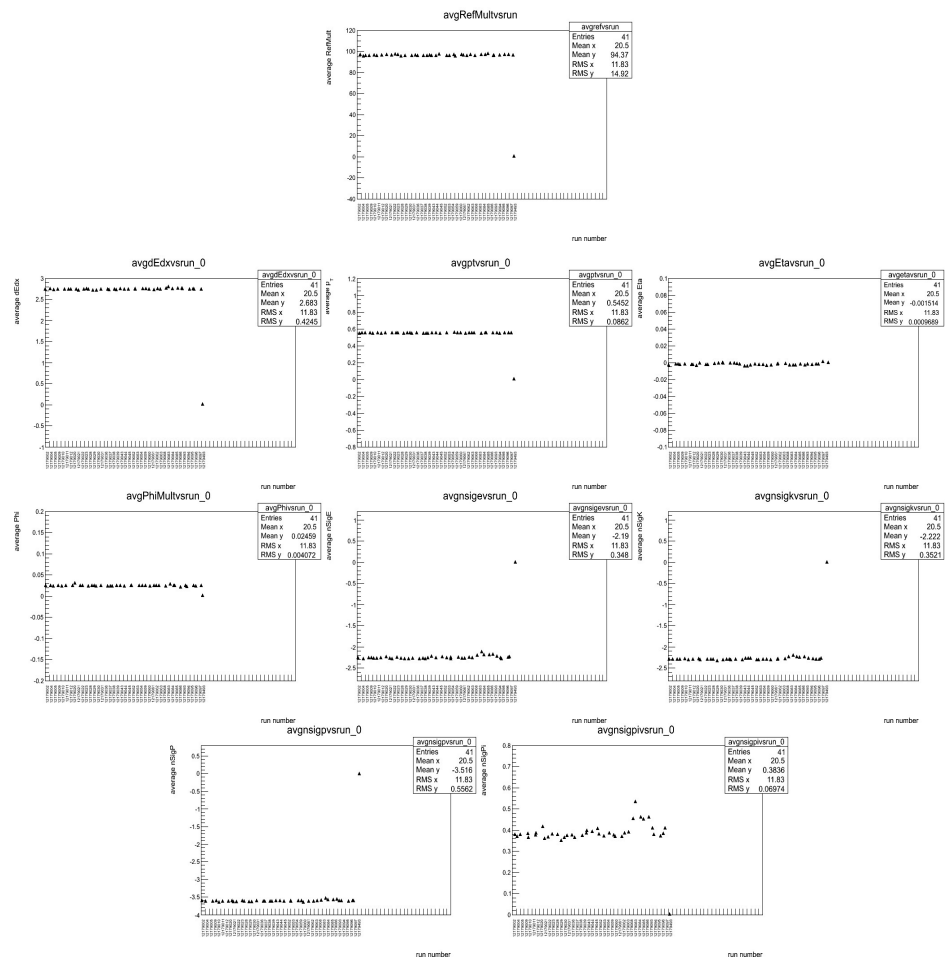
[Follow me back to Day 178.](#)

[< Previous](#) [Next >](#)

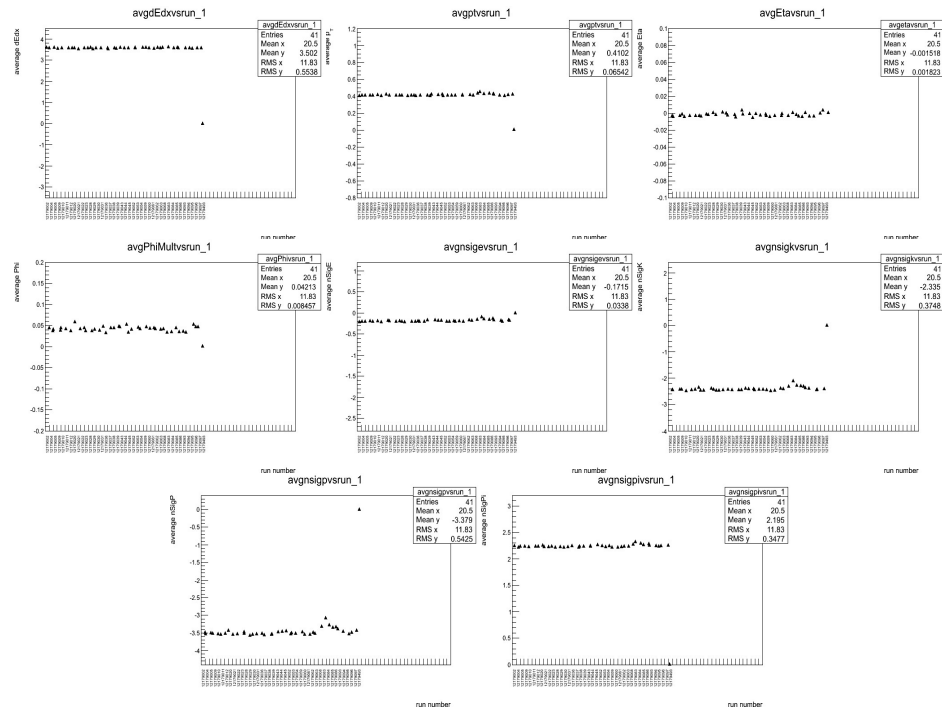
## AuAu 27-Day#: 179

[< Previous](#) [Next](#)

After cuts of  $|Vz| < 70\text{cm}$ ,  $r < 2\text{cm}$ ,  $n\text{HitsFit} > 14$ ,  $n\text{HitsPoss} > 0$ ,  $n\text{HitsFit}/n\text{HitsPoss} > .52$ ,  $n\text{HitsdEdx} > 14$ ,  $\beta > 0$ ,  $|y_{\text{Local}}| < 1.8$ :



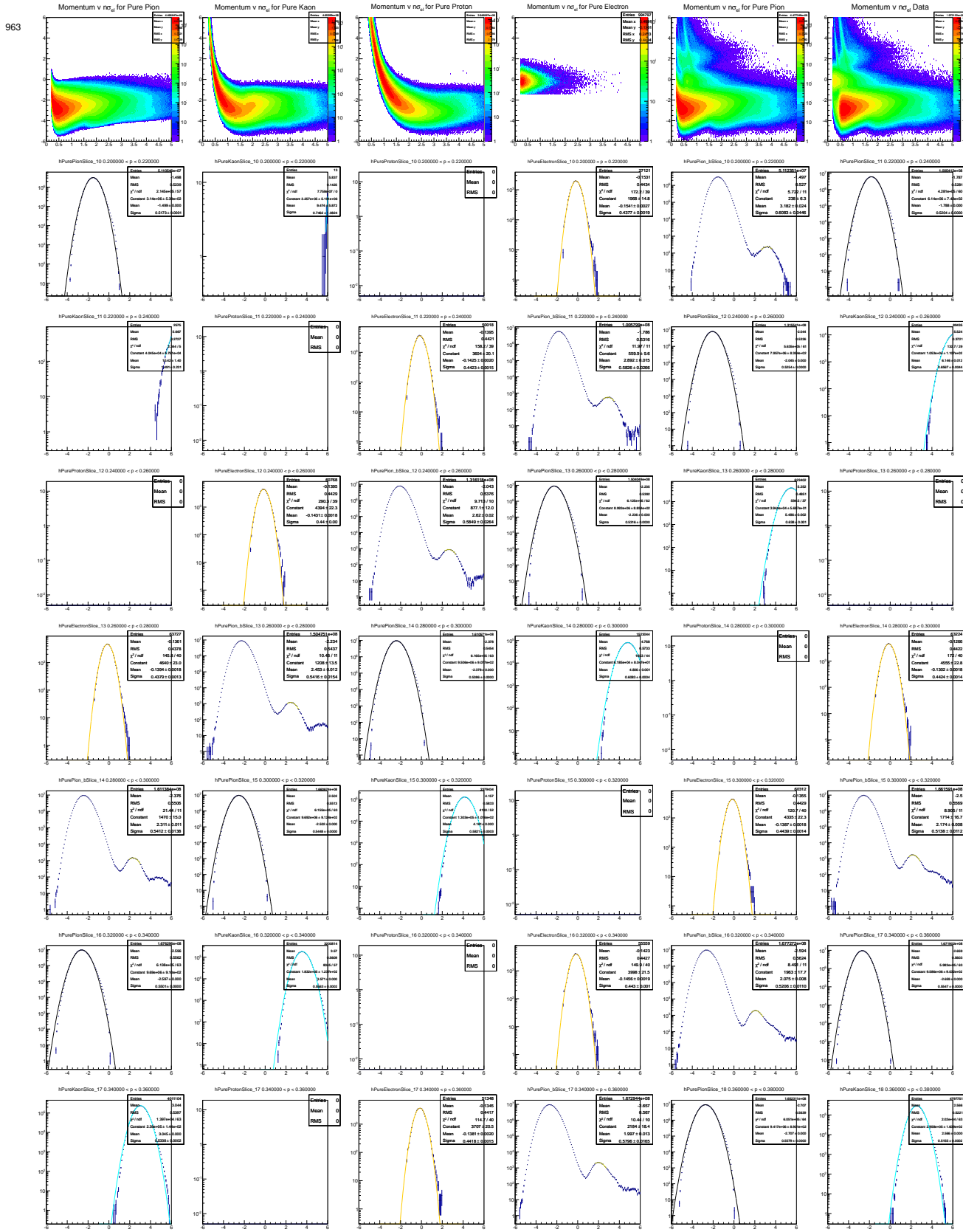
After cutting an ellipse with the equation (invBeta - .999767)^2/(1.01741)^2 + (nSigmaEl + .127321)^2/(0.0180772)^2 <=1

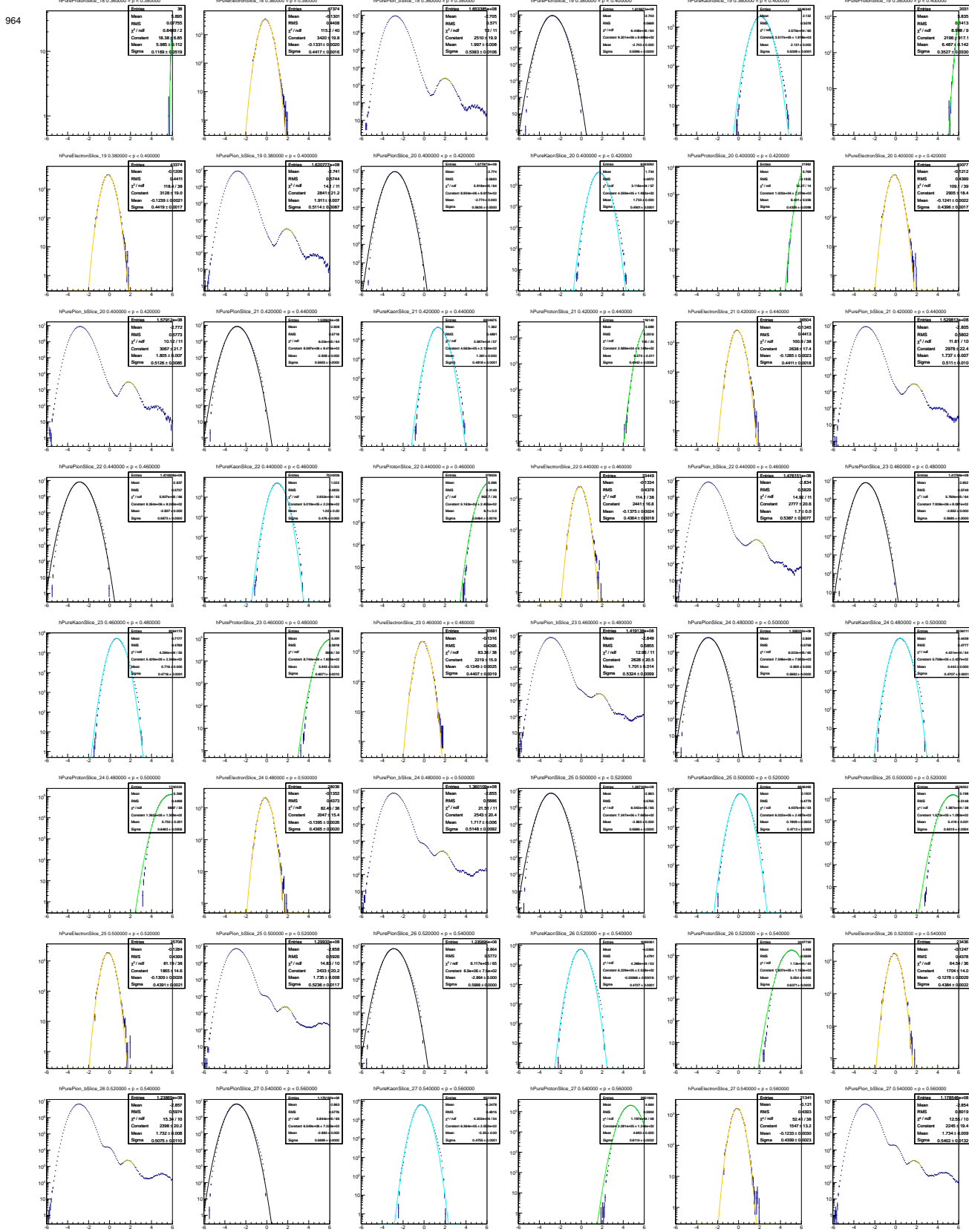


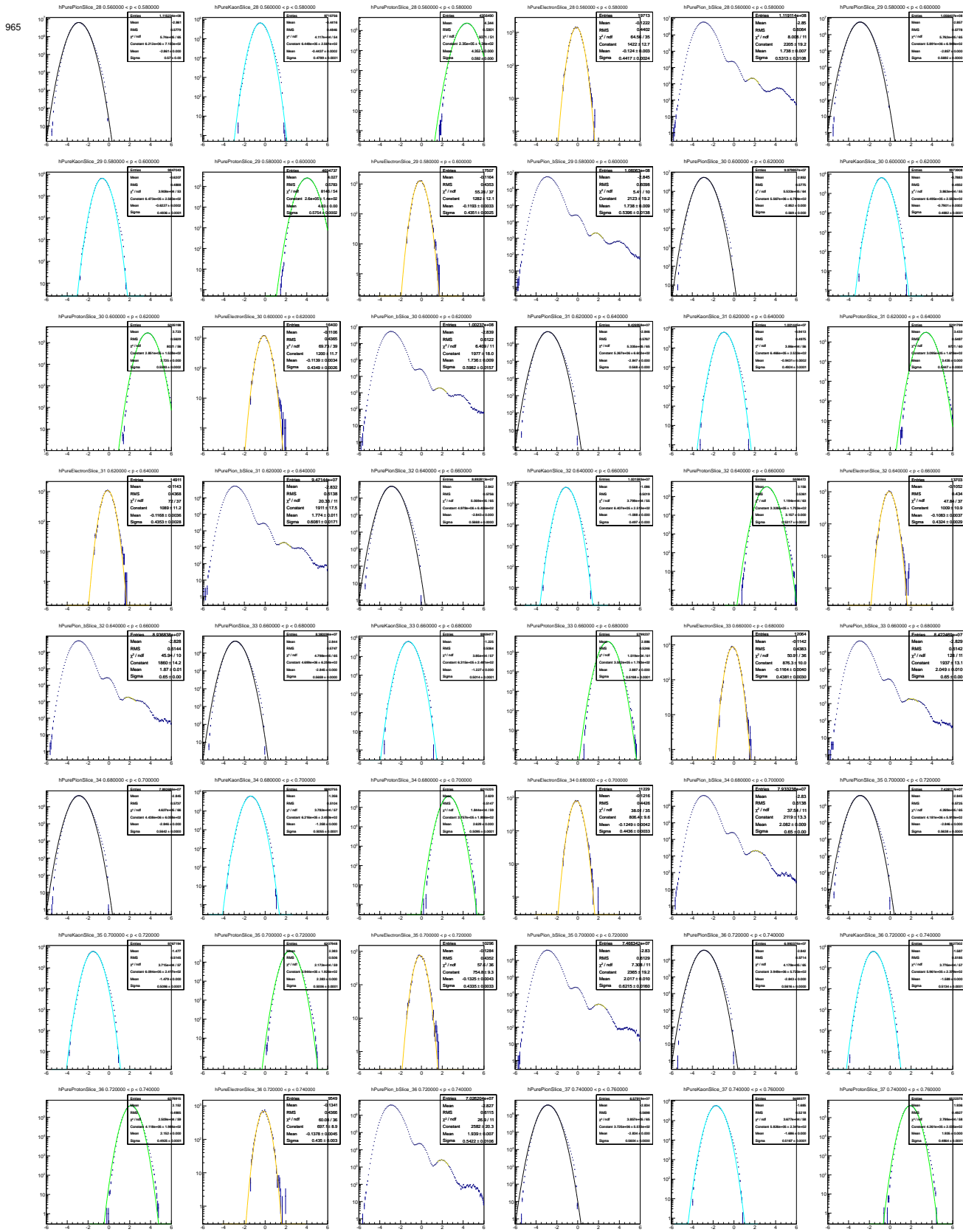
[Follow me back to Day 179.](#)

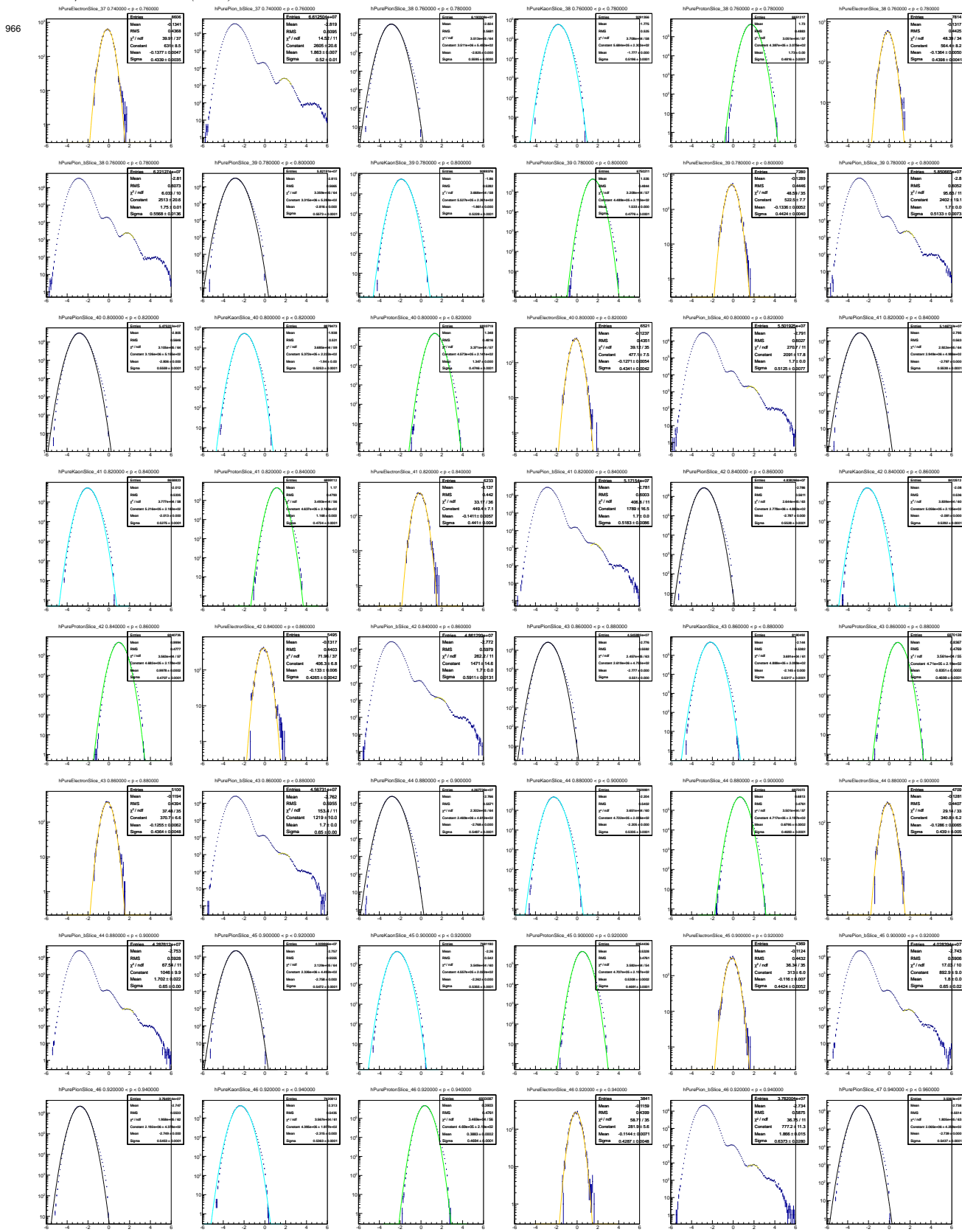
[< Previous](#) [Next >](#)

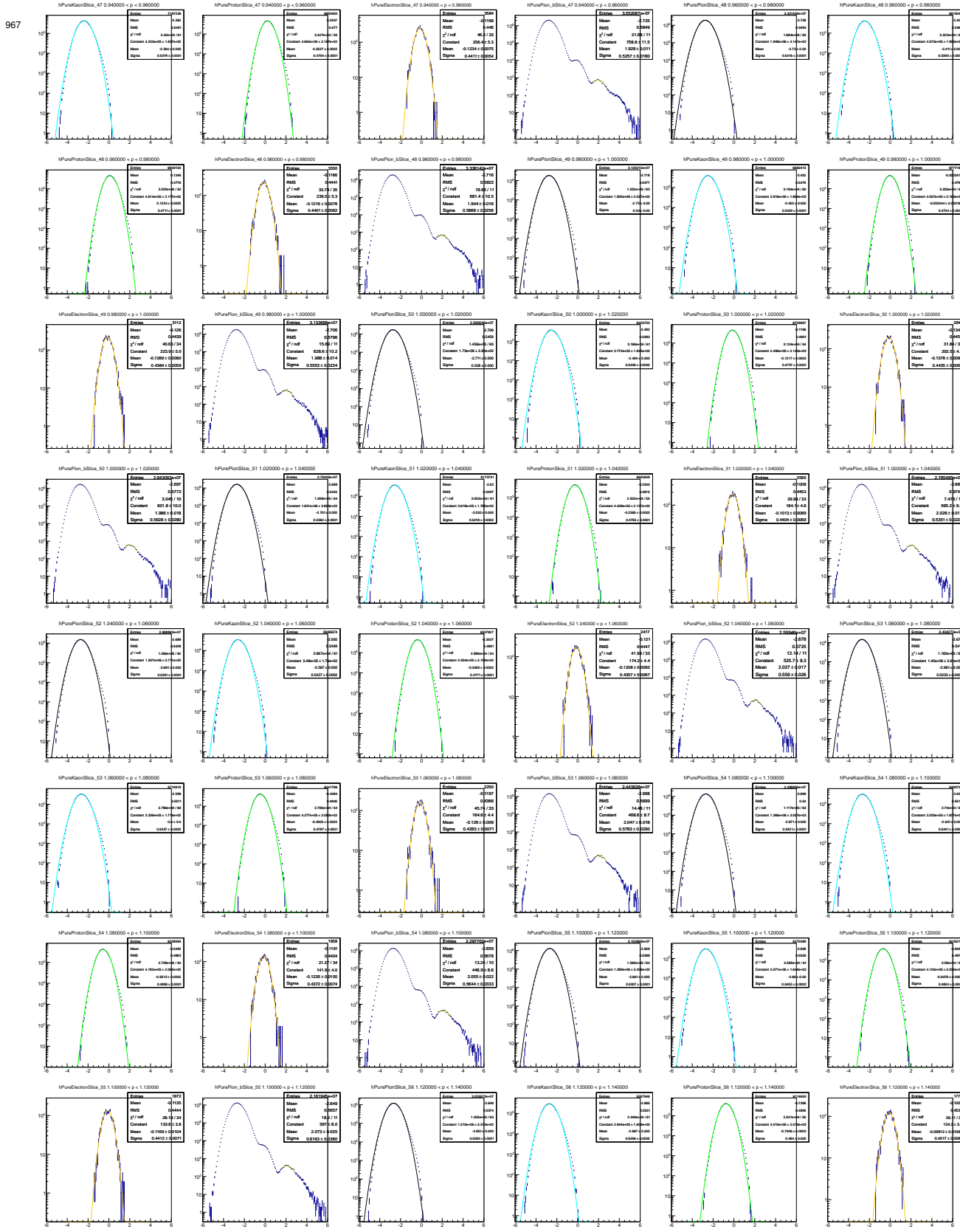
962 **Appendix B. Pure Sample Figures**

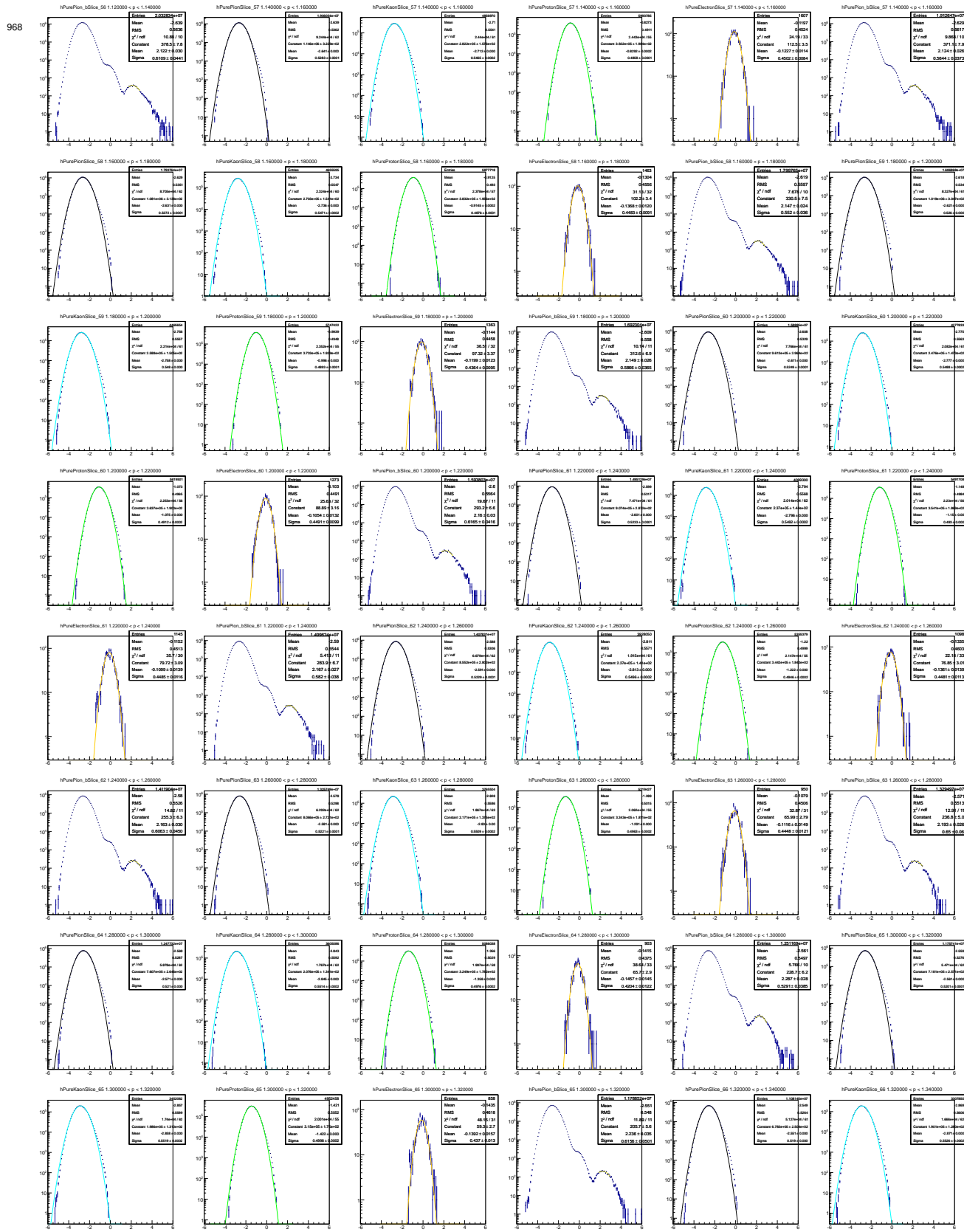


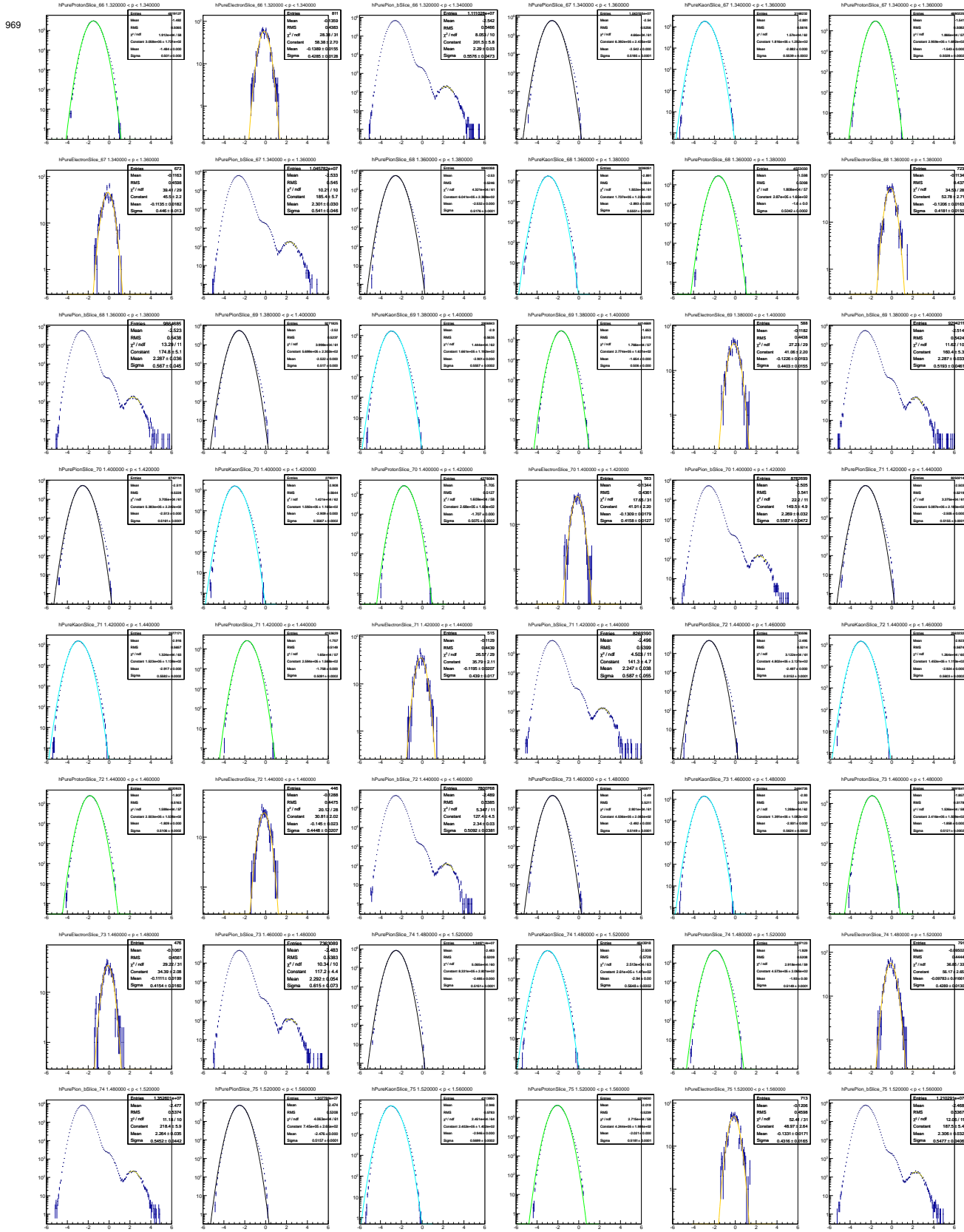


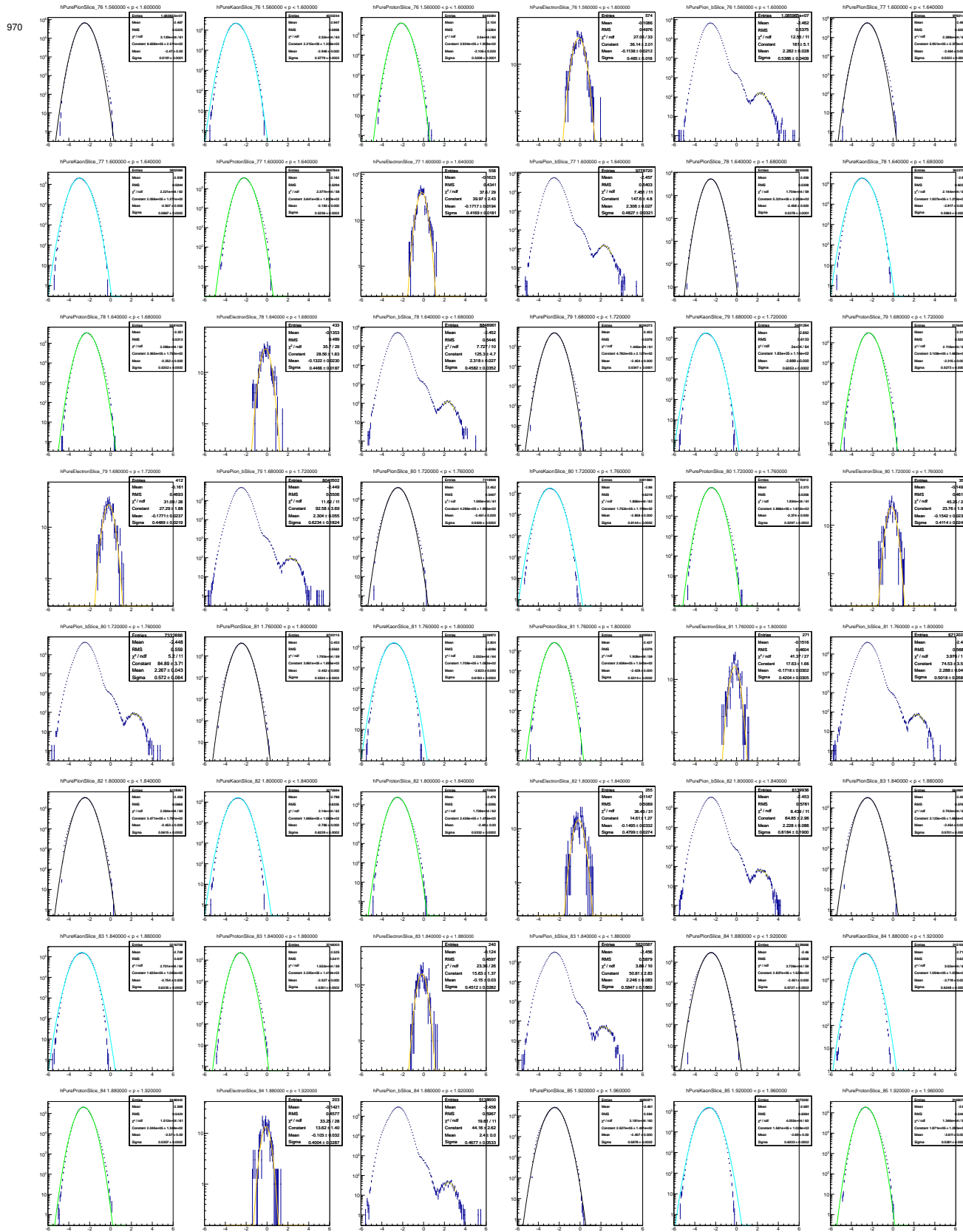


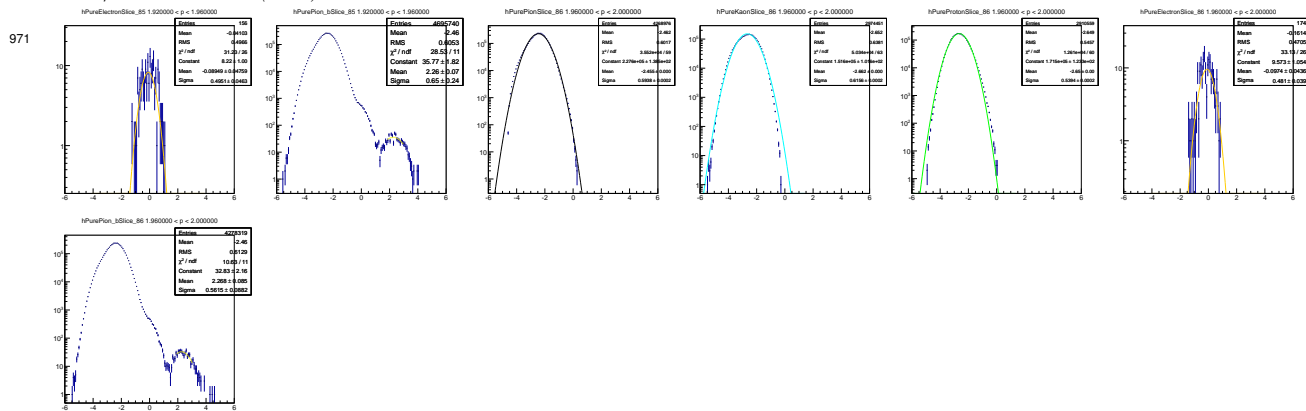




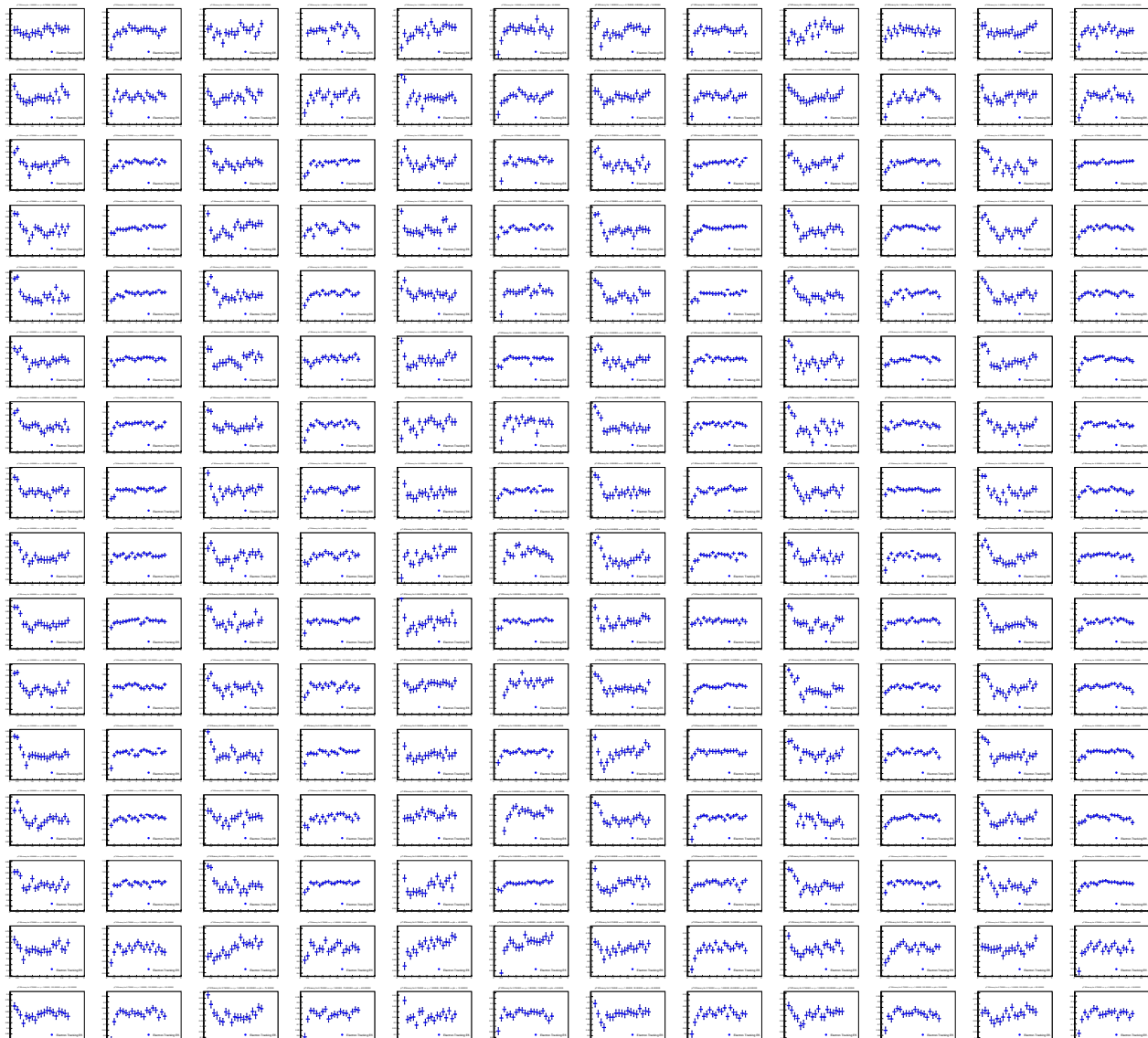




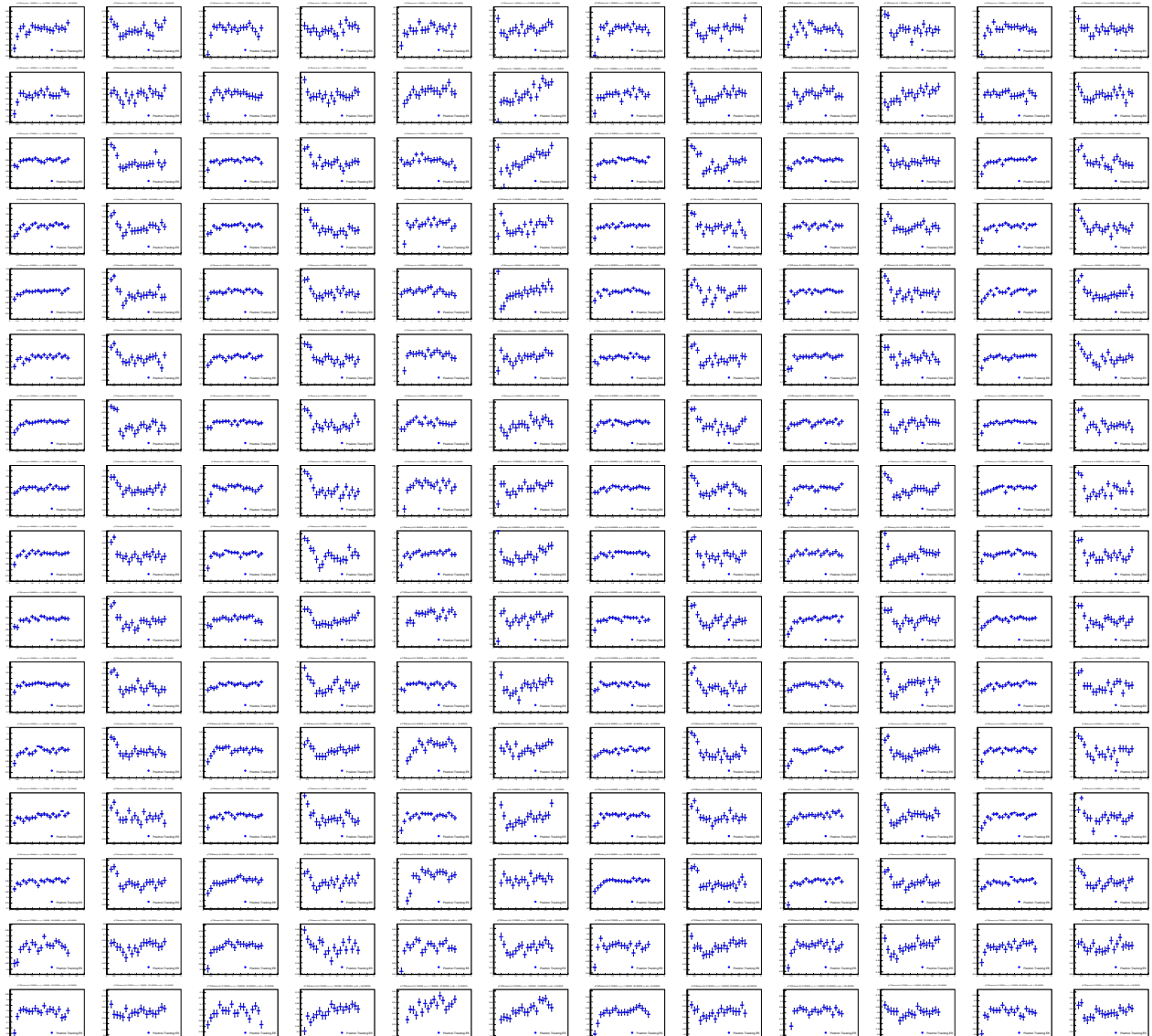




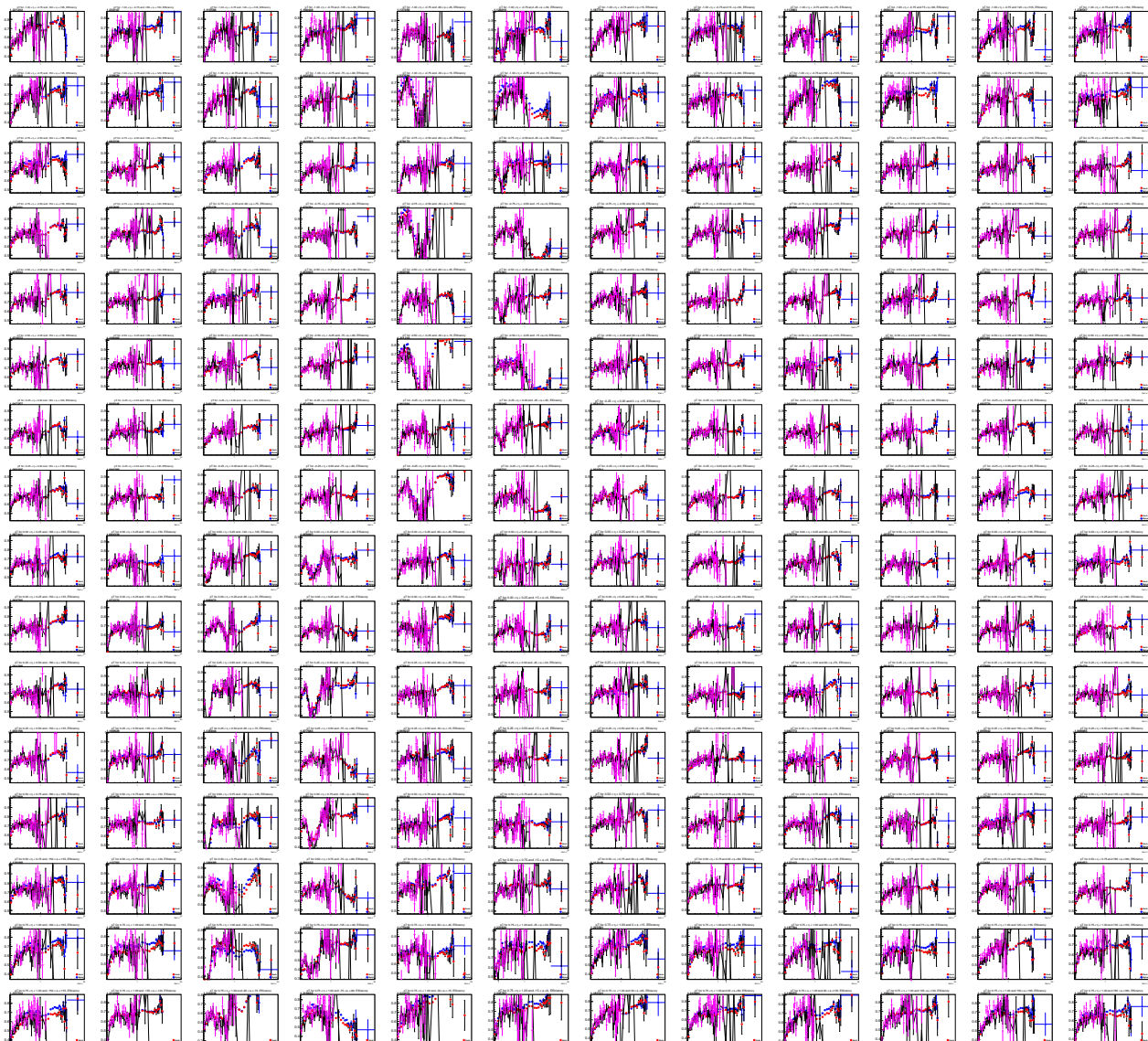
**972 Appendix C. Electron Tracking Efficiency Figures**



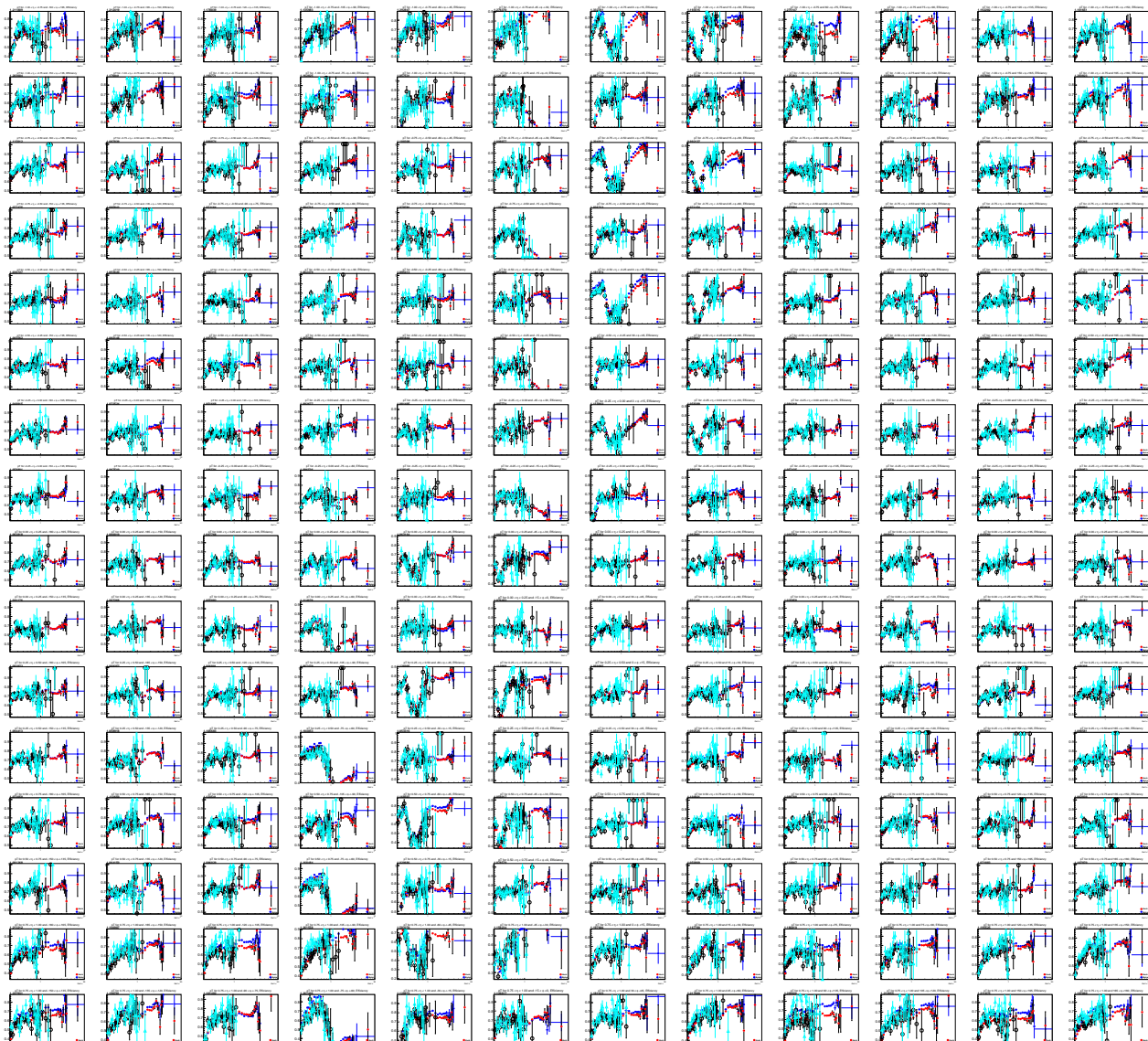
<sup>974</sup> **Appendix D. Positron Tracking Efficiency Figures**



976 **Appendix E. Electron Matching Efficiency Figures**



**978 Appendix F. Positron Matching Efficiency Figures**



980 **Appendix G. Comparison of Matching Efficiency Figures - Acceptance Correcting All Tracks for AuAu200**  
981 **Method**





**984 Appendix H. Comparison of Matching Efficiency Figures - Acceptance Correcting All Tracks and TOF Match  
985 Only Separately for AuAu200 Method**





**988 Appendix I. Comparison of Matching Efficiency Figures - Acceptance Correcting All Tracks for AuAu200  
989 Method and Variance Method**



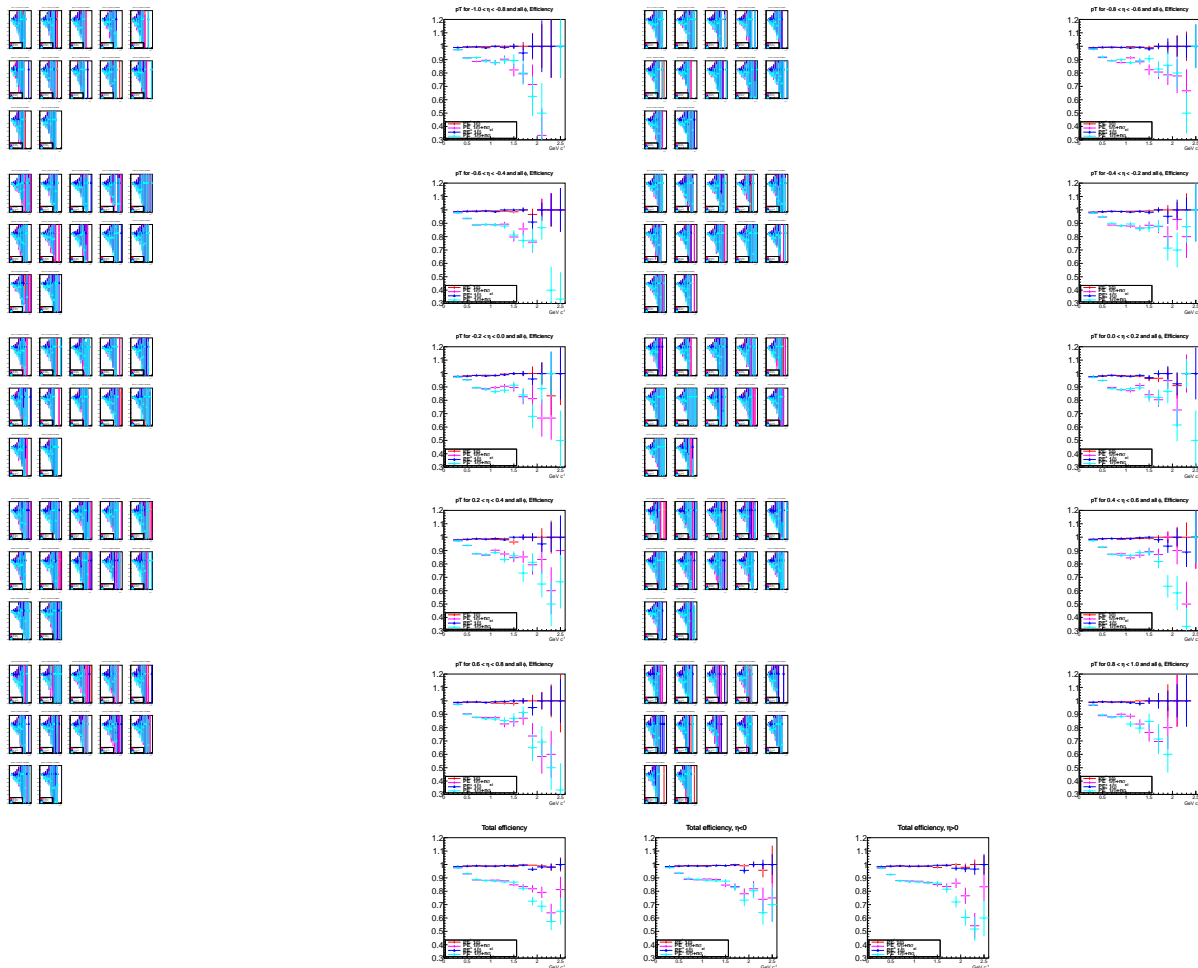


**992 Appendix J. Comparison of Matching Efficiency Figures - Acceptance Correcting All Tracks and TOF Match  
993 Only Separately for AuAu200 Method and Variance Method**

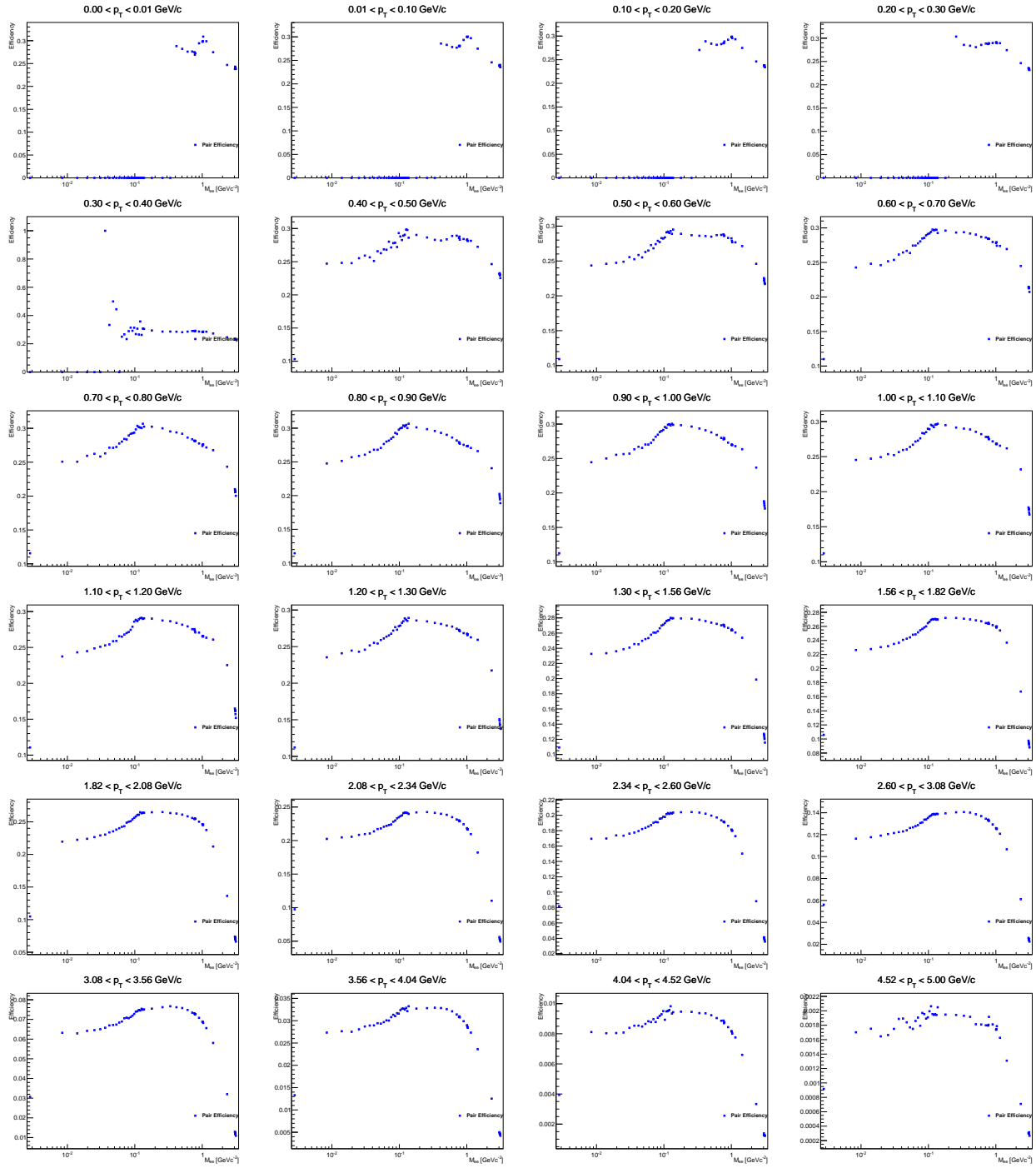




996 **Appendix K. PID Efficiency Figures**



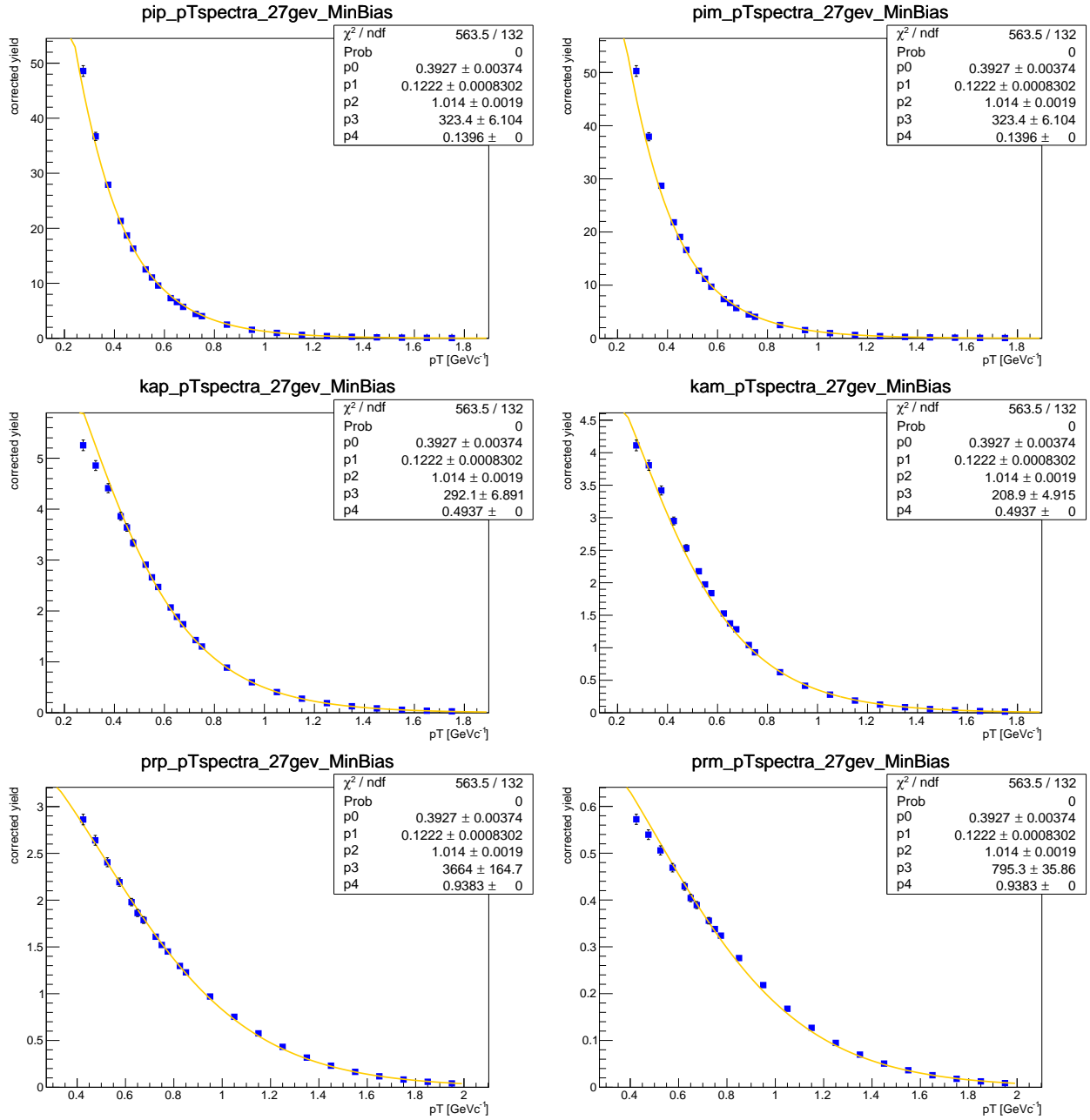
998 **Appendix L. Pair Efficiency Figures**



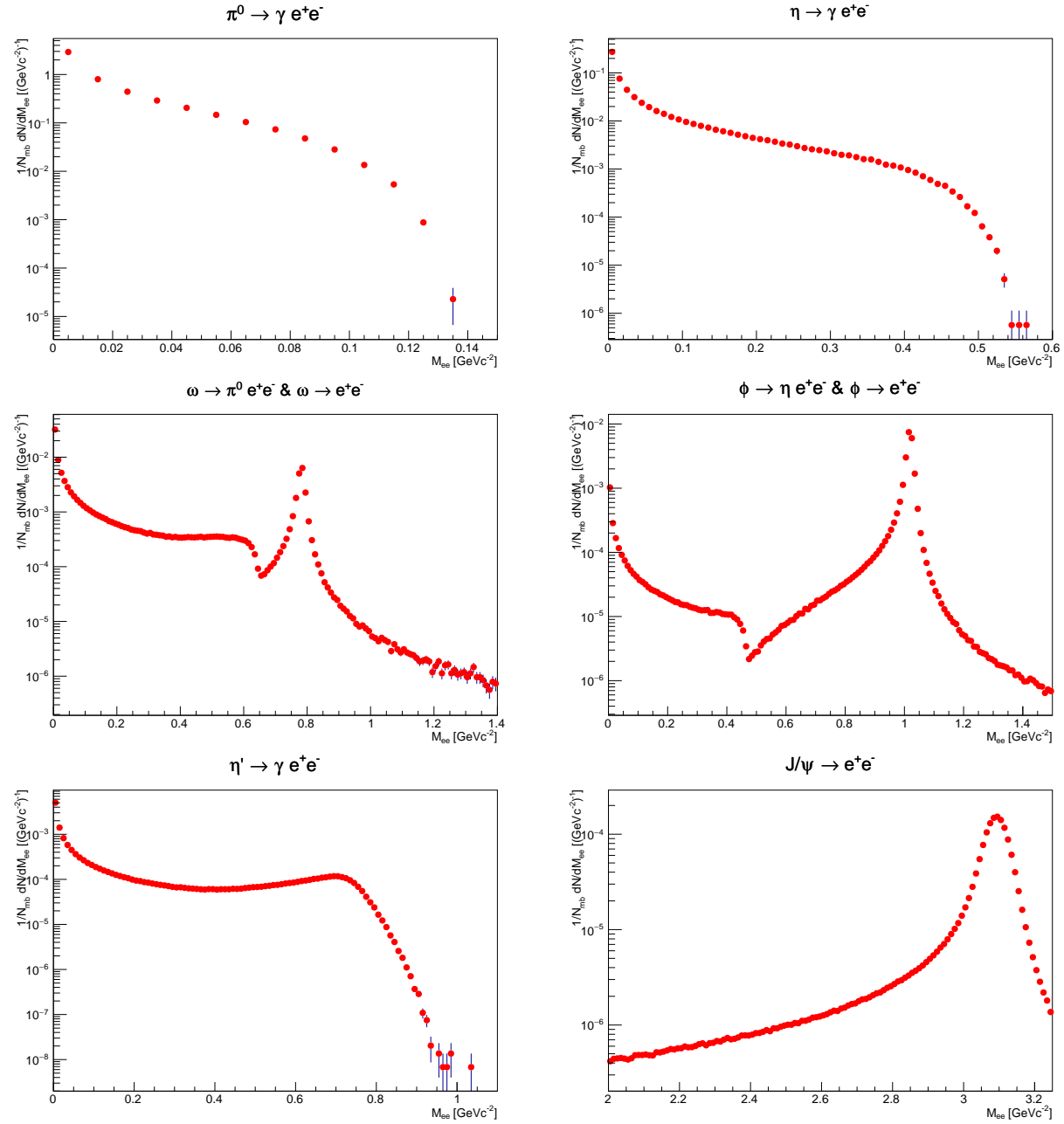
1000 **Appendix M. Analysis Cuts**

1001 A list/table of cuts used in the analysis.

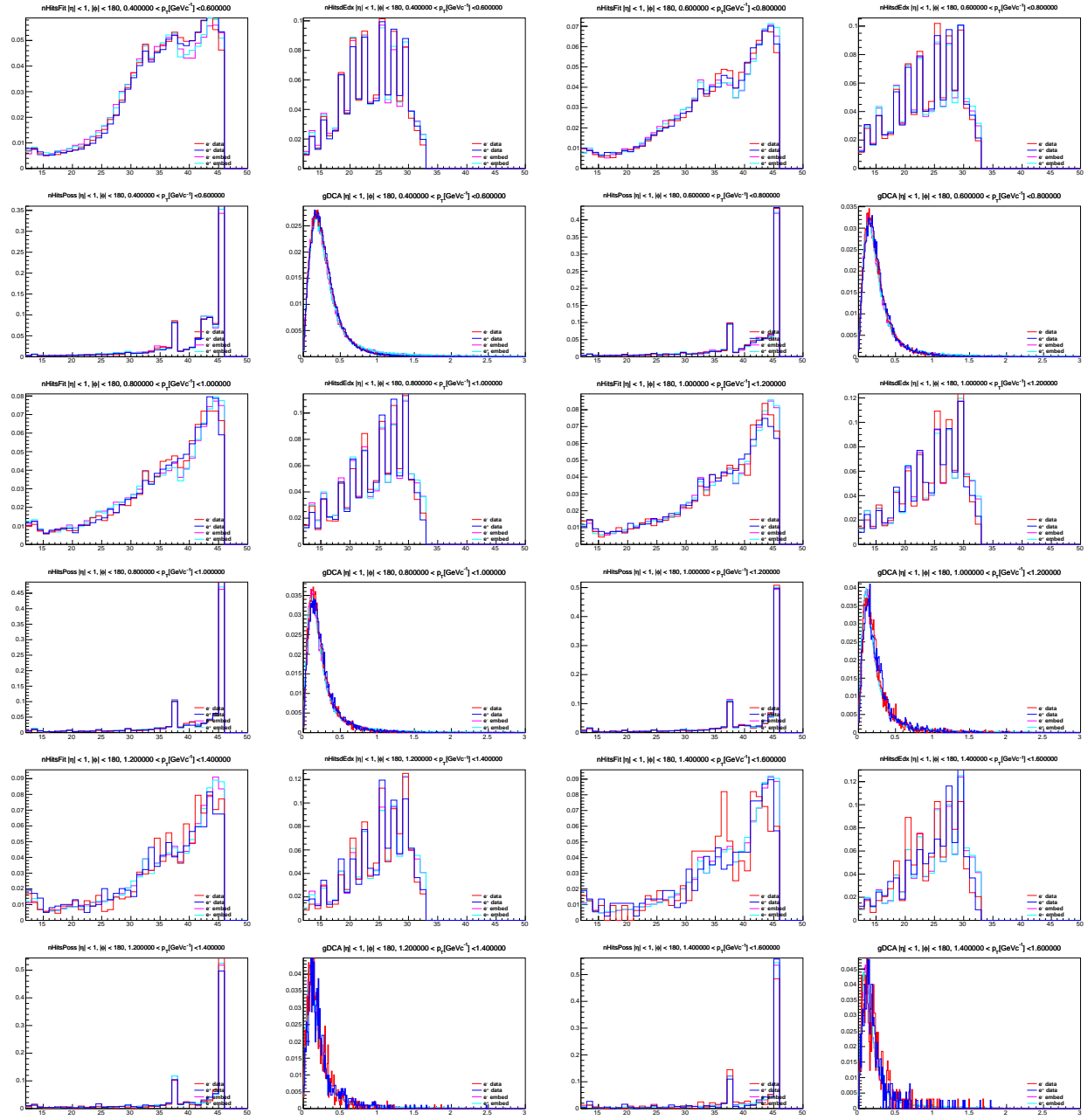
1002 **Appendix N. Tsallis Blast Wave Fits**

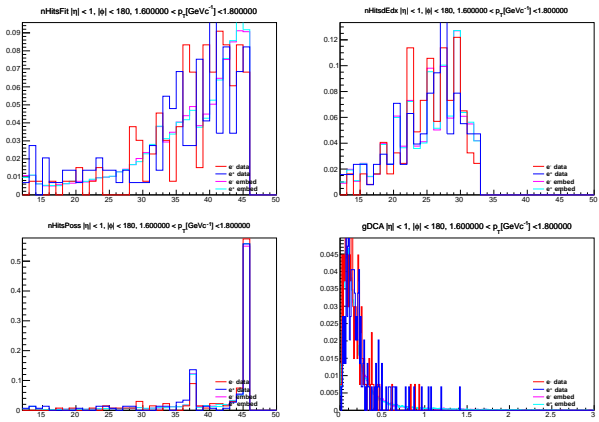


1004 **Appendix O. Hadron Cocktail Yields**

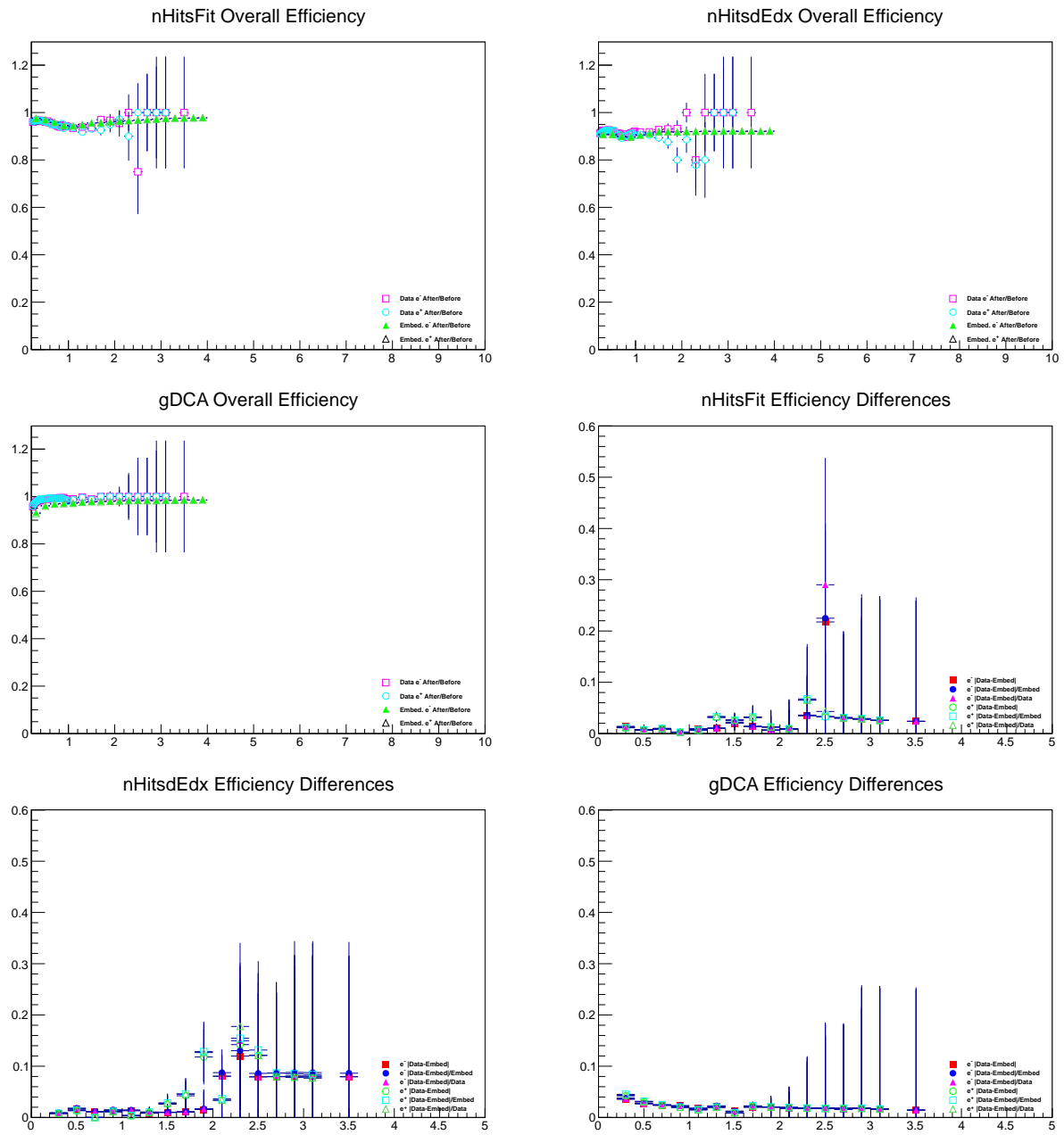


1006 **Appendix P. Tracking Systematic Uncertainties Quality Assurance I**





1009 **Appendix Q. Tracking Systematic Uncertainties Quality Assurance II**



1011 **References**

- 1012 [1] A presentation on different event plane flattening methods. <http://www.star.bnl.gov/protected/bulkcorr/posk/reCentering/ReCentering.ppt.pdf>  
1013 [2] T. Ullrich and Z. Xu, <http://arxiv.org/abs/physics/0701199v1>.  
1014 [3] N. M. Kroll and W. Wada, Physical Review 98, 1355-1359 (1955).  
1015 [4] M. N. Achasov et al., Physics Letters B 504, 275-281 (2001).  
1016 [5] R. Arnaldi et al., Physics Letters B 667, 260-266 (2009).  
1017 [6] L. G. Landsberg, Physics Reports 128, 301-376 (1985).  
1018 [7] K. A. Olive et al. (Particle Data Group), Chinese Physics C 38, 090001 (2014).  
1019 [8] Z. Tang et al., Physical Review C 79, 051901 (2009).  
1020 [9] G. Agakichiev et al. (CERES), European Physical Journal C 41, 475-514 (2005).  
1021 [10] [http://www.star.bnl.gov/protected/common/common2011/centrality/27GeV/table/table\\_Ncoll\\_vs\\_centrality\\_systematicerror.txt](http://www.star.bnl.gov/protected/common/common2011/centrality/27GeV/table/table_Ncoll_vs_centrality_systematicerror.txt)  
1022  
1023 [11] Annual Review Nuclear Particle Science 57, 205-243 (2007).  
1024 [12] T. Sjöstrand et al., Journal of High Energy Physics 05, 26 (2006).  
1025 [13] L. Adamczyk et al. (STAR Collaboration), Phys. Rev. C 92, 104904 (2015).  
1026 [14] K. Aamodt et al. (ALICE Collaboration), Phys. Lett. B 696 328-337 (2011).